REPORT NO. FAA-RD-74-74.I

ANALYSIS OF PREDICTED AIRCRAFT WAKE VORTEX TRANSPORT AND COMPARISON WITH EXPERIMENT

Volume I -- Wake Vortex Predictive System Study

M.R. Brashears
N.A. Logan
S.J. Robertson
K.R. Shrider
C.D. Walters

APRIL 1974

FINAL REPORT

Prepared for
U.S. DEPARTMENT OF TRANSPORTATION
FEDERAL AVIATION ADMINISTRATION
SYSTEMS RESEARCH AND DEVELOPMENT SERVICE
Washington DC 20591

Technical Report Documentation Page

1. Report No.
FAA-RD-74-74.I

2. Government Accession No.

3. Recipient's Catalog No.

4. Title and Subtitle
ANALYSIS OF PREDICTED AIRCRAFT WAKE VORTEX TRANSPORT
AND COMPARISON WITH EXPERIMENT
Volume I - Wake Vortex Predictive System Study

5. Report Date
April 1974

6. Performing Organization Code

7. Author(s) M.R. Brashears, N.A. Logan, S.J. Robertson
K.R. Shrider and C.D. Walters

8. Performing Organization Report No.
DOT-TSC-FAA-74-7.I

9. Performing Organization Name and Address
Lockheed Missiles & Space Company, Inc.*
Huntsville Research & Engineering Center
4800 Bradford Drive
Huntsville AL 35807

10. Work Unit No. (TRAIS)
FA405/R4115

11. Contract or Grant No.
DOT-TSC-593

12. Sponsoring Agency Name and Address
U.S. Department of Transportation
Federal Aviation Administration
Systems Research and Development Service
Washington DC 20591

13. Type of Report and Period Covered
Final Report
April to December 1973

14. Sponsoring Agency Code

15. Supplementary Notes
*Under contract to:
U.S. Department of Transportation
Transportation Systems Center
Kendall Square
Cambridge MA 02142

16. Abstract

A unifying wake vortex transport model is developed and applied to a wake vortex predictive system concept. The fundamentals of vortex motion underlying the predictive model are discussed including vortex decay, bursting and instability phenomena. A parametric and sensitivity analysis is presented to establish baseline uncertainties in the algorithm to allow meaningful comparison of predicted and measured vortex tracks. A detailed comparison of predicted vortex tracks with photographic and groundwind vortex data is presented. Excellent agreement between prediction and measurement is shown to exist when sufficient wind data are available. Application of the Pasquill class criteria is shown to be an effective technique to describe the wind profile in the absence of detailed wind data. The effects of wind shear and the Ekman spiral on vortex transport are discussed. It is shown that the combination of wind shear and ground plane may be possible mechanisms underlying vortex tilting and a theoretical explanation is advanced that is somewhat supported by comparison with the experimental data. Finally, recommendations for further vortex data collection in the vicinity of an airport are presented.

17. Key Words
Vortices
Aircraft Wakes
Wake Turbulence
Wind Shear
Wake Vortex Predictive System
Ground Plane
Vortex Tilting
Vortex Transport

18. Distribution Statement
DOCUMENT IS AVAILABLE TO THE PUBLIC
THROUGH THE NATIONAL TECHNICAL
INFORMATION SERVICE, SPRINGFIELD,
VIRGINIA 22151.

19. Security Classif. (of this report)
Unclassified

20. Security Classif. (of this page)
Unclassified

21. No. of Pages
256

22. Price

Form DOT F 1700.7 (8-72)

Reproduction of completed page authorized

PREFACE

This document represents the final report of Contract DOT-TSC-593 and covers the period 2 April to 2 December 1973.

This study was performed by personnel at the Lockheed Missiles & Space Company, Inc., Huntsville Research & Engineering Center, Huntsville, Alabama. The project engineer and principal investigator for this study was Dr. M. R. Brashears of the Fluid Mechanics Applications Group.

The authors are especially grateful to Dr. J. N. Hallock, TSC Contracting Officer's Technical Monitor, for his contributions and able assistance during the performance of this contract. We also sincerely thank Dr. D. C. Burnham and Mr. Tom Sullivan of TSC for providing the vortex tracking data. To Mr. L. Garodz and Mr. N. Miller of NAFEC, we express our appreciation for their support during the testing and in reduction of the rawinsonde and tower meteorological sensor data.

CONTENTS

Section VOLUME II Page

CONTENTS (Continued)

CONTENTS (Continued)

Volume II

Appendixes

LIST OF ILLUSTRATIONS (Continued)

LIST OF ILLUSTRATIONS (Continued)

SYMBOLS

A	area of vortex pair 2-D oval within limiting streamline
a	radius of vortex core; 1/2 separation distance of vortex pair
b	aircraft wingspan; height of vortex pair above ground plane
b'	instantaneous separation of vortex pair
b''	effective aircraft wingspan
h	height above ground plane
K	diffusivity of atmosphere
K_T	vertical lapse rate of temperature
K_1	wind shear
k	von Karman constant
L'	Monin-Obukhov scaling length
ℓ	mixing length
P	pressure
q	absolute velocity
R	turbulence correlation coefficient
r	distance from vortex center
T	temperature
t	time
U	absolute horizontal wind speed
U*	friction velocity
u	down runway wind speed
V	aircraft speed; induced vortex velocity
V_s	sink rate of vortex
v	cross runway wind speed; crosswind velocity of vortex parcel; circumferential velocity of vortex

Section 1
INTRODUCTION

With the introduction of the large transport aircraft (B-747, DC-10, L-1011) and the ever increasing airport congestion, the wake vortex problem has taken on added significance. The vortices from large aircraft can present a severe hazard to other aircraft which inadvertently encounter the vortices; the following aircraft can be subjected to rolling moments which exceed the aircraft's roll control authority, to a dangerous loss of altitude, and to a possible structural failure. The probability of an aircraft-vortex encounter is greatest in the terminal area where light and heavy aircraft operate in close proximity and where recovery from an upset may not be possible due to the low aircraft altitude. To prevent aircraft-vortex encounters, the present solution (implemented by the Federal Aviation Administration in March 1970) has been to increase the separation standards behind the heavy jets. However, these increased separations decrease the capacity of the airport system and the present and predicted demands on airports cannot be met by just constructing additional runways and airports. Airport and airway system utilization are projected to double by 1980 and to increase five-fold by 1995. Technologically (using dual runways, improved landing aids, etc.), runway capacity can be substantially increased today, but not until the wake vortex problem has been alleviated will a permanent solution exist.

There are two primary approaches to the wake vortex problem which are currently underway. NASA is concentrating on methods to hasten the demise of vortices at the source by modifying the aircraft. Among the many concepts being investigated are wing spoilers, mass injection, wingtip modifications, and the deployment of trailing devices. These concepts, if they can be shown to economically and effectively reduce the vortex hazard, may not be available in the near future and would still entail a massive retrofit program to alter the current fleet of transport aircraft. For future generation aircraft, NASA is examining the efficacy of aircraft design changes such as mounting engines at the wing tips and tailoring the wing design to cause the vortices to burst quickly.

Concurrently, the FAA/Transportation Systems Center (TSC) approach to the vortex problem has been to develop systems which use meteorological sensors and/or vortex tracking sensors to provide safe spacing between aircraft and to issue a warning should a hazardous condition exist or be forecast. This approach is predicated on the observation that the separation criteria are conservative most of the time as they ignore conditions such as strong crosswinds which will cause the vortices to dissipate rapidly or to blow clear of the path of a following aircraft. Measurements have shown that vortices rarely remain stationary and do not persist indefinitely. The frequency of occurrence of an aircraft-vortex encounter can be shown to be small; traffic is thus unnecessarily delayed by always adhering to the present inflexible regulations.

A warning system is being implemented (Ref. 1) which provides a protected region in the approach corridor of a runway by constantly monitoring the corridor with vortex tracking sensors. More advanced systems will require the ability to forecast vortex motions and decay. A simple vortex predictive system has been recently proposed (Ref. 2) but has not been validated. Preliminary results on forecasting the transport and decay of vortices have been reported by Brashears and Hallock (Ref. 3) and Tombach (Ref. 4) who conducted flight experiments with smoke-marked vortices from a Cessna 170 and correlated the time-to-linking of a vortex pair and vortex bursting with the ambient turbulence level. A new analysis (Ref. 5) for the Crow instability (Ref. 6) expresses the time-to-linkage as an explicit function of the turbulence dissipation rate and is corroborated by the limited flight test data.

To develop a model for the transport of the vortex pair, fluid mechanic representations of the various vortex-induced and atmospheric effects have been combined into a unified computer simulation. A series of flight tests using B-747, B-707, B-727 and DC-6 aircraft were done at the National Aviation Facilities Experimental Center (NAFEC), Atlantic City, New Jersey, in which both the motion of the vortices and the attendant meteorological conditions were recorded. The purposes of the tests were to examine the efficacy of a simple transport model and to extend the model by a parametric analysis of the ambiguities between the measured and predicted vortex motions.

Section 2
VORTEX TRANSPORT MODEL

2.1 FUNDAMENTALS OF VORTEX MOTION

The idealized flow about a circular vortex consists of an inverse radial velocity distribution (see Fig. 2-1); but this predicts an infinite velocity at the vortex center. However, in reality, the vorticity is not concentrated at a point but is distributed over some non-zero area. The fluid in this area (the core) moves like a rigid body rotating about the center of the vortex (Fig. 2-1). The vortex has a velocity field with the magnitude at any point called the induced velocity. (It is customary to refer to this velocity as induced by the vortex but it should be noted that this is merely a representation and that actually it is the velocity that would coexist with the vortex in an otherwise undisturbed fluid.)

The transport model approximates the aircraft vortices by two free vortices with finite cores. The induced velocity field of each vortex is shown in Fig. 2-2 along with the distribution of circulation (vorticity). The defining equations are derived by equating the static pressure distribution to the centrifugal acceleration with the results given in the figure. The instantaneous streamlines of the flow field due to a vortex pair are shown in Fig. 2-3a while the relative streamlines produced by the sinking motion are shown in Fig. 2-3b. Neither vortex induces any motion to itself; thus the sink velocity is given by

$$w_s = \frac{-\Gamma}{2\pi b'}$$

where Γ is the circulation or "strength" of the vortex and b' is the instantaneous separation of the vortex pair. A limiting streamline exists and that fluid inside the oval defined by the streamline travels with the vortices in the

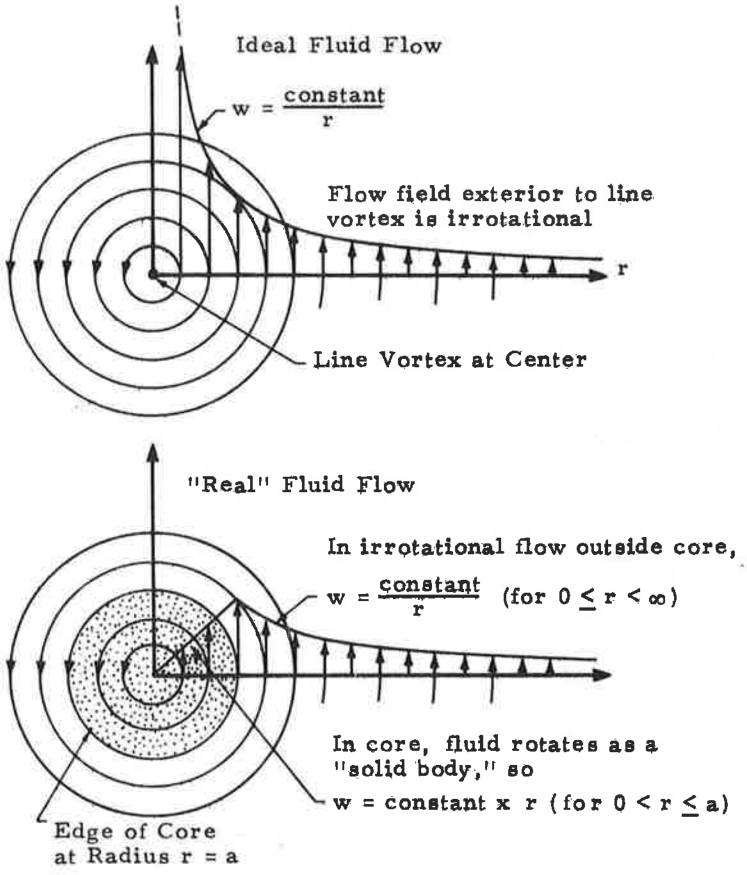

Fig. 2-1 - Comparison of Ideal and "Real" Flow Fields for Two-Dimensional Flow About a Vortex

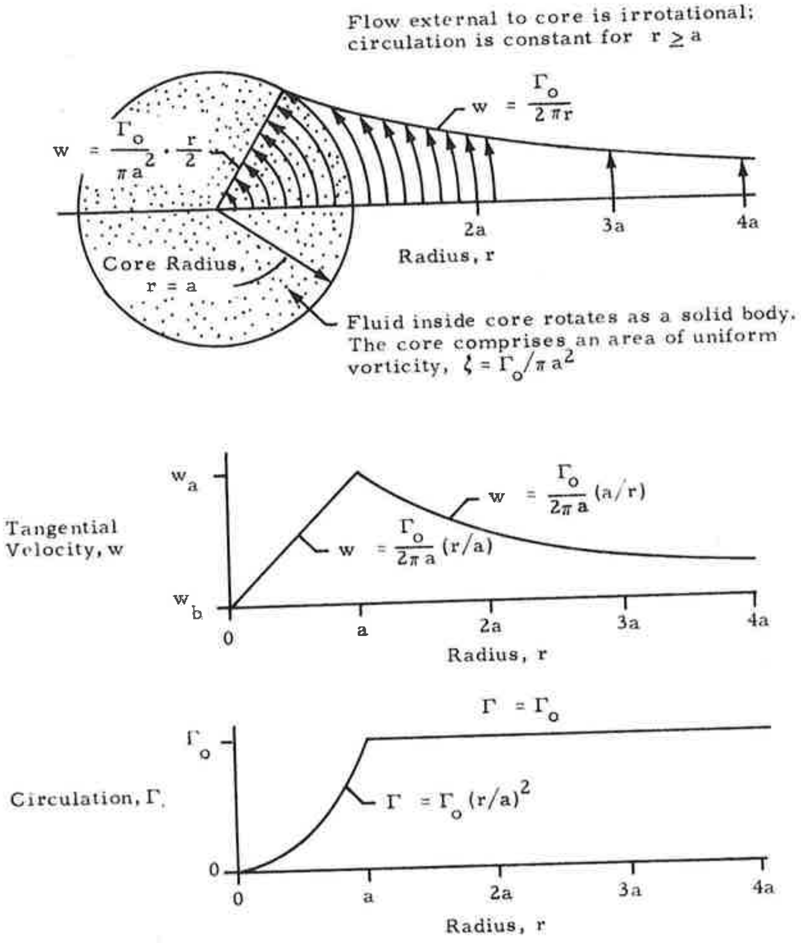

Fig. 2-2 - Rankine Vortex (Two-Dimensional Model)

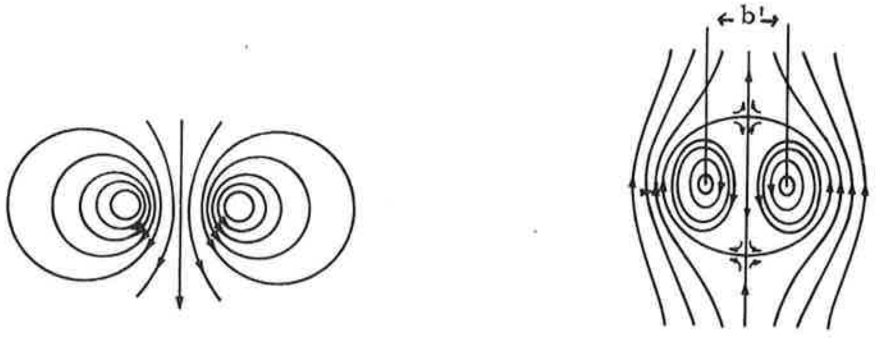

a. Instantaneous Streamlines Due to a Vortex Pair

b. Steady Streamlines Due to a Vortex Pair

Fig. 2-3 - Streamlines of a Vortex Pair

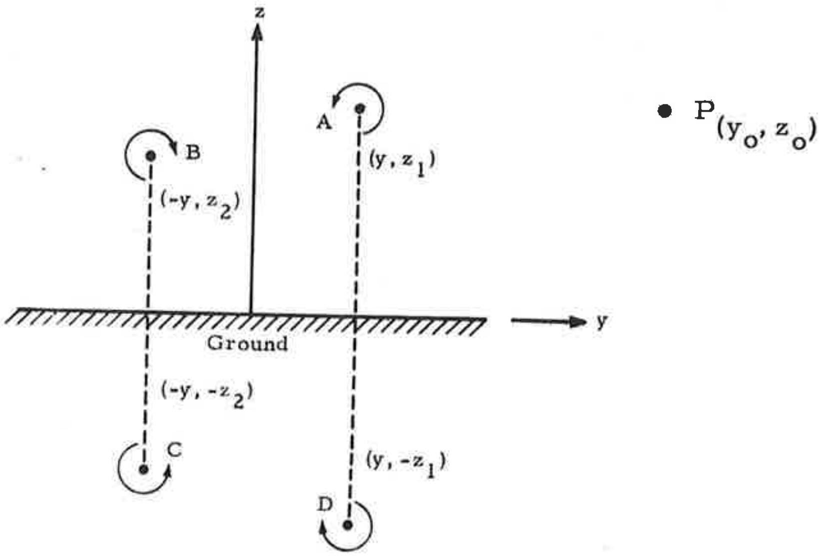

Fig. 2-4 - Vortex Image System for Ground Plane Interaction absence of mixing. The size and shape of the oval can be calculated from potential flow theory (Ref. 7) and is found to be nearly elliptical and of area:

$$A \cong 11.42 \left(\frac{b'}{2}\right)^2$$

To establish the transport of the vortex pair, the relationships of the defining parameters to the generating aircraft must be found. This can be done by relating the final conditions of the rollup process to the aircraft parameters and using these values as initial conditions.

The circulation-loading distribution of a wing defines all the properties of the inviscid vortex development; however, at the present stage of the transport model development, it is merely assumed that an organized vortex pair motion exists. The pair moves in its induced field causing the vortices to convect downward with a velocity directly proportional to the aircraft lift coefficient and velocity and inversely proportional to the aspect ratio. Using classical dynamics and the elliptic lift approximations (Ref. 8), the initial wake can be classified by:

$$\Gamma = \frac{4W}{\pi \rho V b}$$

where W is the aircraft weight, ρ is the air density, V is the aircraft speed, and b is the wingspan. Accordingly, the initial vortex spacing will be:

$$b' = \frac{\pi}{4} b$$

The aircraft weight, flight speed, and wingspan are thus the only aircraft parameters used. The effect of flaps can be considered by replacing the wingspan b with an effective wingspan b''; larger flap settings alter the load distribution by concentrating the load distribution more inboard and thus $b'' < b$.

Future modifications to the model may use as the initial condition the vorticity distribution as calculated by some procedure such as the Betz model (Ref. 9). The Betz model replaces the precise details of the inviscid rollup of the vortex sheet with a local axisymmetric distribution of vorticity, so constituted and so positioned to conserve vorticity and moments of vorticity behind each half of a wing. Recently (Ref. 10) the Betz model has been modified to take into account the deflection of flaps, and the comparisons with experiment are very encouraging.

2.1.1 Ground Effect

Next to the local wind, the ground effect is the most important mechanism affecting the transport of the vortices and is readily calculated by using the image system of classical hydrodynamical theory (Ref. 7). For two-dimensional line vortices, the velocity of any one vortex is due solely to the remaining vortices (real and image) in the system.

In general, the vortex system near the ground can be represented by two counter-rotating vortices along with their respective images as depicted in Fig. 2-4. The corresponding horizontal velocity at any point, P, can easily be seen to be

$$\dot{y}_P = \frac{V_A(z_1 - z_o)}{r_{AP}} - \frac{V_B(z_2 - z_o)}{r_{BP}} - \frac{V_C(z_2 + z_o)}{r_{CP}} + \frac{V_D(z_1 + z_o)}{r_{DP}} + v$$

$$\dot{z}_P = \frac{V_A(y_o - y)}{r_{AP}} - \frac{V_B(y_o + y)}{r_{BP}} + \frac{V_C(y_o + y)}{r_{CP}} - \frac{V_D(y_o - y)}{r_{DP}} + w \qquad (2.1)$$

where

$$r_{AP} = \sqrt{(y - y_o)^2 + (z_1 - z_o)^2} \text{ and } V_A = \frac{\Gamma_A}{2\pi\, r_{AP}}$$

$$r_{BP} = \sqrt{(-y - y_o)^2 + (z_2 - z_o)^2} \text{ and } V_B = \frac{\Gamma_B}{2\pi\, r_{BP}}$$

$$r_{CP} = \sqrt{(-y - y_o)^2 + (-z_2 - z_o)^2} \text{ and } V_C = \frac{\Gamma_C}{2\pi r_{CP}}$$

$$r_{DP} = \sqrt{(y - y_o)^2 + (-z_1 - z_o)^2} \text{ and } V_D = \frac{\Gamma_D}{2\pi r_{DP}}$$

and

v = crosswind velocity

w = vertical velocity.

When the initial altitudes are the same, it is readily seen that the equations reduce to the well known motion of a vortex filament parallel to two perpendicular planes (the axis of symmetry and the ground). The initial sink velocity is determined by the instantaneous separation of the wake vortices; thus the motion of vortices created just above an altitude of b'/2 will travel as if they were initially created at a separation somewhat less than b'. If, however, the vortices are created at an altitude less than b'/2, the initial horizontal velocity will be greater and the spreading will occur more rapidly than in the previous case. The vortices will then descend to an altitude less than that corresponding to $\pi b/8$.

2.1.2 Wind and Wind Shear

The effect of a wind field on the transport of the vortex pair can be calculated by superimposing the wind vector on the existing motion. This vector is defined in terms of the magnitude and azimuth at various altitudes for the horizontal portion and with a variable vertical component. This is in effect assuming that the wind merely has a translating effect upon the mass of air contained in the oval.

The concept of wind shear is included to explain trends known to exist from experiment. The downwind vortex often rises after encountering the ground plane and this can be explained by considering the pressure gradients that flow in the boundary layer. The sinking oval containing the aircraft vortices produces a relative flow field about its boundary. In the presence of a groundplane, cross flow in the earth's boundary layer begins to operate against an adverse pressure gradient beneath the pair. As the vortex transport brings the pair closer to the ground, this adverse pressure gradient may become strong enough to separate the flow producing a bubble containing vorticity opposite in sense to the downwind aircraft vortex. Harvey and Perry (Ref. 11) depicted the bubble as moving rapidly in the downwind direction and finally detaching from the surface as a secondary vortex fed by a vortex sheet from the separation point. This secondary vortex induces an upward component to the total induced velocity field, thus causing the downwind vortex to rise. This is shown schematically in Fig. 2-5.

Burnham (Ref. 12) has suggested modeling this phenomenon by simulating the shear layers by rows of discrete vortices where all of the vorticity in the earth's boundary layer is contained within these vortices. An image system of identical vortices is used to satisfy the boundary condition of no vertical wind component at the surface. The system of shear vortices can be described in terms of any number of vortices per row and any number of rows (plus the corresponding images). The magnitude of the circulation of each vortex is calculated from the geostrophic wind condition and this value can be distributed over the boundary layer in any fashion by assigning each row a fractional strength corresponding to the desired distribution.

The general effect of using wind shear vortices is shown in Figs. 2-6 through 2-8. Figure 2-6 shows the effect of the wind shear with all of the vorticity concentrated in one row at an altitude of 30 feet with a spacing of 50 feet between the discrete vortices. It is seen that the downwind vortex does indeed rise while no apparent difference is noted in the upwind vortex motion. Figure 2-7 depicts the effect of changing the number (I) of shear layers (rows) where each row has equal fractional strength (F). Again, the upwind vortex path is essentially unchanged. However, the downwind vortex transport shows a rising trend that is weakly dependent on the number of rows. A single row is noted to produce the largest change for a given instant of time. The effect of distributing the vorticity within the shear layer on the

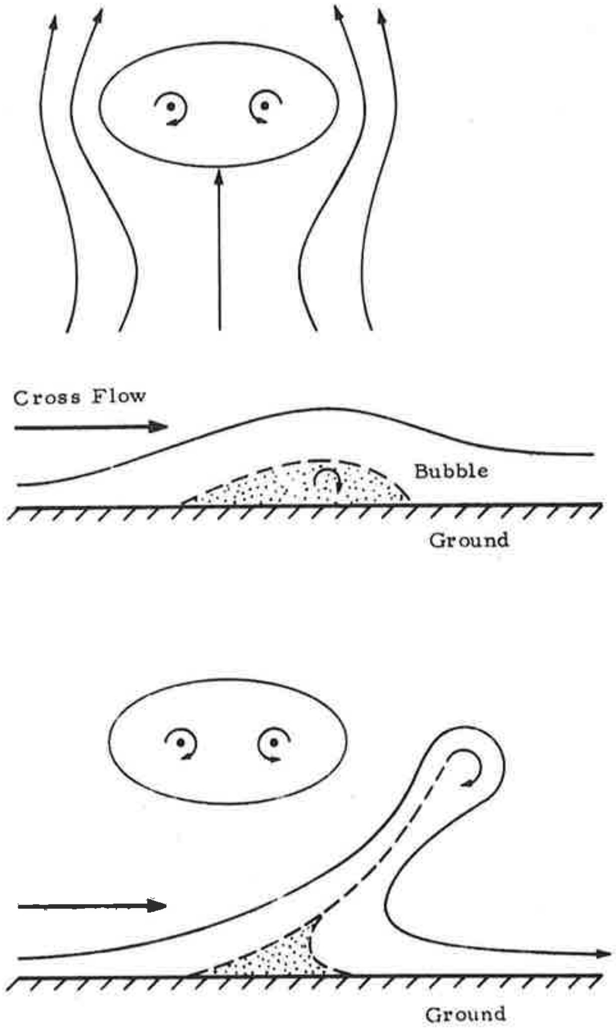

Fig. 2-5 - Schematic of Wind Shear (Ref. 11)

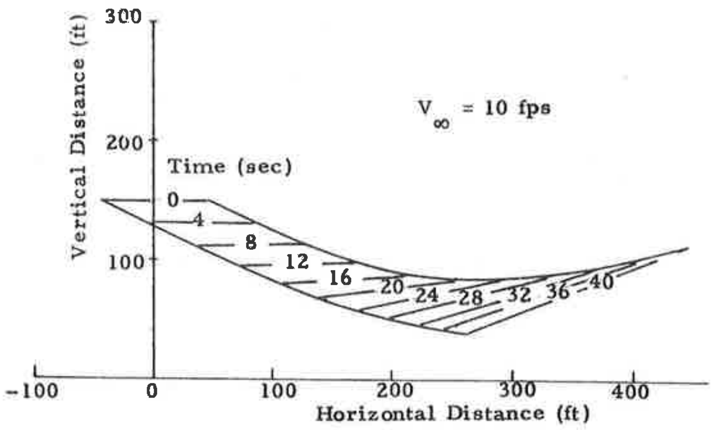

Fig. 2-6 - Transport Path for Vortex Pair in Wind Shear

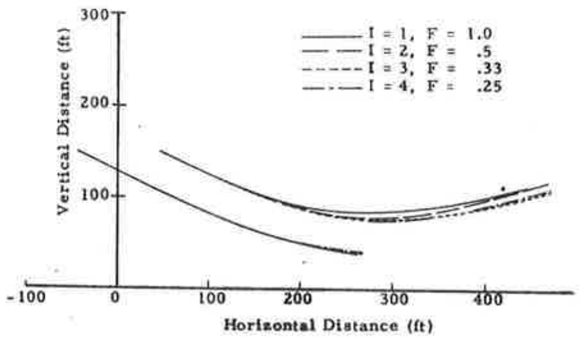

Fig. 2-7 - Comparison of the Effect of the Number of Rows on Transport Path

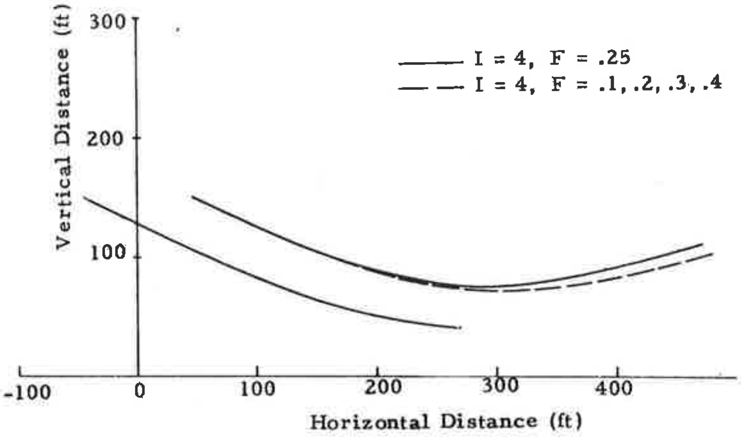

Fig. 2-8 - Comparison of the Effect of the Vorticity Distribution on Transport Path

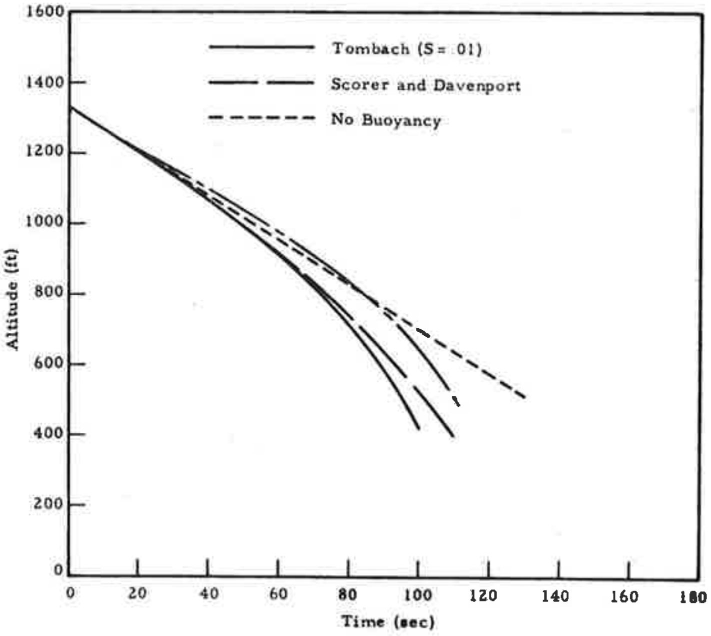

Fig. 2-9 - Altitude vs Time in Isothermal Atmosphere with No Shear motion is shown in Fig. 2-8 where the largest fractional strength (0.4) is contained in the row nearest the ground.

Recently Lissaman, et al. (Ref. 5) analyzed the effect of a uniform shear on the vortex recirculating cell of the vortex pair. It was shown that as the strength of the uniform shear increases, the size of the upwind vortex cell also increases. It was implied that this phenomena could give rise to vortex tilting that has been observed from experiments (Ref. 4) as the vorticity diffusing radially outward would reach the downwind cell boundary first thus causing a circulation mismatch between the vortex pair. This phenomena would cause the upwind vortex to rise; a result contrary to the aforementioned concept.

2.1.3 Buoyancy

The vertical descent of the vortex wake is expected to vary as a function of atmospheric conditions and there are indications that buoyancy may be a significant factor. The driving force for producing changes in the initial motion is a result of the difference in density created during the descent of the pair through a stratified fluid. Even for the case of no initial density difference (no engine exhaust entrainment), a difference is produced if the nearly adiabatic compression of the oval (due to increasing atmospheric density) is different from the stratification of the atmosphere. The resulting density difference produces a buoyant force that affects the vertical momentum of the vortex pair. Buoyancy generated in this manner alters the circulation (Ref. 13); however, the manner of alteration has not been established. Tombach (Ref. 14) maintains that the buoyancy generated vorticity is entrained through mixing of the ambient air and the recirculating flow at the upper boundary of the oval. Scorer and Davenport (Ref. 15) derived a model that shows just the opposite, namely detrainment of the vorticity (a consequence of the assumption of constant circulation). Three other models also predict entrainment (Ref. 16, 17 and 18). Tombach (Ref. 4) and Lissaman (Ref. 5) thoroughly review the theoretical formulations for the descent of wakes in a stably stratified atmosphere.

An experimental observation that supports the entrainment idea (or at least partial entrainment) is the fact that the vortex pair has been known to descend at nearly constant spacing and finally come to rest at some altitude. To explain this, the concept of entrainment of buoyancy generated circulation must be used in that the internal distribution of the generated vorticity must be such that the vorticity of one vortex is negated at the location of the other vortex so there is no induced sink velocity.

The models chosen to represent the effect of buoyancy in the transport model are Tombach's (Ref. 14) and Scorer and Davenport's (Ref. 15). The reasons for choosing these two theories is that a representation of the full spectrum of events is contained in these two models.

A comparison of the two theories is shown in Figs. 2-9 and 2-10. In Tombach's model the solution may be generated in terms of an unknown mixing parameter, S (S = 0 corresponds to the Scorer and Davenport model). The effect of buoyancy on the descent is depicted in Fig. 2-9, where it is seen that for the first minute of life the difference is less than 10%. Figure 2-10 shows the effect of buoyancy on the separation of the vortex pair. Here the relative difference is somewhat greater (15%) during the first minute.

Lissaman, et al. (Ref. 5) recently developed a new theory for trailing vortices in a stably stratified atmosphere. No attempt will be made here to discuss the results but merely to note that the result is that buoyancy always produces a convergence in vortex separation and thusly a downward acceleration.

2.2 VORTEX DECAY, BURSTING AND INSTABILITY

The inclusion of vortex viscous decay is based on the methods of classical hydrodynamics (Ref. 7). A laminar solution for an isolated vortex is obtained from the momentum equation written in terms of the vorticity:

$$\zeta = \frac{\Gamma}{4\pi\nu t} e^{-r^2/4\nu t}$$

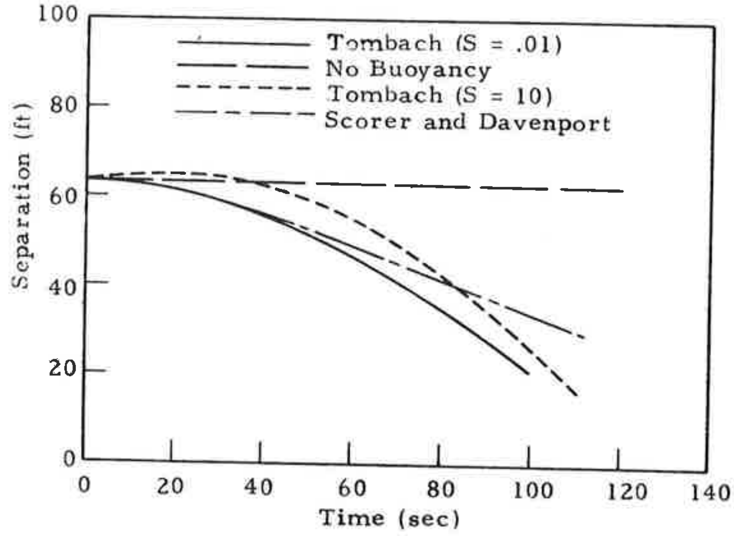

Fig. 2-10 - Separation vs Time in Isothermal Atmosphere with No Shear

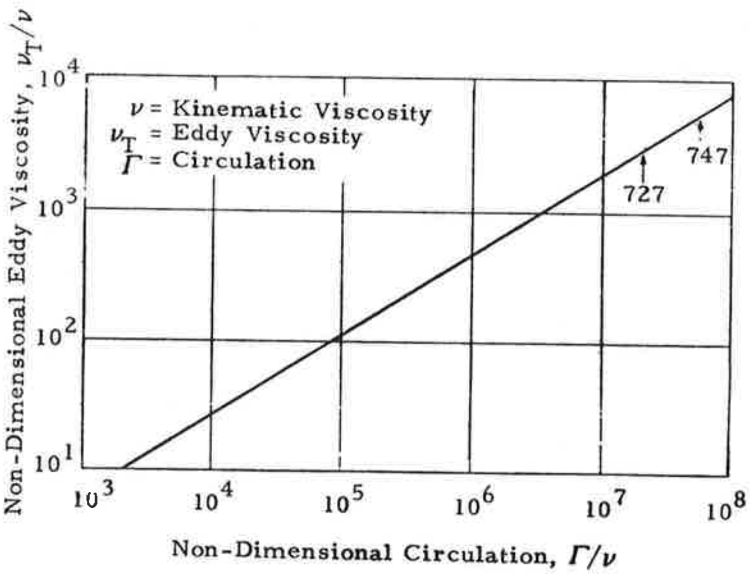

Fig. 2-11 - Circulation Curve for Eddy Viscosity and Circulation (from Ref. 20)

Replacing the kinematic viscosity ν with the sum of an eddy and kinematic viscosity (Ref. 19) yields

$$\zeta = \frac{\Gamma}{4(\nu+\epsilon)t} e^{-r^2/4(\nu+\epsilon)t}$$

and the corresponding solution for the circumferential velocity is

$$v = \frac{\Gamma}{2\pi r}\left[1 - e^{-r^2/4(\nu+\epsilon)t}\right]$$

As time increases to infinity, the velocity decreases to zero. However, the vorticity increases from zero up to a maximum value and then asymptotically approaches zero. The circumferential velocity equation is used in the model to calculate a decay using a value of the eddy viscosity obtained from Fig. 2-11. The curve represents a correlation between the circulation developed by an aircraft and the measured eddy viscosity (Ref. 20).

Vortex bursting (Refs. 21, 22 and 23) represents a phenomenon that is poorly understood. To date, no satisfactory models are known to exist that can be used for computational purposes. Tombach (Ref. 4) reports observing (in most cases) vortex bursting over a broad range of atmospheric and flight conditions. The phenomenon manifests itself as a rapid increase in core diameter followed by an axial flow of a conical front. The axial movement can be in either direction or in both directions for the same vortex (at different locations).

To include the Crow type of instability (Ref. 6) into the model, the vortex core size is calculated using Spreiter and Sacks theory (Ref. 8) and when the spacing between the vortex pair is equal to the core diameter, breakdown is predicted. This assumes that breakdown occurs upon core contact. At present, however, there is some thought that an overlap must occur before this happens (Ref. 24). It is felt that this represents a relatively good assumption for this application due to its simplicity.

2.3 THE EFFECT OF MUTUAL AND SELF-INDUCTION

Thus far, the discussion of vortex motion has centered around the concept of a system of two-dimensional line vortices. Since flight paths for both approach and departure corridors are of interest, it remains to be established how the assumption of the two-dimensionality affects the vortex location. In other words, how does the gradient of the ground effect affect vortex motion?

For the two-dimensional system, all of the motion is due to the mutual induction of the total vortex system (aircraft, image and shear vortices) and is readily calculated. To allow for aircraft flight paths that deviate from the horizontal (approach and departure), it has been assumed that the image system and mutual induction computational techniques are unchanged.

To check the assertion that the computed vortex paths will not differ significantly depending upon the dimensionality of the computational scheme, the model calculations for the distance traversed by a vortex shed at a 100-foot altitude by a B-747 are compared (see Fig. 2-12). The two-dimensional model used was that of Dee and Nicholas (Ref. 25), and the three-dimensional model was one developed by TSC (Ref. 26). As can be seen in the figure, even after 100 seconds the two- and three-dimensional models agree for the typical three-degree glide-slope employed for landing operations. However, when takeoff operations are considered (15-degrees is typical for the B-747), the full three-dimensional model must be used to be able to predict to within even 500 feet after 40 seconds where the vortices have drifted.

2.4 UNIFICATION OF THE WAKE VORTEX TRANSPORT MODEL

All of the previous mechanisms have been incorporated into a unifying wake vortex transport model. Since the buoyancy models chosen are applicable outside the ground plane region, a transformation altitude is defined to divide the geometric regions of interest into two computational regions. This altitude is normally chosen as 500 feet since at this height the ground plane

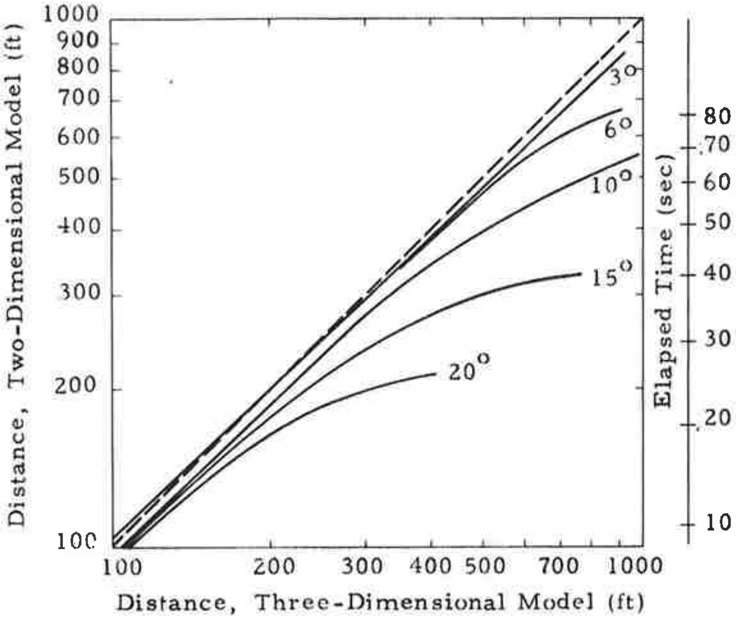

Fig. 2-12 - Comparison of Two-Dimensional and Three-Dimensional Model Calculations for Transport Distance of a Vortex Created at an Altitude of 100 Feet by a B-747

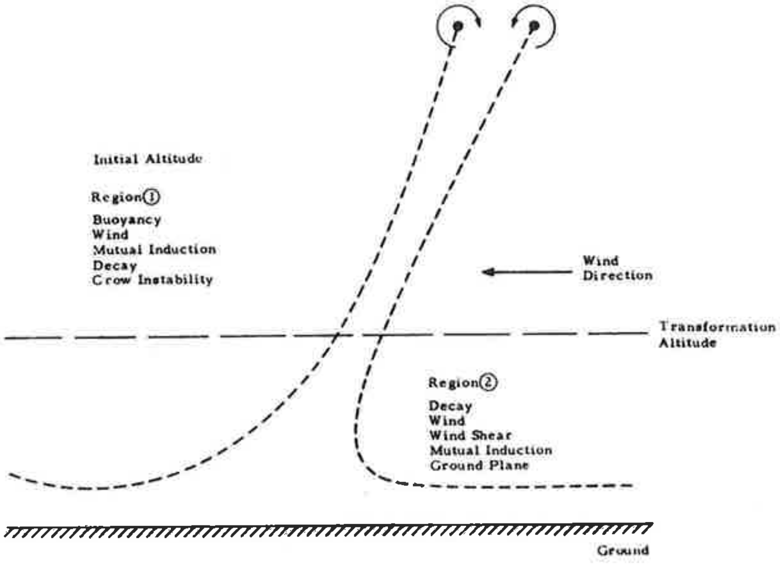

Fig. 2-13 - Schematic of Computation Regions effects are less than 2% of the transport. A superposition scheme is used to yield an explicit formulation in the velocity domain, while a Runge-Kutta numerical integration is employed in the transport domain. A schematic of the computational region is shown in Fig. 2-13.

A complete description of the vortex transport code is presented in Appendixes C through F for reader convenience. Appendix C presents a description of the output plots presented later in this report while Appendixes D through F define user information.

Section 3

MODEL SENSITIVITY ANALYSIS AND PARAMETRIC STUDY

The vortex transport model contains a large number of parameters to simulate a wide variety of aircraft types, trajectories and meteorological conditions. To simplify the model as much as possible, and to determine input data accuracy requirements, an analysis was performed to determine the sensitivity of the model to variations in these parameters. The model parameters may be grouped in the following categories: (1) wind field data; (2) aircraft mix; (3) corridor spread; (4) vortex circulation and separation; and (5) vortex decay. The results of the sensitivity analyses are discussed in the following paragraphs according to the above grouping.

3.1 WIND FIELD DATA

Variations in the wind are probably the most conspicuous source of error among the vortex transport parameters. They are also probably the least susceptible to error reduction. For these reasons, this source of error will be analyzed first and will be used as a standard for evaluating the significance of other error sources.

The wind field includes a mean wind velocity with superimposed fluctuations characterized by a standard deviation. Both the mean velocity and standard deviation are determined over some period of time. Since the maximum vortex residence time of interest in the flight corridors is of the order of two minutes, the mean velocity and standard deviation will most likely be measured over the two-minute interval immediately preceding the vortex generation (aircraft passage. (This is discussed in detail in Section 4.) These wind data will then be used to predict vortex motions over the following two or three minutes that the vortex will be in the vicinity of flight corridors. Assuming only the measured mean velocity field is used as inputs to the transport model, the errors which are considered in this analysis include the deviation in the mean wind field and the effect of fluctuations for the period of time that the vortex motion is being predicted.

Experimental data averaged over two-minute periods during vortex tracking tests (NAFEC, Atlantic City, N. J., 17 October 1972) showed wind fluctuations with standard deviations of about 25%. This was true for all altitudes along the 140-foot test tower where data were taken. The 25% value is in fair agreement with the value of 20% estimated by theory presented in Ref. 27 for longitudinal component fluctuations. The estimate was made for an altitude of 60 feet above ground level and for a roughness height of 0.113 feet (corresponding to high grass). For purposes of this analysis, therefore, it is assumed that the wind velocity during the period of predicted vortex motion may deviate as much as 25% from the mean velocity as measured during the preceding two minute interval. It is further assumed that the velocity fluctuates with an intensity corresponding to a standard deviation of 25%.

Based on these assumptions, an estimate can be made of the possible error in predicted vortex position due to wind variations. Consider the ideal, constant circulation vortex pair descending over flat terrain with a zero wind field as shown in Fig. 3-1.

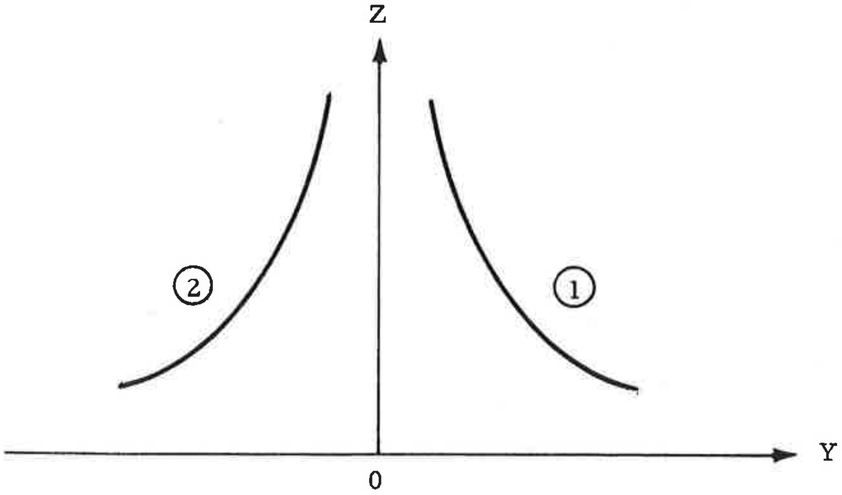

Fig. 3-1 - Vortex Pair Descending in Zero Wind Field

The positions Y and Z of the vortex pair may be computed as a function of time t as follows:

$$\begin{aligned} Y_1 &= f(t) & \qquad Y_2 &= -f(t) \\ Z_1 &= g(t) & \qquad Z_2 &= g(t) \end{aligned}$$

where the subscripts 1 and 2 refer to the positive and negative Y vortices, respectively. For a vortex pair descending in a constant, uniform horizontal wind field, the preceding computed positions are simply translated with the wind as follows:

$$\begin{aligned} Y_1 &= f(t) + \bar{v}(t) \cdot t & \qquad Y_2 &= -f(t) + \bar{v}(t) \cdot t \\ Z_1 &= g(t) & \qquad Z_2 &= g(t) \end{aligned}$$

where $\bar{v}$ is the mean cross runway (positive Y component) velocity. If an error of $\Delta\bar{v}$ exists in the input value of $\bar{v}$, a resulting error of $\Delta\bar{v}t$ will exist in the computed values of Y. With the assumed possible deviation of ±25% in the mean velocity, the resulting possible error ΔY is given by

$$\Delta Y = \pm \frac{1}{4} \bar{v} t$$

This error is illustrated in Figs. 3-2 through 3-5 for vortices generated by a Boeing 747 at the middle marker (altitude 208 feet) and threshold (altitude 60 feet) points of an approach glidepath. Predicted lateral positions and possible errors are shown as a function of time for various cross runway velocities. The error in the predicted lateral position after 2 minutes is seen to be as much as 150 feet for a 5 ft/sec wind and 600 feet for a 20 ft/sec wind. Of particular interest is the upwind vortex which tends to become stationary over the middle marker position with cross winds of about 5 ft/sec, and over the threshold with cross winds of about 10 ft/sec.

In addition to the errors due to deviation of the mean velocities from the input values, errors will exist due to random fluctuations in the velocity field.

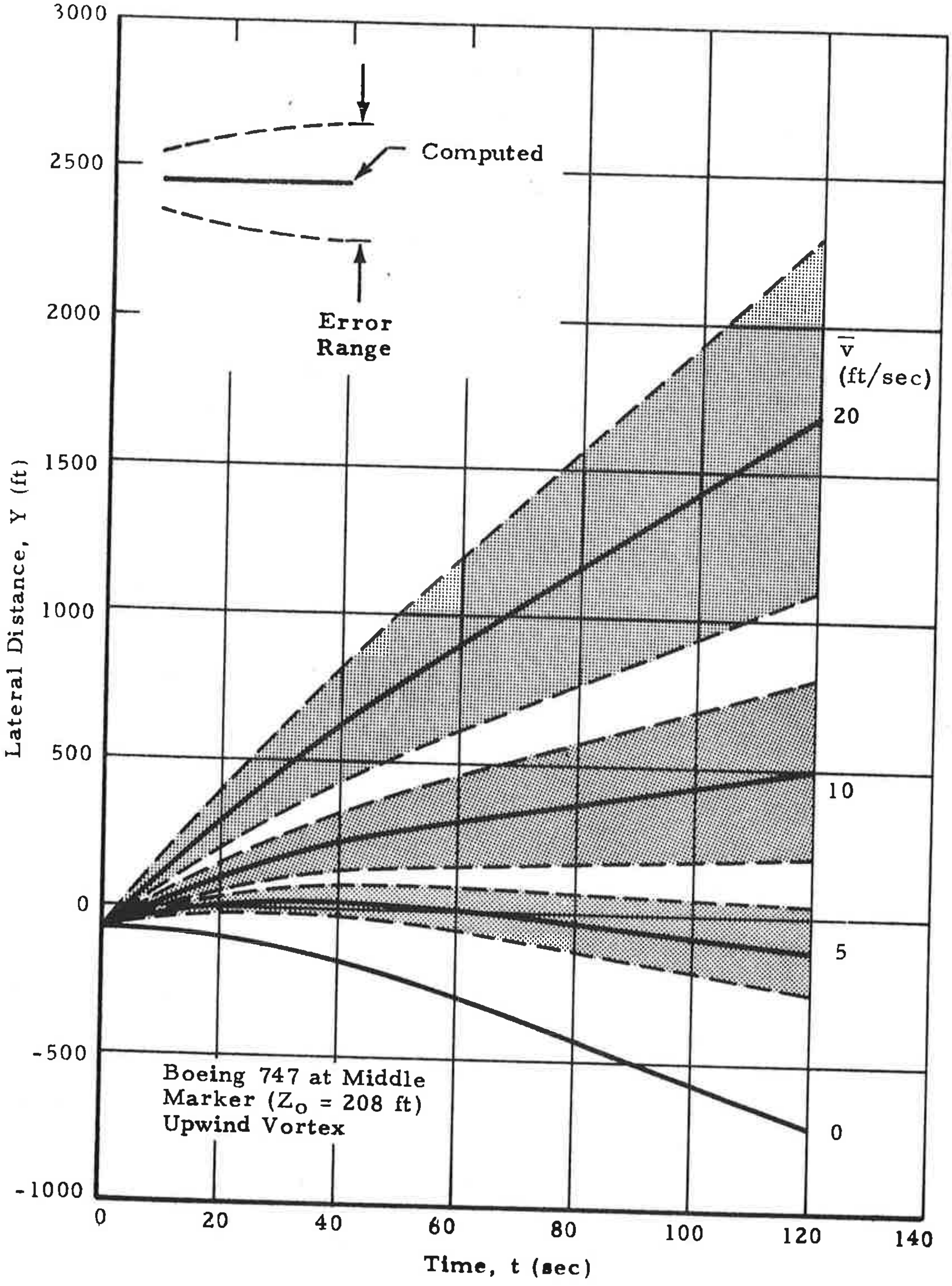

Fig. 3-2 - Possible Error in Computed Lateral Position Due to Deviation from Input Mean Velocity, $\overline{v}$

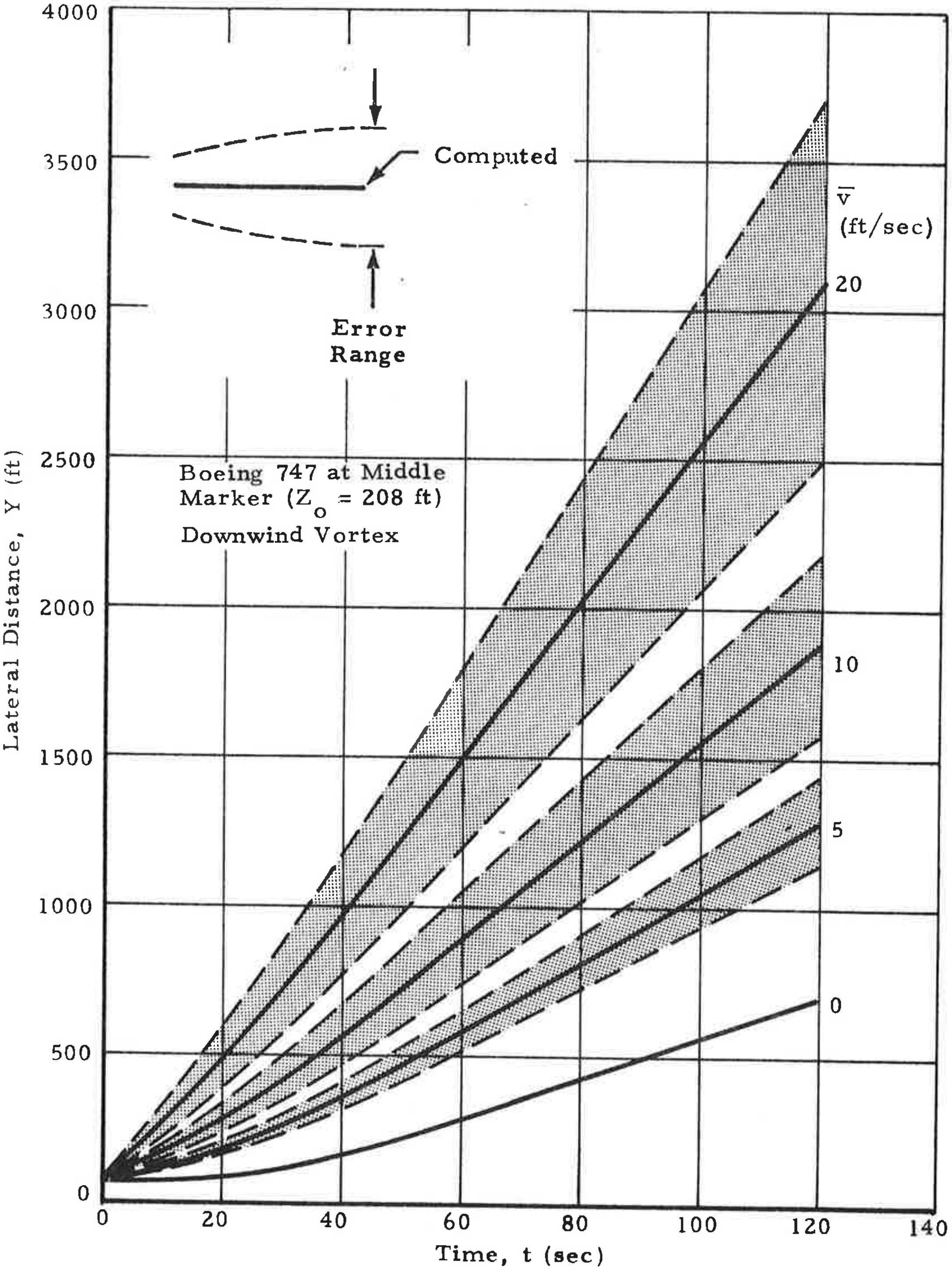

Fig. 3-3 - Possible Error in Computed Lateral Position Due to Deviation from Input Mean Velocity, $\bar{v}$

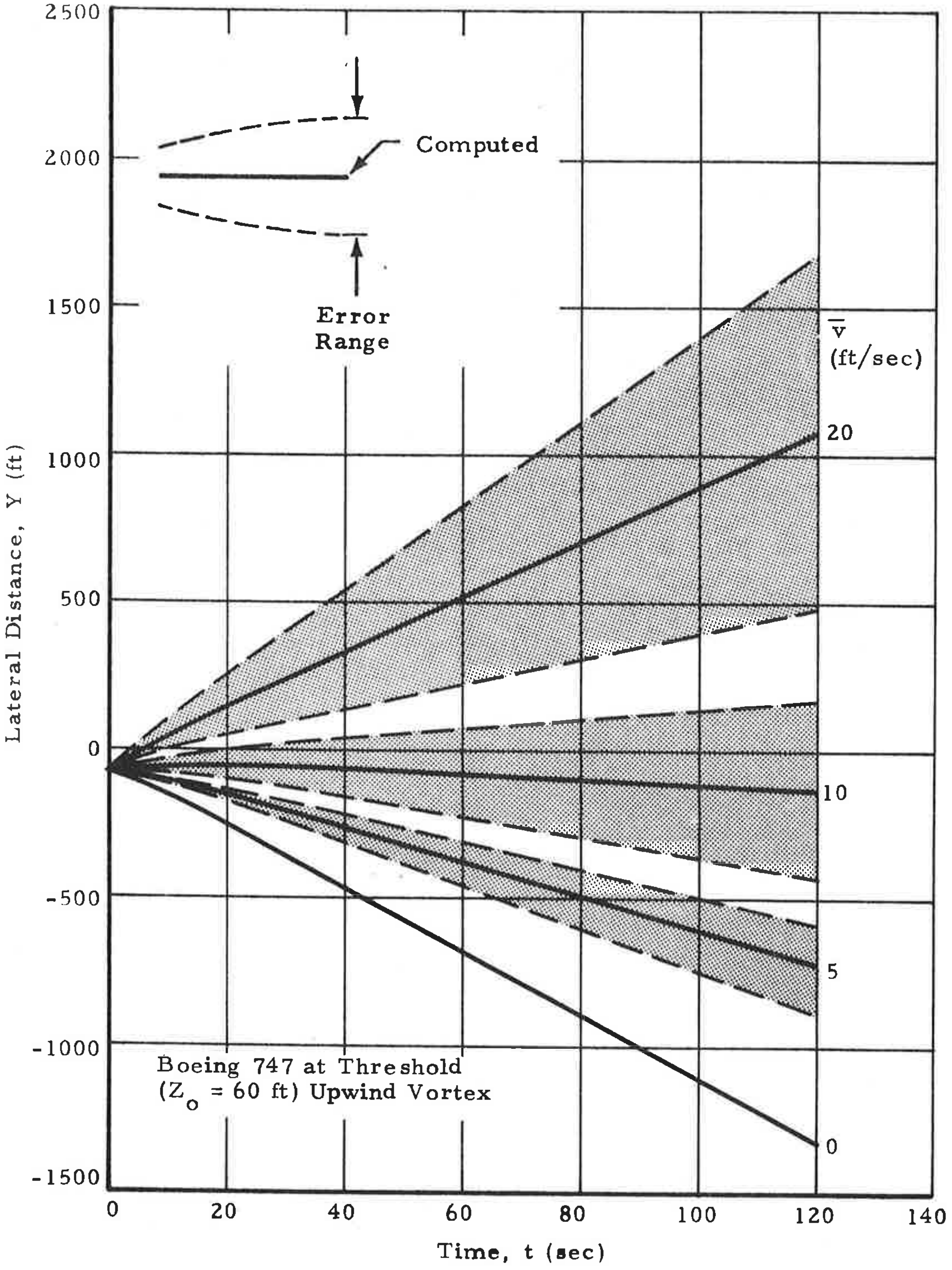

Fig. 3-4 - Possible Error in Computed Lateral Position Due to Deviation from Input Mean Velocity, $\overline{v}$

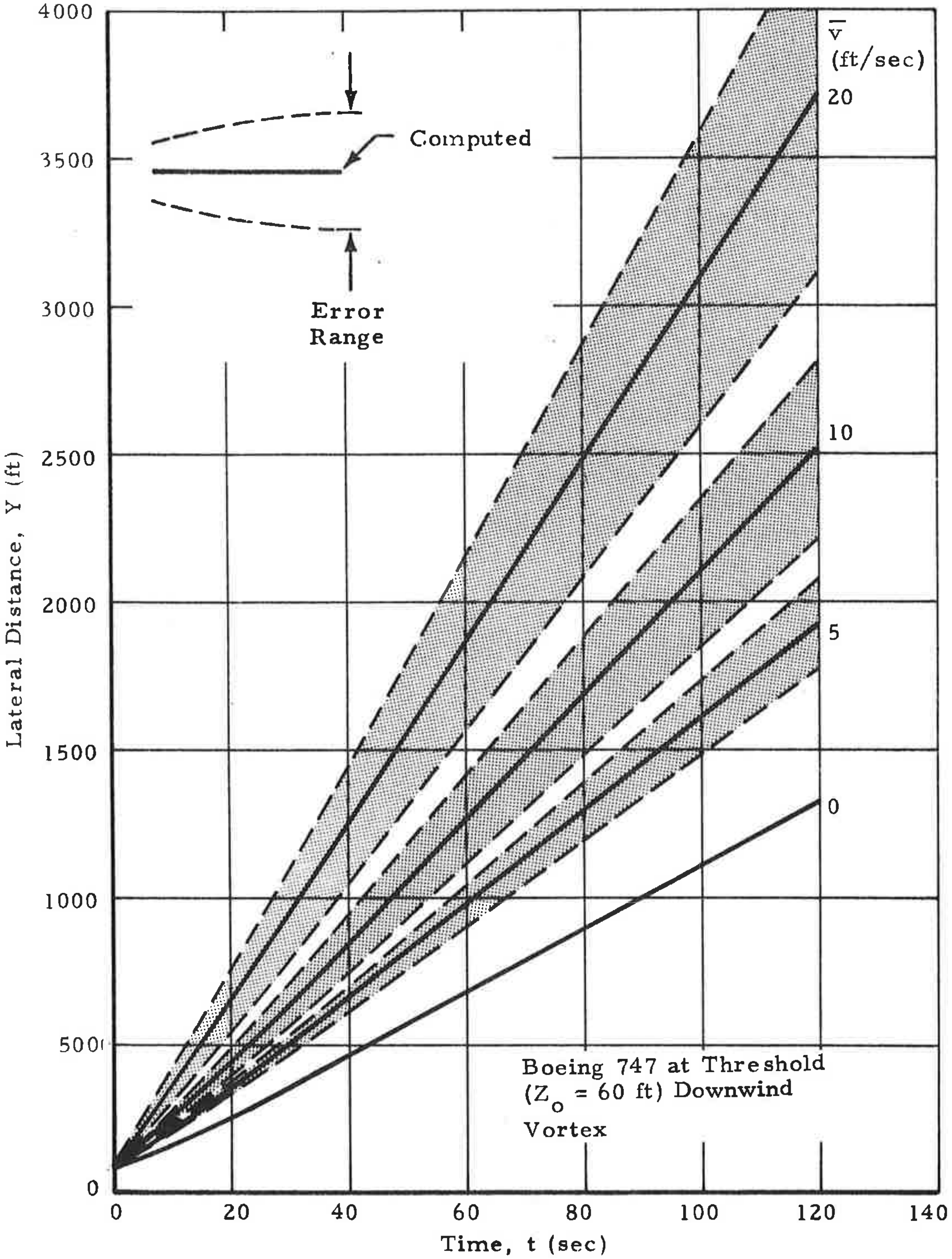

Fig. 3-5 - Possible Error in Computed Lateral Position Due to Deviation from Input Mean Velocity, $\overline{v}$

These random fluctuations will cause the vortex position to deviate from the predicted position in "random walk" fashion. The amount of this deviation can can be estimated from diffusion theory.

The root mean square diffusion distance, σ_i, for particles diffusing from an instantaneous point source is given by

$$\sigma_i = \sqrt{2 K_i t}$$

where K is the diffusivity, and the subscript i refers to rectangular coordinate directions. The distance σ_i may be considered the standard deviation for the random drifting of the vortex away from its predicted position. The diffusivity K may be estimated from Prandtl's mixing length hypothesis:

$$K_i = \ell \sqrt{\overline{\Sigma v_i^2}}$$

where ℓ is the mixing length and the v_i's are the velocity fluctuations from the mean. It is again assumed that the velocity fluctuates with 25% standard deviation. Further consider that the mixing length ℓ is proportional to altitude Z above ground level:

$$\ell = 0.4 Z$$

where the fraction 0.4 is the von Karman constant. The diffusivity K is estimated, therefore, from

$$K = 0.1 Z \overline{v}$$

and the standard deviation σ expression becomes

$$\sigma = \sqrt{0.2 Z \overline{v} t} \qquad (3.1)$$

The standard deviation in the vertical, lateral and longitudinal directions may all be assumed to be approximately of this magnitude.

A vortex generated by a Boeing 747 at the middle marker point on the glidepath will descend to a limiting altitude of about 72 feet. A vortex generated at the threshold will descend to about 47 feet. These values were used in Eq. (3.1) to estimate the error in the predicted vortex lateral position due to random velocity fluctuations. The results are shown in Figs. 3-6 through 3-9. After two minutes, the errors are seen to be about 100 feet for a 5 ft/sec wind and 200 feet for a 20 ft/sec wind. This error is considerably less than that estimated due to deviation of the mean wind from the input value. This in effect represents an improvement in the uncertainty in the mean statistics by realizing that, in general, a completely biased situation will not occur due to the randomness of the deviation from the mean wind. It is felt that this representation of the uncertainty in the transport of the upwind vortex represents a meaningful baseline deviation from which to measure other possible sources of error.

3.2 AIRCRAFT MIX

Because of variations of lift, speed and wingspan, different aircraft types produce vortices of different circulation and separation distance, and, hence, sink velocity. Consequently, the vortex tracks will differ depending on aircraft. The amount of variation with aircraft type is of interest to this sensitivity analysis because if the variation is sufficiently small compared to other variations, a single composite aircraft type could be incorporated into the program to represent all aircraft types.

Figures 3-10 and 3-11 show the computed lateral distances, Y, as a function of time for a variety of aircraft at the middle marker and threshold positions. The spread in the computed distances are seen to be much greater for the threshold position than the middle marker. Also, the results for the different aircraft, especially at the threshold, are seen to lie in groups corresponding to heavy, medium and light aircraft weight classifications. The overall spread

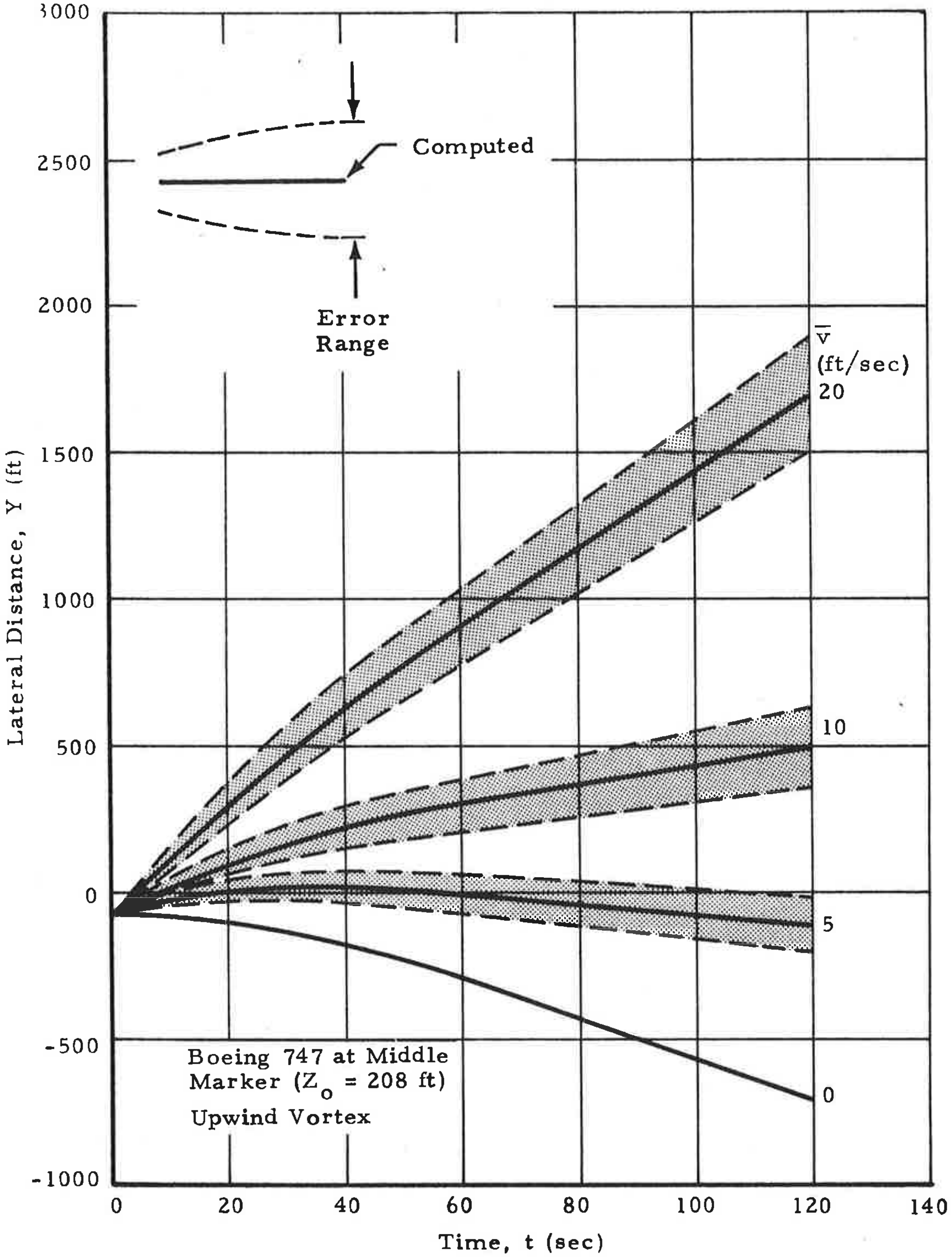

Fig. 3-6 - Standard Deviation from Computed Lateral Position Due to Random Velocity Fluctuations

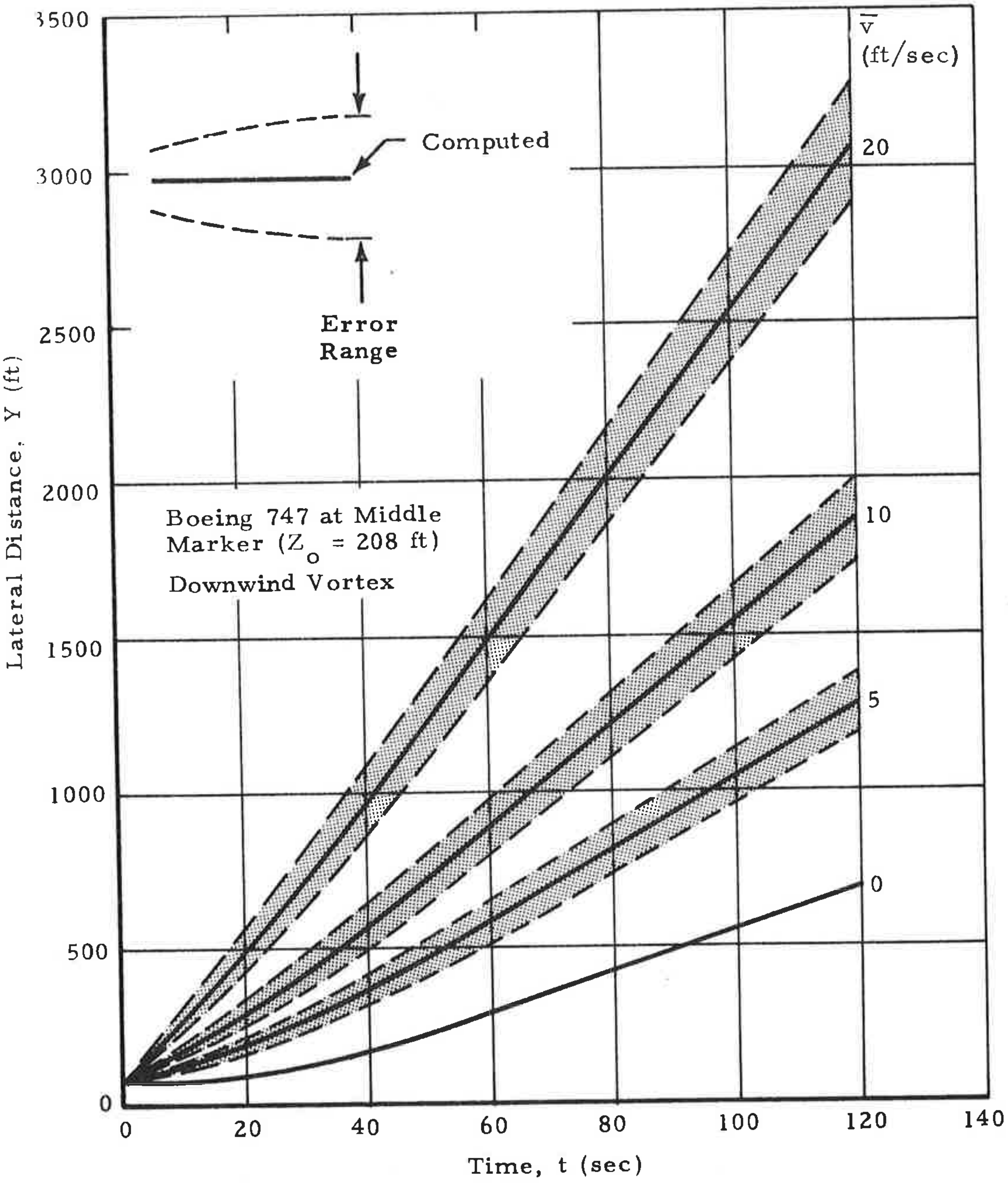

Fig. 3-7 - Standard Deviation from Computed Lateral Position Due to Random Velocity Fluctuations

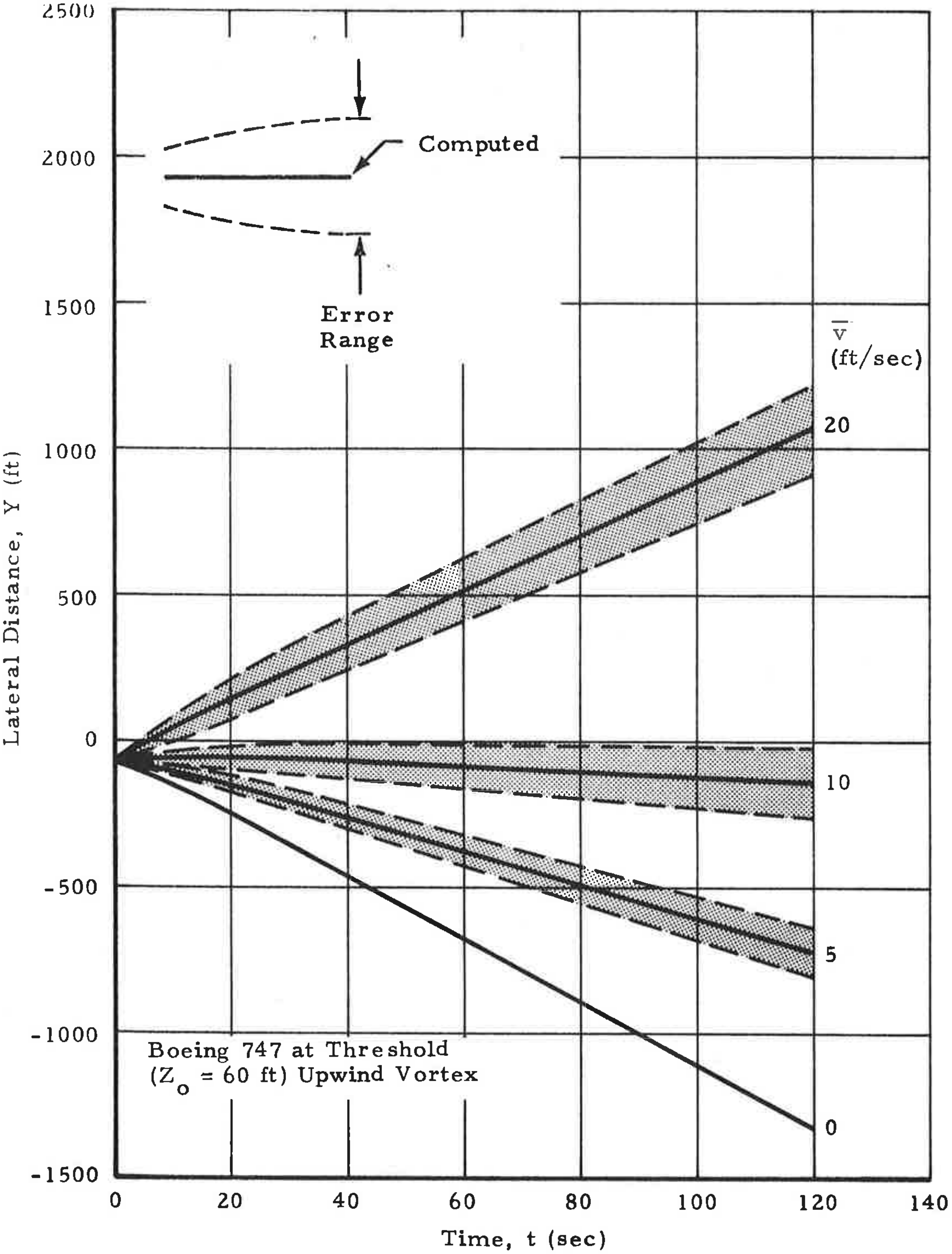

Fig. 3-8 - Standard Deviation from Computed Lateral Position Due to Random Velocity Fluctuations

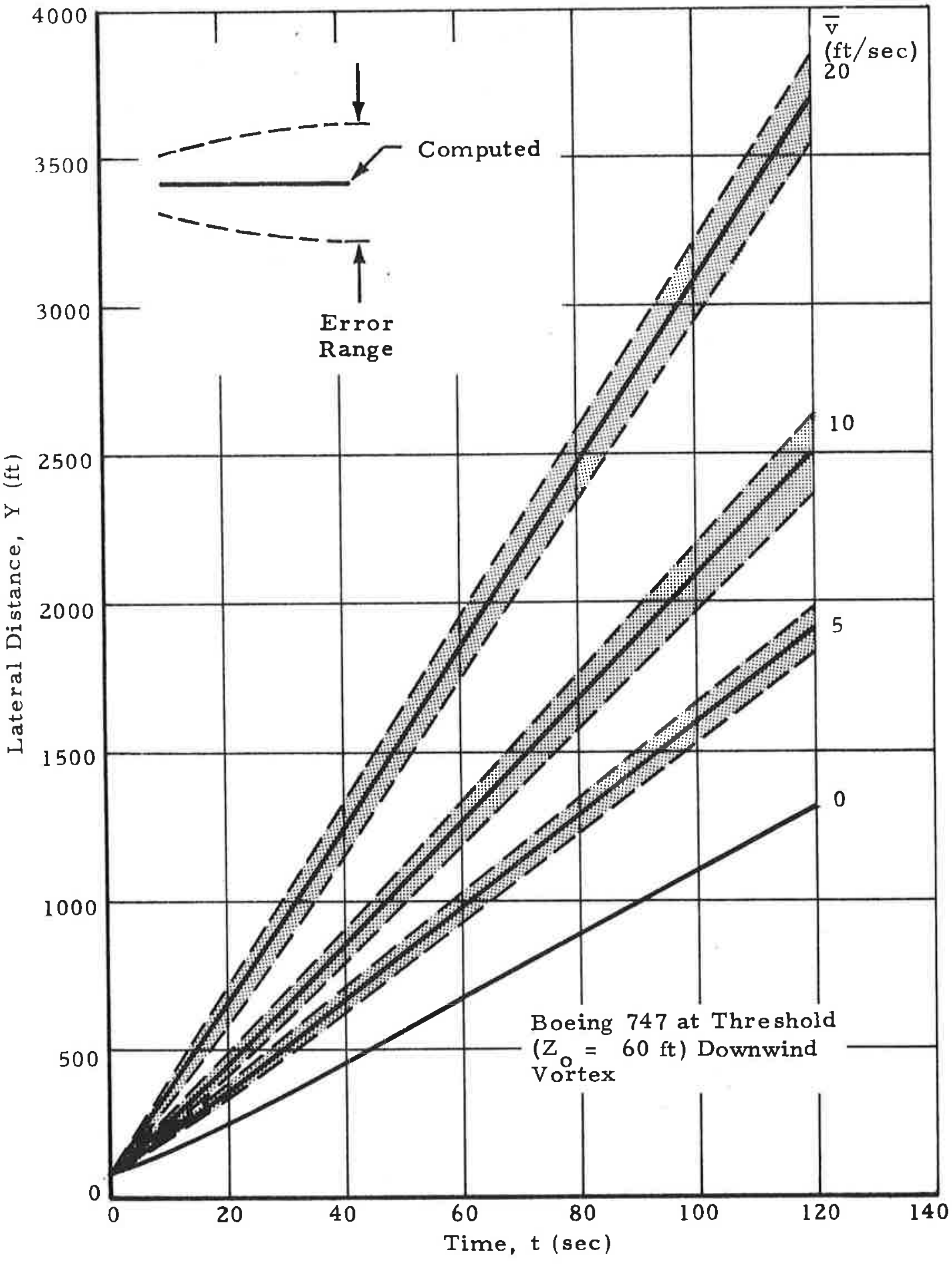

Fig. 3-9 - Standard Deviation from Computed Lateral Position Due to Random Velocity Fluctuations

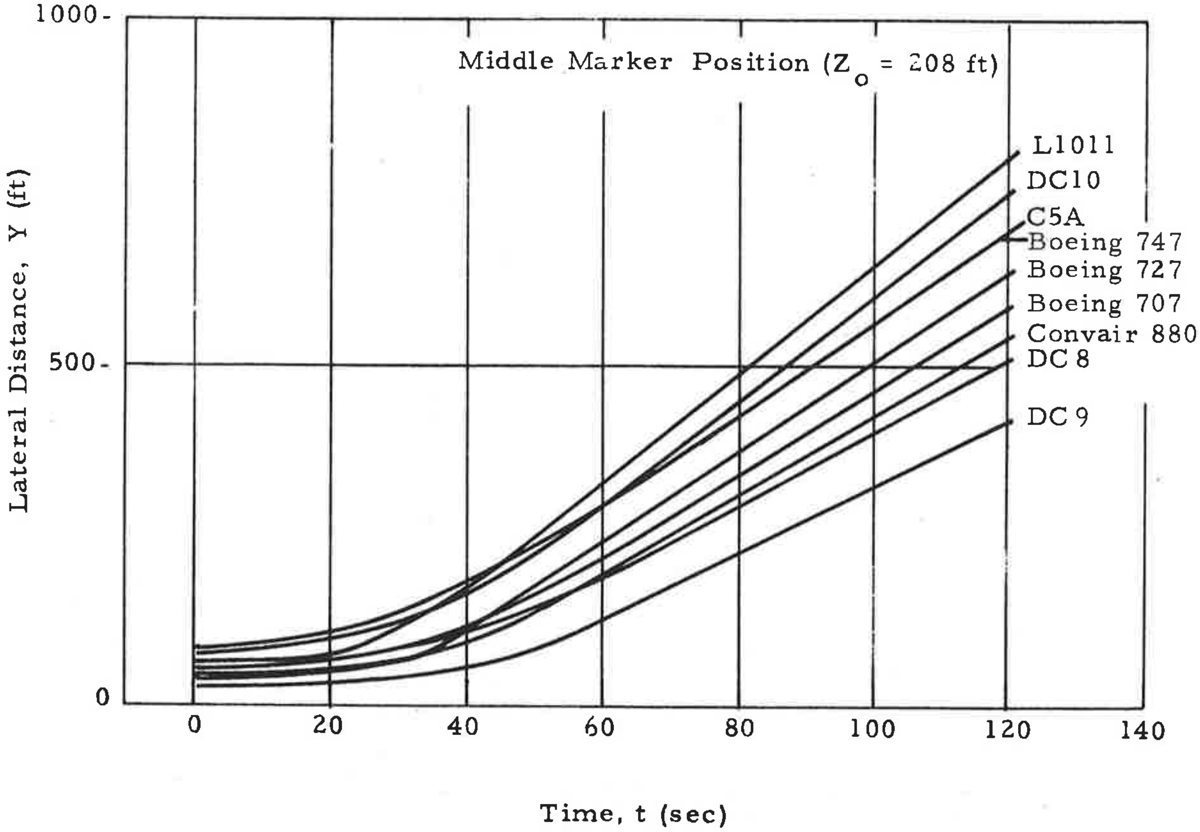

Fig. 3-10 - Variation of Computed Lateral Position with Aircraft Type

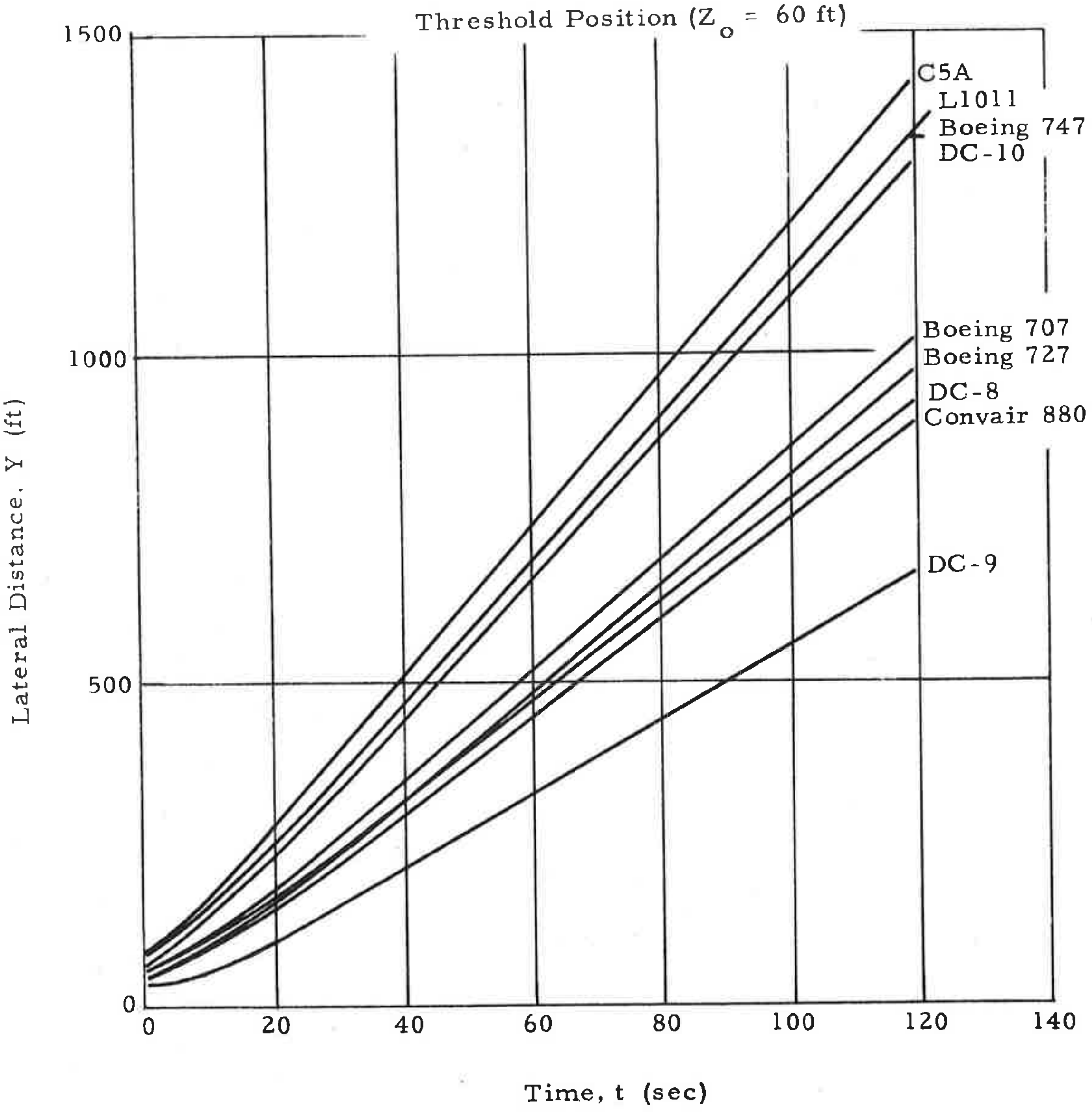

Fig. 3-11 - Variation of Computed Lateral Position with Aircraft Type in the results due to aircraft variation is compared in Figs. 3-12 and 3-13 to the baseline variation due to random wind fluctuations.

At the middle marker, the spread due to aircraft variation is roughly the same as for wind fluctuations for mean winds greater than about 10 ft/sec. At the threshold, the spread due to aircraft variation is considerably greater for all wind speeds. However, if the aircraft are grouped according to heavy, medium and light classifications, the spread within these groups would be considerably less than for the entire aircraft mix. For the heavy aircraft group (C5A, L1011, Boeing 747 and DC-10) the spread is shown in Figs. 3-14 and 3-15 to be considerably less than the variation due to random wind fluctuations for all mean wind speeds greater than about 5 ft/sec. This is significant in that a "representative heavy aircraft" might be incorporated into the predictive algorithm with no appreciable loss of applicability and accuracy.

3.3 CORRIDOR SPREAD

The actual aircraft trajectory will deviate from the nominal trajectory according to a statistical pattern, with the 3σ variation defining a corridor. At the middle marker, the corridor is bounded by an altitude deviation of ±48 feet from the 208 feet nominal, and a horizontal deviation of ± 127 feet from the runway centerline. At the threshold, the altitude bounds are ±14 feet from the 60 feet nominal, and the horizontal bounds are ±95 feet. To test the sensitivity of the model to deviations in aircraft trajectory, vortex tracks were made for the Boeing 747 at altitudes corresponding to the upper and lower altitude bounds at the middle marker and threshold points. The deviations in vortex track due to horizontal deviations in the aircraft trajectory can be determined from a simple horizontal translation from the runway centerline. The spread in computed lateral distances Y is shown in Figs. 3-16 and 3-17 for altitude deviations at the middle marker and threshold. The computations are again seen to be more sensitive at the threshold than at the middle marker. These spreads are compared in Figs. 3-18 and 3-19 to the baseline variation due to random velocity fluctuations. The spread due to altitude deviations at the middle marker is seen to

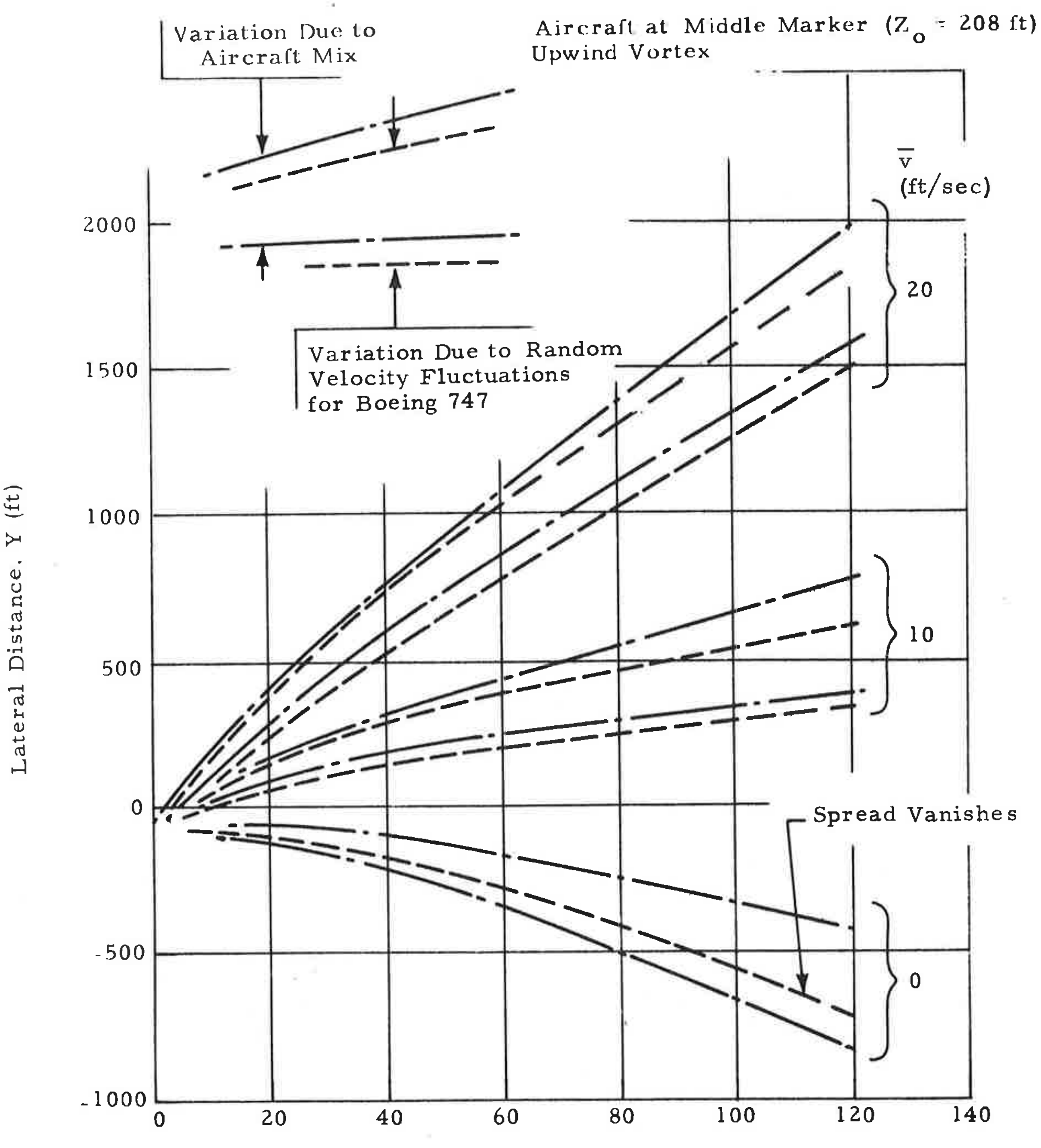

Fig. 3-12 - Variation Due to Aircraft Mix Compared to Variation Due to Random Velocity Fluctuations

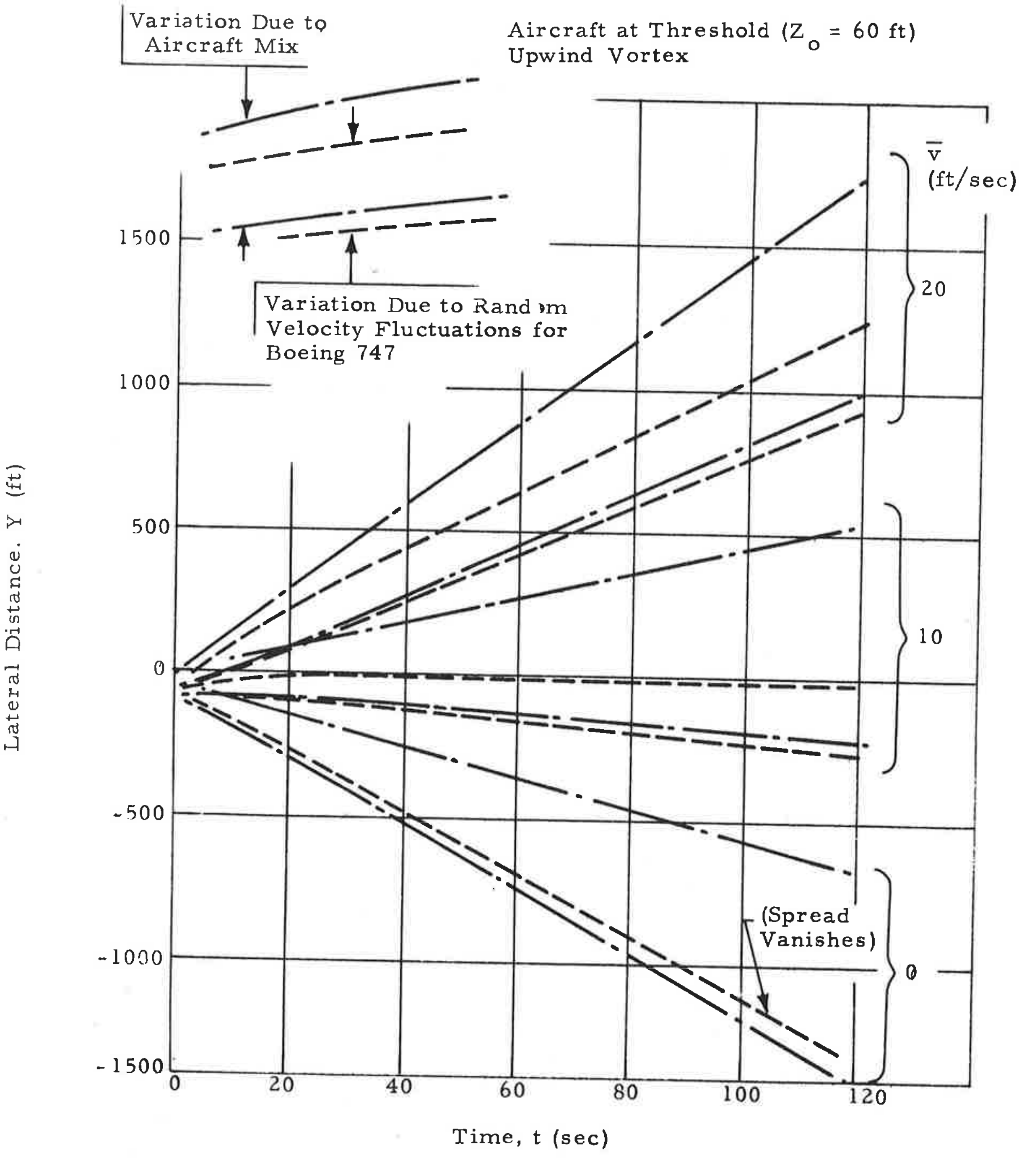

Fig. 3-13 - Variation Due to Aircraft Mix Compared to Variation Due to Random Velocity Fluctuations

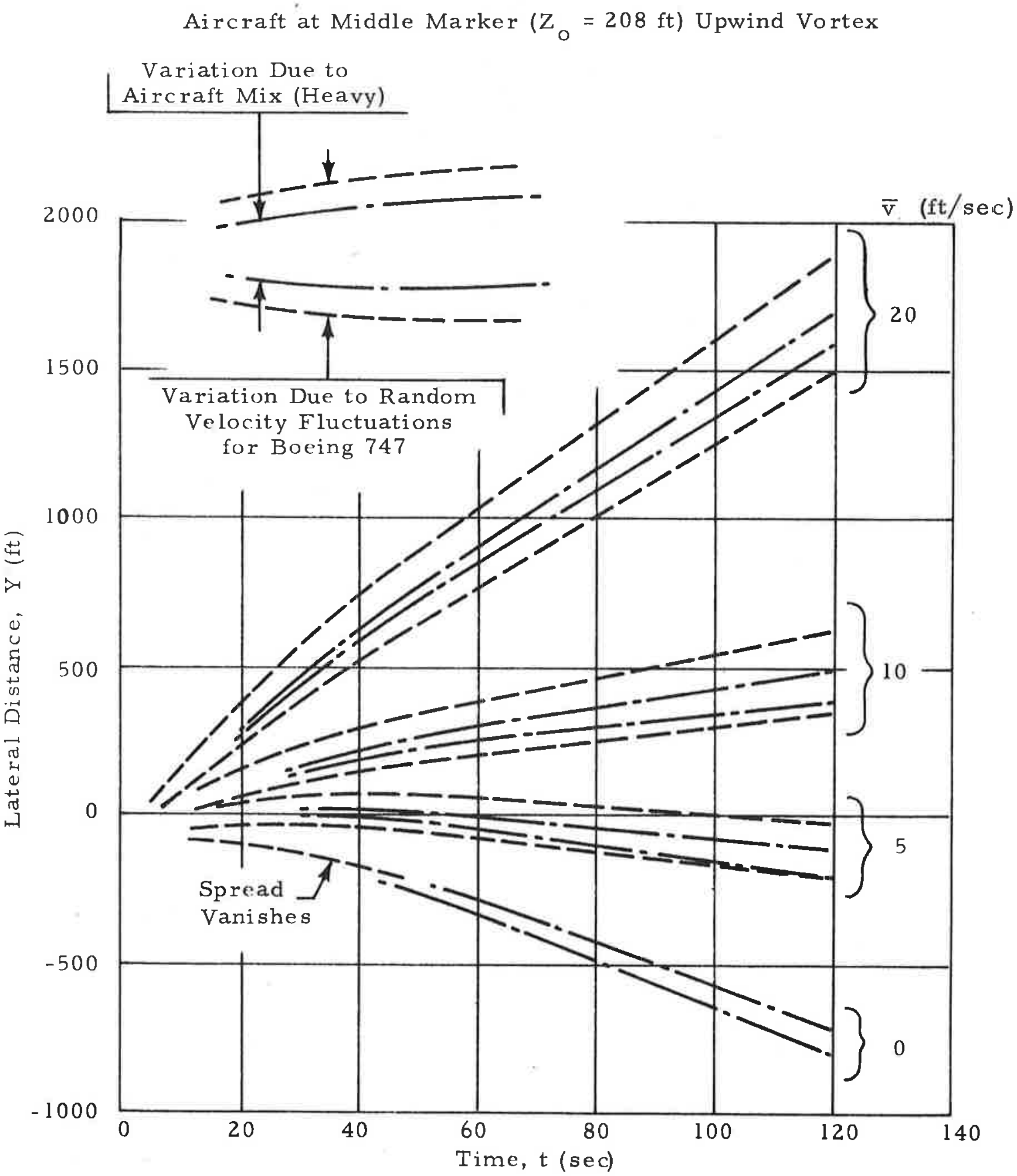

Fig. 3-14 - Variation Due to Aircraft Mix (Heavy) Compared to Variation Due to Random Velocity Fluctuations

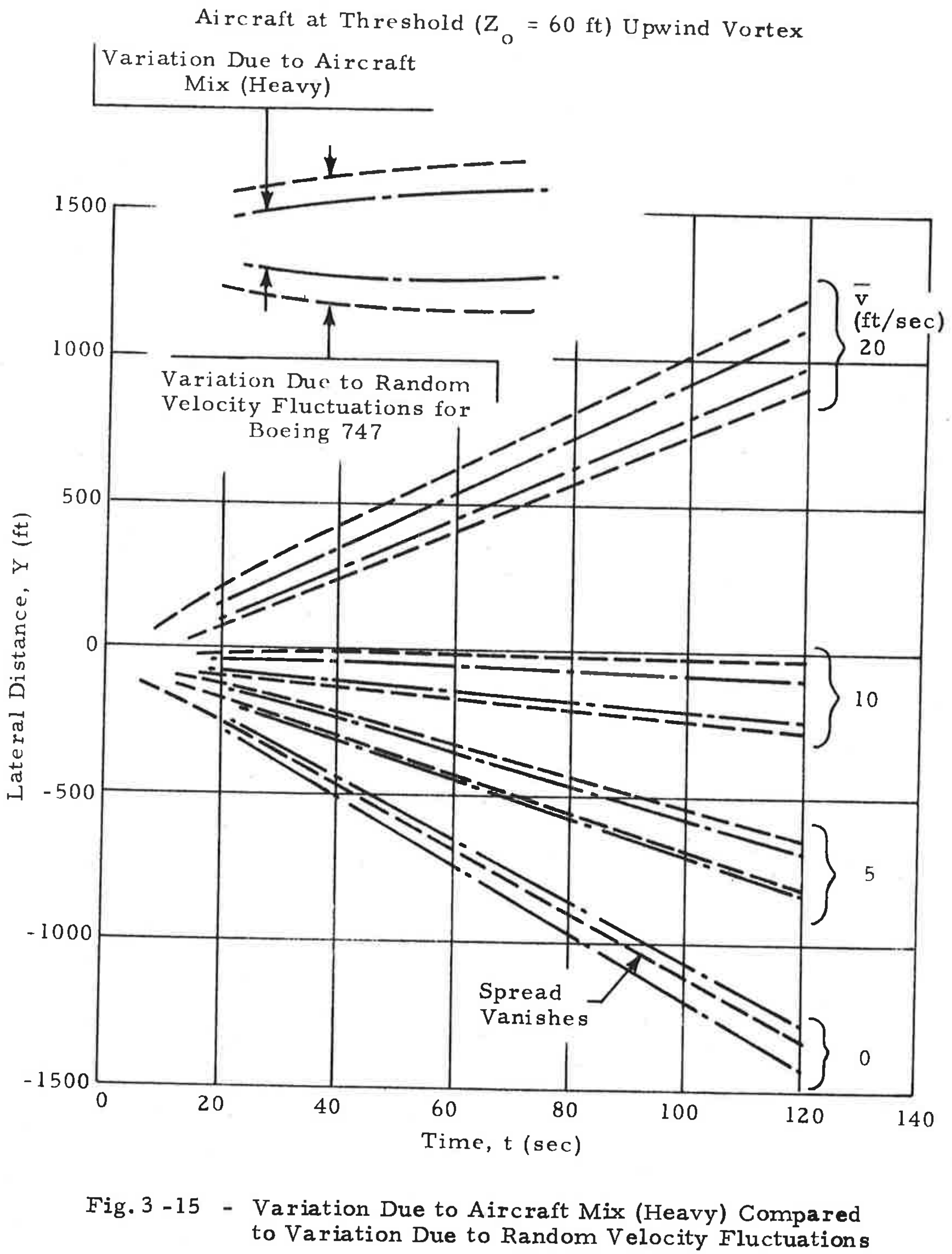

Fig. 3 -15 - Variation Due to Aircraft Mix (Heavy) Compared to Variation Due to Random Velocity Fluctuations

Boeing 747

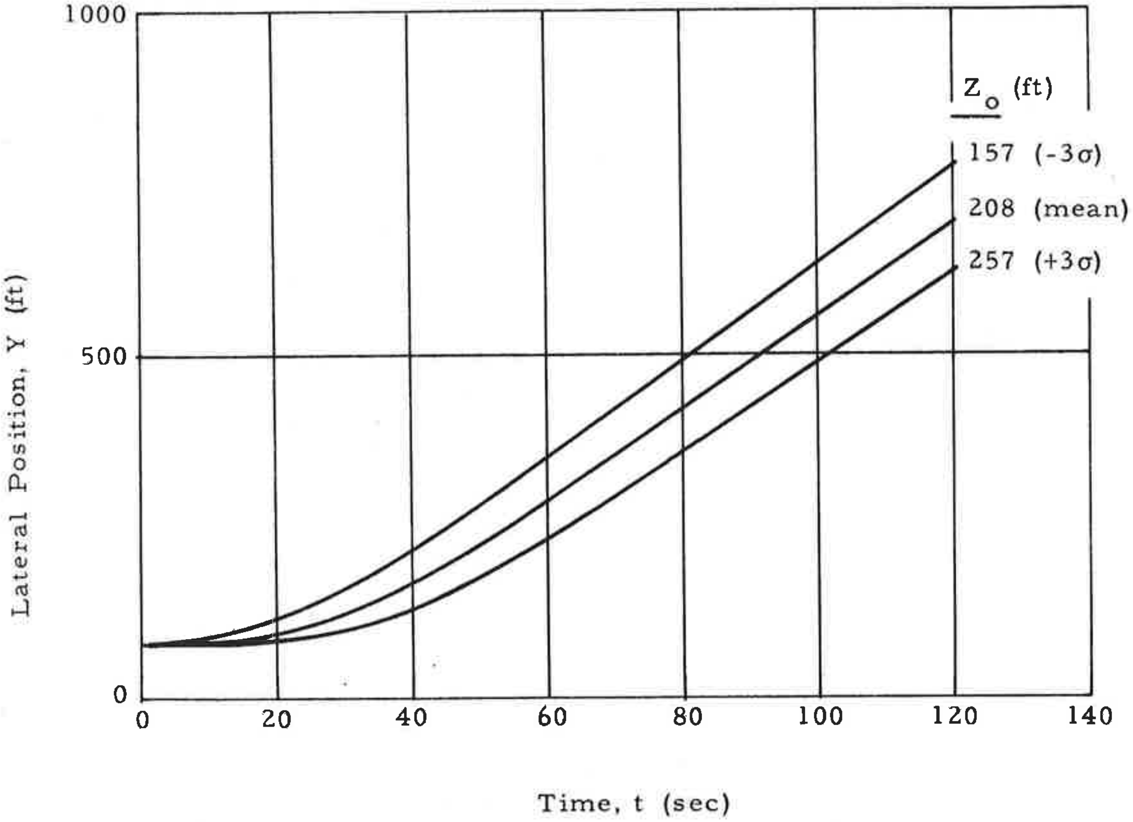

Fig. 3-16 - Variation of Computed Lateral Position with Altitude Variations at Middle Marker

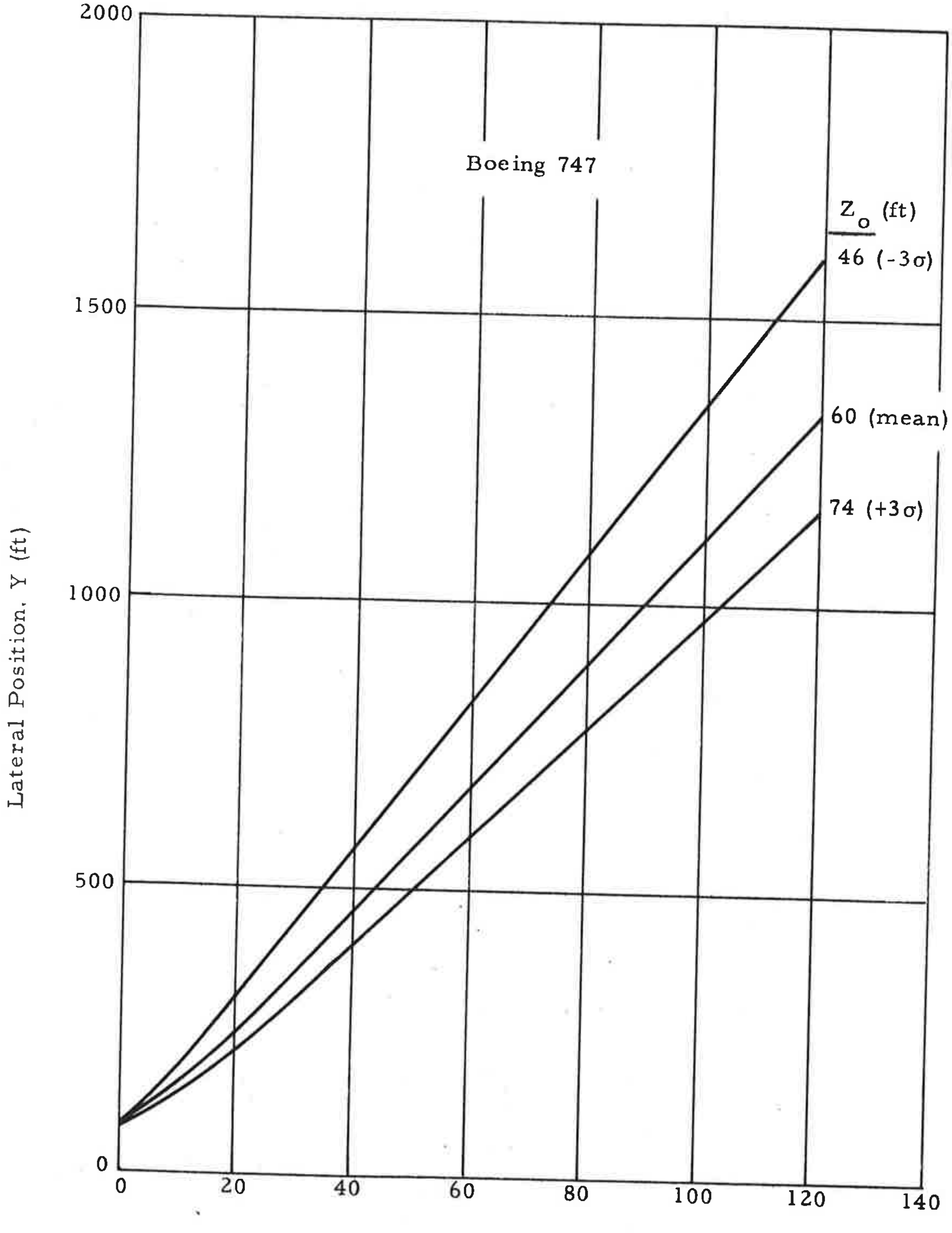

Fig. 3-17 - Variation of Computed Lateral Position with Altitude Variations at Threshold

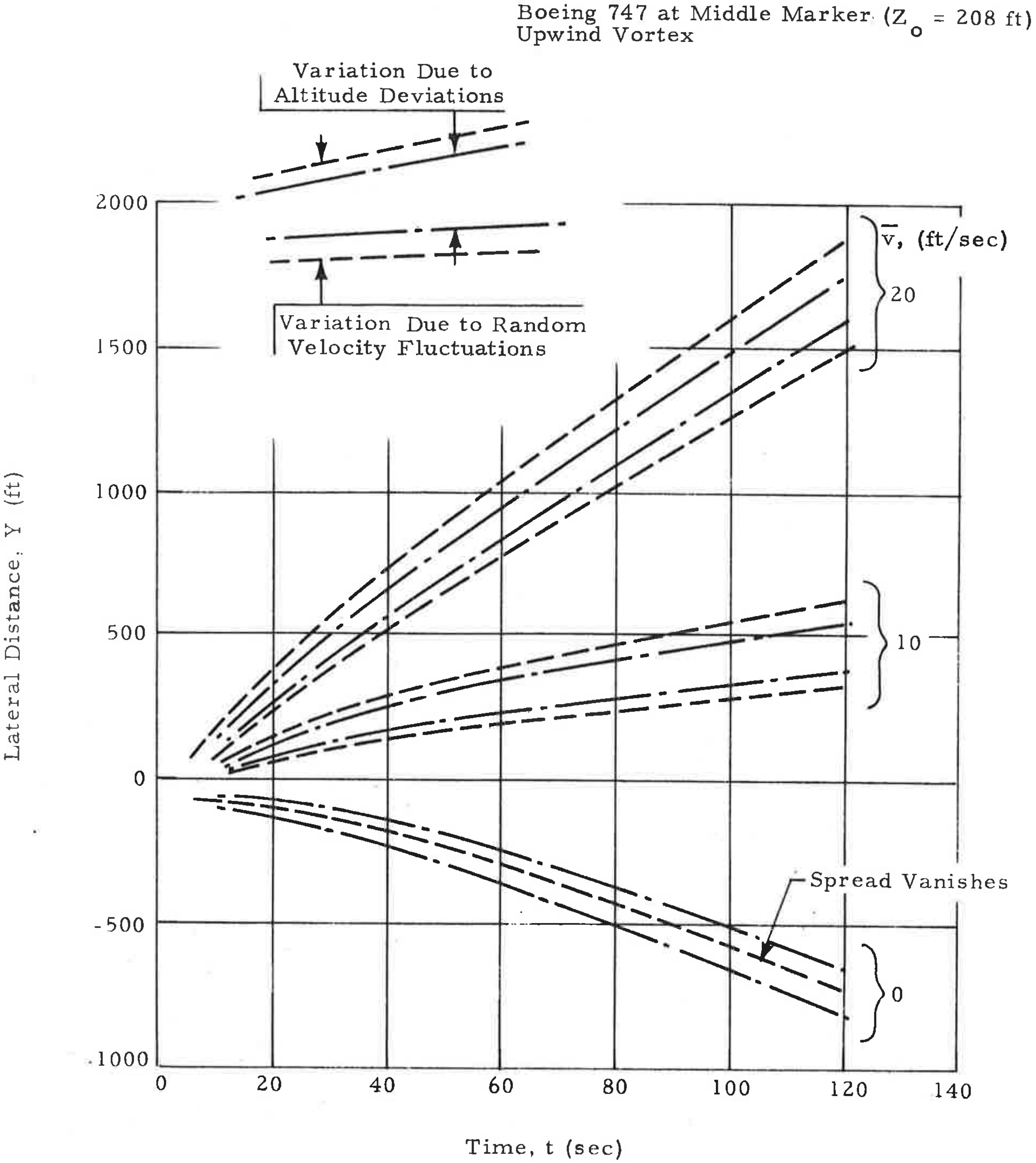

Fig. 3-18 - Variation Due to Altitude Deviations Compared to Variations Due to Random Velocity Fluctuations

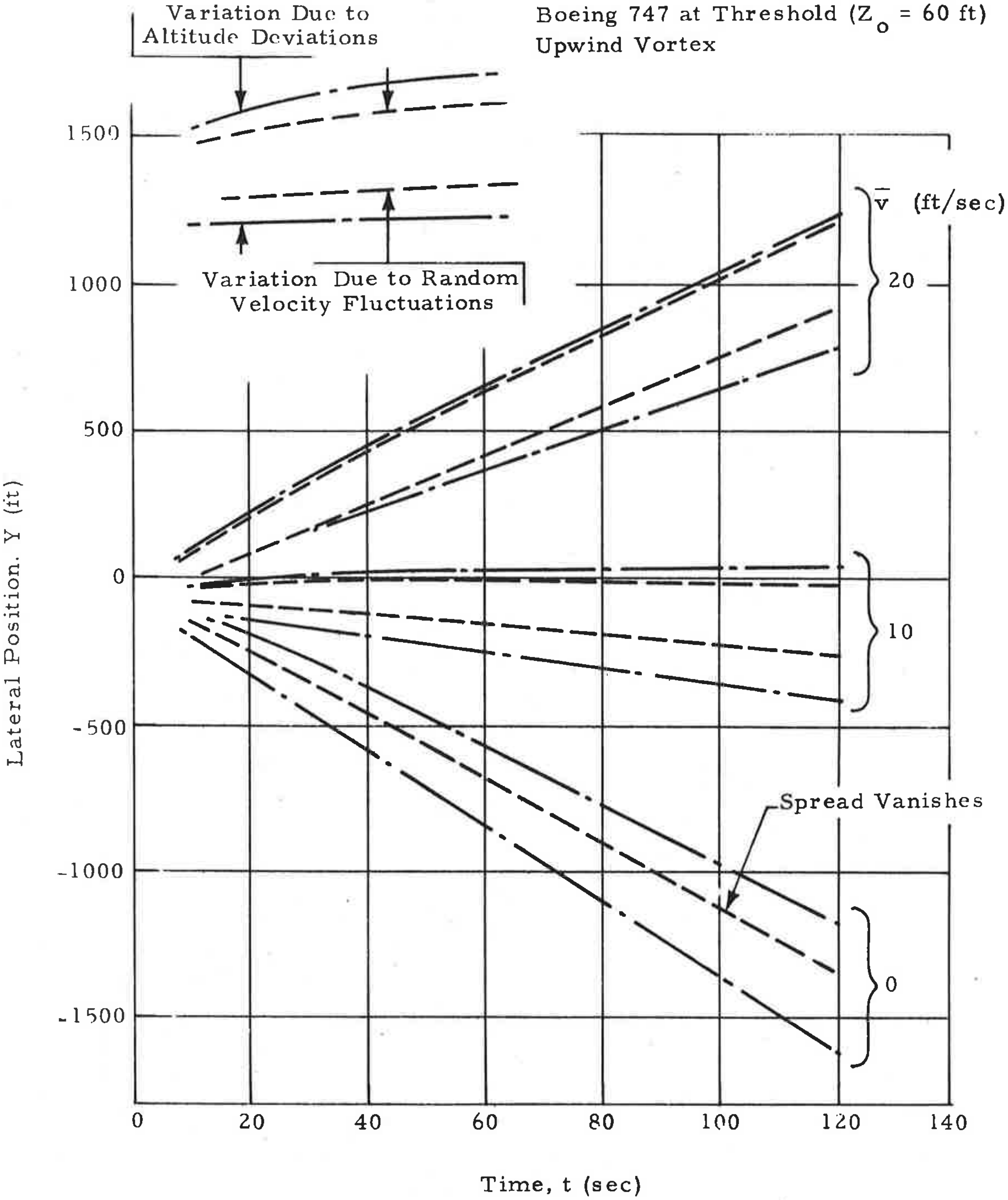

Fig. 3-19 - **Variation Due to Altitude Deviations Compared to Variation Due to Random Velocity Fluctuations** be well within the variation due to velocity fluctuations for mean winds greater than 10 ft/sec. The spread at the threshold is seen to be somewhat greater than but still of the same order as that due to velocity fluctuations.

3.4 VORTEX CIRCULATION AND SEPARATION

The vortex circulation and separation distance depend on aircraft lift, speed and wingspan and may be calculated based on certain assumed lift distributions along the wing. The equations used in the present study for calculating circulation and separation distance were based on an elliptical distribution. The vortex circulation for a given aircraft type will vary depending on speed and overall aircraft weight, including fuel, passengers and cargo. In addition, the lift distribution varies from an elliptical loading depending on configuration. The vortex separation distance depends only on wingspan and lift distribution. For a given aircraft type, therefore, variations in separation distance will be due to variations from an elliptical loading. The model was tested for sensitivity to variations in circulation and separation distance by performing calculations for a Boeing 747 at altitudes corresponding to the middle marker and threshold with variations in circulation and separation of ±10% and 25% from the nominal. The spread in computed lateral positions is shown in Figs. 3-20 and 3-21 for variations in circulation. These spreads are compared in Figs. 3-22 and 3-23 to variations due to random velocity fluctuations. The spreads for ±10% deviations are seen to be about the same as the variations due to random velocity fluctuations for mean winds greater than about 5 ft/sec. The ±25% deviations, however, produce spreads greater than the variations due to random velocity fluctuations up to approximately 15 ft/sec as seen in Figs. 3-24 and 3-25.

The spread in computed lateral positions is shown in Figs. 3-26 and 3-27 for variations in separation distance, and these spreads are compared in Figs. 3-28 through 3-31 with variations due to random velocity fluctuations. The ±10% deviation spreads are seen to be well within the variations due to random velocity fluctuations for both the middle marker and threshold positions. The ±25% deviation spreads are seen to be within the variation due to random velocity fluctuations for mean winds greater than about 10 ft/sec at the threshold and about 20 ft/sec at the middle marker.

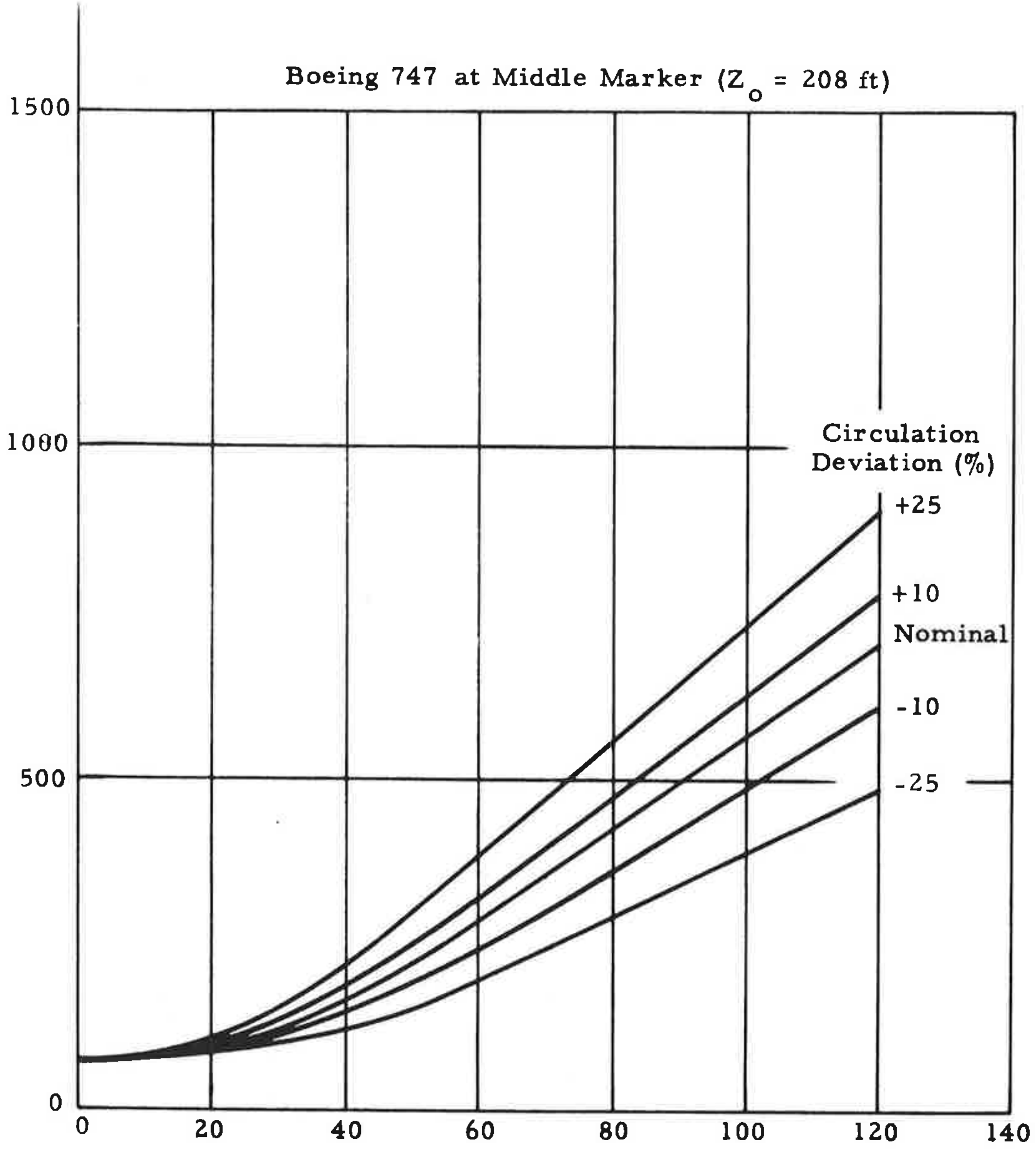

Fig. 3-20 - Variation of Computed Lateral Position with Deviation of Circulation

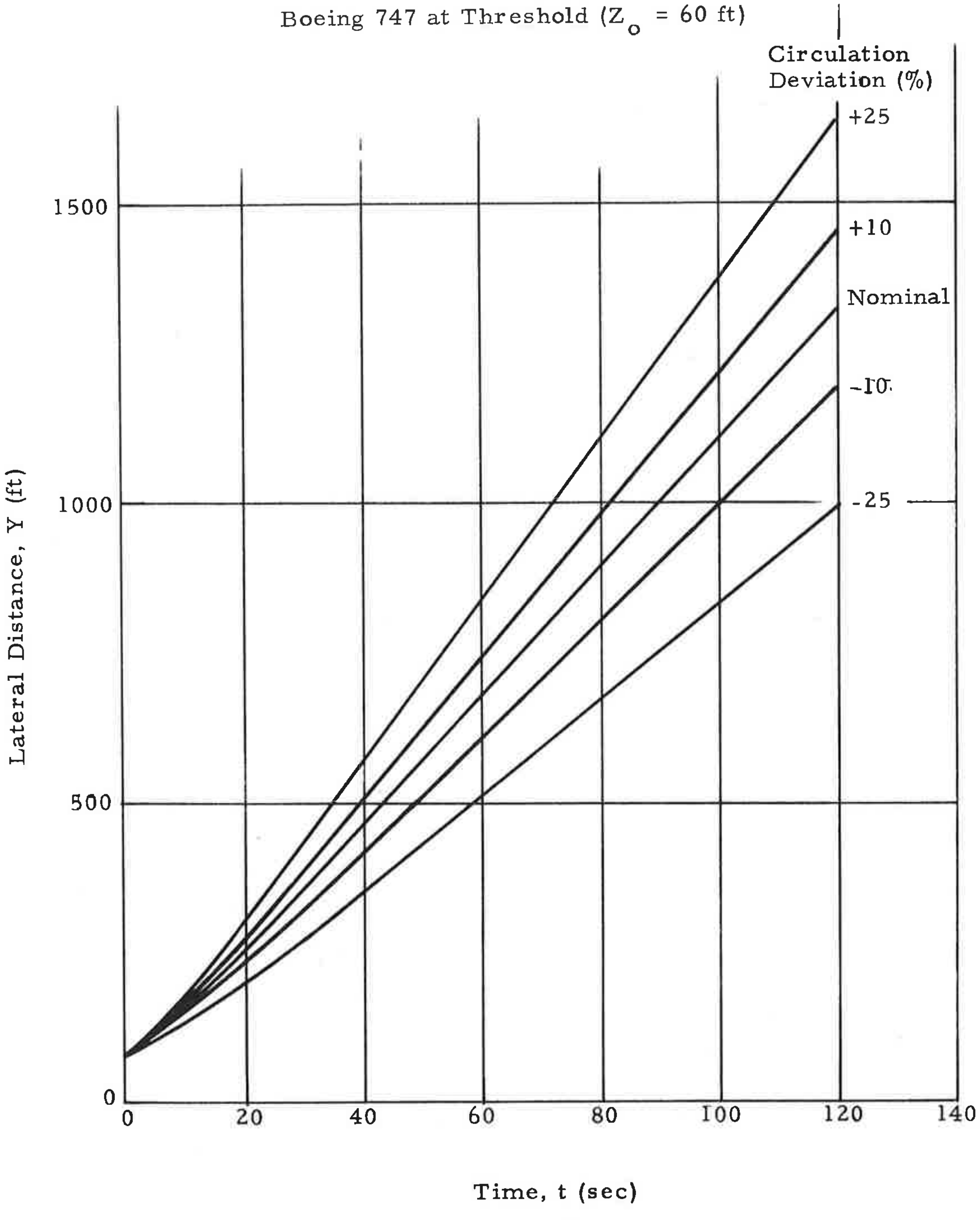

Fig. 3-21 - Variation of Computed Lateral Position With Deviation of Circulation

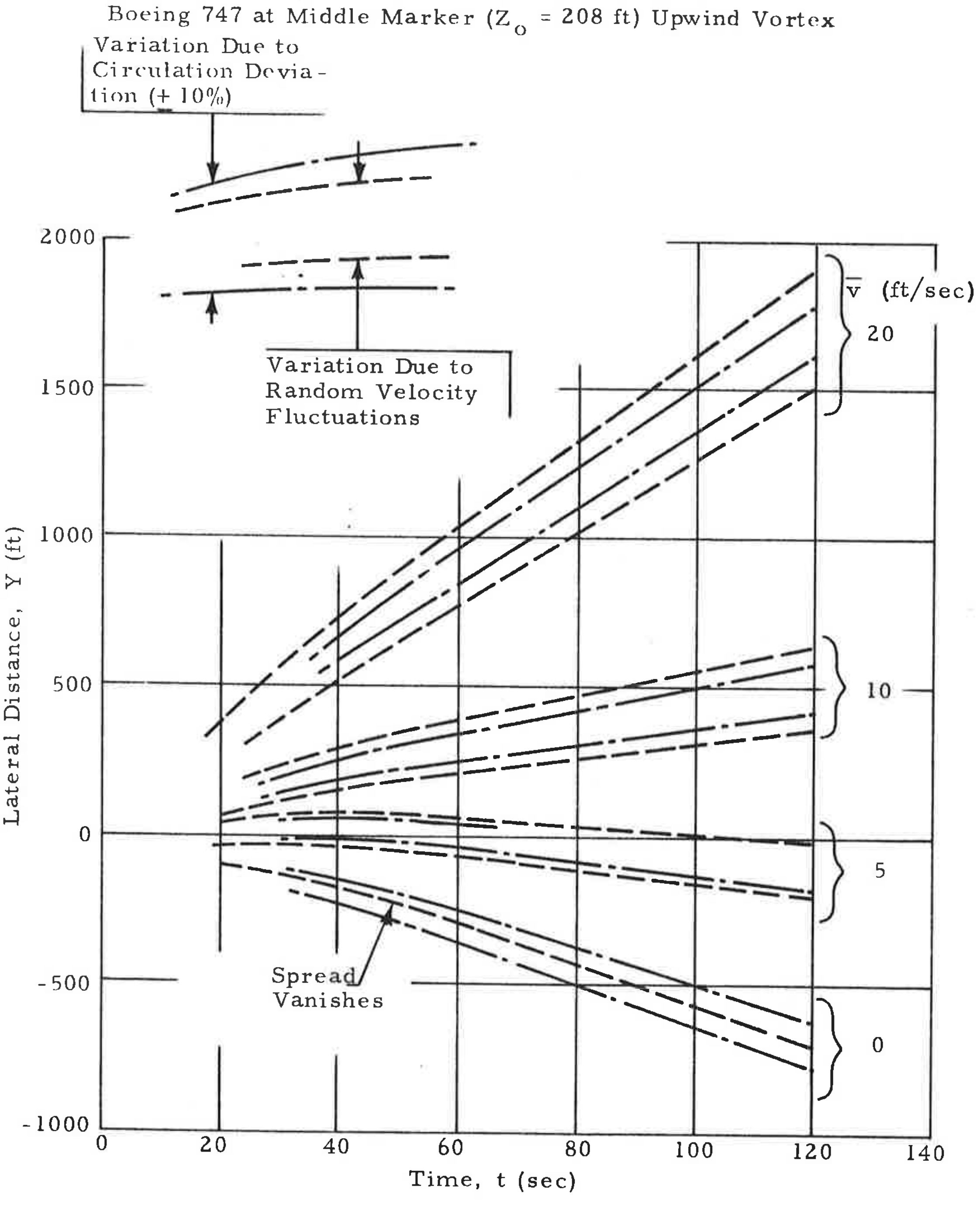

Fig. 3-22 - Variation Due to Circulation Deviation Compared to Variation Due to Random Velocity Fluctuations

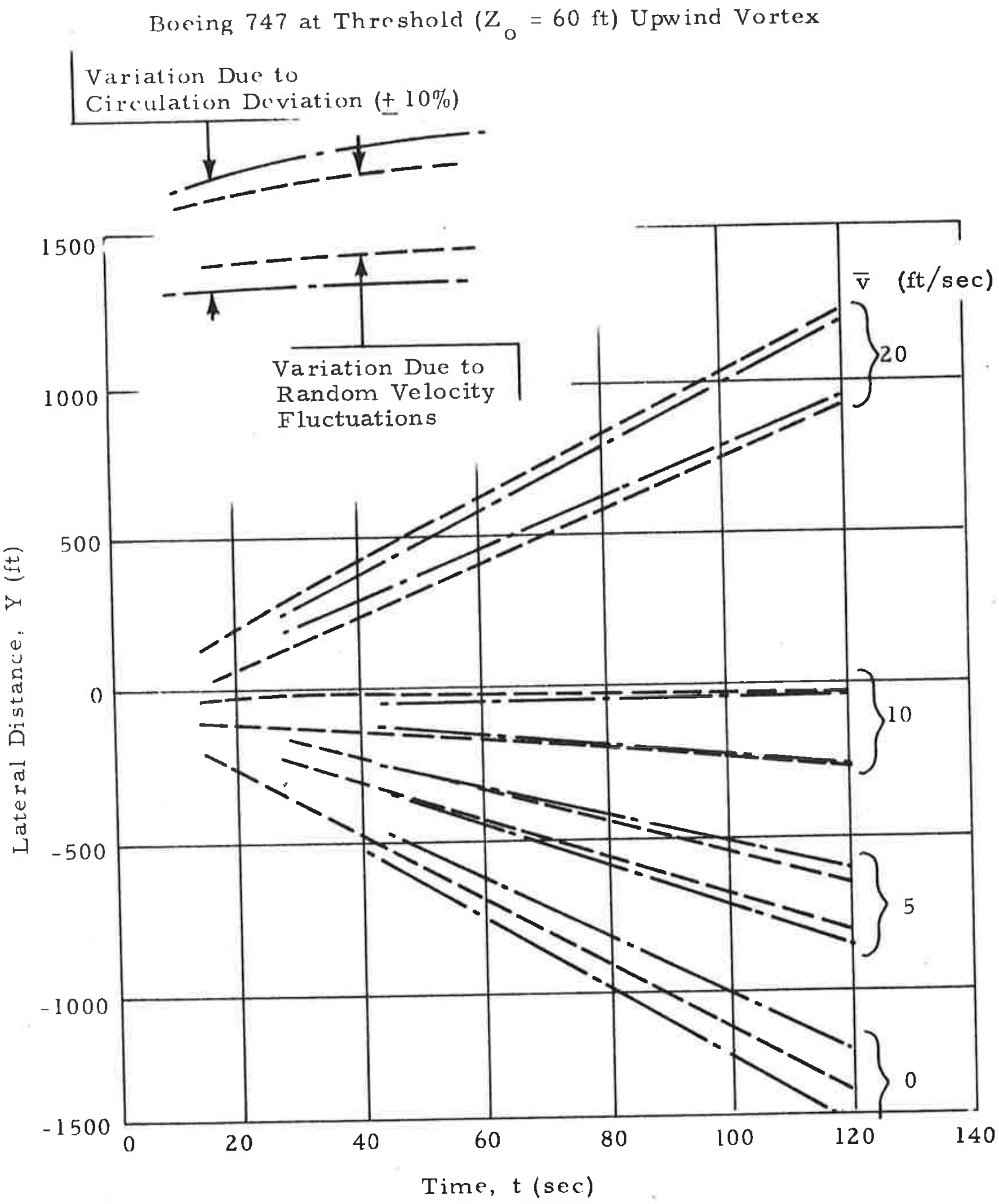

Fig. 3-23 - Variation Due to Circulation Deviation Compared to Variation Due to Random Velocity Fluctuations

Boeing 747 at Middle Marker (Z_o = 208 ft) Upwind Vortex

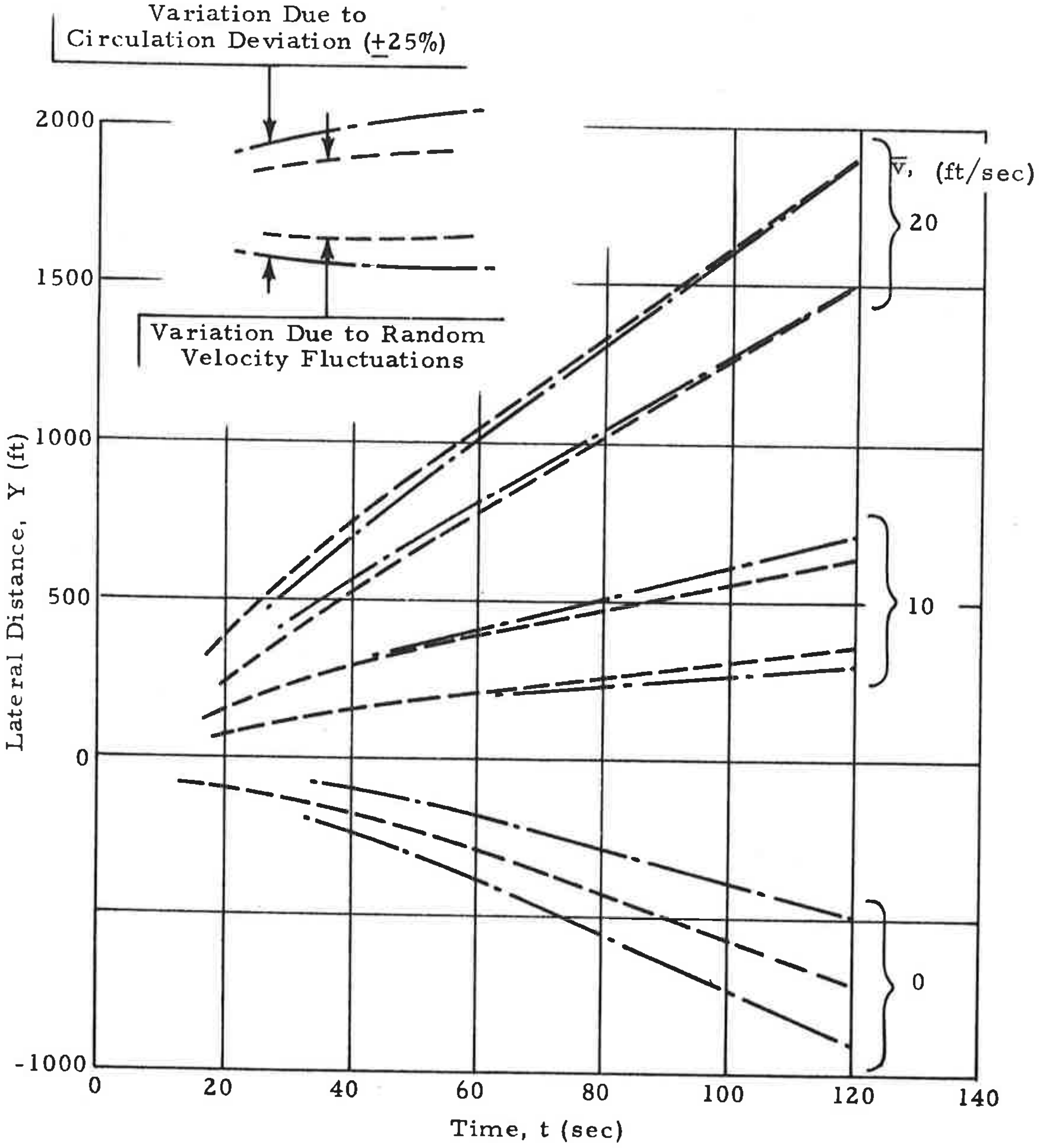

Fig. 3-24 - Variation Due to Circulation Deviation Compared to Variation Due to Random Velocity Fluctuations

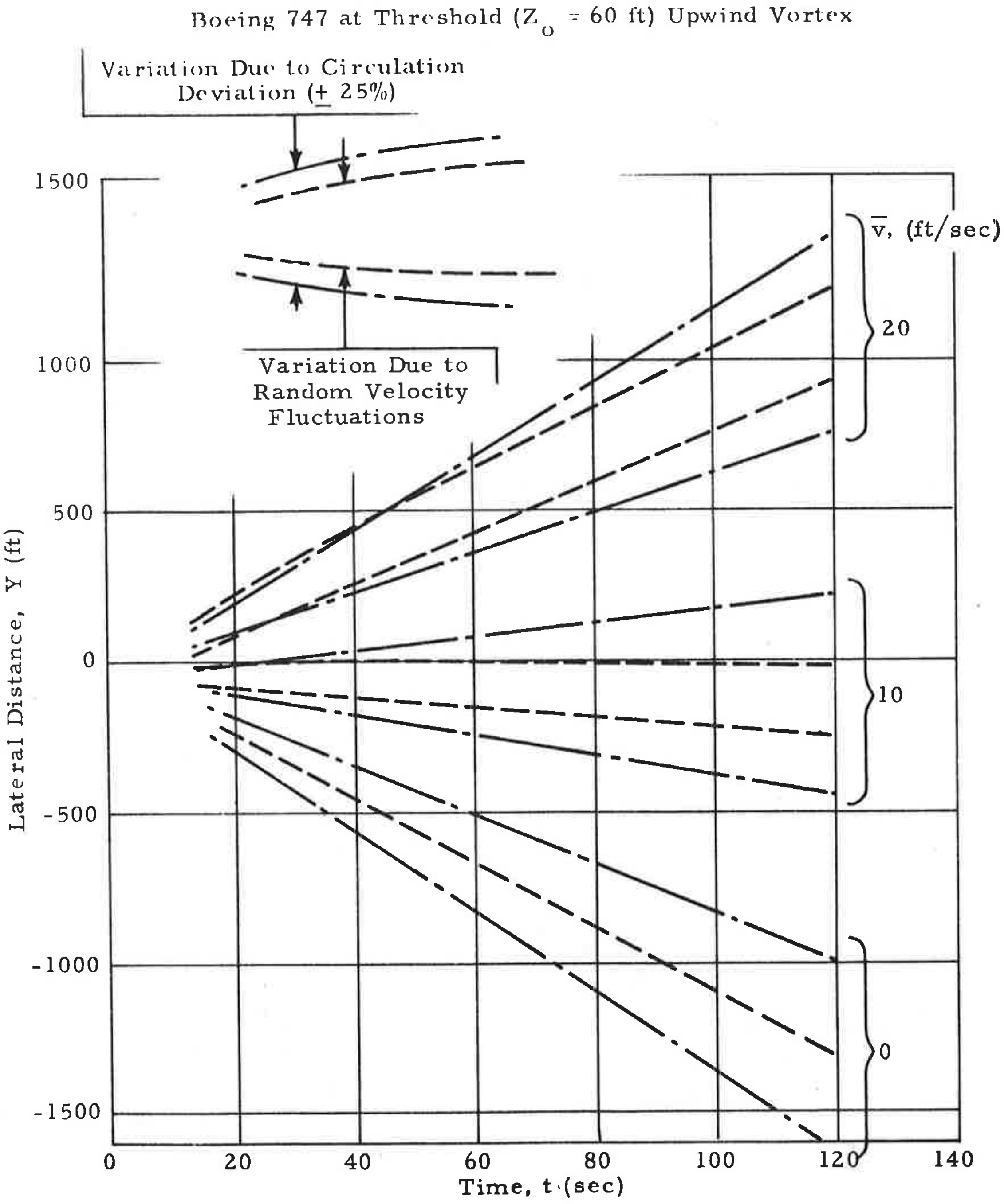

Fig. 3-25 - Variation Due to Circulation Deviation Compared to Variation Due to Random Velocity Fluctuations

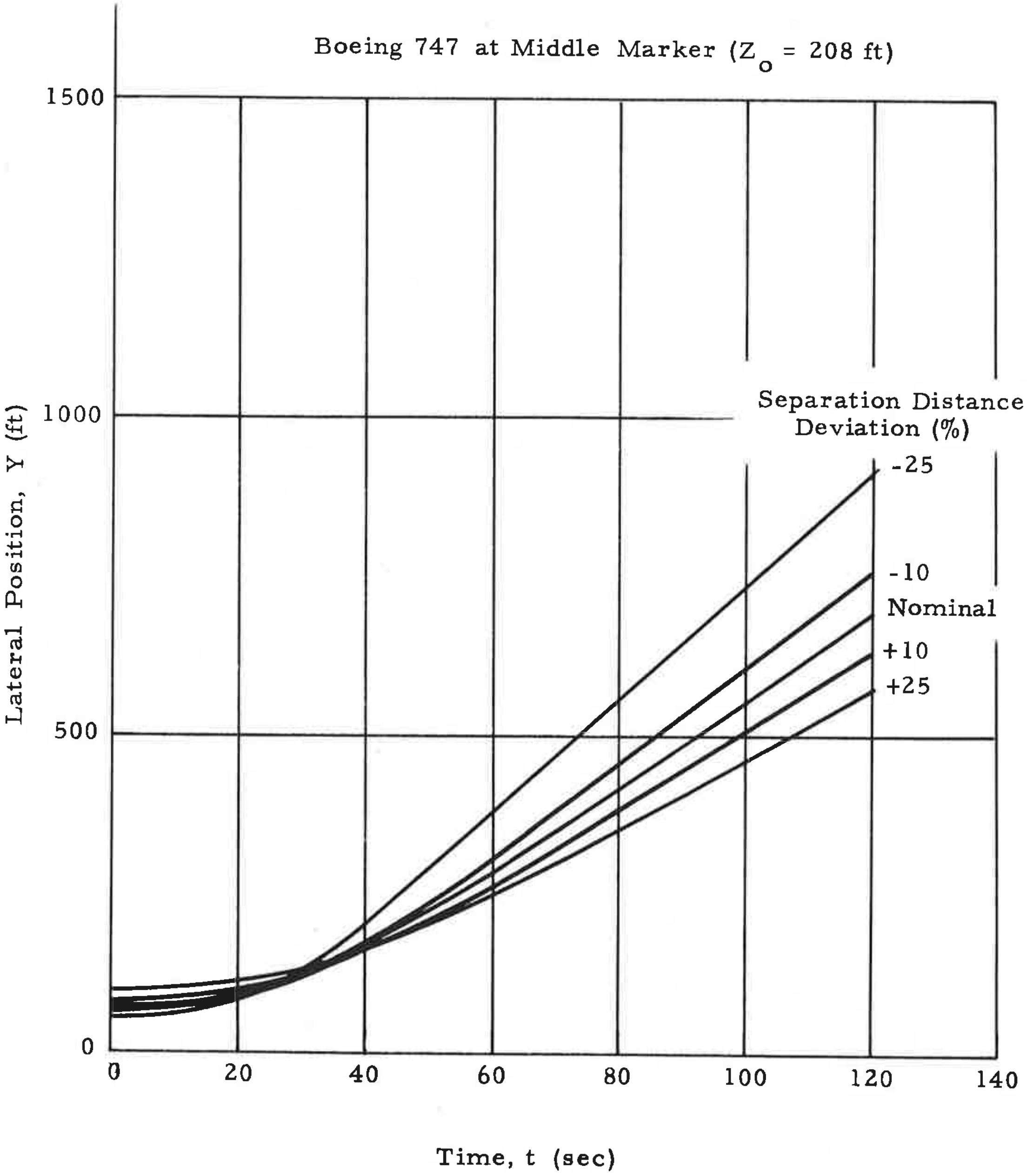

Fig. 3-26 - Variation of Computed Lateral Position with Deviation in Vortex Separation

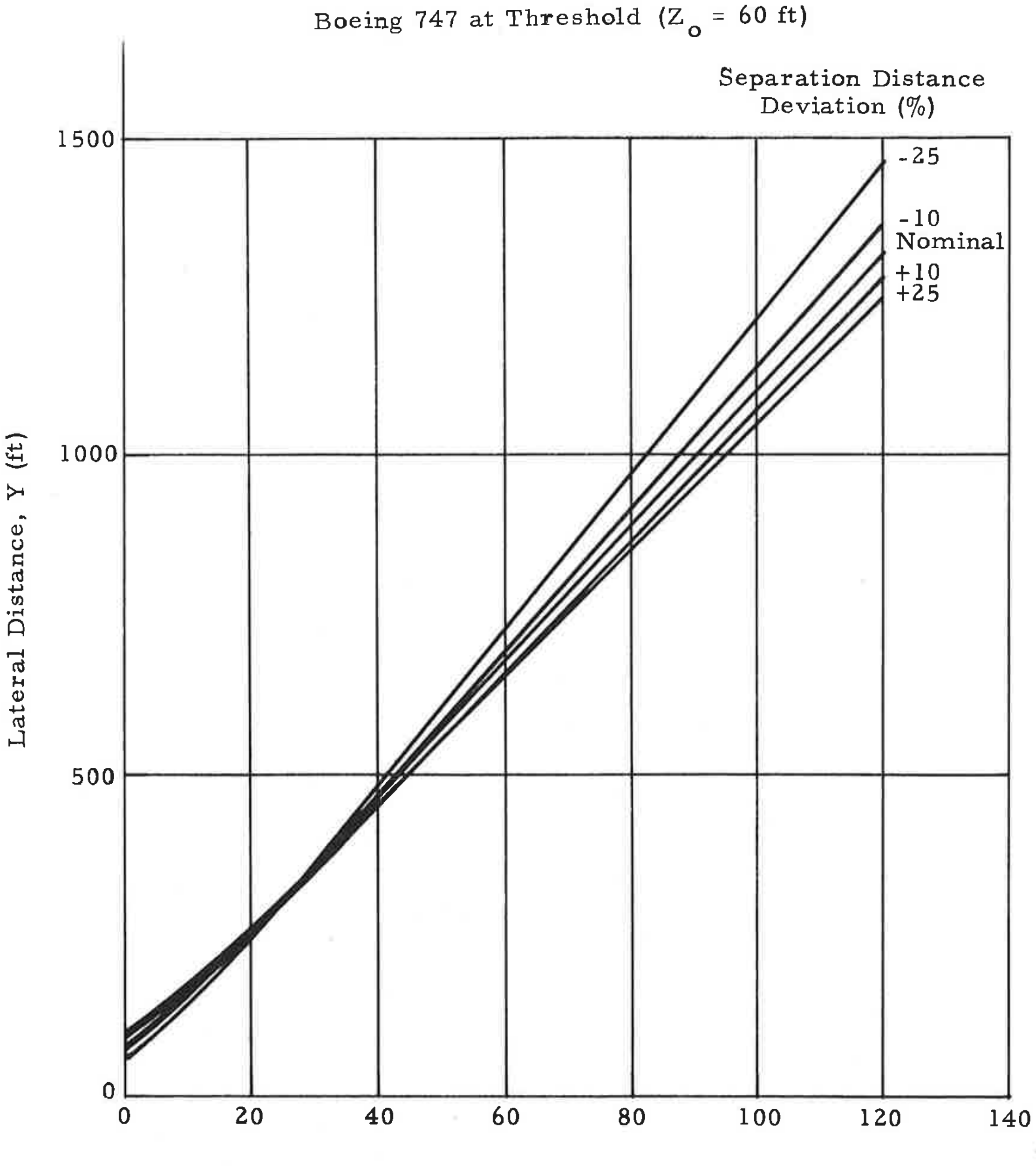

Fig. 3-27 - Variation of Computed Lateral Position with Deviation in Vortex Separation

Boeing 747 at Middle Marker (Z_o = 208 ft) Upwind Vortex

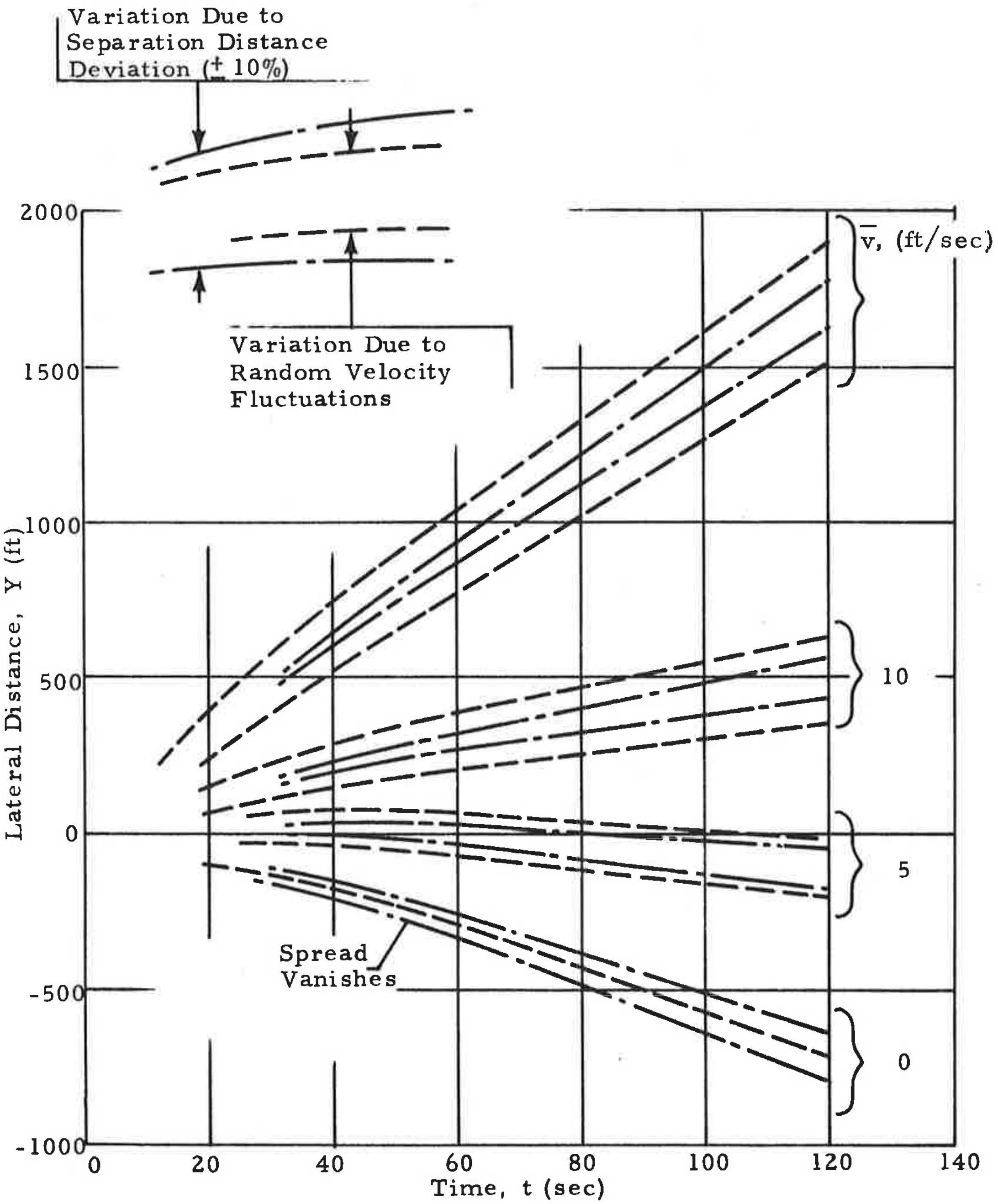

Fig. 3-28 - Variation Due to Separation Distance Deviation Compared to Variation Due to Random Velocity Fluctuations

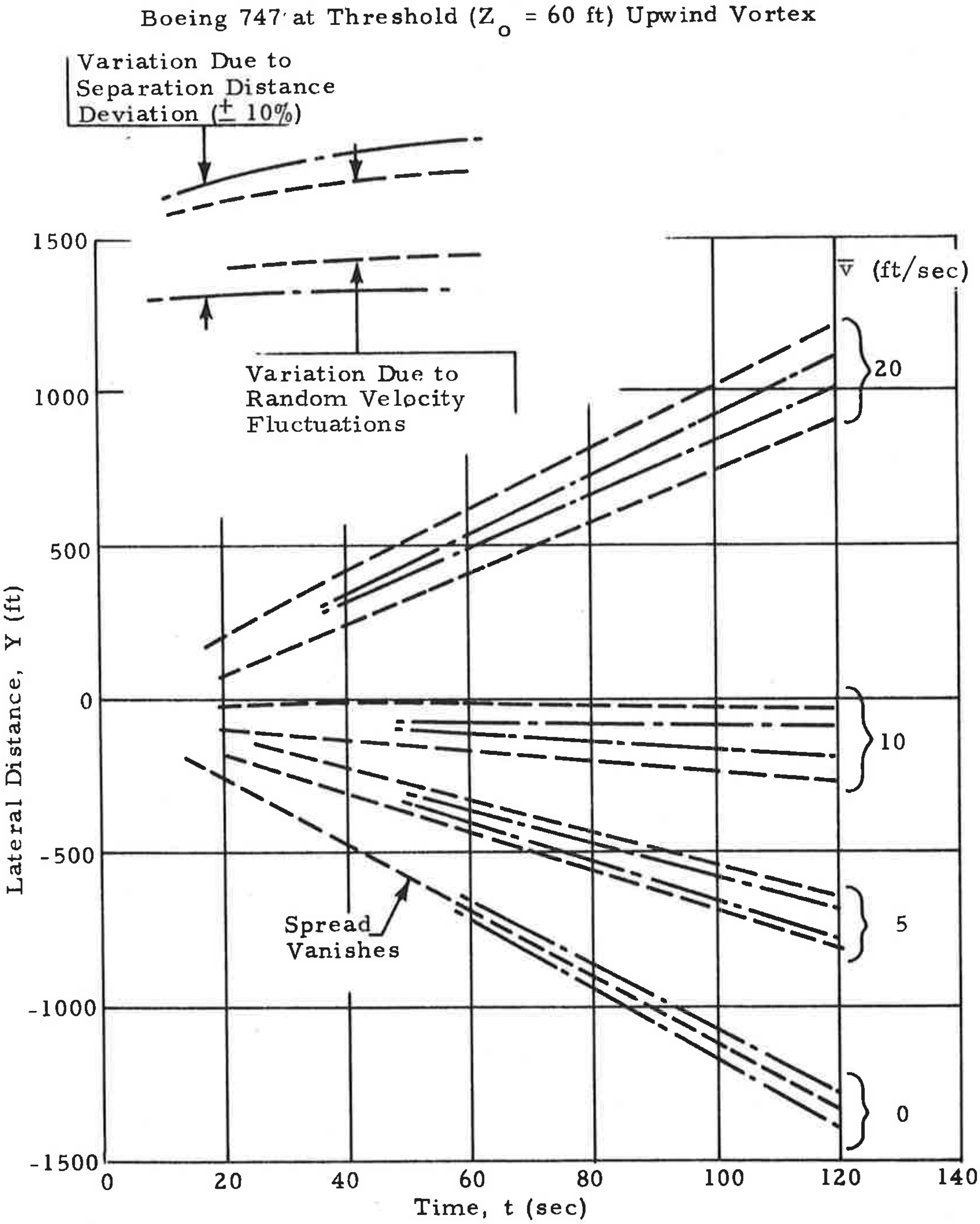

Fig. 3-29 - Variation Due to Separation Distance Deviation Compared to Variation Due to Random Velocity Fluctuations

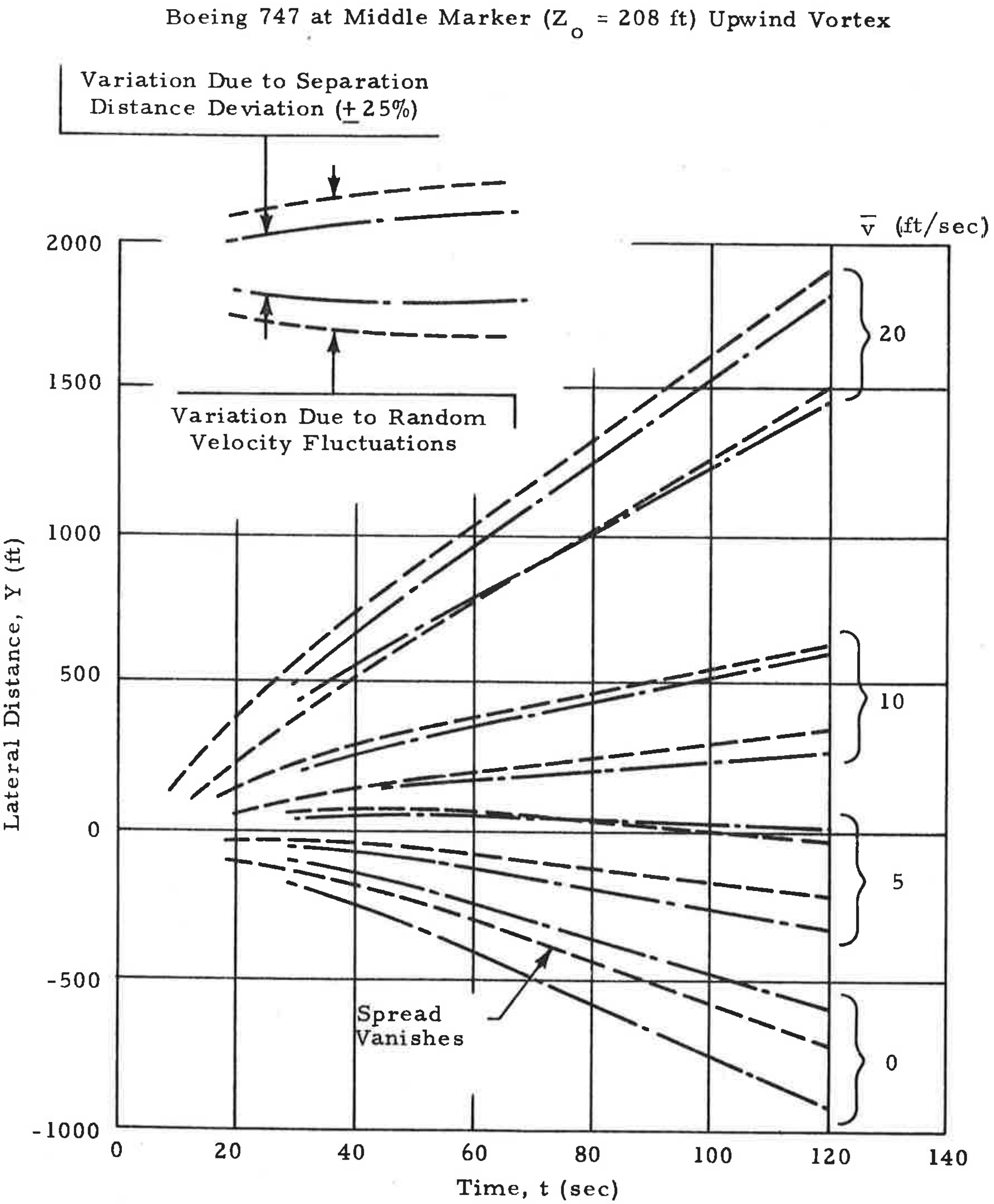

Fig. 3-30 - Variation Due to Separation Distance Deviation Compared to Variation Due to Random Velocity Fluctuations

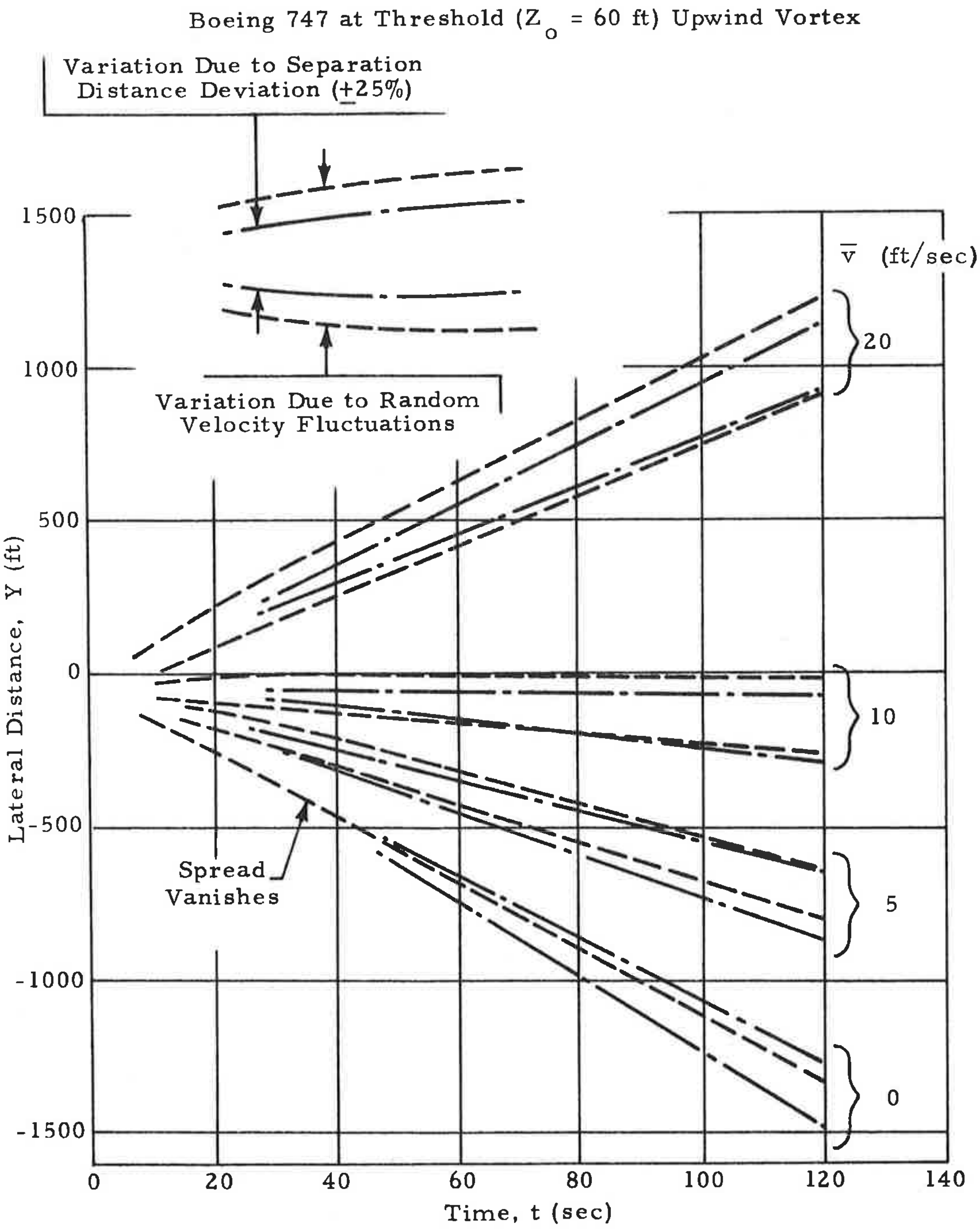

Fig. 3-31 - Variation Due to Separation Distance Deviation Compared to Variation Due to Random Velocity Fluctuations

Thus, the general conclusion is that the model appears able to tolerate variations in circulation and separation up to around ±10% and still be within the error produced by the random velocity fluctuations.

3.5 VORTEX DECAY

The vortex circulation decays with time at a rate determined by a vortex decay eddy viscosity. This eddy viscosity is determined as a function of the initial circulation (Ref. 20). Since there is some uncertainty in the values of the eddy viscosity, the model was tested for sensitivity to variations in eddy viscosity from the nominal. The computed lateral distances are shown in Figs. 3-32 and 3-33 for variations in eddy viscosity by factors of 10, 50 and 100 from the nominal. It is seen that for the baseline cases under consideration (Boeing 747 at middle marker and threshold positions), the vortex decay constant may vary up to a factor of 10 and be within the baseline tolerances.

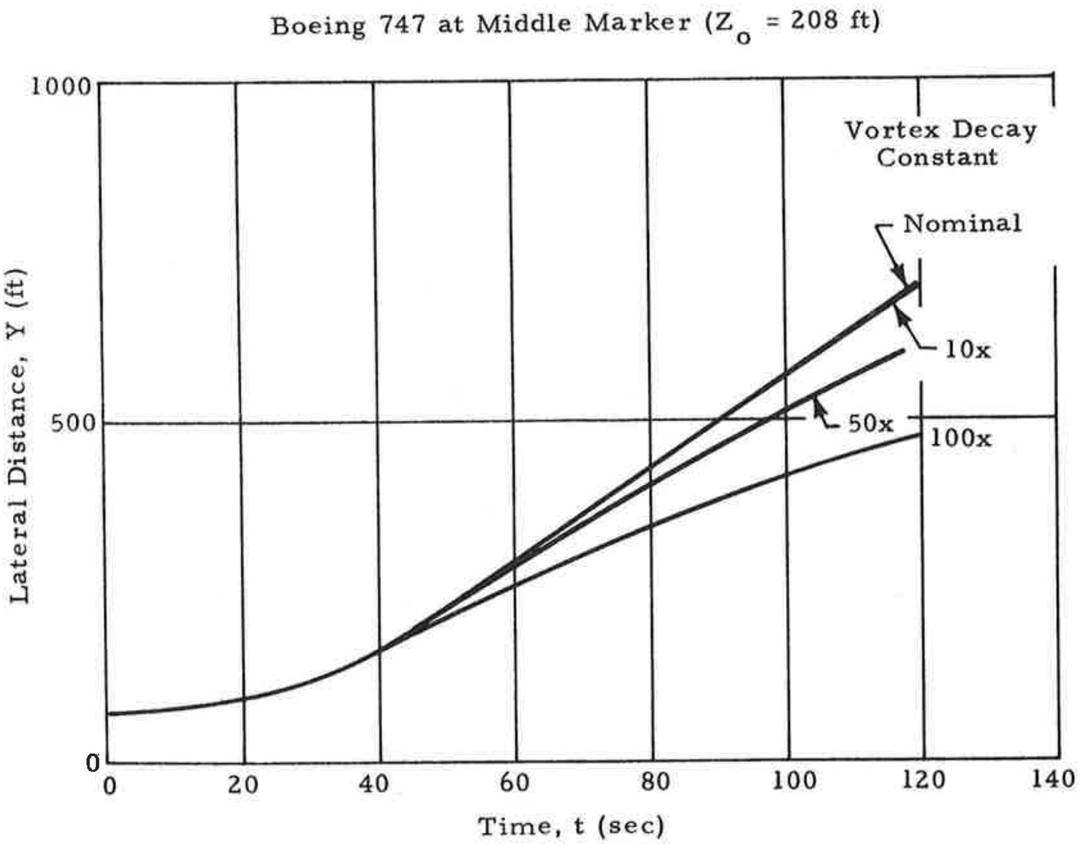

Fig. 3-32 - Variation of Computed Lateral Position with Vortex Decay Constant

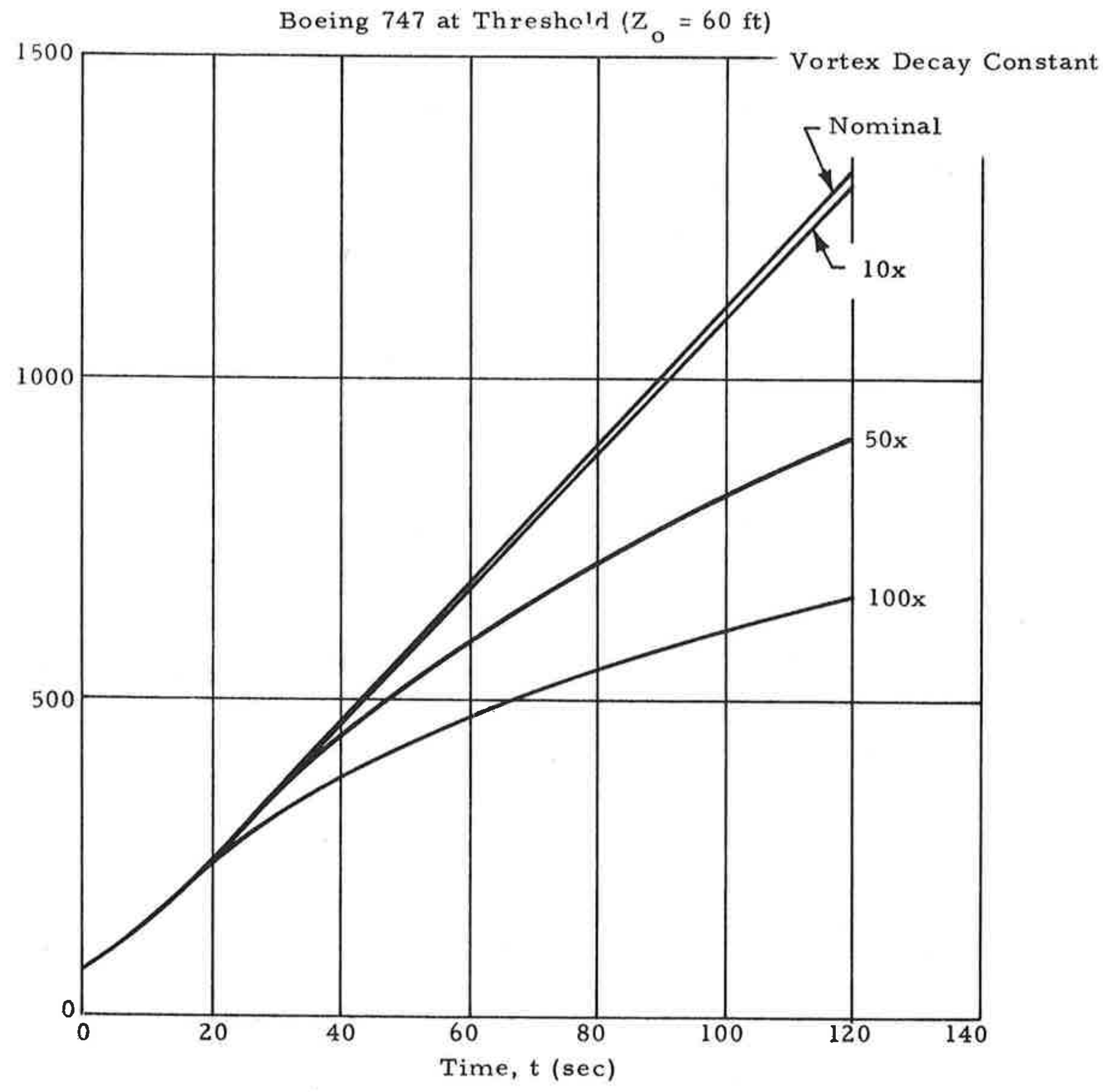

Fig. 3-33 - Variation of Computed Lateral Position with Vortex Decay Constant

Section 4

PROOF OF CONCEPT TESTS

4.1 NAFEC TEST FACILITIES

During October and November 1972 proof of concept tests were performed at the National Aviation Facilities Experimental Center (NAFEC) in Atlantic City, New Jersey. The test consisted of

- Measuring the atmospheric conditions
- Forecasting the vortex transport, and
- Performing the aircraft flybys and monitoring the vortex tracks.

The NAFEC Vortex Flight Test Facility consists of a 140-foot tower instrumented with hot-film anemometers, colored smoke dispensers and meteorological instrumentation. The smoke was used to visualize the vortex tracks. A 35-mm camera was located approximately 2000 feet from the tower and chosen to lie in a line nearly normal to the prevailing wind direction. Photographs were taken every second and the vortex tracks were obtained by visually examining each print in turn and locating the center of the vortices by scaling photographic distances against known distances.

Supplementing the visual tracks were ground-wind sensor tracks. Propeller anemometers were set out on a baseline near the tower and the local wind velocity perpendicular to the aircraft flight path was recorded as a function of time. Often the lowest smoke dissipated quickly but the ground wind sensors were able to extend the range of the visual measurements. Required aircraft parameters (configuration, gross weight, airspeed, heading, etc.) were recorded by the pilots and radioed to the test controller immediately after the aircraft passed the tower. The height and lateral position of the aircraft with respect to the tower were measured by the phototheodolite facilities at NAFEC. The atmospheric conditions were monitored before, during and after the aircraft flybys to determine the conditions during the test and to forecast the vortex transport. Atmospheric variables were recorded from meteorological instrumentation located at five levels on the NAFEC tower (ambient wind velocity, absolute temperature and relative humidity). The tower data were recorded hourly beginning six hours before the flights to four hours after the flights and continuously during the tests. The means of the velocity and temperature histories were computed over the two minutes prior to aircraft passage along with the corresponding standard deviations. The higher altitude conditions were monitored by radiosonde releases which recorded pressure, temperature and winds from the surface (actually around 500 feet above MSL) to 5000 feet. The upper air data were recorded hourly beginning three hours before the tests to three hours after the tests were completed.

The primary days of interest for proof of concept considerations were 17 and 18 October and 1 November 1972. However, additional data were made available to allow comparison of predicted vortex tracks with experimentally determined tracks over a wider range of meteorological conditions. These tests were 19 and 22 August, and 13 through 17 September 1972 and were chosen because tower meteorological data were available. A complete summary of the runs of interest are given in Appendix A. A more detailed discussion of vortex tests at NAFEC is presented in Ref. 28.

4.2 DETERMINATION OF THE WIND PROFILE

Basically two different techniques have been investigated to determine a wind profile over the range of altitude from the aircraft flight path to the surface. The first technique uses discrete measured values (usually 5 values over the range of altitude of the tower) to determine either segment-interpolated (or extrapolated) wind speeds and directions or least squares representations of the data. The second technique requires utilizing one wind speed and direction to construct a profile representation which can be blunt or of the power law form. The former technique is considered to be somewhat more than would presumably be required for an operational wake vortex predictive system. However, a reliable wind profile should be used when evaluating predictive vortex tracks to allow meaningful comparisons to be made. The following is a brief description of these techniques.

- A linear interpolation or extrapolation technique is used to determine the wind speed and direction at all altitudes of interest, or
- A non-linear least squares analysis is performed to determine a reference velocity and power law exponent at a given reference height for an arbitrary number of observed wind speeds.
- A polynomial least square analysis is performed on the wind direction variation with height. The order is optional but a quadratic is normally used, then
- The component wind profiles are computed from a combination of these techniques. This yields both the cross wind and longitudinal wind profiles.

A few words of caution are presented for application of these simple concepts. Normally the aircraft is flying at an altitude greater than any of the wind measurement stations. The linear extrapolation technique was first used to determine the wind field at the aircraft altitude. It was found that detectable errors result as a consequence of this extrapolation; this will be discussed fully in Section 5. This was one reason the power law concept was investigated. This also requires extrapolating the wind direction data to the maximum altitude and some judgement must be used in connection with the direction curve-fit. The quadratic fit of direction versus height produces very acceptable results throughout the range of the data. However, extrapolation can produce serious errors as indicated in Fig. 4-1. This plot shows the effect of extrapolating the wind direction from 140 feet to 200 feet. It is seen that this can easily produce errors of tens of degrees and in some cases as much as 180 degrees. To overcome this difficulty a linear extrapolation is used to determine an approximate wind direction at the aircraft altitude. Note the linear extrapolation only defines one point and not the wind direction over the extrapolation range. Thus, this one point is used with the measured values to perform a least square polynominal fit over the entire range of altitudes. This results in a superior representation of the wind profile as evidenced in Fig. 4-2. This plot shows the effect on the cross wind profile of neglecting the error in the wind direction. The corresponding effect on the longitudinal wind profile is shown in Fig. 4-3.

4.3 PHOTOGRAPHIC TRACKING OF AIRCRAFT VORTICES

The photographic data used in this analysis were obtained by Transportation Systems Center personnel with techniques developed at TSC. Furthermore, the photographs were reduced at TSC according to the procedure outlined in Ref. 28. A typical tracking sequence is shown in Fig. 4-4. Time equal zero corresponds to aircraft passage; the smoke grenades are detonated at a time prior to the first vortex arrival. At a time of 10 seconds the starboard vortex hits the tower near the 140-foot level. The downwind drift of the first vortex is seen in the frame corresponding to 18 seconds. The second vortex hit at the 120-foot level of the tower at 20 seconds. Note the equal altitudes of the two vortices. Also the core formation is evident in the frames corresponding to 38 and 54 seconds. The remaining frame shows the downwind drift of vortices and the smoke detrainment. As previously mentioned, the absence of smoke does not infer that the vortex has dissipated. This will be discussed further in Section 5.

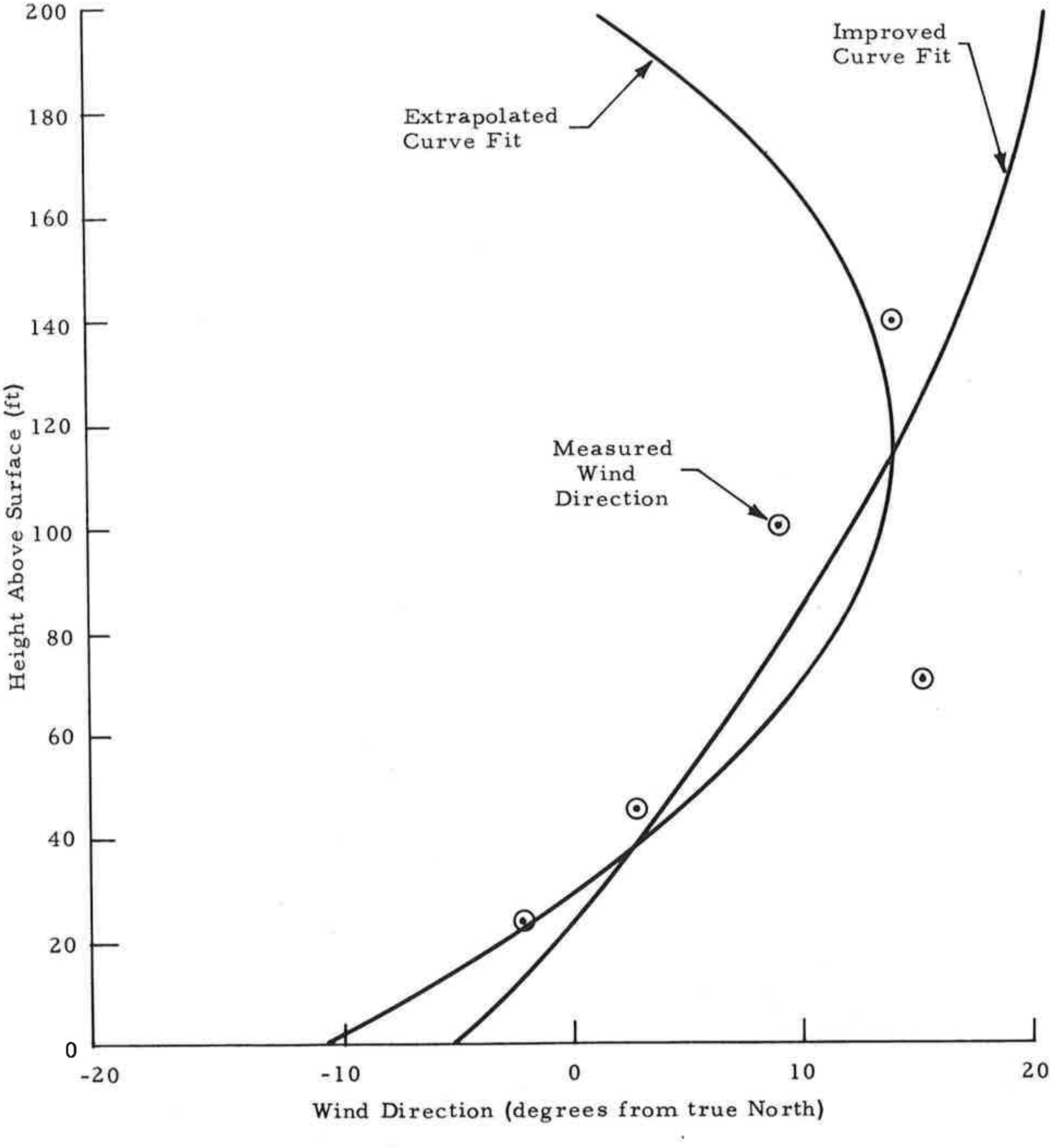

Fig. 4-1 - Comparison of Extrapolation Techniques for Wind Direction (Data from Run 8, 18 October 1972)

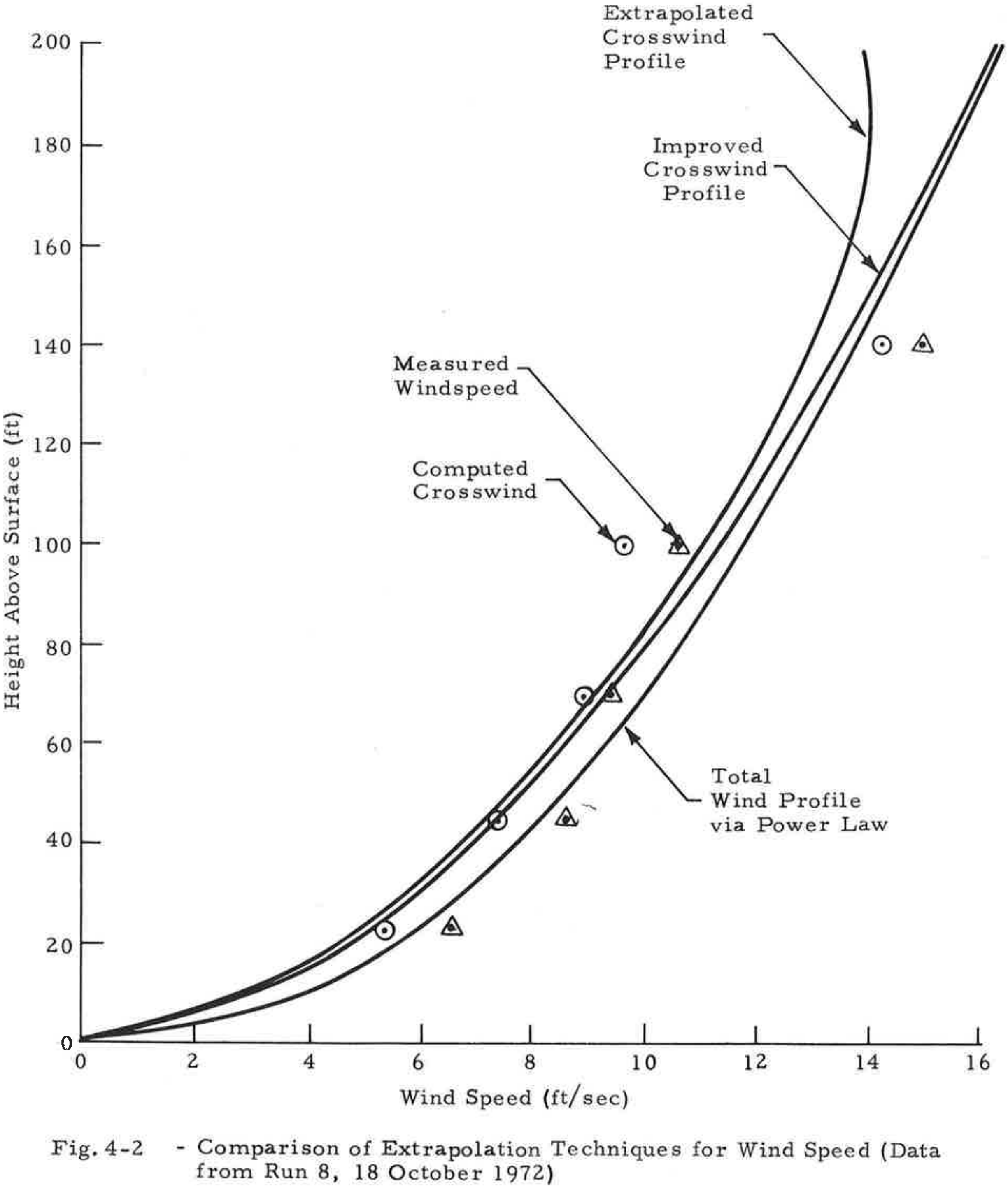

Fig. 4-2 - Comparison of Extrapolation Techniques for Wind Speed (Data from Run 8, 18 October 1972)

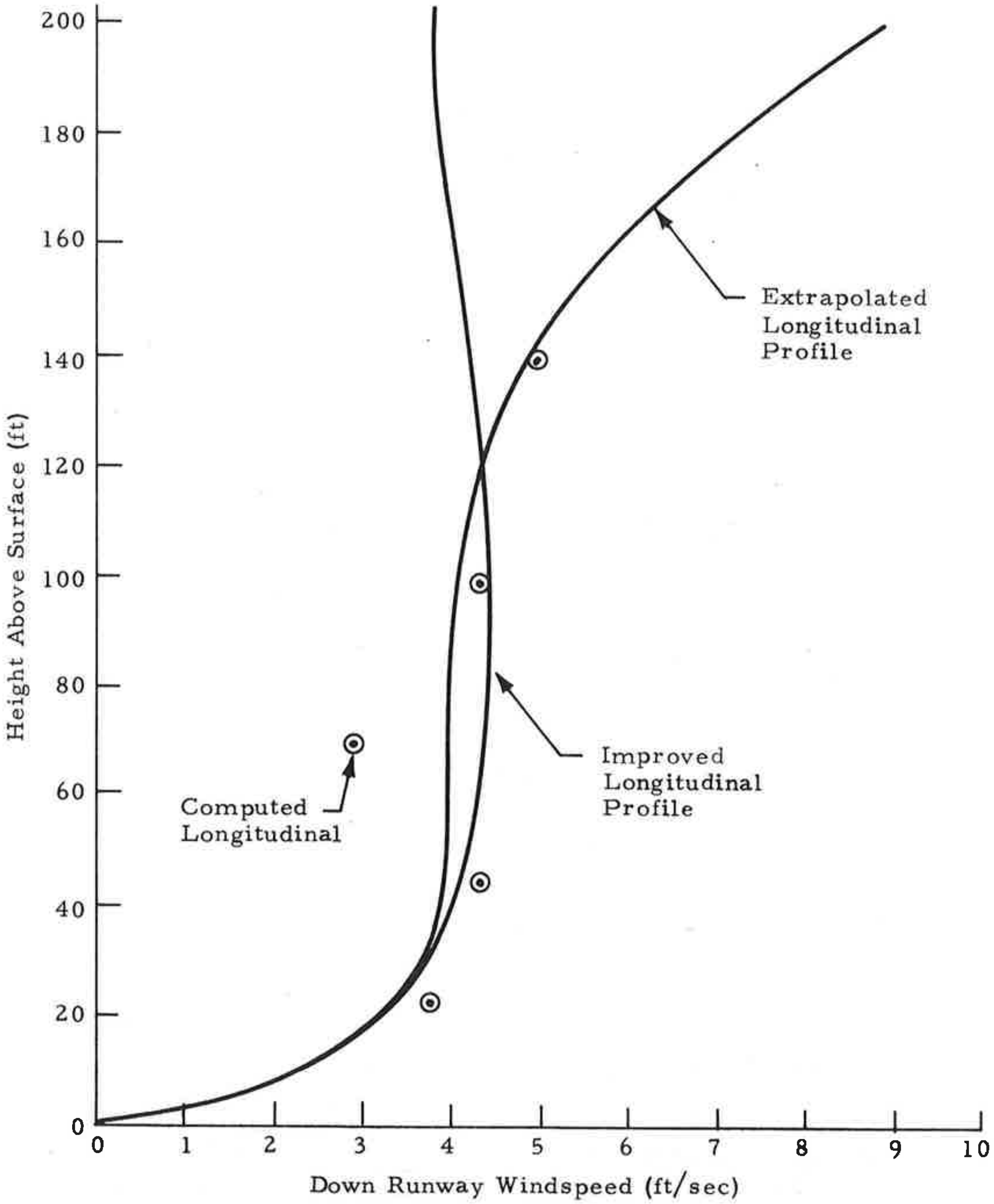

Fig. 4-3 - Comparison of Extrapolation Techniques for Longitudinal (Down Runway) Windspeed (Data from Run 8, 18 October 1972)

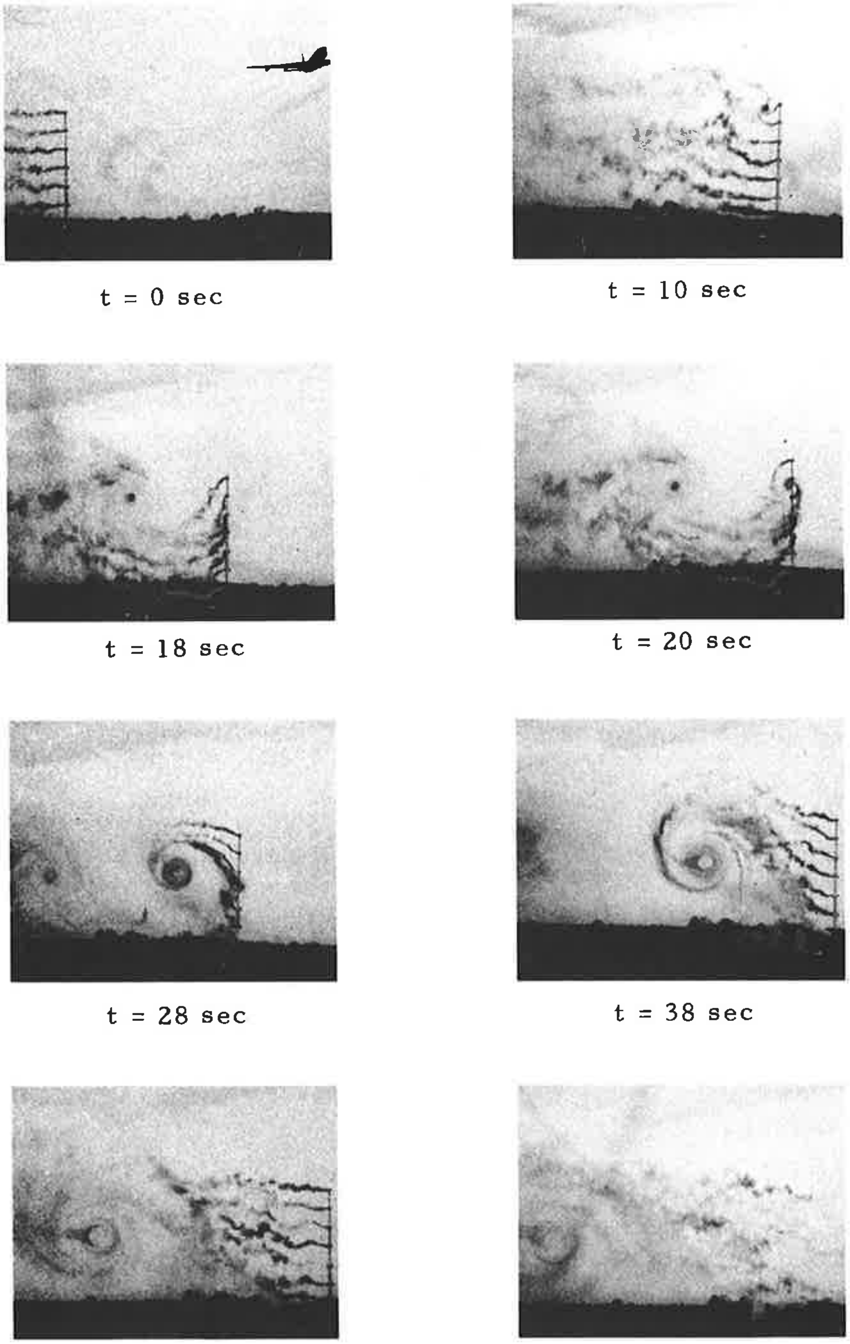

t = 0 sec

t = 10 sec

t = 18 sec

t = 20 sec

t = 28 sec

t = 38 sec

t = 54 sec

t = 62 sec

Fig. 4-4 - Typical Sequence of Tracking Photographs

4.4 GROUND WIND VORTEX TRACKING CONSIDERATIONS

Vortex tracking by ground wind measurement was first mentioned by Thomson (Ref. 29) where it was suggested that the induced pressure near the surface be monitored with an array of pressure probes. Since experiments have been made to determine the pressure rise near the ground (Ref. 30 and 31) and since an understanding of the vortex signature is of fundamental importance in designing a Wake Vortex Avoidance System, some discussion is presented here concerning the use of ground wind measurements. Also ground-wind data were recorded at the proof of concept test for use in model verification.

Attempts have been made to deduce vortex characteristics from time histories of pressure both in the intrinsic structure of turbulent jets (see Lau, et al., Ref. 32) and in the study of aircraft vortices near the ground (see Burnham, et al., Ref. 31 and Hallock, Ref. 30, as previously mentioned).

In all cases, and in the original discussion by Thomson, the steady Bernoulli equation was used to relate the velocity to the pressure. However, since the source is being convected in the moving media and a stationary transducer is involved, the unsteady Bernoulli equation <u>must be used</u>, i.e.,

$$P + \rho \frac{\partial \phi}{\partial t} + \frac{1}{2} \rho q^2 = \text{constant} \tag{4.1}$$

where ϕ is the velocity potential, q is the magnitude of the velocity vector and P and ρ are the fluid pressure and density. For the situation of interest this reduces to the following

$$P + \rho \frac{\partial \phi}{\partial t} + \frac{1}{2} \rho q^2 = P_\infty + \frac{1}{2} \rho q_\infty^2 \tag{4.2}$$

where the subscript ∞ refers to far field conditions (in absence of vortex effects). This equation was used in Ref. 32 in modeling the shear layer of a jet. The unsteady term ($\rho\ \partial\phi/\partial t$) can readily be determined for the case of horizontal transport of a vortex at constant velocity. This corresponds to the equilibrium ground plane condition. For this simple case the vortex and its image constitute a vortex pair traveling at the constant speed $q_v = q_s + q_\infty$, where q_s is the vortex sink rate prior to encountering ground plane effects. Thus, from a moving reference frame moving at the velocity of the vortex pair, the overall flow field appears to be steady. Thus, the Bernoulli equation referred to this frame becomes:

$$P + \frac{1}{2}\rho q''^2 = P_\infty + \frac{1}{2}\rho q_s^2 \tag{4.3}$$

where q'' is the velocity referenced to the moving frame. Subtracting Eq. (4.3) from Eq. (4.2) yields:

$$\frac{\partial\phi}{\partial t} = \frac{1}{2}(q_\infty^2 - q_s^2 - q^2 + q''^2) \tag{4.4}$$

Since $\vec{q}'' = \vec{q} - \vec{q}_v$ and $\vec{q} = \vec{q}_\infty + \vec{q}'$, where $\vec{q}'$ is the vortex induced velocity, Eq. (4.4) may be further reduced to:

$$\frac{\partial\phi}{\partial t} = - q'_x q_v \tag{4.5}$$

where q'_x is the horizontal component of $\vec{q}'$.

With this result, Eq. (4.2) becomes

$$P - \rho q'_x q_v + \frac{1}{2}\rho q^2 = P_\infty + \frac{1}{2}\rho q_\infty^2 \tag{4.6}$$

at points along the ground (neglecting ground shear), $q'_x = q - q_\infty$, so that after rearranging and non-dimensionalizing Eq. (4.6) becomes:

$$\frac{P_\infty - P}{\frac{1}{2}\rho q_s^2} = \left(\frac{q}{q_s}\right)^2 - \left(\frac{q_\infty}{q_s}\right)^2 - 2\left(\frac{q_v}{q_s}\right)\left(\frac{q}{q_s}\right) + 2\left(\frac{q_v}{q_s}\right)\left(\frac{q_\infty}{q_s}\right) \tag{4.7}$$

This equation is a simple quadratic in q and may be solved explicitly.

The last two terms in Eq. (4.7) are due to the unsteady condition. To determine the relative magnitude of the unsteady terms, we assume for simplicity a zero wind condition ($q_\infty = 0$), thus reducing Eq. (4.7) to:

$$\frac{P_\infty - P}{\frac{1}{2}\rho q_s^2} = \left(\frac{q}{q_s}\right)^2 - 2\left(\frac{q}{q_s}\right) \qquad (4.8)$$

Vortex transport theory shows that, at the midpoint between a vortex pair which would be at ground level directly under the real vortex, $q/q_s = 4$. The magnitude of the unsteady term on the right hand side of Eq. (4.8), therefore, would be 8 compared to 16 for the steady term. This shows that the unsteady terms are nearly as important as the steady terms. The important point is that formulating the Bernoulli principle correctly reduces (by a factor of 2 in the example) the theoretical pressure differential. This effect would certainly go a long way in explaining the discrepancy between theory and experiment that resulted in Ref.31. Also any ground pressure measuring system must take this effect into account by extending this analysis to at least a two-dimensional account of the events if amplitude information is used to convey vortex altitude.

4.5 DESCRIPTION OF THE VORTEX SIGNATURE

To determine the vortex signature at any given spatial location, the concepts established in Section 2, i.e., Eq. (2.1) applies. Several special cases of interest should be pointed out. First consider the case of the downwind vortex directly over the ground wind sensor of interest, namely point P. Thus $y = y_o$ and

$$\dot{y}_{y=y_o} = \frac{\Gamma}{2\pi}\left[\frac{2z_1}{z_1^2 - z_o^2} - \frac{(z_2 - z_o)}{4y_o^2 + (z_2 - z_o)^2} - \frac{(z_2 + z_o)}{4y_o^2 + (z_2 + z_o)^2}\right] + v_{CW} \qquad (4.9)$$

Secondly, consider only one vortex and its image (i.e., $z_2 \rightarrow \infty$). This corresponds to considering only one vortex as influencing a particular sensor when that vortex is directly over the sensor in question:

$$\dot{y}_{\substack{y=y_o \\ z_2 \rightarrow \infty}} = \frac{\Gamma}{\pi}\left[\frac{z_1}{z_1^2 - z_o^2}\right] + v_{CW} \qquad (4.10)$$

This is a quadratic in the vortex altitude that can be solved explicitly in terms of the maximum vortex velocity (vortex directly above the sensor) and the sensor altitude. This yields

$$\text{Vortex altitude} = z_1 = \frac{1}{2}\left[\frac{\Gamma}{\pi v_y} + \sqrt{\frac{\Gamma^2}{\pi^2 v_y^2} + 4 z_o^2}\right] \qquad (4.11)$$

where $v_y = \dot{y}_{max} - v_{CW}$. Thus v_y corresponds only to the vortex-induced component. Of course, this reduces to the well known equation as the sensor height approaches zero, i.e.,

$$z_1 = \frac{\Gamma}{\pi v_y} \quad \text{as} \quad z_o \rightarrow 0 \qquad (4.12)$$

The details of the theoretical vortex signatures have been generated as a function of aircraft type, crosswind conditions, sensor type (response), location and altitude, and digital sampling rate. A schematic of the sensor array and parameter range is shown in Fig. 4-5.

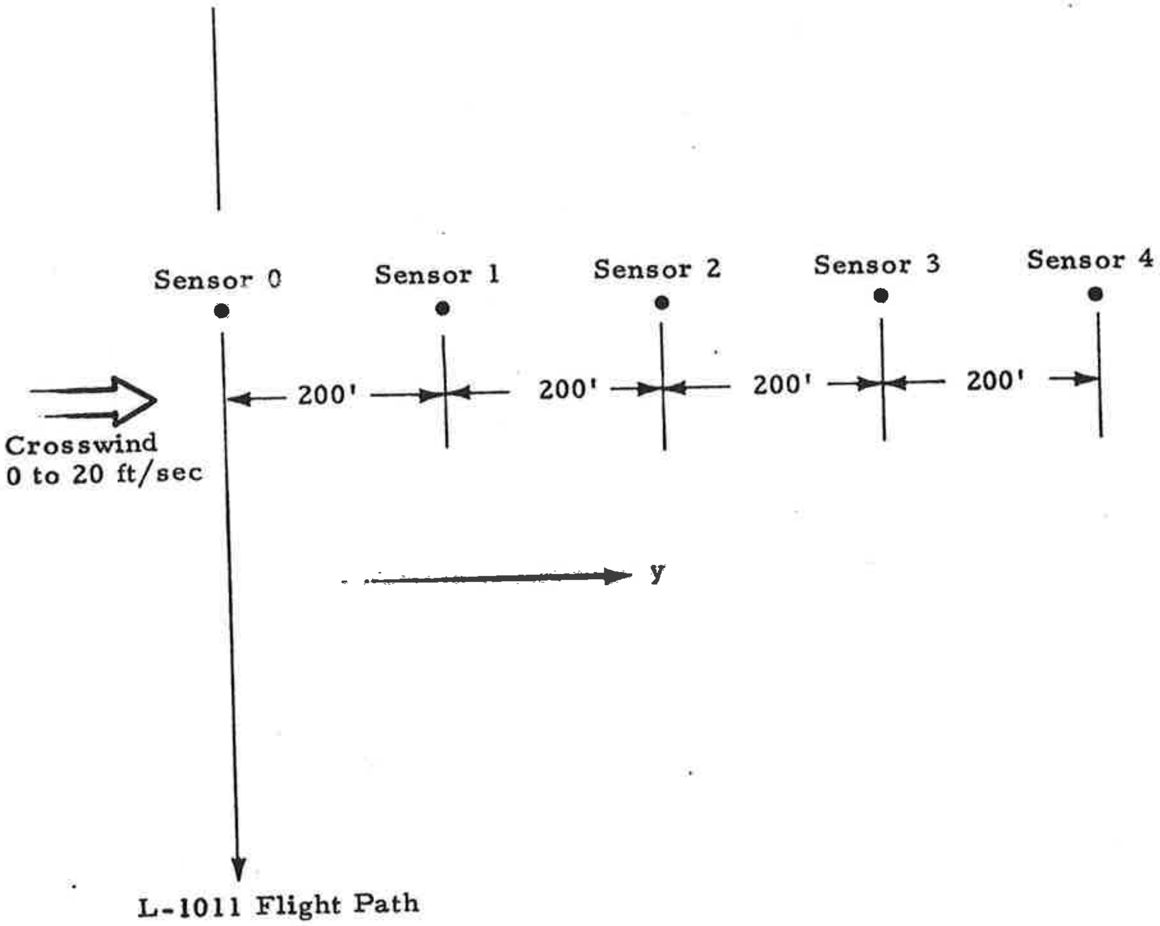

Fig. 4-5 - Schematic of Sensor Arrangement

Careful study of the trends depicted in ground wind signature simulations must be accomplished before attempting to analyze experimental measurements. Figure 4-6a shows the vortex track for the no wind case. Note the sensor on the aircraft flight path sees a continuous input of zero horizontal velocity corresponding to the symmetric vortex pair and images system.

At the 200-foot location the first vortex induced peak is encountered at approximately 29 seconds, and 50, 74 and 99 seconds for sensors 1, 2, 3 and 4, respectively. The smaller amplitude at 200 feet is, of course, because the vortex is above its equilibrium height. The curves were generated with a sampling rate of one sample per second and for this wind condition appears sufficient. For higher winds, however, a greater sampling rate is required. Figure 4-6c shows the effect of a low crosswind. The wind produces an asymmetric system with the upwind vortex transport retarded, thus inducing a negative velocity in the centerline sensor location. Note that the downwind vortex signature is shifted up by the mean crosswind with essentially the same amplitude for sensors 2, 3, and 4. However, the amplitude for sensor 1 is diminished by 4 ft/sec. This is due to two effects, namely that a crosswind produces a "younger" vortex at any given sensor location due to increased translation and secondly the closer proximity of the upwind vortex. The magnitude of the two effects will be discussed later. An important point is that the negative peak does not guarantee a vortex location for a sensor on the flight path. It is also seen that the non-vortex contaminated mean velocity is approached after downwind vortex passage (i.e., a constant 4 ft/sec). The same events are encountered for a crosswind of 8 fps as shown in Fig. 4-7a. In Fig. 4-7c the crosswind is shown to be sufficient to negate the upwind movement of the starboard vortex, thus the negative peaks for sensors 0 and 1 at approximately 9 and 55 seconds, respectively. Note the broader upwind vortex signature due to the slower transport. This implies the sampling rate should be dictated by the downwind vortex characteristics. Also the amplitude of the third and fourth sensor is essentially the same (i.e., 36 ft/sec = 48 - 12). However, sensors 1 and 2 are influenced by the upwind vortex as evidenced by the appreciable negative-induced velocity. This is evident because the velocity after vortex passage does not return to 12 ft/sec for sensor 2 and the close proximity of the negative and positive peaks of sensor 1.

Horizontal Velocity

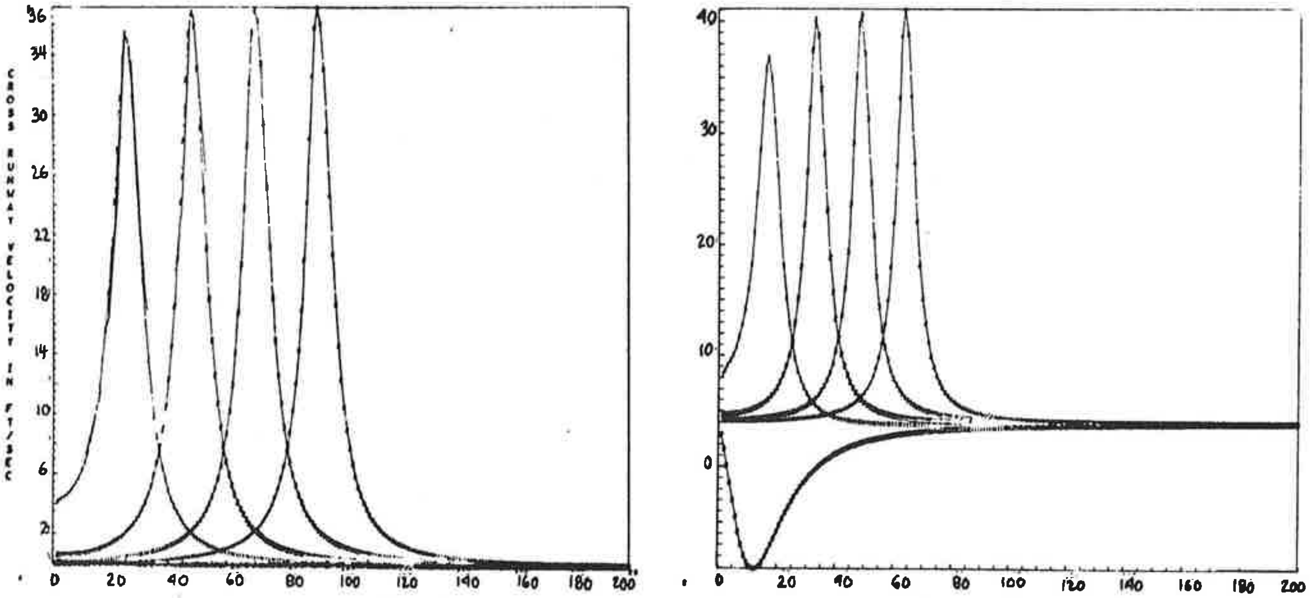

a. Wind Speed = 0 ft/sec

c. Wind Speed = 4 ft/sec

Vertical Velocity

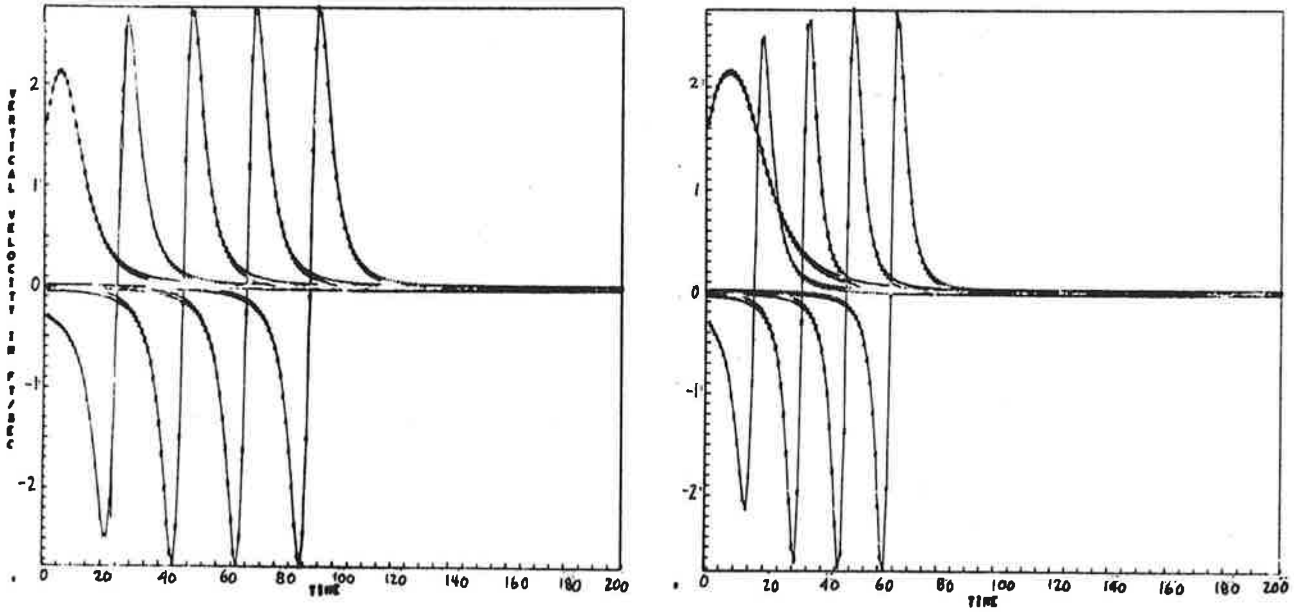

b. Wind Speed = 0 ft/sec

d. Wind Speed = 4 ft/sec

Fig. 4-6 - Horizontal and Vertical Velocity Histories for an L-1011 Aircraft at an Altitude of 100 Feet (Wind Speed = 0 and 4 ft/sec)

Horizontal Velocity

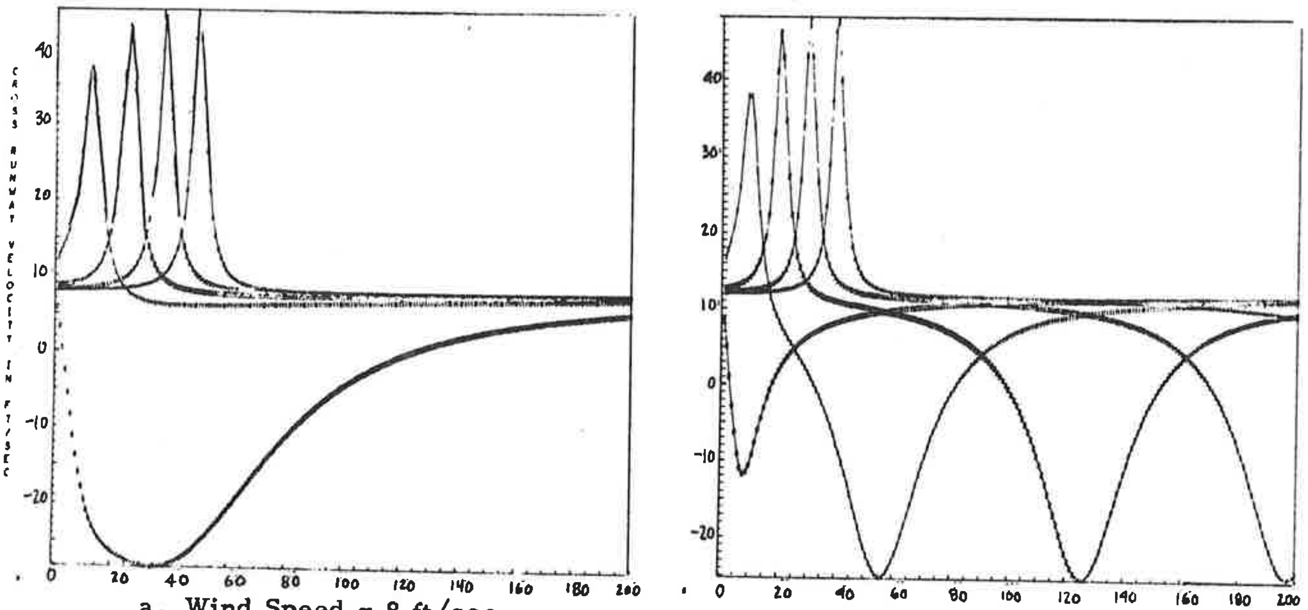

a. **Wind Speed = 8 ft/sec**

c. **Wind Speed = 12 ft/sec**

Vertical Velocity

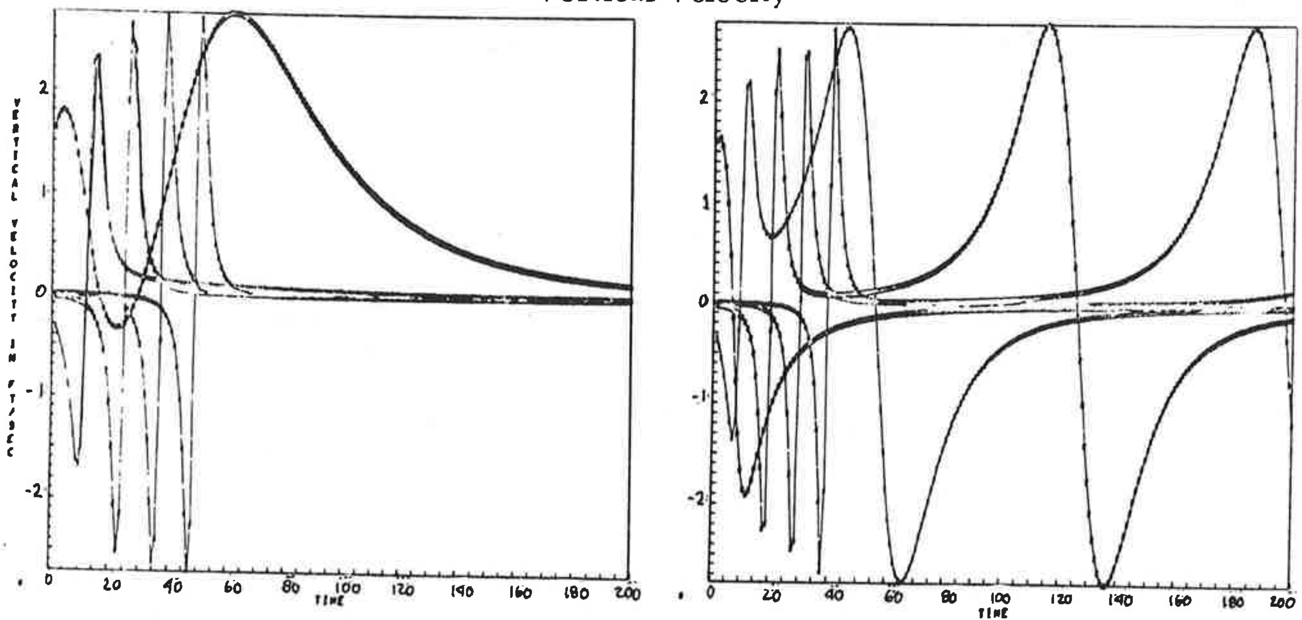

b. **Wind Speed = 8 ft/sec**

d. **Wind Speed = 12 ft/sec**

Fig. 4-7 - Horizontal and Vertical Velocity Histories for an L-1011 Aircraft at an Altitude of 100 Feet (Wind Speed = 8 and 12 ft/sec)

If the time scale were extended beyond 200 seconds the same phenomena would occur for sensor 4 as far as the negative peak is concerned. Above this velocity the general effect of increasing wind speed is to shorten the time scale thus narrowing the signals, especially that of the downwind vortex as seen in Fig. 4-8a. The case depicted by sensor "1" explains the small positive peak relative to the large negative peak that has been noticed in some experiments (Ref. 31). This is again explained in a twofold manner: (1) the altitude of the downwind vortex is greater at the sensor 1 encounter due to a "younger vortex" than that corresponding to the negative peak at the same location, and (2) the mutual induction of both vortices cannot be separated due to the close proximity of the pair. The events for a wind of 20 ft/sec are depicted in Fig. 4-8c and are essentially unchanged except for a reduced time scale.

Corresponding vortex signatures for the vertical velocity component are presented in Figs. 4-6b, 4-6d, 4-7b, 4-7d, 4-8b and 4-8d. The vortex position can be obtained by locating the approximate zero crossing (for a zero-mean vertical wind). The exact time does not correspond to precisely zero vertical velocity for vortex passage as the other vortex is inducing a velocity from a far field condition. The negative peak (upper peak) for the centerline sensor (sensor "0") does not represent vortex passage but merely the vertical velocity due to the four vortices at a sensor height of 6 feet. A detailed discussion of each graph will not be presented in the interest of brevity, but only general comments made about the effect of wind. However, much can be learned from a detailed analysis and the full set of graphs are presented to allow the reader to do so if he chooses.

As the crosswind increases the time scale is again reduced and above a certain value the upwind vortex will move downwind and introduce a second zero crossing. This does not occur in the 200-second time frame until a wind of 12 ft/sec is reached (actually some place between 8 and 12 ft/sec) and occurs for all sensors except 4. This is shown in Fig. 4-7d. At 8 ft/sec (Fig. 4-7b) the second zero crossing occurs after 200 seconds but the second vortex can be seen to be between sensors "0" and "1". Above 12 ft/sec events will occur on a reduced time scale. Note the local minimums in all of the vertical tracks.

Horizontal Velocity

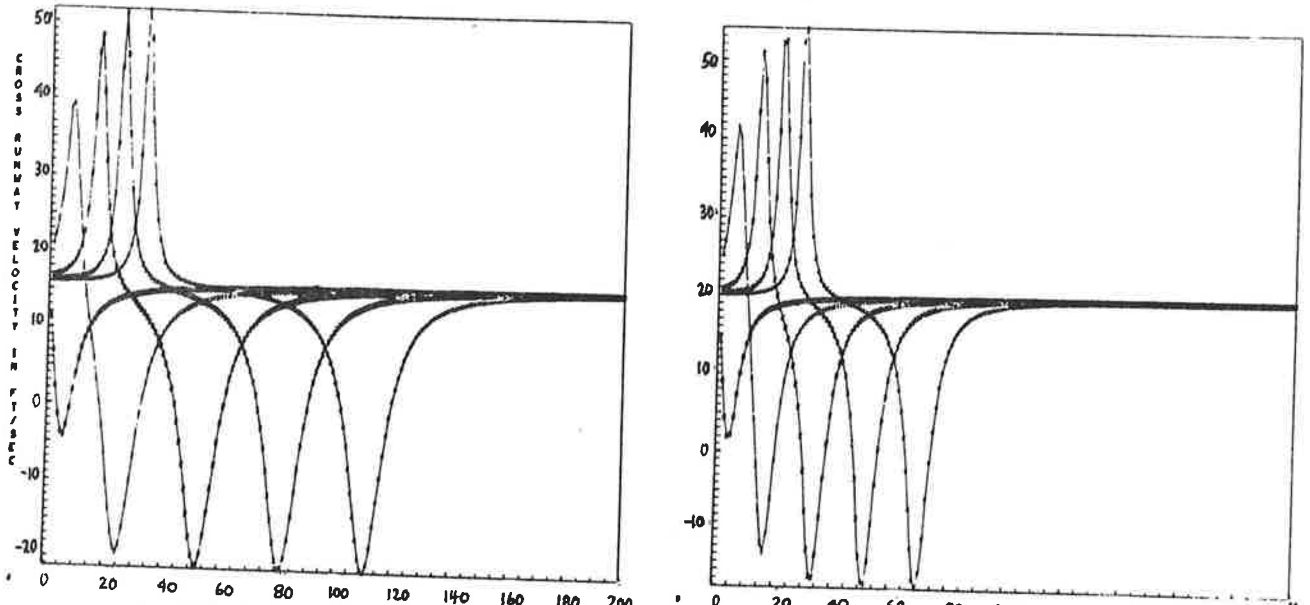

a. **Wind Speed = 16 ft/sec**

c. **Wind Speed = 20 ft/sec**

Vertical Velocity

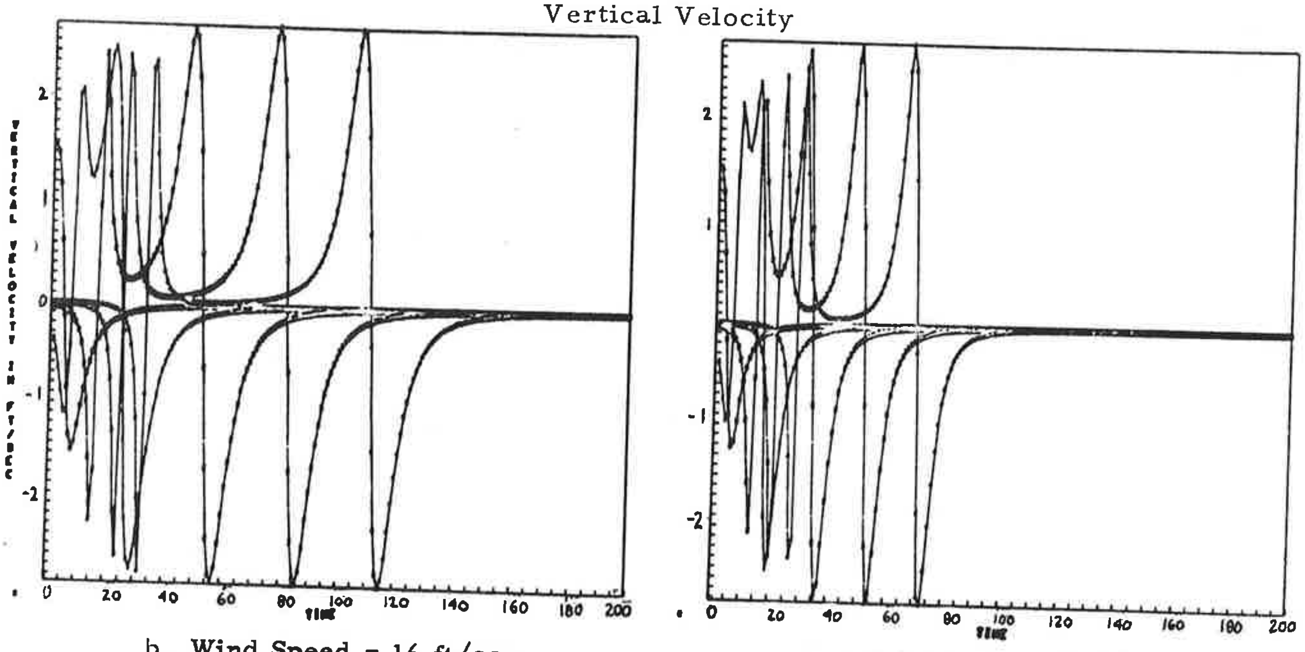

b. **Wind Speed = 16 ft/sec**

d. **Wind Speed = 20 ft/sec**

Fig. 4-8 - Horizontal and Vertical Velocity Histories for an L-1011 Aircraft at an Altitude of 100 Feet (Wind Speed = 16 and 20 ft/sec)

These points correspond to the point where the particular sensor in question is midway between the two aircraft vortices. Thus, more track information is available than that corresponding to only sensor location.

The primary source of noise will, of course, be due to the temporal gradients that exist in the wind field. The computer simulation discussed in a previous section also possesses the capability to superimpose the unsteady vortex velocity on an unsteady wind field. Numerous runs have been made superimposing actual wind field data measured by a Gill anemometer on the calculated vortex signature. The wind data used was also subjected to variance and power spectral density analyses to establish the general effect of temporal gradients. It has been concluded from this analysis that even for relatively small standard deviations, isolated transients exist of sufficient amplitude and reduced frequency that the vortex maximums and minimums are "disguised." Therefore, it has been concluded that a data processing system relying only on locating maximums and minimums is certainly not the most reliable technique. Since the vortex signature is well understood at this point, the same consideration must be given the "noise" in order to optimize the entire system.

It is convenient to restrict the discussion of "noise" to wind components without any loss of generality. This is accomplished by considering u, v, w, as the longitudinal, lateral and vertical components of velocity with primes representing standard deviation, instantaneous fluctuations from the mean and bars indicating means (i. e., $u = \bar{u} + u'$, etc.). Thus at an airport u will generally be in the negative direction of the aircraft flight path with v in the direction of the starboard wing and w positive up.

The spatial variation of large eddies can be statistically defined in terms of a correlation coefficient as

$$R(x) = \frac{\overline{u'_1 u'_2}}{u'^2}, \text{ etc.} \qquad (4.13)$$

The dependence of R(x) on x is a measure of the eddy size and is given by

$$\ell_x = \int_0^\infty R(x)\, dx, \text{ etc.} \qquad (4.14)$$

and is called the scale of turbulence. A time-correlation coefficient, $R(t)$, can be defined in terms of two events occurring at different times at the same point and in particular if the concept of frozen turbulence is employed (unchanging pattern of turbulence convected at the mean speed), it follows that

$$R(t) = R(x) \text{ when } x = ut \tag{4.15}$$

(see Ref. 33). This is equivalent to saying that events occurring upwind are seen downwind at some time later ($t = x/u$) with the validity of such an extrapolation being represented by the magnitudes of either the correlation or the autocorrelation function.

In deducing the magnitude of the transients ("noise") contained in the wind field it is convenient to define the standard deviation of each component relative to the friction velocity

$$u^{*} = \sqrt{\tau_s/\rho} \tag{4.16}$$

where τ_s is the surface shearing stress and ρ is the fluid density. Thus following Pasquill (Ref. 33) and Lumley and Panofsky (Ref. 27) the following equations result

$$\sigma_{u,v,w} = A_{u,v,w}\, u^{*} \tag{4.17}$$

where

$$\begin{aligned} A_u &= 2.5 && \text{for all atmospheric stability} \\ A_v &= 3 && \text{for unstable air} \\ A_v &= 2 && \text{for stable air} \\ A_w &= 1.3 - .3z/L' && \text{as a function of the stability } L' \text{ (1.3 for neutral)} \end{aligned} \tag{4.18}$$

Here L' is equal to the length scale stability parameter L divided by the ratio of eddy diffusivities for heat and momentum (see Pasquill, Ref. 33). In neutral conditions $L' \rightarrow \infty$ thus $A_w \rightarrow 1.3$. These equations allow wind speed and turbulent intensity to be correlated to establish the concept of maximum allowable wind speed for detection of vortex by a ground wind sensing as previously discussed in this section in reference to the curves set forth by Burnham, et al. (Ref. 31). In particular, since the principal component of interest in the vicinity of an airport is the lateral, these concepts will be confined to σ_v for brevity. Now the assumption of absolute neutrality yields

$$u^* = \frac{U_1 k}{\ln z_1/z_o} \tag{4.19}$$

where

$$\ln z_o = \frac{U_1/U_2 \ln z_2 - \ln z_1}{U_1/U_2 - 1} \tag{4.20}$$

and U_1 is total magnitude of wind vector. Since z_o is a terrain feature and is independent of wind speed for the surfaces of concern here, then

$$\sigma_v \cong \left(\frac{3+2}{2}\right) \frac{U_1 k}{\ln z_1/z_o} \tag{4.21}$$

implies that near the ground σ_v is proportional to wind speed only.

A sensor height of 6 feet at an airport would yield an order of magnitude of 3 for $\ln z_1/z_o$. Therefore with $k = 0.4$

$$\sigma_v \approx 0.33\, U_1 \tag{4.22}$$

Note that this is a function of the mean wind at 6 feet, not a high altitude mean. This can, however, be related to any reference level mean wind by

$$U_1/U_{ref} = (z_1/z_{ref})^p \tag{4.23}$$

where p is a function of stability and wind speed.

In addition to the temporal gradients in the wind field giving rise to sources of error in ground wind tracks there are several possibilities that lead to differences between predictive and experimental tracks. Any deviation in the initial vortex circulation or vortex separation distance will produce an uncertainty in the sink rate of the oval. For example, if the separation between the vortices is less than elliptical calculations yield, the vortex pair will descend faster than predicted. This has an opposing effect on vortex position. First the altitude of the actual motion will be less than that calculated giving rise to less horizontal displacement due to wind profile considerations. However, a lower equilibrium altitude will result producing an increased horizontal translation after encountering ground plane effects. Since these mechanisms produce opposite effects the relative magnitudes of each must be considered to establish the overall trend. It has been found that initially when most of the momentum is vertical, the decrease in horizontal translation is less than the increased horizontal translation that occurs at later times due to the lower equilibrium altitude. The superimposed effect is shown by the sketch in Fig. 4-9. This sketch represents the induced horizontal velocity at a sensor near the ground for two different vortex separations, b_1 and b_2.

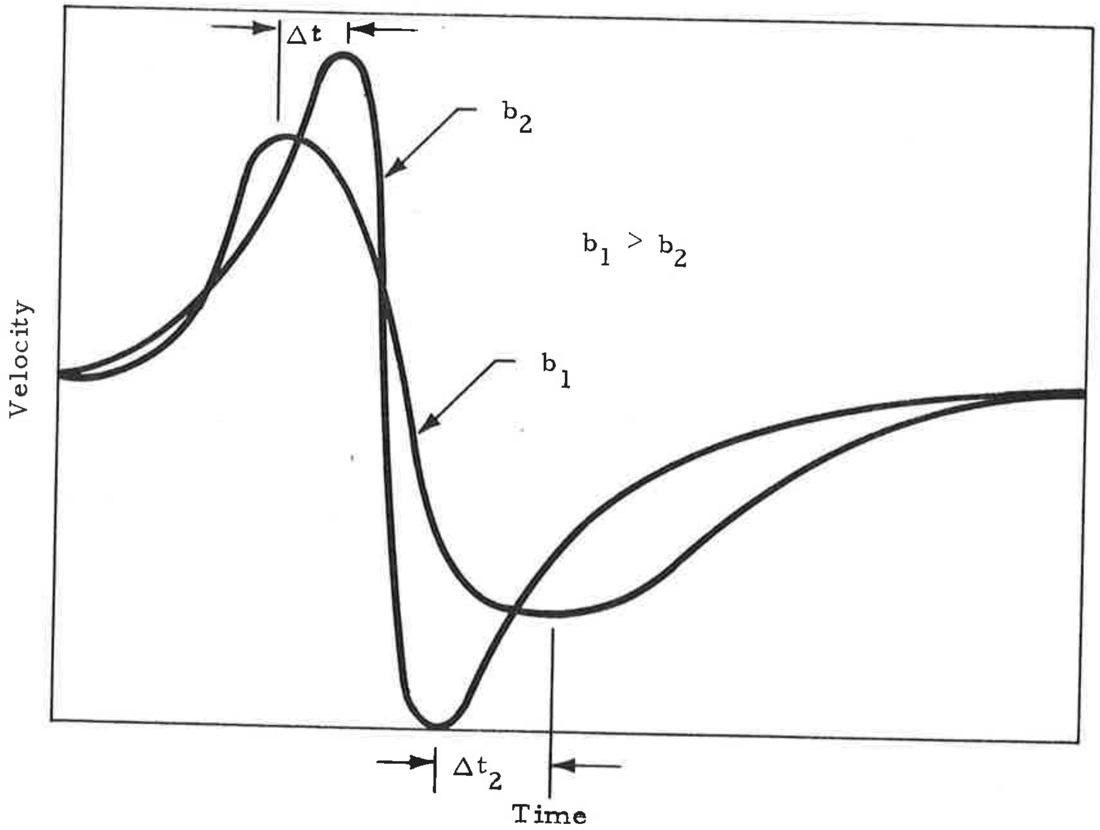

Fig. 4-9 - Sketch of Induced Horizontal Velocity at Ground Wind Sensor for Two Different Vortex Separations

Initially the track corresponding to the vortex pair with the smaller separation has a larger induced downwind velocity and it remains that way until the vortex with the increased translation due to the higher altitude wind induces a greater velocity at the sensor as a result of a closer proximity to the sensor. For moderate creation altitudes the pair with the larger separation will arrive at a sensor near the flight path first and also induce a smaller velocity at vortex passage. As ground plane effect begins to determine the motion of the vortices the pair with the smaller separation will overtake the other vortex due to the larger spreading velocity as shown in the sketch. These relative effects depend on the magnitude of the wind shear with the larger the shear the greater Δt. For no shear Δt will be negative; the shear value corresponding to a Δt of zero can be computed from $(b_2 - b_1)$. Δt_2 has an inverse trend with wind shear in that for no shear Δt_2 is a maximum. Similar reasoning can be used for increases or decreases in the circulation.

Probably the most important parameter controlling the difference between the predicted and measured ground wind vortex tracks is the uncertainty in the mean wind, especially at low altitude. The wind was measured at five altitudes on the tower (from 23 feet to 140 feet) for all flybys at NAFEC. However, even though this is sufficient information to define the wind profile through that range (23 to 140 feet) and extrapolation can be made to the actual aircraft altitude with confidence, the wind profile from the surface to 23 feet is difficult to ascertain. The mean wind below 23 feet will not affect the predicted vortex transport for the aircraft flyby of interest as the vortices are always higher. This error, however, will affect the mean velocity of the vortex signatures computed at the ground wind sensor heights. This is purely a shifting phenomena and is shown in the sketch on the following page. This assumes that the only error in the mean occurs below 23 feet. In actuality there is uncertainty in the mean for all altitudes and in general this uncertainty will produce not only the aforementioned shifting phenomena but also an extension or reduction of the time scale. For a given stability the uncertainty in the mean wind will almost certainly be biased, e.g., an increase in the mean wind at all levels (or vice versa). Figure 4-11 illustrates the phenomena.

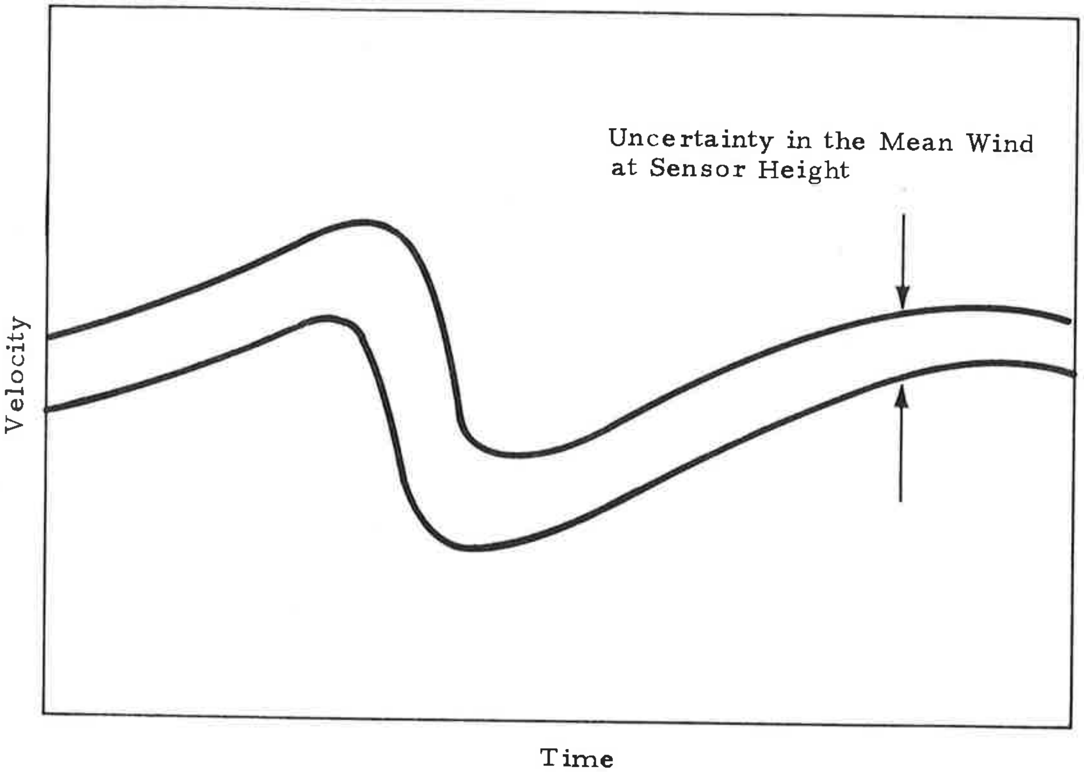

Fig. 4-10 - Sketch of Effect of Uncertainty in the Mean Wind on Predicted Vortex Tracks

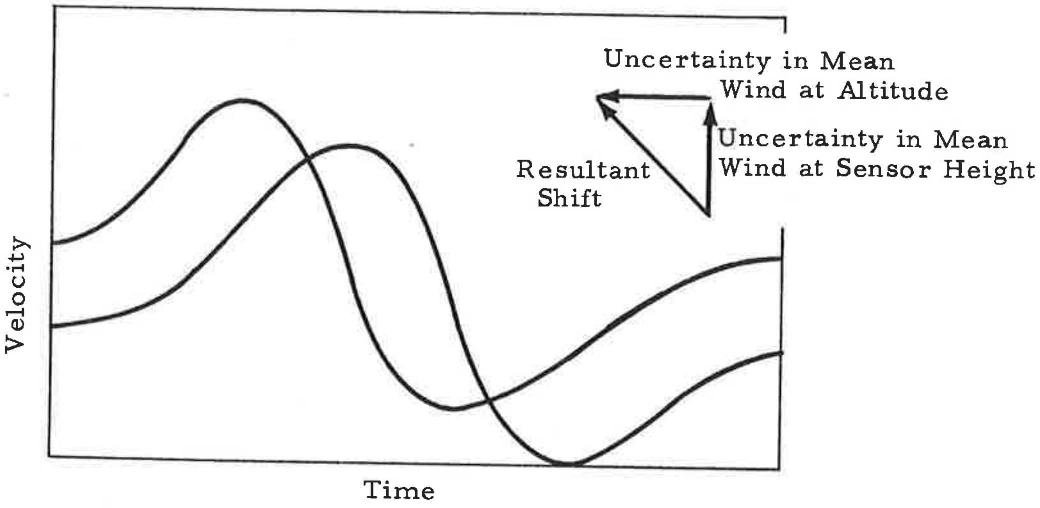

Fig. 4-11 - Sketch of Effect of Uncertainty in the Wind Profile on Predicted Ground Wind Track

The errors are greatest near the ground. For example, Fig. 4-12 shows the calculated wind profiles as a function of a stability related parameter using the wind measurement at the top of the tower (140 feet). Profile bluntness decreases with increasing stability, thus appreciable uncertainty lies in the magnitude of the wind at low levels. As previously mentioned this will not affect the predicted vortex transport at altitude but will shift the predicted ground wind induced velocity by the error in the mean. In most situations it has been observed that this error in the ground level mean wind is usually an under prediction of the magnitude of the mean wind. This gives rise to the events shown in Fig. 4-13. The reverse situation for each case is obvious.

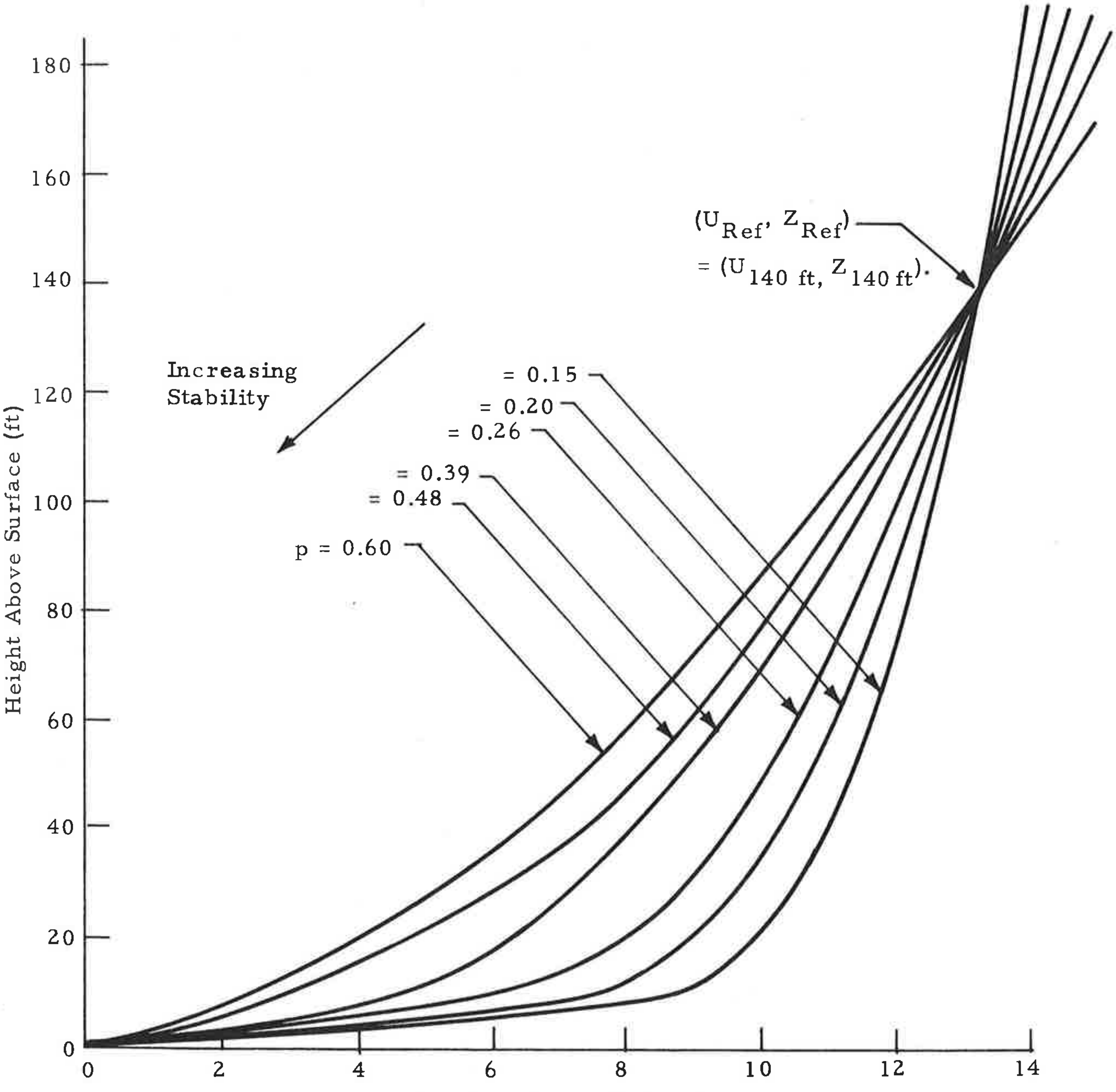

$$U/U_{Ref} = (Z/Z_{Ref})^p$$

Fig. 4-12 - Effect of Stability on Wind Profile (Constant Roughness Parameter Assumed)

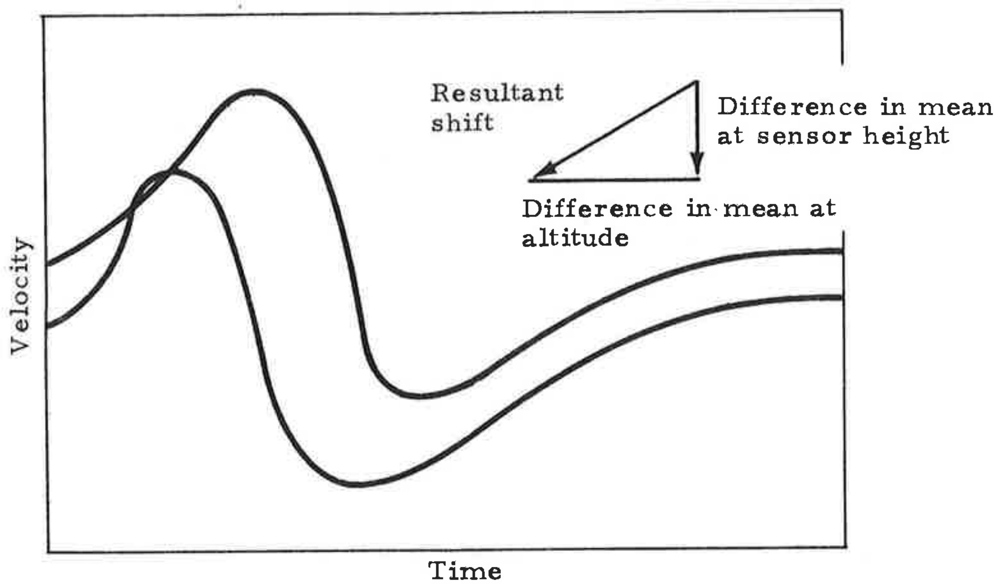

Fig. 4-13 - Shift in Ground Wind Signature Due to Uncertainty in Mean Wind

Section 5
COMPARISON OF PREDICTED VORTEX TRANSPORT WITH EXPERIMENTAL RESULTS

5.1 COMPARISON OF PREDICTED AND MEASURED GROUND WIND VORTEX SIGNATURES

Histories are shown in Fig. 5-1 for the observed and predicted vortex tracks for Run 1 on 18 October 1972. This run is for a B707 aircraft at an altitude of 197 feet displaced from the tower by 232 feet. Flight conditions dictated a circulation of 2616 ft^2/sec. The wind profile used for the predictive analysis is shown in Fig. 5-2 along with the measured values of wind speed. The approximate altitude of each vortex as it crossed the ground sensors is also given in Fig. 5-1. Note that for the vortices between 170 and 195 feet altitude, the predicted and measured vortex signature agree very well. This corresponds directly to that portion of the wind profile which is in error less than 1 ft/sec. As the vortices descend to approximately 80 feet at the 250-foot sensor, the maximums and minimums agree quite closely. Note also the shifting trend, as previously discussed, in that the computed mean at a sensor height of 6 feet is consistently underpredicted. This causes the nearly constant difference between the predicted and measured signatures. Beyond the 250-foot sensor it appears that the wind increased (between 55 to 65 seconds) as there is a consistent trend of the second vortex passage occurring earlier than the corresponding predictions; this will be discussed later as possibly due to another effect. A second comparison is shown in Fig. 5-3 for Run 17 on 18 October 1972. This is also a B707 aircraft cruising at 191 feet, 271 feet from the tower. The same general remarks discussed previously apply for this set of data also. The predicted mean at 6 feet is somewhat low giving rise to the shift between the two tracks. Also note the amplitude of the measured signatures appears to be decreasing after reaching the 250-foot sensor location. This could be due to a decrease in circulation at a faster rate than predicted

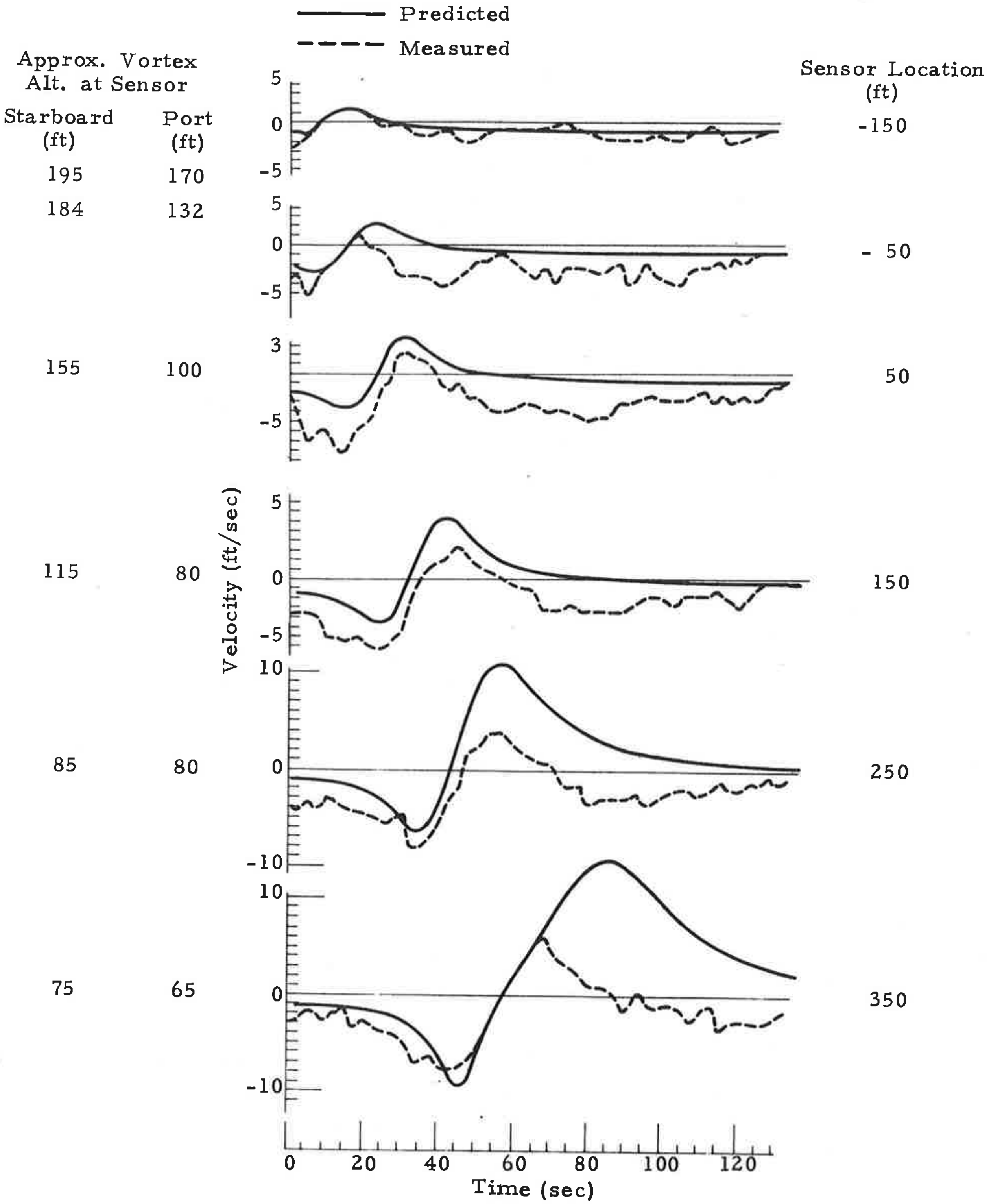

Fig.5-1 - Comparison of Predicted and Measured Ground Wind Vortex Tracks for Run 1 on 18 October 1972

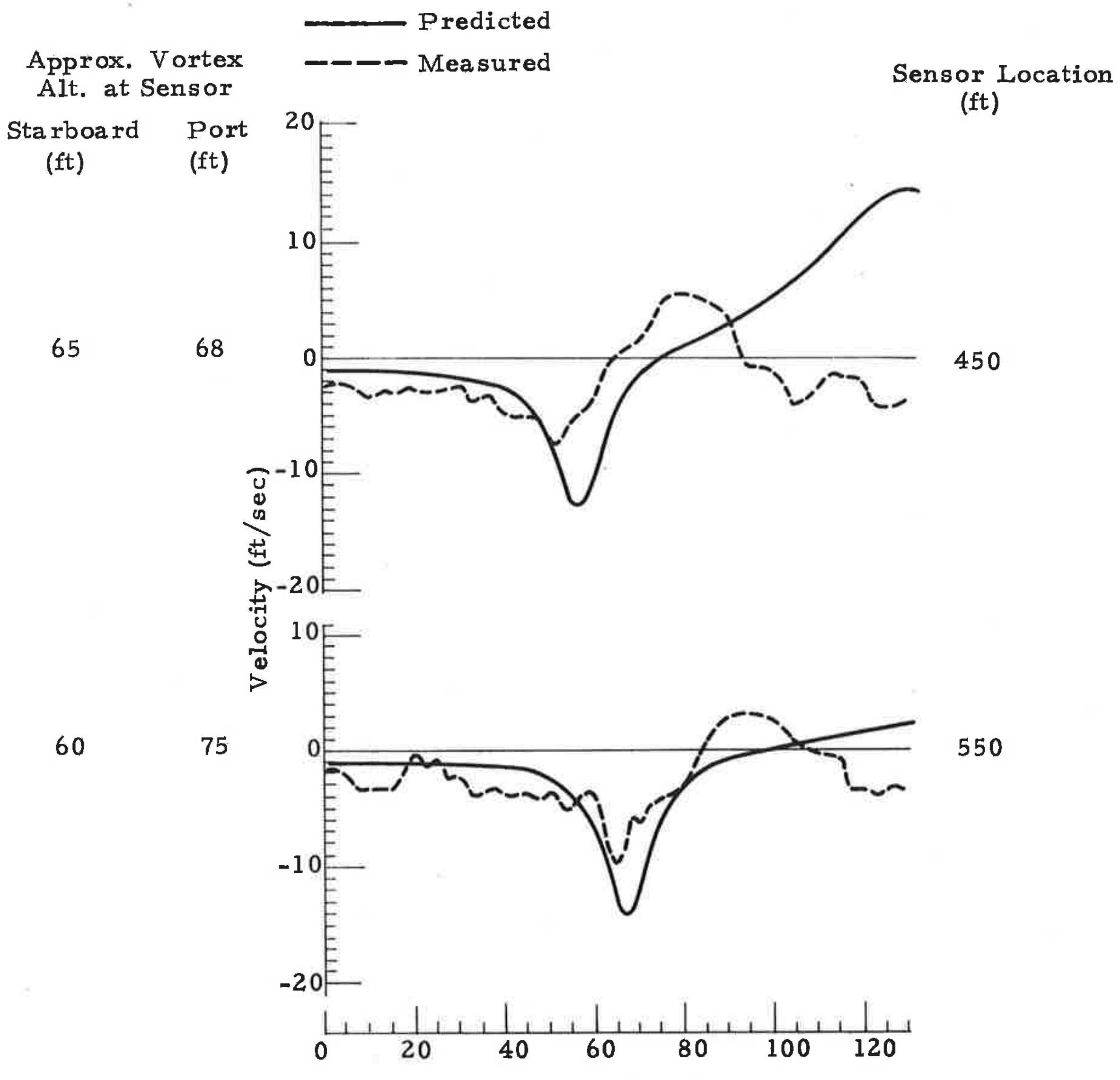

Fig. 5-1 - (Concluded)

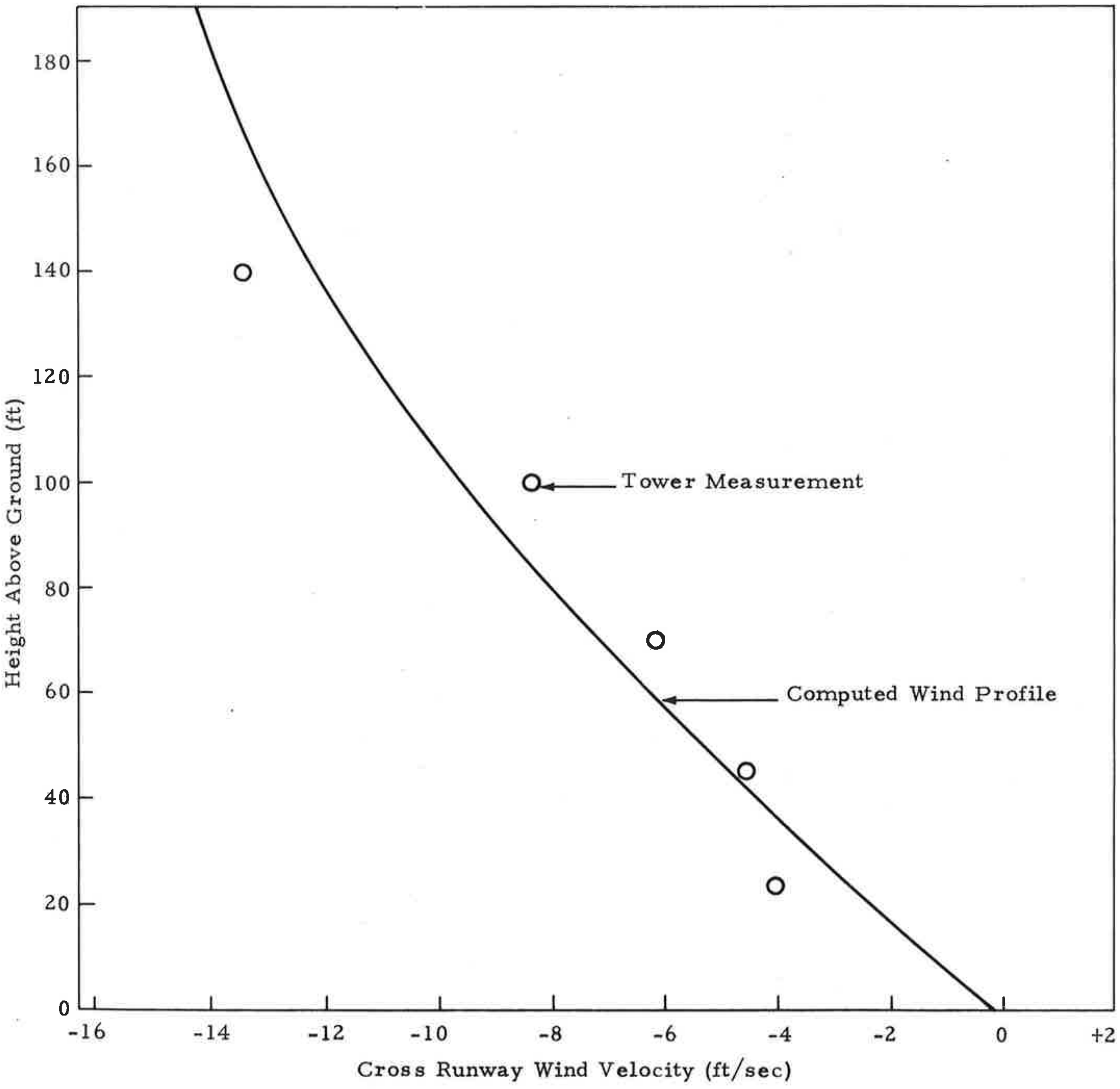

Fig. 5-2 - Measured and Computed Wind Profile for Run 1 on 18 October 1972

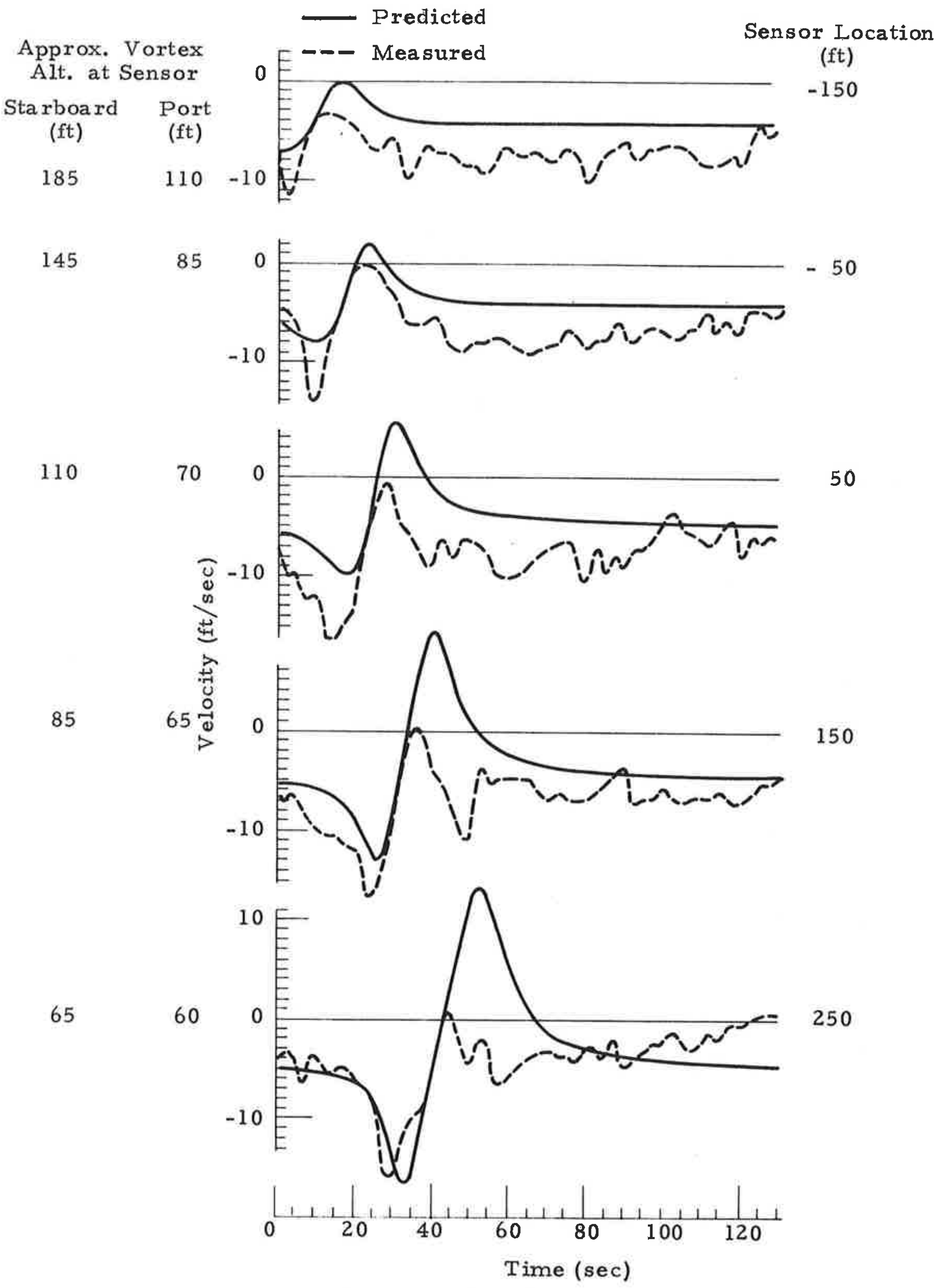

Fig. 5-3 - Comparison of Predicted and Measured Ground Wind Vortex Tracks for Run 17 on 18 October 1972

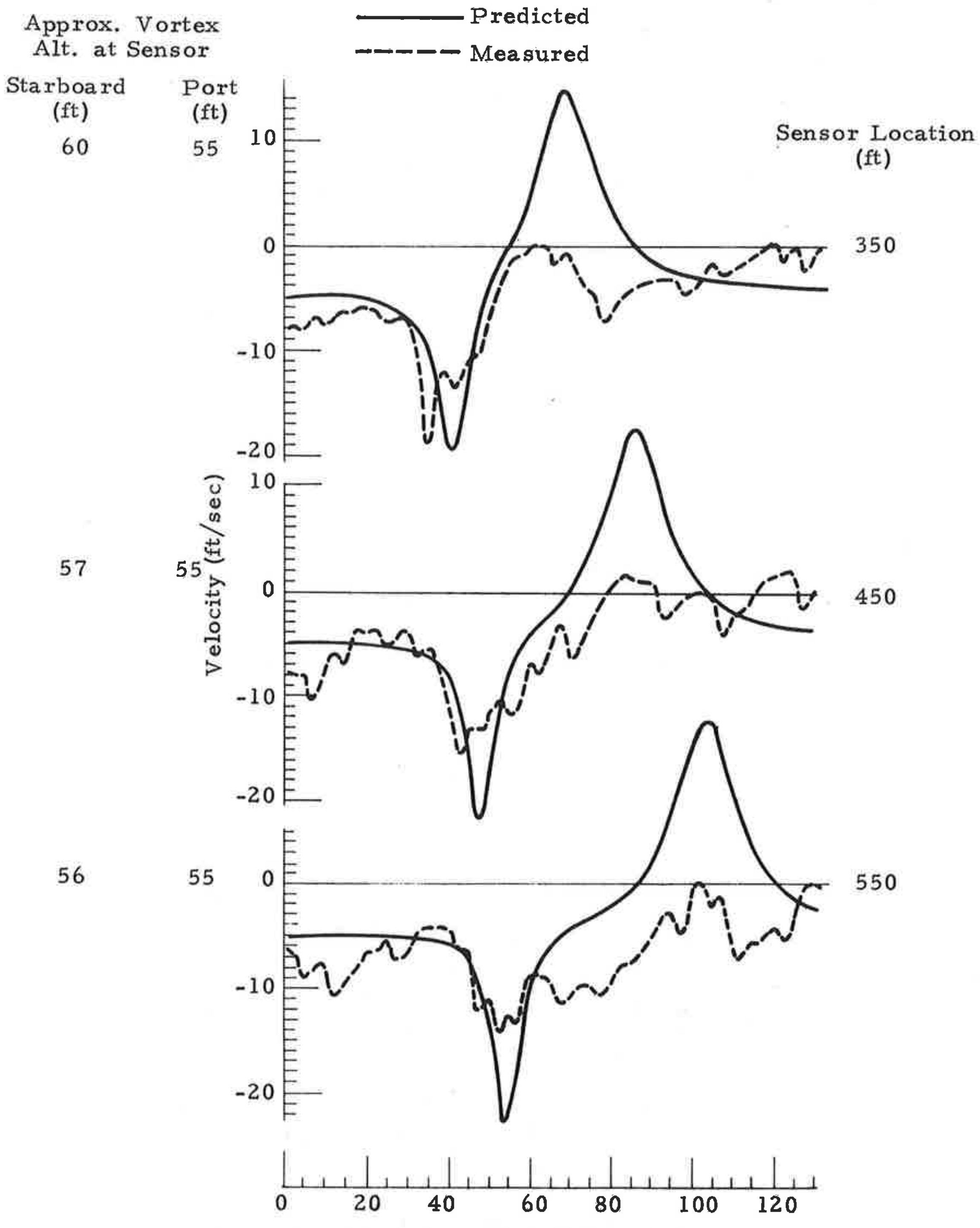

Fig. 5-3 - (Concluded)

or to the upwind vortex rising. The altitudes listed in the figure are known only for the first 30 seconds as smoke detrainment caused the photographic data to be meaningless after 30 seconds.

5.2 COMPARISON OF PREDICTED AND MEASURED VORTEX TRACKS

As a preliminary to a detailed examination of predicted and measured vortex tracks, the vortex tracks corresponding to the run discussed in the previous subsection will be analyzed. The cross sectional vortex track for run 17 on 18 October 1972 is shown in Fig. 5-4 (see also Fig. 5-3). Three predictive curves are shown, two represent the linear interpolation/extrapolation technique for the five measured wind speeds and the other the power law profile technique. The before and after cases correspond to using the mean wind field for the two minutes prior and post to aircraft passage, respectively. The effect appears to not be significant in this cross section vortex track; however, this is misleading. Photographic data exist only for the first 30 seconds due to smoke detrainment (diffusion). Thus, any discrepancy in the predictive tracks due to wind profile consideration might not show up in this plot as the largest uncertainty in the wind profile occurs in the lower altitudes (highest shear). A more meaningful comparison can be made from the ground wind track as shown in Fig. 5-5. The important point for this case is that the power law wind profile accounts for the difference of the 50 to 100 feet discrepancy observed between the linear interpolation wind profile predictive track and the measured vortex position. Figure 5-6 depicts the same series of curves for run 1 on 18 October (see Fig. 5-1 for vortex signature). The same general comments apply to this case; however, note that the improvement due to considering the power law is readily seen in the cross sectional plot. Again the greater improvement is noticed at the lower altitudes due to a more accurate wind shear representation. Also some improvement is due to a reduced error accumulation effect. The corresponding ground wind track is shown in Fig. 5-7. The improvement is again evident in both the port and starboard tracks. The improvement is not quite as good as the previous case as there is a remaining 20 to 30% difference after 90 seconds between the predicted and measured tracks. It has been found that this type error (upwind predictive vortex lag) is a consistent trend and is probably due to the upwind vortex rising or a decrease in tangential velocity at a greater rate than predicted.

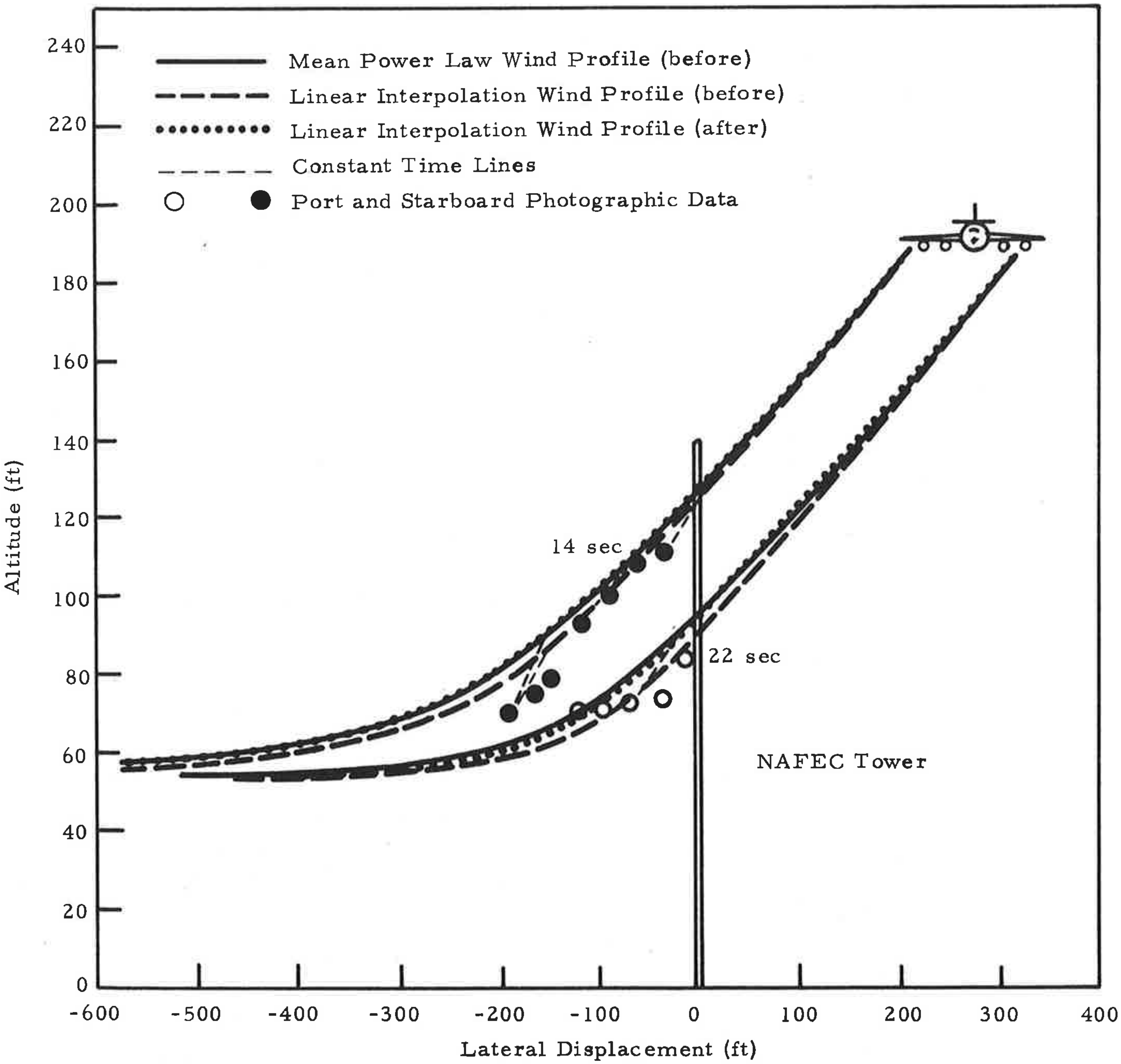

Fig. 5-4 - Comparison of Predictive Vortex Tracks with Photographic Data for Run 17 on 18 October 1972

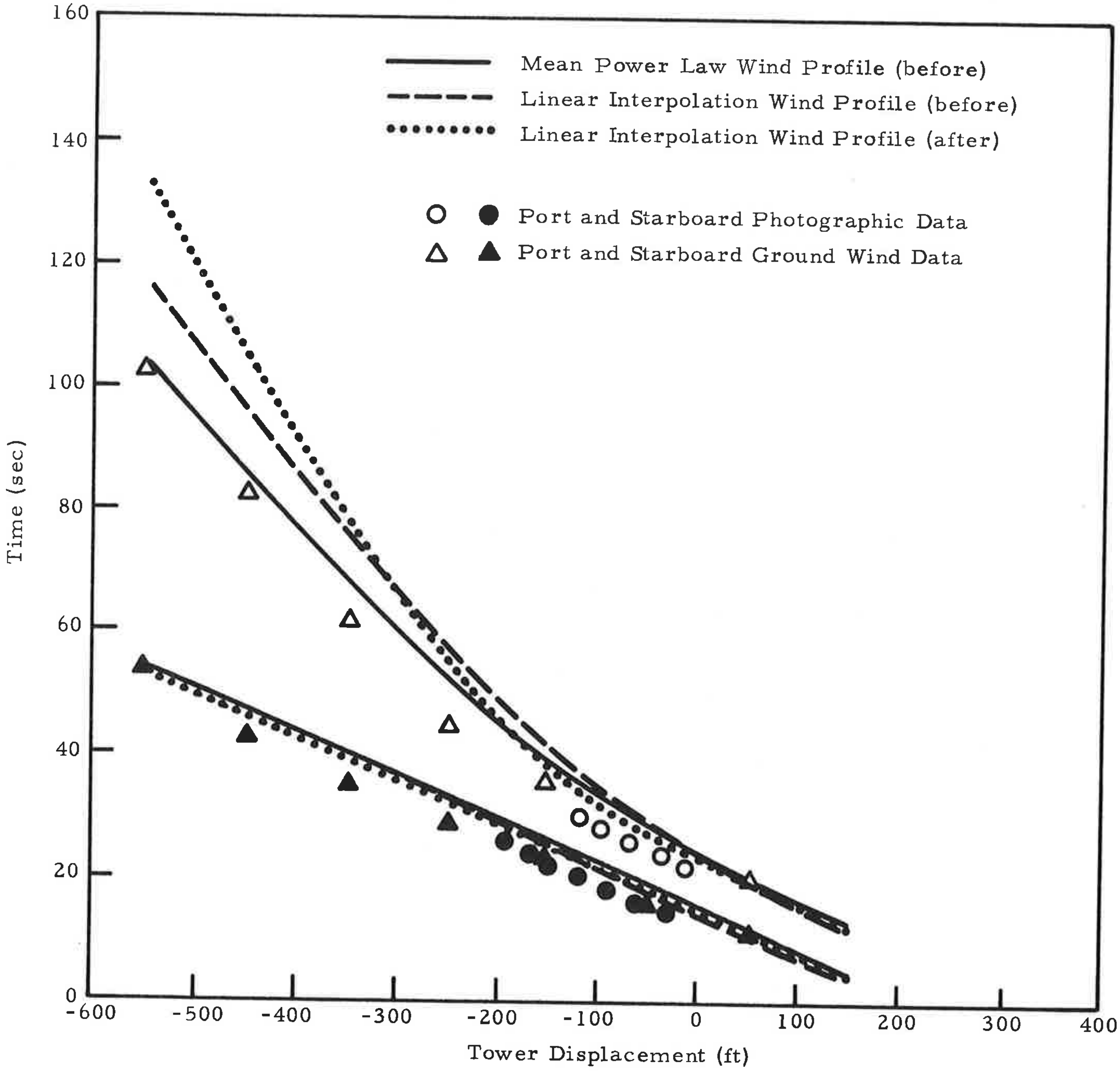

Fig. 5-5 - Comparison of Predicted Vortex Track with Measured Ground Wind Data for Run 17 on 18 October 1972

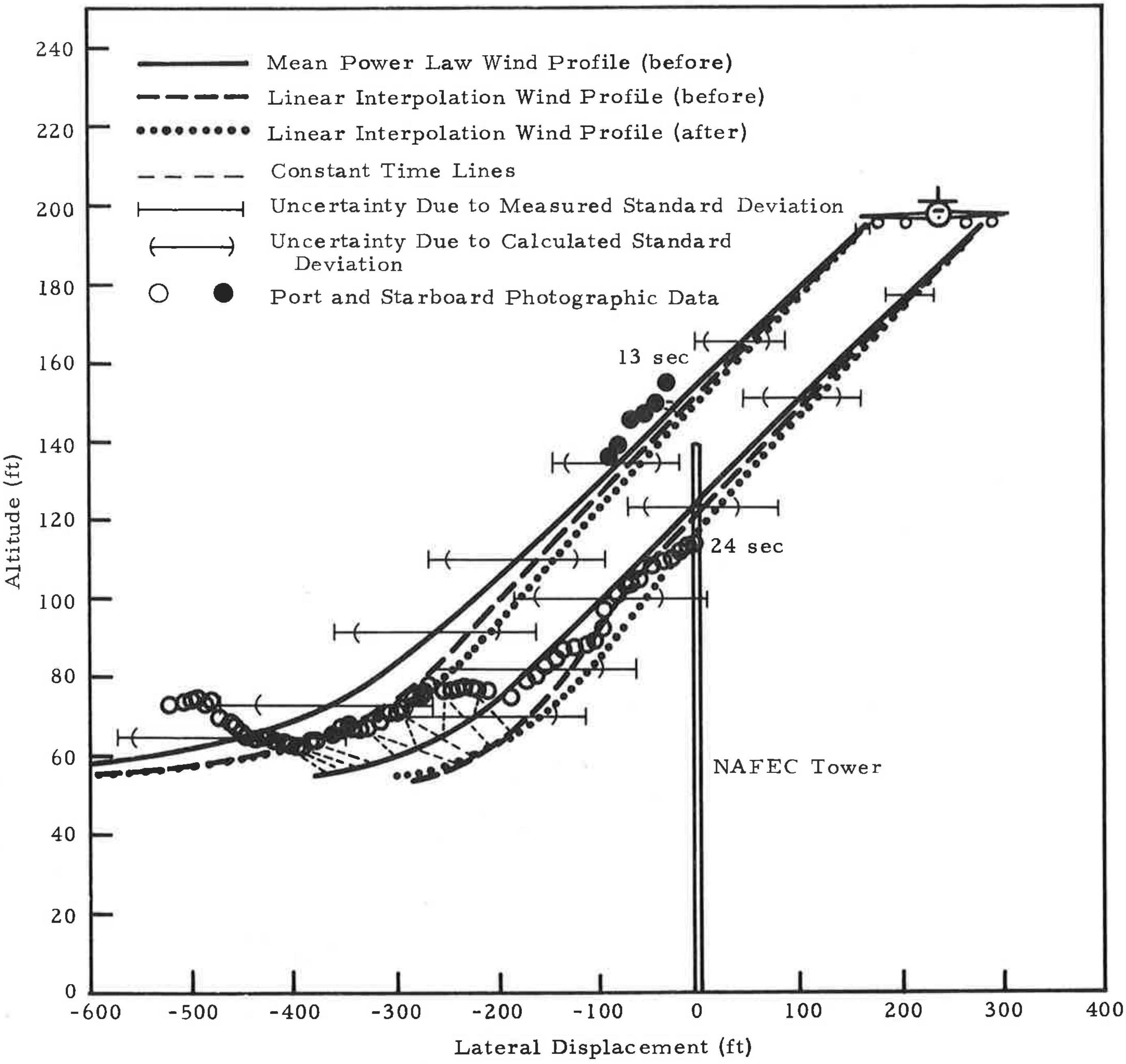

Fig. 5-6 - Comparison of Predicted Vortex Tracks with Photographic Data for Run 1 on 18 October 1972

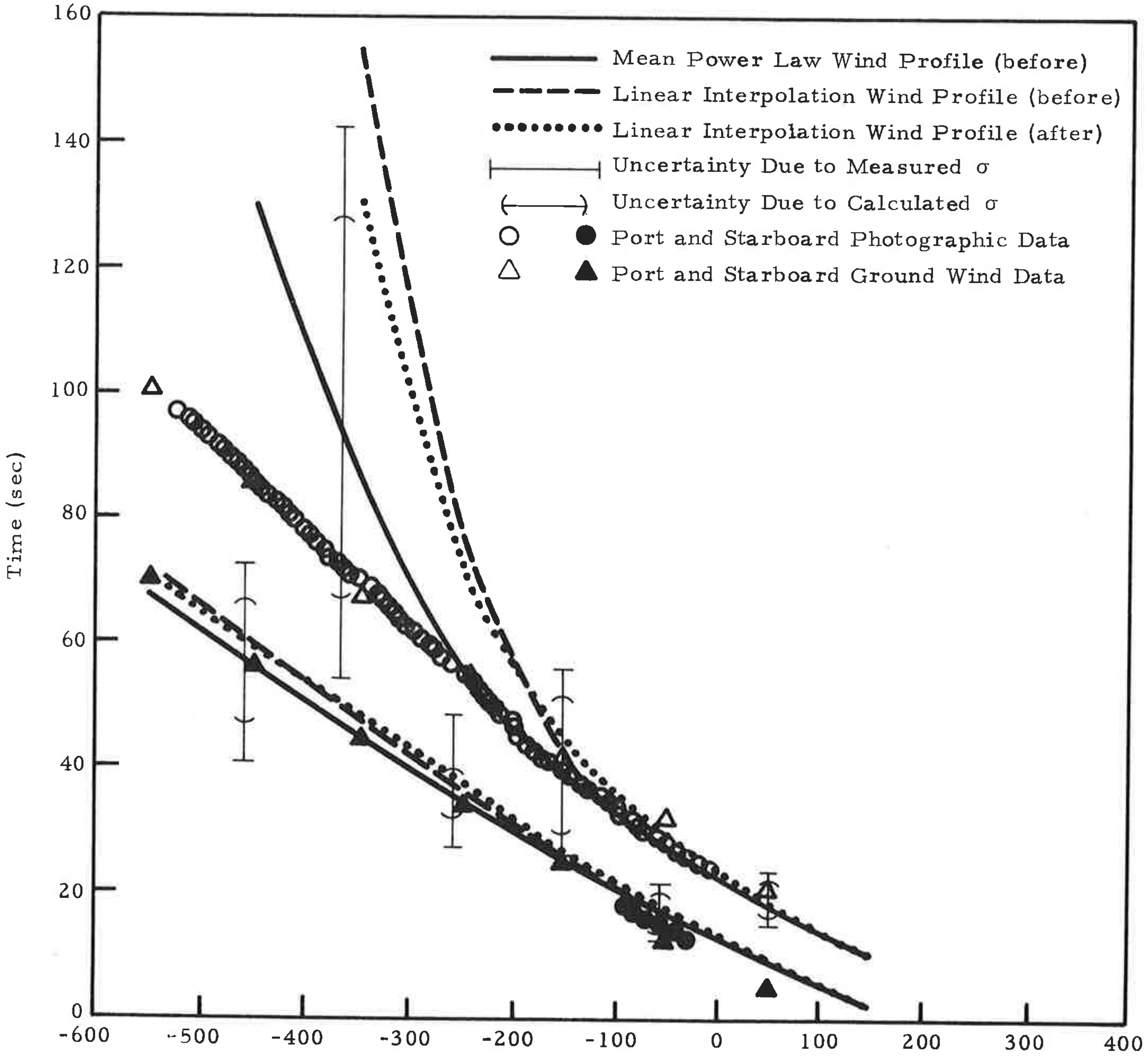

Fig. 5-7 - Comparison of Predicted Vortex Tracks with Measured Ground Wind Data for Run 1 on 18 October 1972

The bars on the predictive tracks in both the cross sectional and ground wind plots are uncertainties computed from the measured standard deviations in the wind field and from the computed uncertainty in the transport due to random fluctuations in the wind field (see Section 3). Note that the differences between the predicted and measured vortex tracks fall well within these error bars. This in effect says that with reasonable mean statistics for the wind field, conservative predictive tracks can easily be generated that define a region in which each vortex will lie within a high degree of confidence. However, it remains to establish if this relatively large uncertainty is meaningful for application to a wake vortex predictive system. The aforementioned conclusion is consistent with analysis of 75 predictive tracks consisting of mean and plus and minus one standard deviation profiles.

The effect of short time variations in the mean wind statistics on the vortex transport was investigated for several runs on 18 October 1972 and 1 November 1972 by using the previously mentioned before and after measured wind field as input to the transport model. The results of these comparisons are shown in Fig. 5-8 for the photographic data. These data represent the predicted tower hit time versus that measured by the photographic technique with the solid line representing a one to one correspondence between predicted and measured tower hit times. It appears to be a consistent trend for the predicted time to be somewhat less than that observed, especially when older vortices hit the tower. Before attempting to analyze any possible trend, it should be shown that the short time temporal aspects of the wind field do not appreciably affect this trend. Figure 5-9 shows the difference between the predicted tower hit times based on before and after winds versus the observed photographic time. The length of the vertical line represents the uncertainty of using mean statistics not corresponding to the precise time of interest. The before and after times correspond to the two minutes prior to the aircraft passage for two consecutive flybys. The time between measurements is on the average 5 minutes (time for aircraft turn around). It is seen from Fig. 5-9 that the aforementioned trend is still evident in that the mean predicted tower hit time is consistently less than observed from photographic data. This is consistent with the

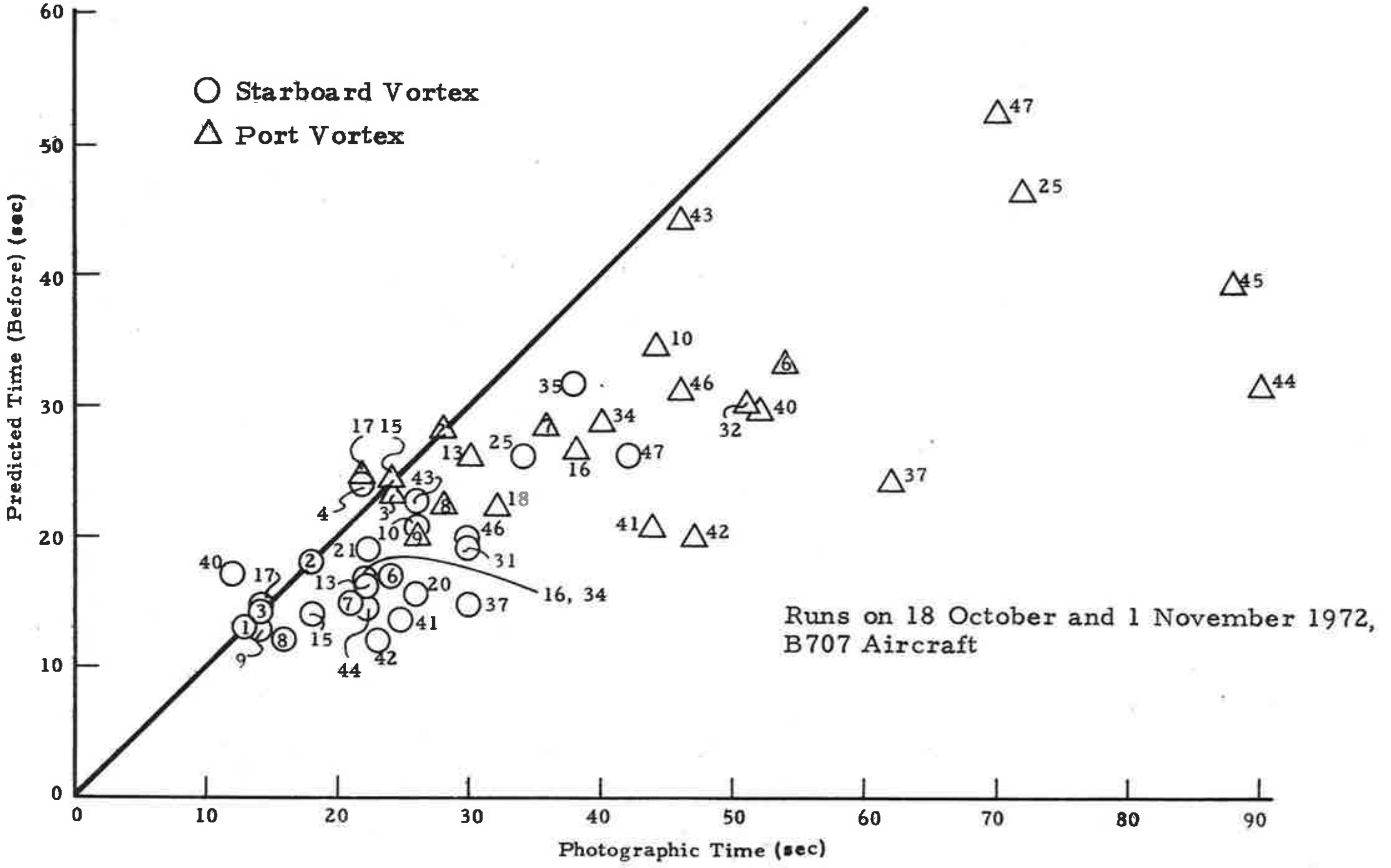

Runs on 18 October and 1 November 1972, B707 Aircraft

Fig. 5-8 - Comparison of the Predicted Times Versus the Photographically Measured Times for Each Vortex to Hit the NAFEC Tower (based on recorded wind before flyby)

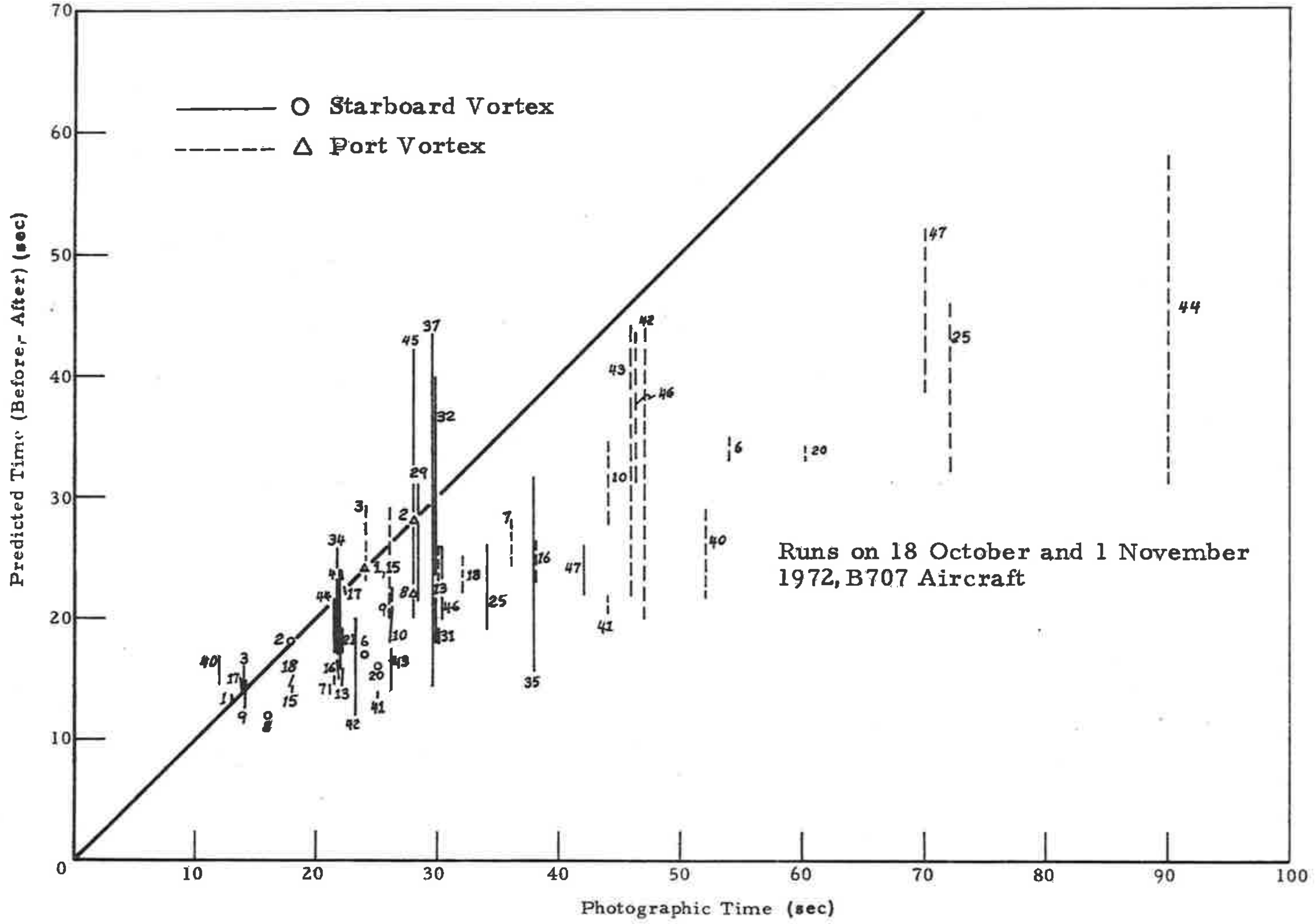

Fig. 5-9 - Comparison of Predicted Tower Hit Time Differences for Before and After Winds Versus the Photographically Measured Times observation that the predicted sink rates based on elliptical loading assumptions are somewhat less than that measured. There are certainly two separate mechanisms for causing this phenomena. First, deviation from a clean wing configuration appears to cause a decrease in rolled up vortex separation distance (Ref. 10). Also, buoyancy effects probably cause a decrease in vortex separation (Ref. 5). This has not been shown for a vortex pair in ground effect; however, studies to date indicate that this is probably true. The difference between the predicted and measured sink rates also depends on aircraft type as will be shown in this section.

There are several effects that must be discussed before attempting to ascertain any general trends. First, consider the case of run 25 which exhibits one of the greatest differences between prediction and measurement. The detailed predictive information is shown in Figs. 5-10 through 5-12. Note the very consistent trend of the predicted vortex location being further downwind than the experimentally determined location for both the photographic and ground wind data. Even though the difference between prediction and measurement is never more than 100 feet, the port vortex tower hit time, when taken alone, indicates significant differences between prediction and experiment. Thus the plots of tower hit times do not tell the entire story as evidenced by this example. This same discussion applies to Run 45 as seen in Figs. 5-13 through 5-15 as the wind again appears to produce consistent predictive tracks that are downwind of the measured locations. Note also that both vortices are rising which is certainly contrary to observation of many runs. In this case the vortex velocity measurements were made during the tests. The important observation is that in both of these cases the vortex position uncertainty is always less than 120 feet but still show up on the tower hit time plots as the runs with the largest errors. Secondly, the predicted sink rate is consistently less than the observed which gives rise to a vortex location in a greater wind and is thus transported downwind faster. This produces early prediction tower hit times. Thirdly, all of these comparisons are based on predictive information calculated from wind profile data in accordance with the previously discussed linear interpolation/extrapolation technique. This certainly causes predicted tower hit times on the

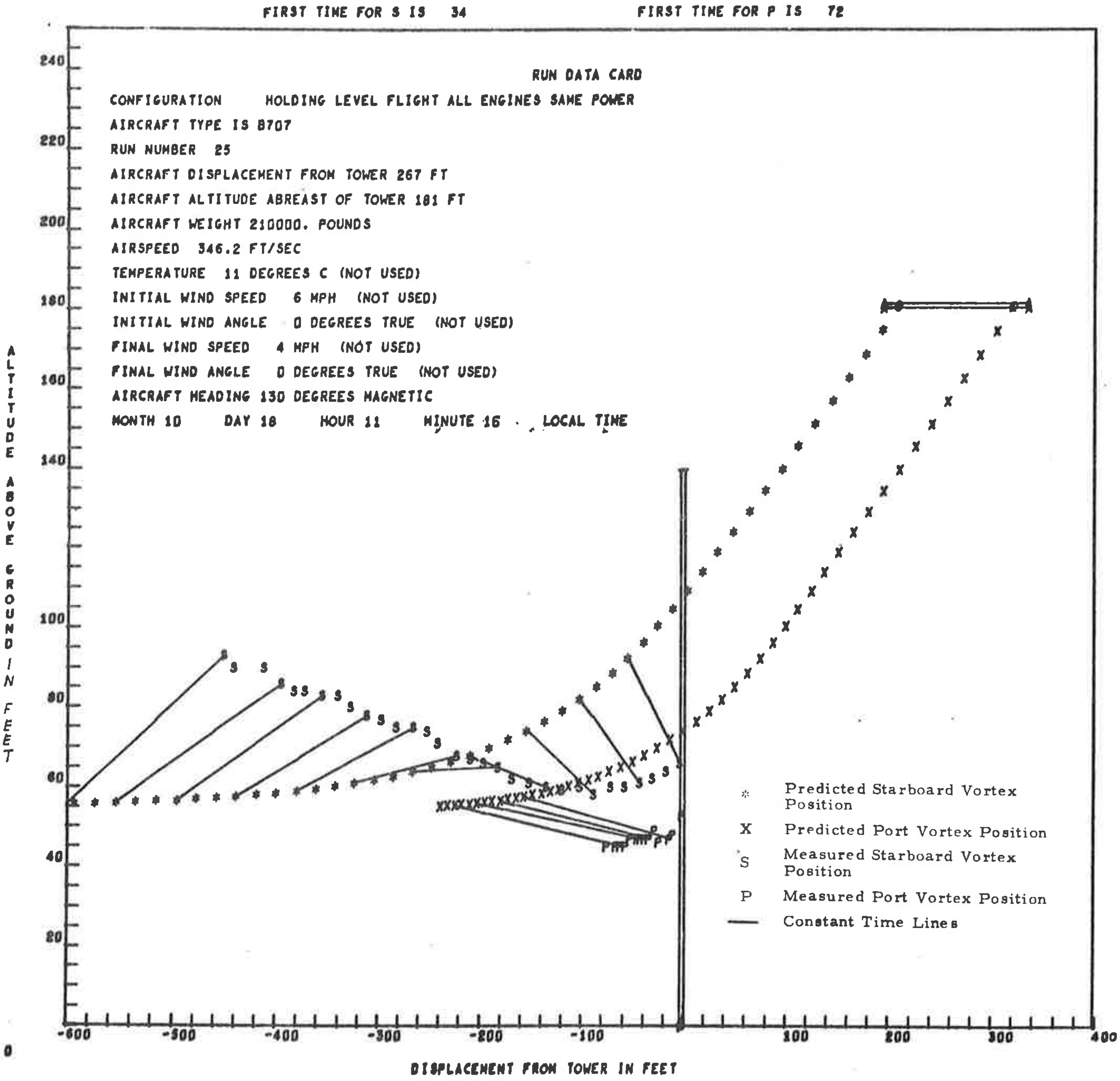

RUN DATA CARD

CONFIGURATION HOLDING LEVEL FLIGHT ALL ENGINES SAME POWER
AIRCRAFT TYPE IS B707
RUN NUMBER 25
AIRCRAFT DISPLACEMENT FROM TOWER 267 FT
AIRCRAFT ALTITUDE ABREAST OF TOWER 181 FT
AIRCRAFT WEIGHT 210000. POUNDS
AIRSPEED 346.2 FT/SEC
TEMPERATURE 11 DEGREES C (NOT USED)
INITIAL WIND SPEED 6 MPH (NOT USED)
INITIAL WIND ANGLE 0 DEGREES TRUE (NOT USED)
FINAL WIND SPEED 4 MPH (NOT USED)
FINAL WIND ANGLE 0 DEGREES TRUE (NOT USED)
AIRCRAFT HEADING 130 DEGREES MAGNETIC
MONTH 10 DAY 18 HOUR 11 MINUTE 16 LOCAL TIME

Fig. 5-10 - Predicted Vortex Track vs Measured Photographic Data for Run 25 on 18 October 1972

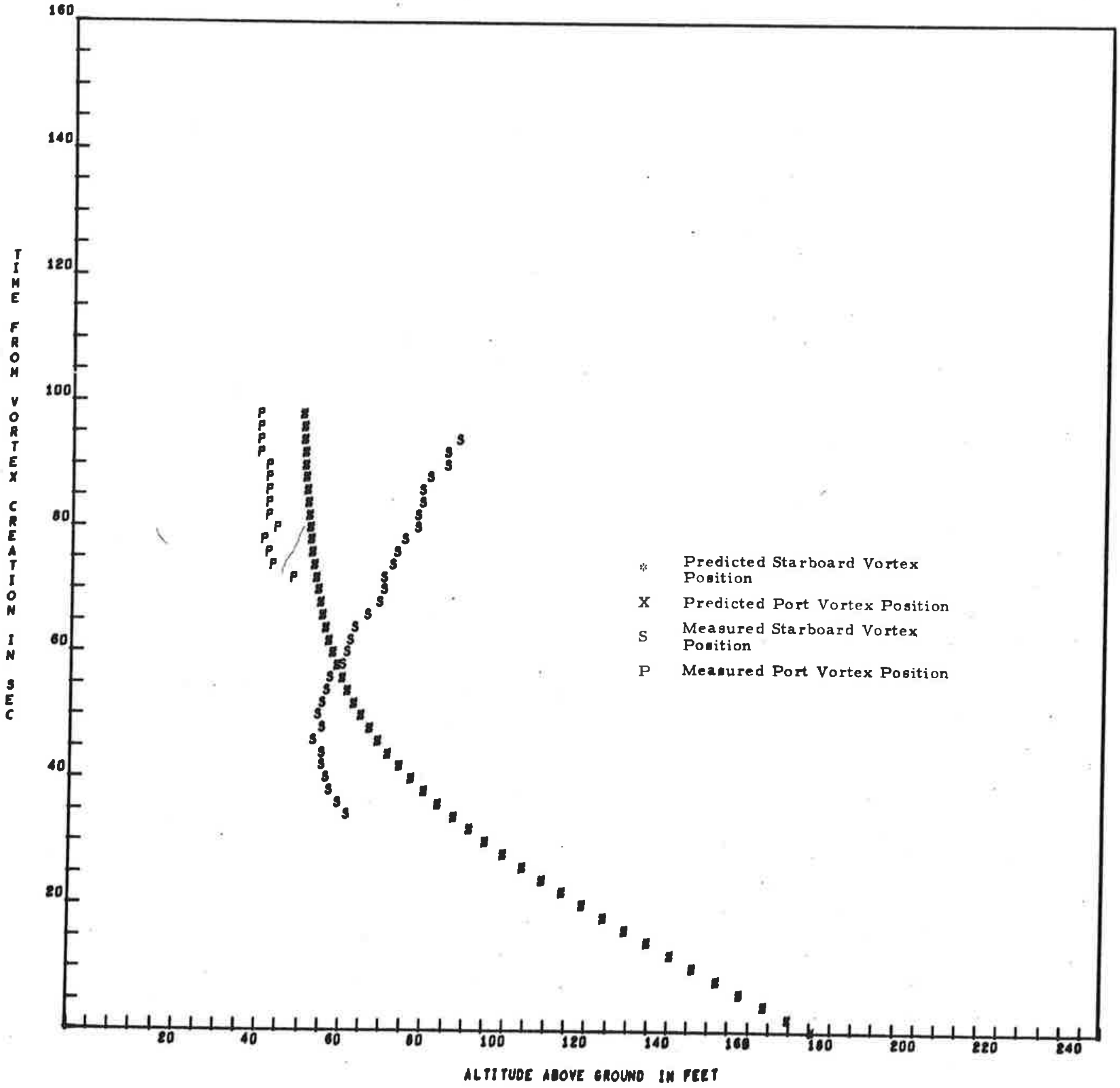

Fig. 5-11 - Comparison of Predicted and Measured Vortex Altitude vs Time for Run 25 on 18 October 1972

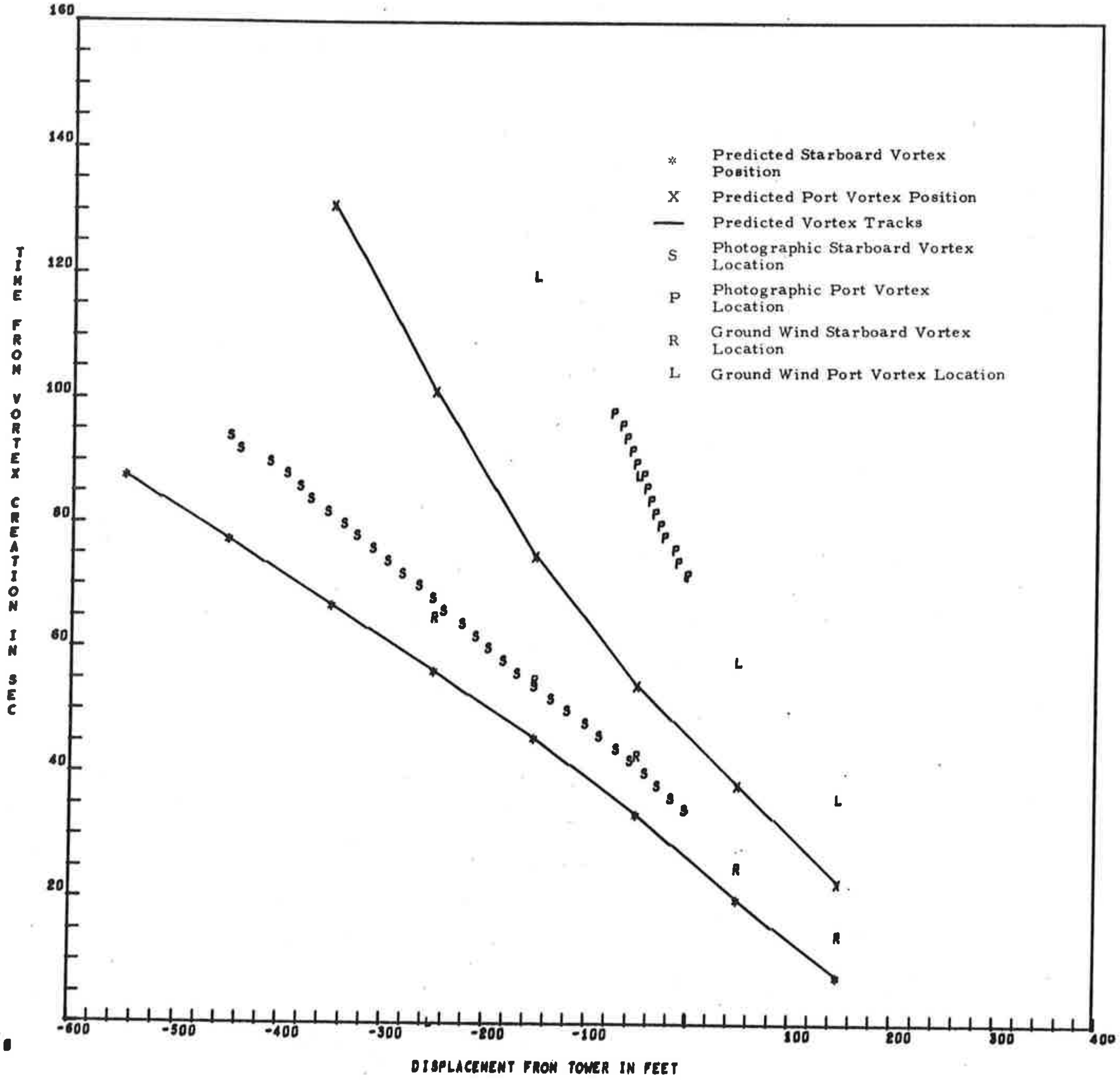

Fig. 5-12 - Comparison of Predicted and Measured Ground Wind Tracks for Run 25 on 18 October 1972

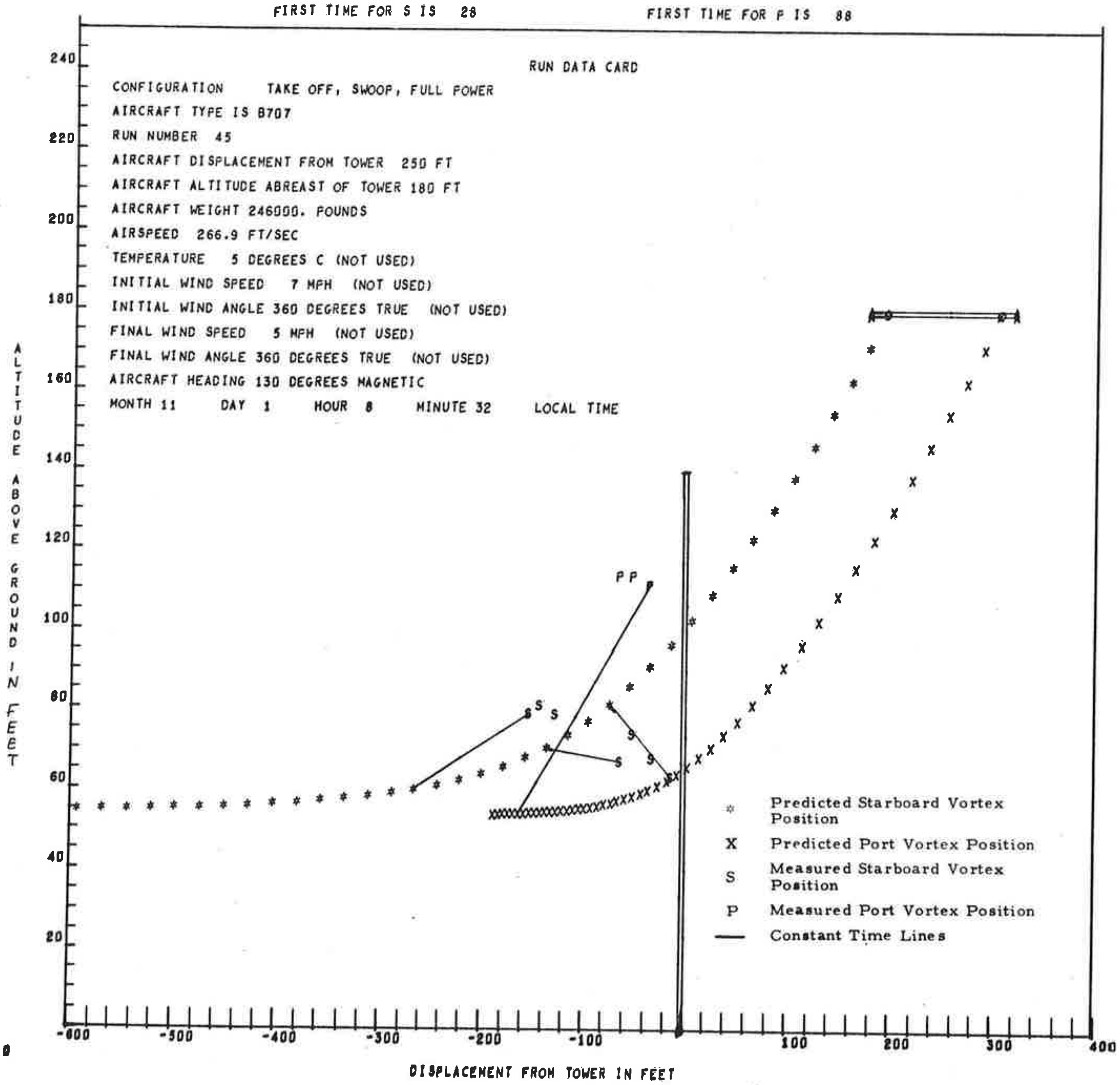

Fig. 5-13 - Predicted Vortex Track versus Measured Photographic Data for Run 45 on 1 November 1972

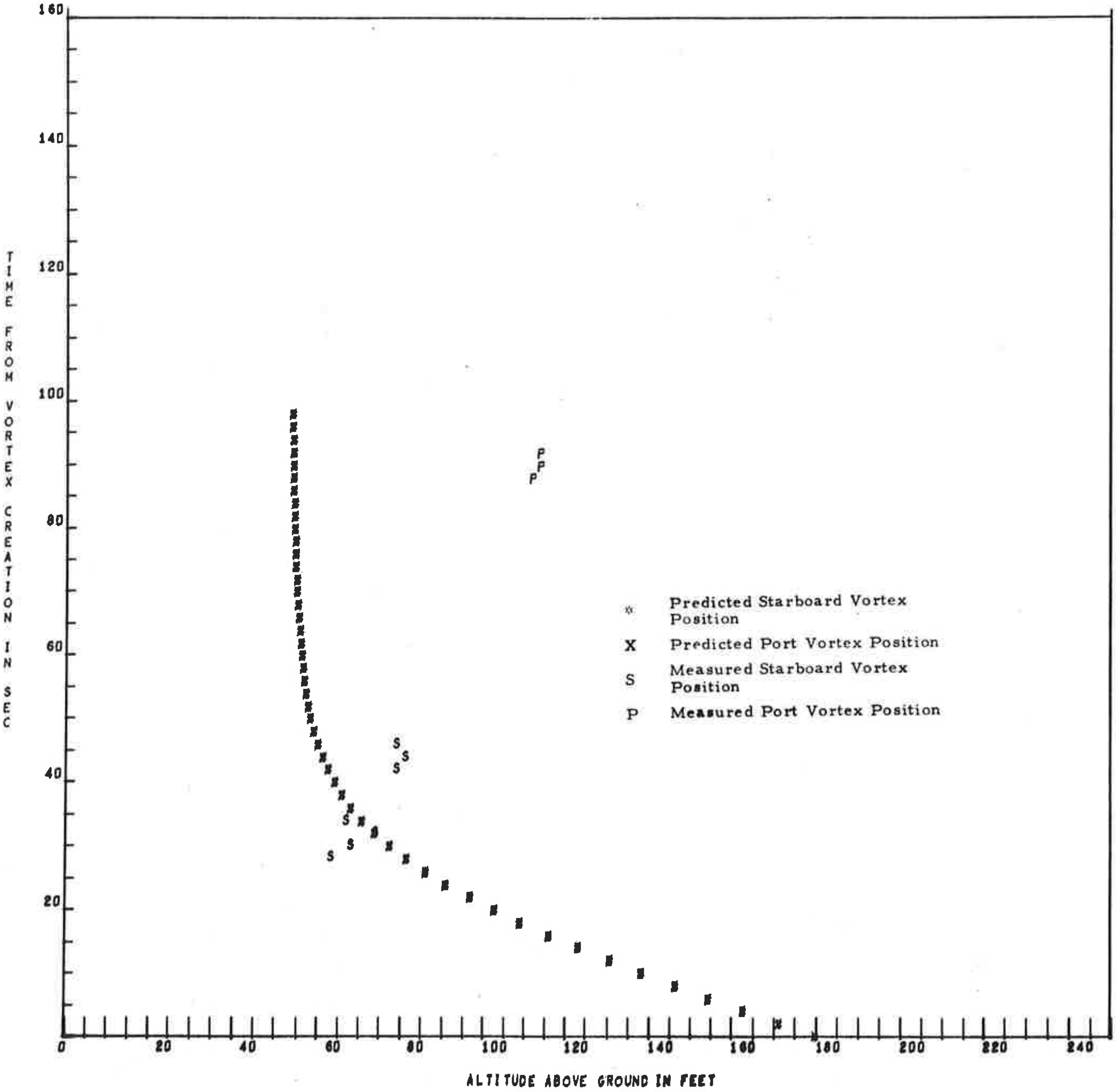

Fig. 5-14 - Comparison of Predicted and Measured Vortex Altitude versus Time for Run 45 on 1 November 1972

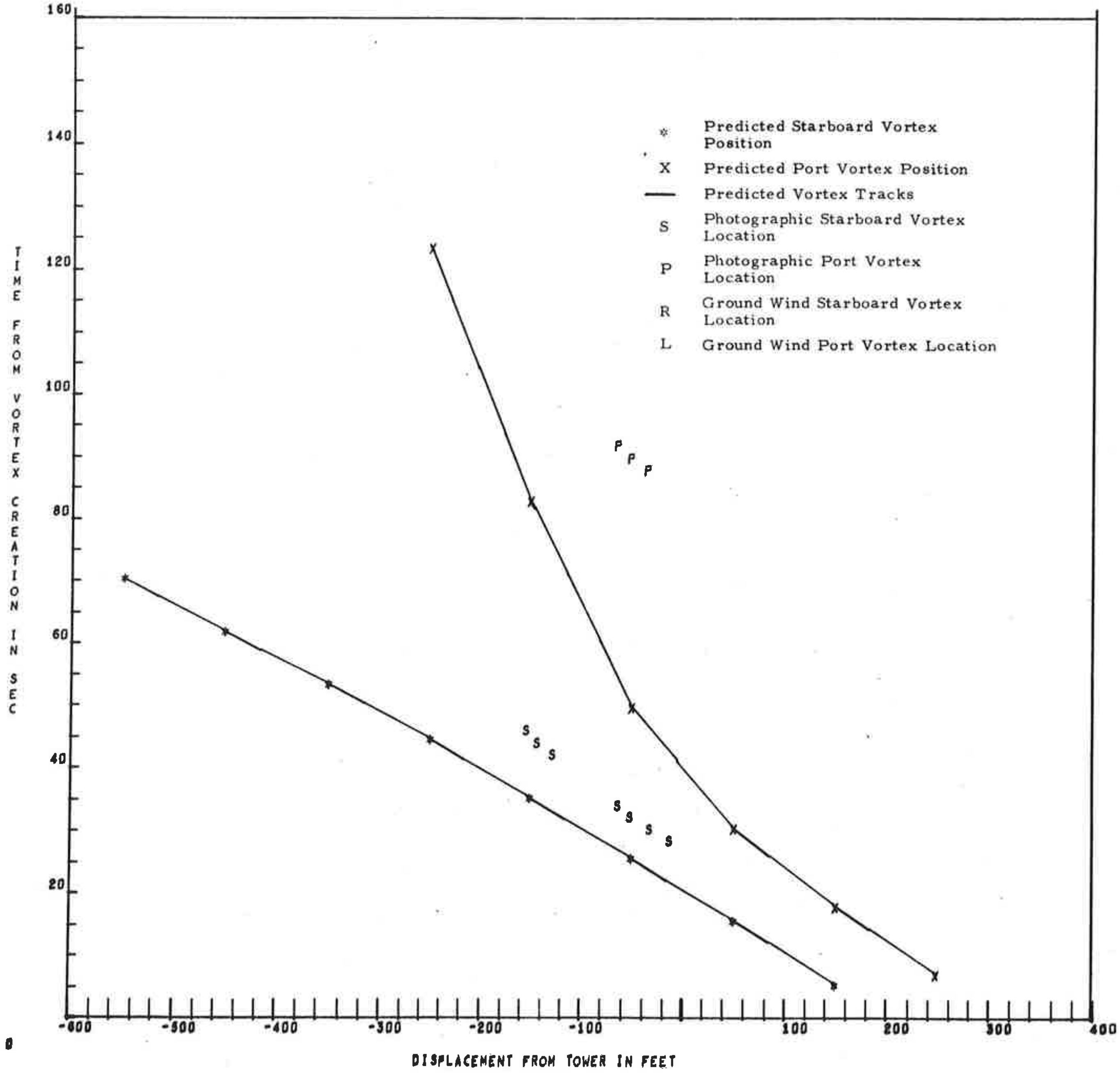

Fig. 5-15 - Comparison of Predicted and Measured Ground Wind Tracks for Run 45 on 1 November 1972 early side as the calculated higher altitude wind is larger than the actual value. Figure 5-16 shows the predicted tower hit times based on before and after winds versus the tower hit time determined from ground wind measurements. This comparison is essentially the same as the photographic data plots; this is further evidenced in Fig. 5-17 where a nearly one to one correspondence is seen to exist between photographic tower hit times and those determined from ground wind measurement.

The difference between the predicted altitude at tower hit point versus that determined from the photographs is seen in Fig. 5-18 for both the before and after wind profiles. The length of the line is the change in predicted altitude for the before and after winds. When comparing predicted altitudes versus time with that obtained from measurement, no effect will be found due to the horizontal wind. However, when one spatial point is isolated deviations will last as the vortex will be a different age when the tower is encountered. It is apparent that in general the predicted sink rate is somewhat less than the actual descent as the predicted altitude is greater at tower encounter. As previously discussed this is probably due to non-elliptical wing loading.

All of these comparisons were obtained with the linear interpolation/ extrapolation wind profile. This technique has been shown to produce detectable errors; thus these same runs were recalculated using the power law wind profile as previously discussed. These comparisons are shown in Fig. 5-19. There is significant improvement in most of the runs; however, there are a few runs where the same words of caution apply as previously discussed for Run 25. The corresponding comparison for the predicted altitude is shown in Fig. 5-20. The adjustment for wind direction utilizes the extrapolated wind direction to the aircraft altitude based on the top two levels of the tower. This improves the high level wind direction as extrapolation of the wind direction via the curve fit is unreliable (this was discussed in Section 4).

Additional comparisons for other aircraft are shown in Figs. 5-21 through 5-24. The DC-6 data for 19 August 1972 are shown in Figs. 5-21 and 5-22 for

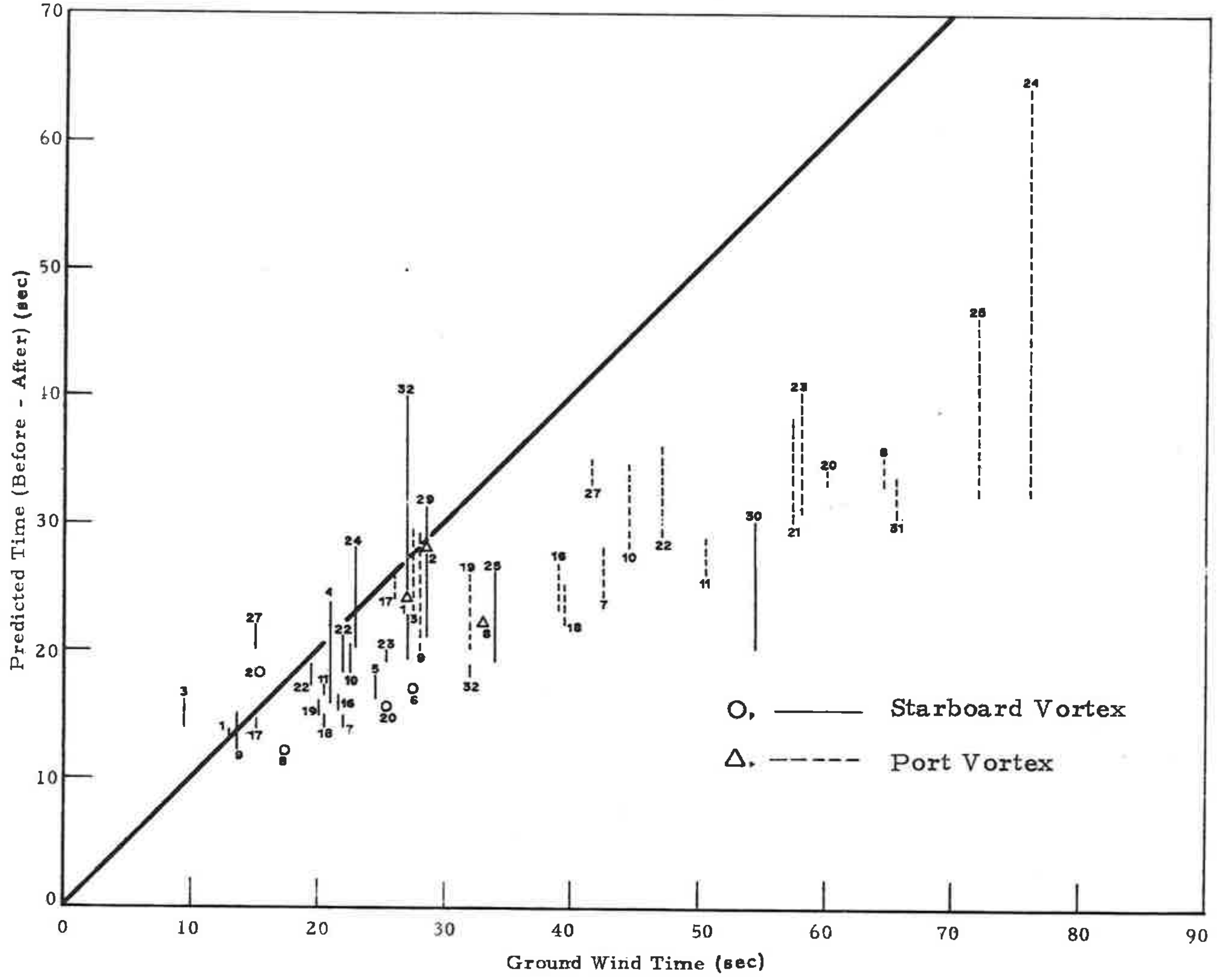

Fig. 5-16 - Comparison of Predicted Tower Hit Time Differences for Before and After Winds versus Measured Ground Wind Times

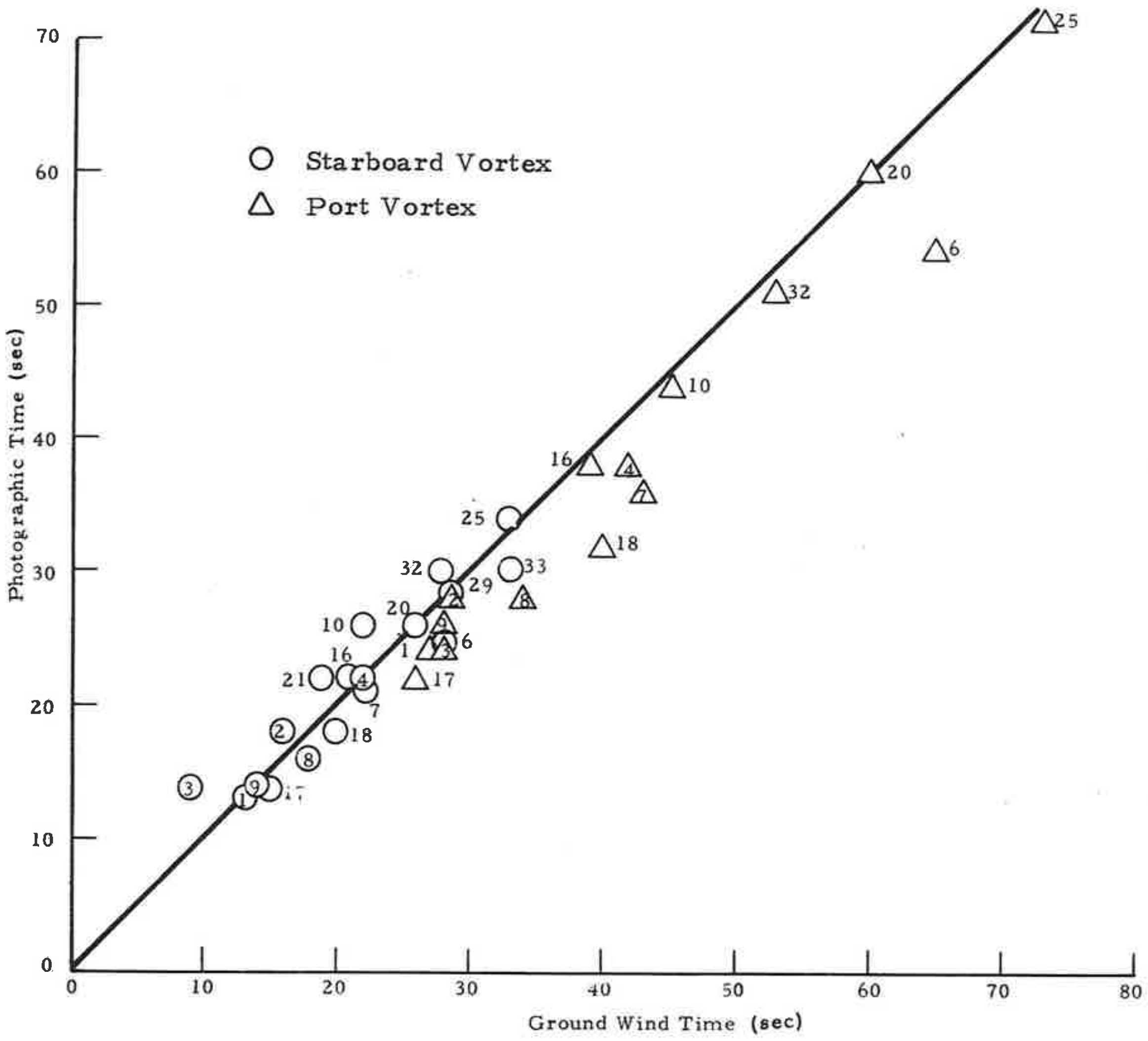

Fig. 5-17 - Comparison of Photographic Tower Hit Times versus Ground Wind Times

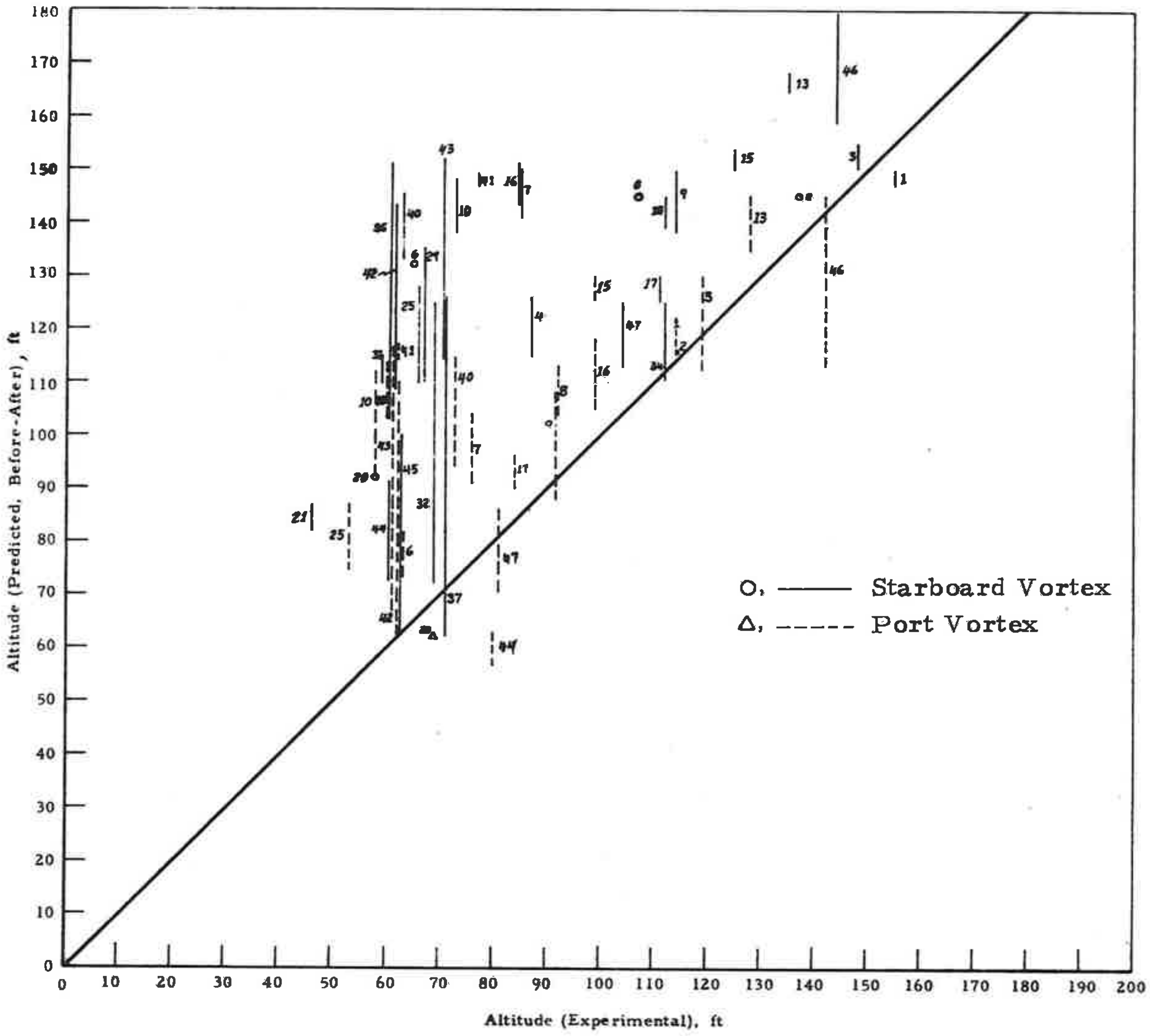

Fig. 5-18 - Comparison of Predicted Vortex Altitude Differences for Before and After Winds versus Measured Vortex Altitudes

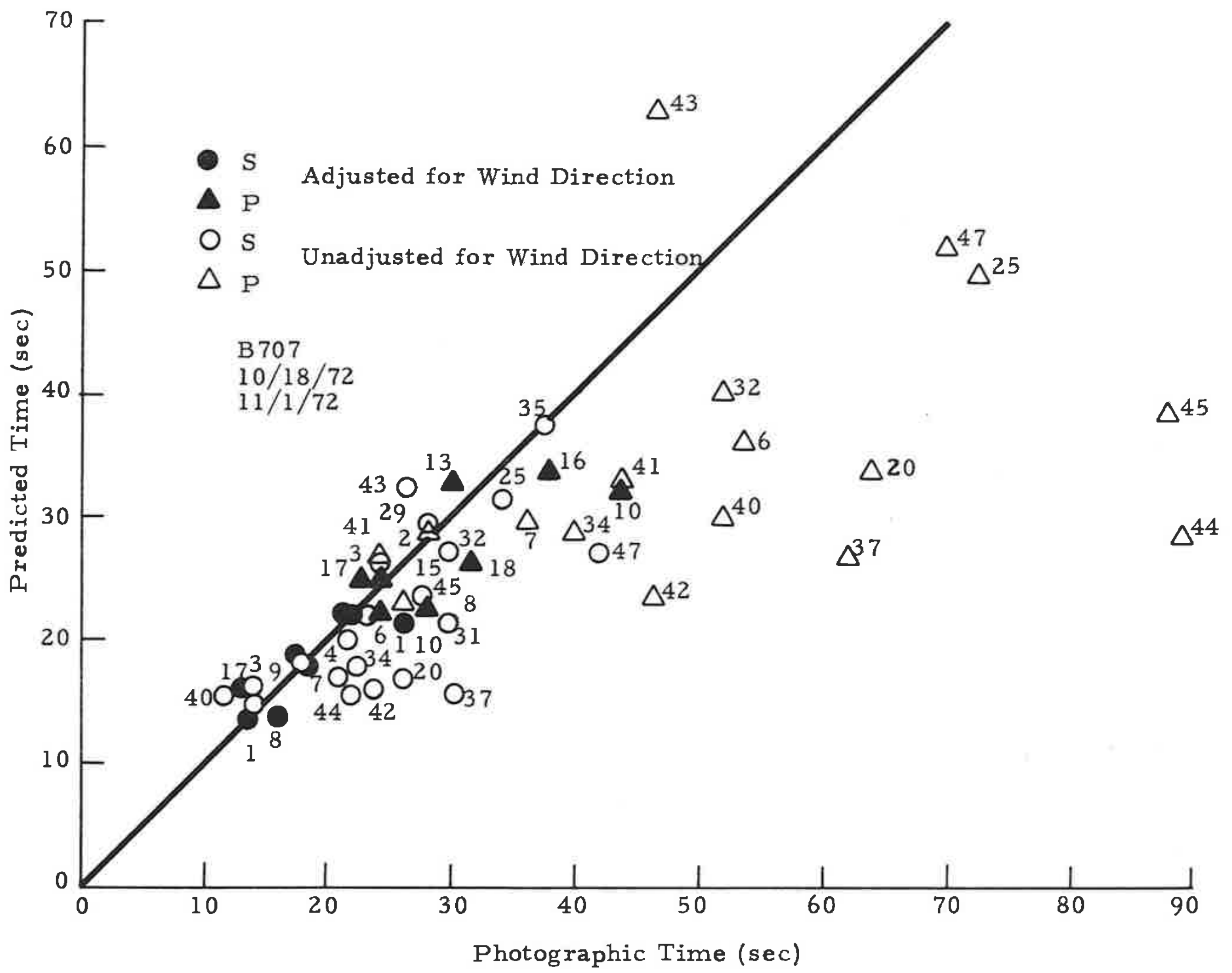

Fig. 5-19 - Comparison of Predicted Vortex Hit Times Based on Power Law Wind Profile Versus Photographic Times

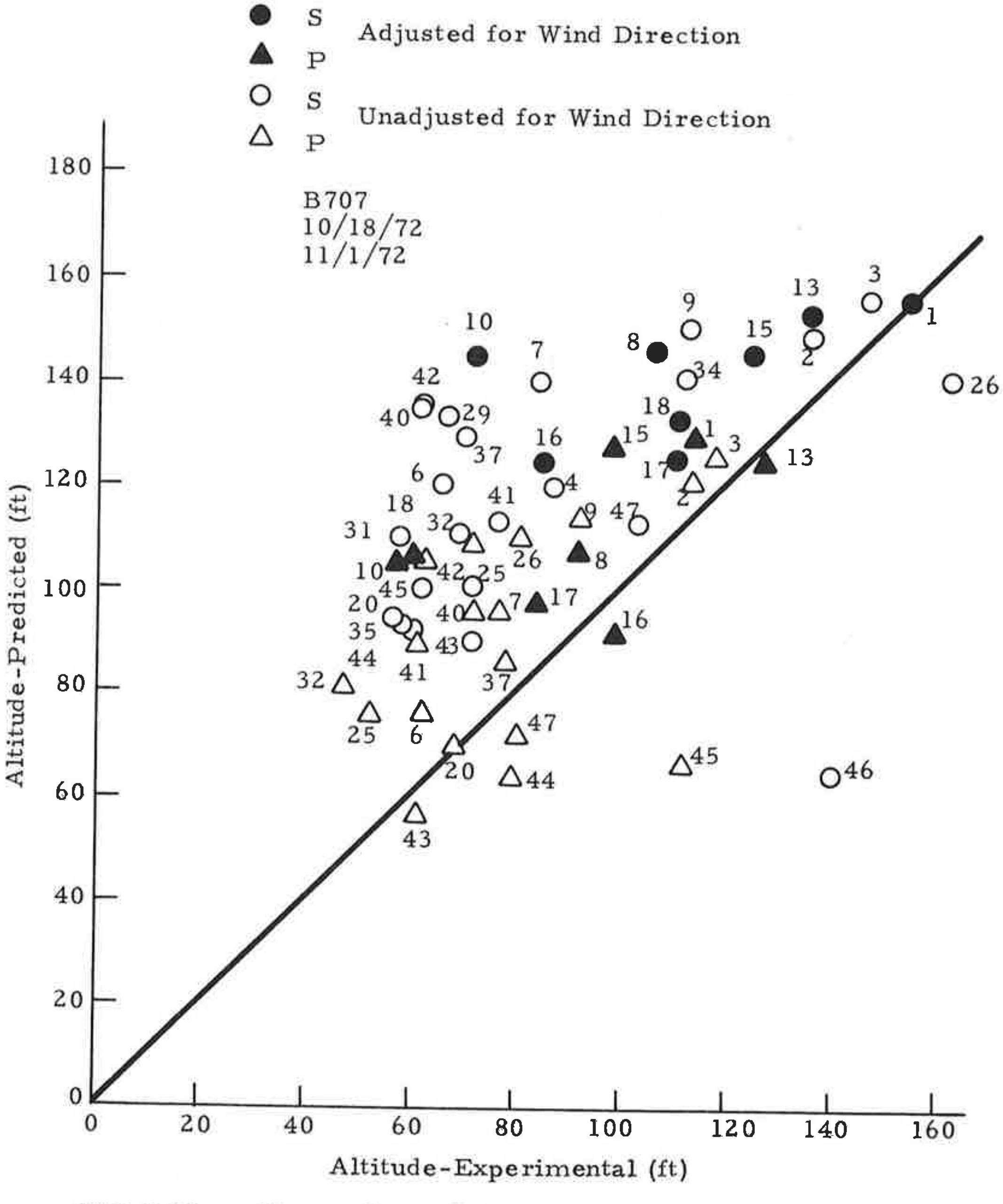

Fig. 5-20 - Comparison of Predicted Vortex Altitudes Based on Power Law Wind Profile Versus Photographic Altitudes

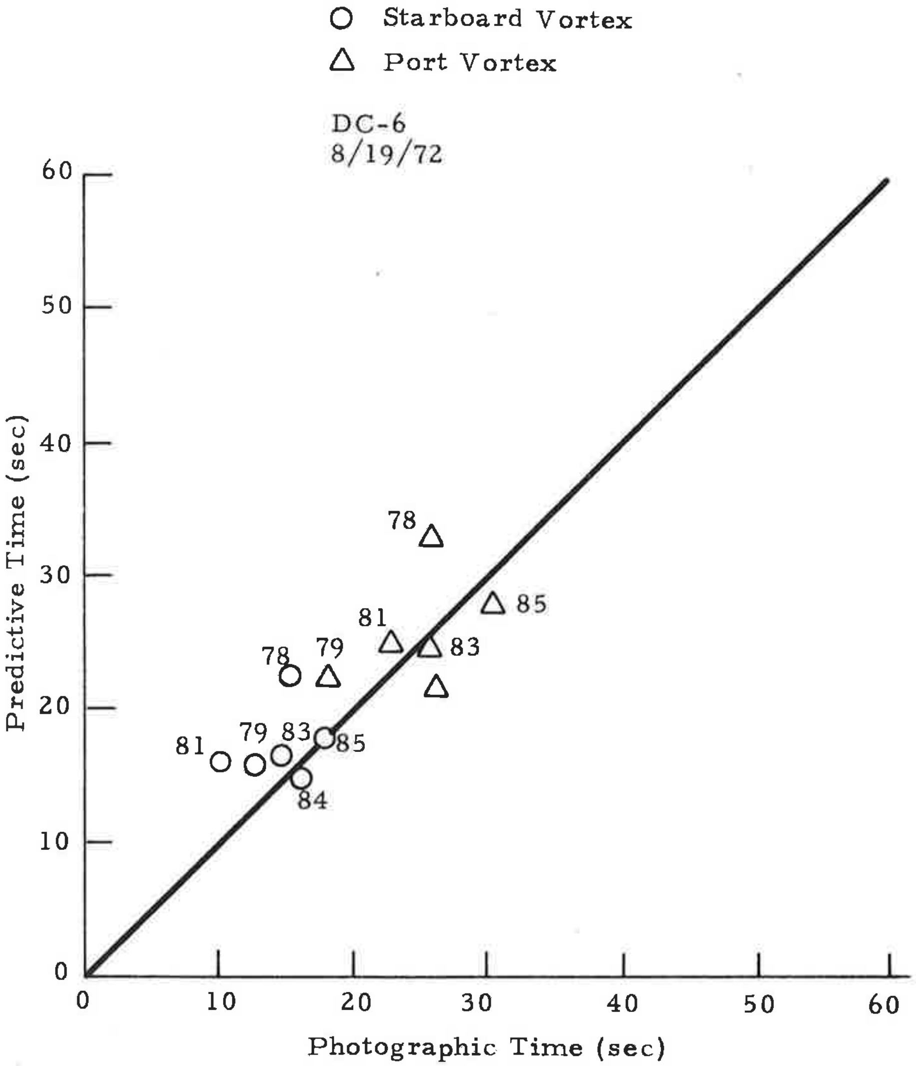

Fig. 5-21 - Comparison of Predicted Tower Hit Times Versus Photographic Time for DC-6 Aircraft Flybys

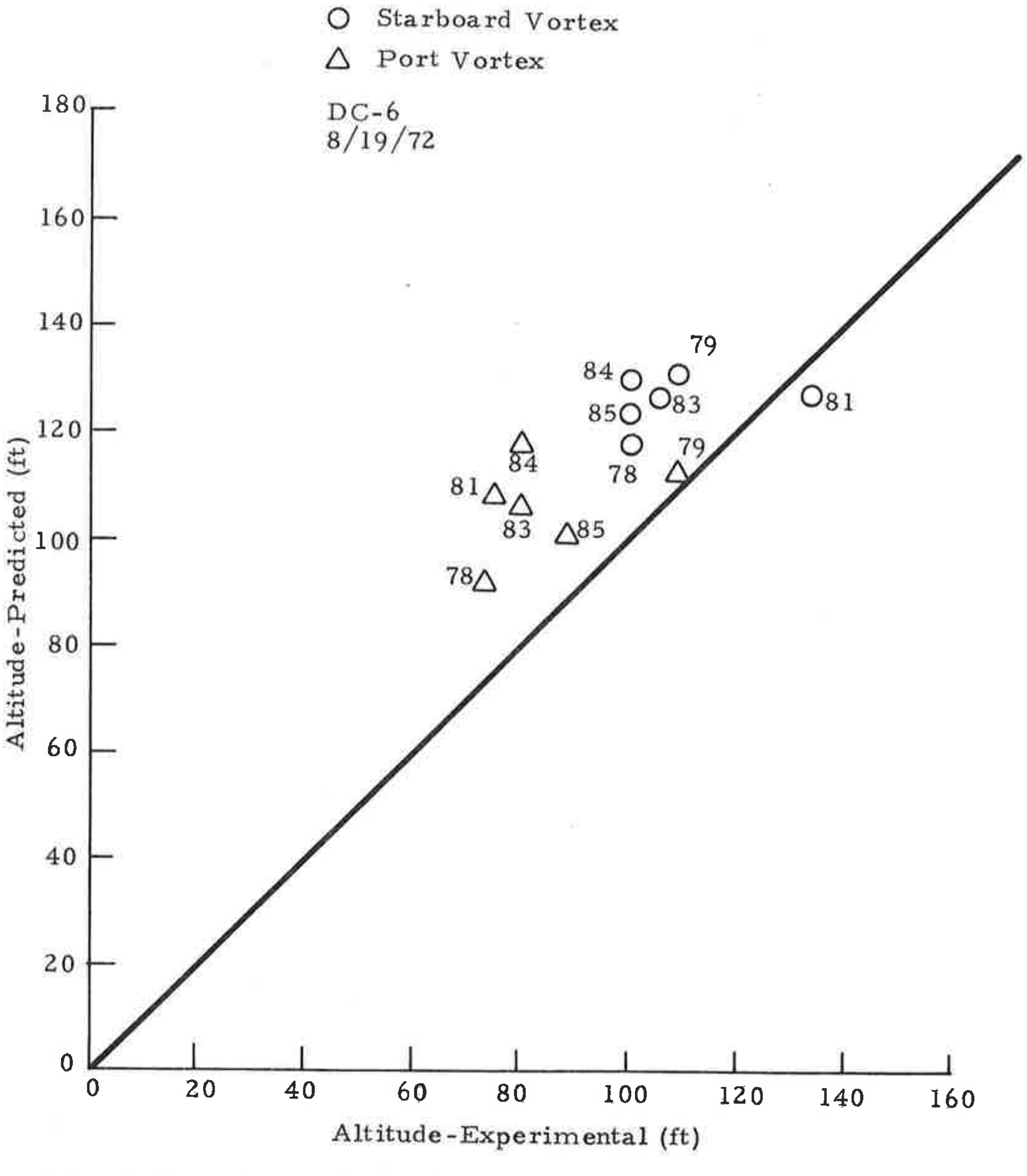

Fig. 5-22 - Comparison of Predicted Altitudes Versus Observed Altitudes for DC-6 Aircraft Flybys the predicted tower hit time and altitude, respectively. The data are scattered about the one-to-one correspondence line with an average difference of less than 5 seconds. The altitude is predicted somewhat high and is consistent with the non-elliptical loading conclusion.

Figures 5-23 and 5-24 show similar results for B747 flybys for 16 September and 17 October 1972, respectively. The results for 16 September show that the scatter in the prediction increases with the age of the vortex at tower encounter. These results do not confirm the trend previously observed based on the few points showing the greatest differences in Fig. 5-19. It is felt that this situation is more representative of the actual situation.

The predictions for 17 October in Fig. 5-24 were made with only one instantaneous wind velocity and direction that was recorded manually for each flyby during the test. The recorded value corresponds to the windspeed and direction as measured at the 140-foot level of the tower prior to each flyby. A wind profile was constructed based on a power law formulation with the exponent dictated by the measured stability of the atmosphere. This concept is pursued according to the Pasquill class criteria as discussed below.

5.3 THE PASQUILL CLASSES AND THEIR APPLICATIONS

Lissaman et.al. (Ref.5) listed seven stability classes suggested by Pasquill (Ref. 33). The classes as such are provided as a "rule of thumb" and are a function of very general meteorological conditions (i.e., cloud cover and wind speed). These classes are defined in Table 5-1. Table 5-2 relates temperature gradient criteria to the various Pasquill classes and also provides a p value for use in the power law:

$$U_2/U_1 = (z_2/z_1)^p \tag{5.1}$$

where U and z are wind speed and altitude, respectively, and the subscripts correspond to two different heights with $z_2 > z_1$.

It is important to note that Eq. (5.1) is a useful relationship for engineering applications providing the correct p value is selected. Actually, this p value is based on the lapse rate and the surface roughness length.

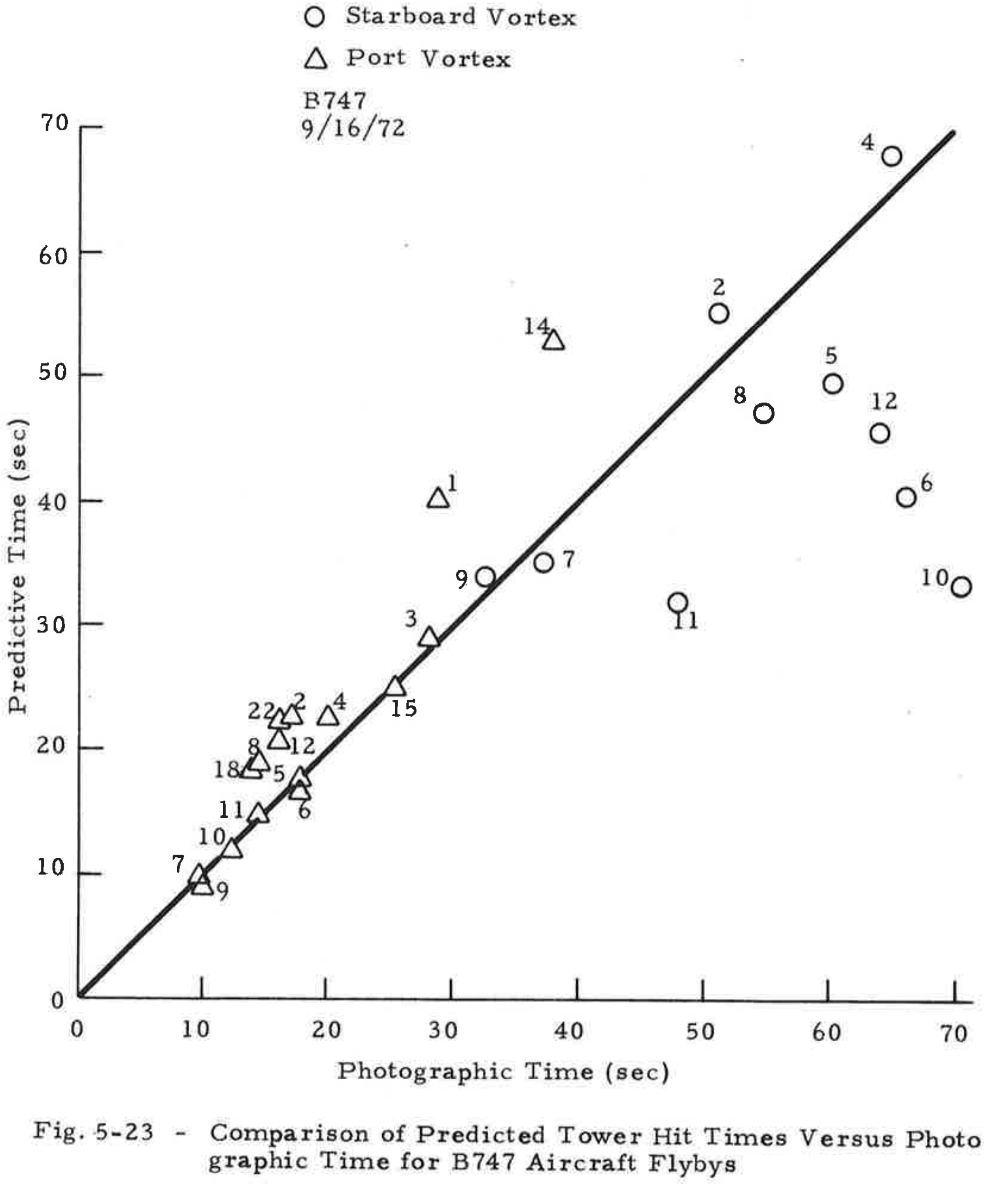

Fig. 5-23 - Comparison of Predicted Tower Hit Times Versus Photographic Time for B747 Aircraft Flybys

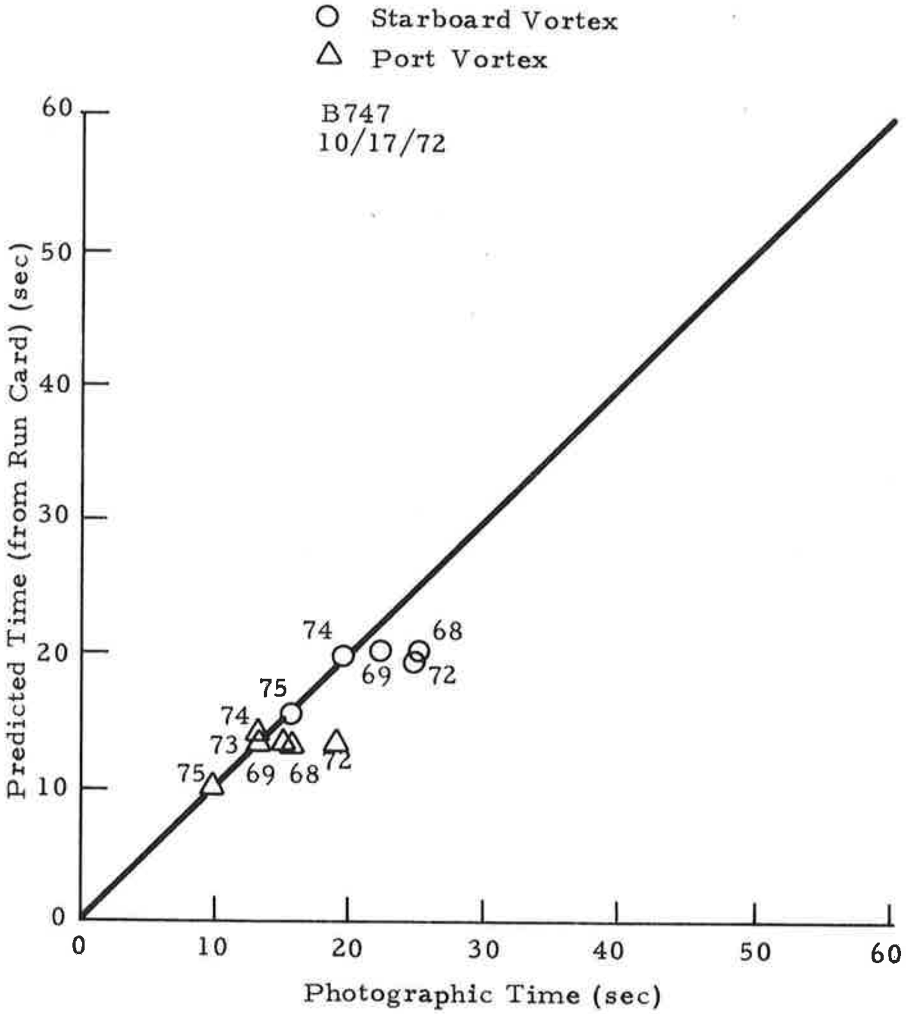

Fig. 5-24 - **Comparison of Predicted Tower** Hit Times Based on Application of Power Law Technique vs Photographically Determined Time

TABLE 5-1*

RELATION OF TURBULENCE TYPES TO WEATHER CONDITIONS

A— Extremely unstable conditions
B— Moderately unstable conditions
C— Slightly unstable conditions
D— Neutral conditions*
E— Slightly stable conditions
F— Moderately stable conditions

Surface wind speed, m/sec	Daytime insolation			Nighttime conditions	
	Strong	Moderate	Slight	Thin overcast or ≥ $^4/_8$ cloudiness†	≤$^3/_8$ cloudiness
<2	A	A–B	B		
2	A–B	B	C	E	F
4	B	B–C	C	D	E
6	C	C–D	D	D	D
>6	C	D	D	D	D

*Applicable to heavy overcast, day or night.

†The degree of cloudiness is defined as that fraction of the sky above the local apparent horizon which is covered by clouds.

These classes can be used to summarize data as follows:

TABLE 5-2*

PASQUILL CLASSES AND RELATED PARAMETERS

Pasquill Class	$\delta T/\delta z$	T_g	p (Z_o~0.1 to 1 m)
A	≤-0.6 °C/100'	25°	.15
B	-0.5	20°	.17
C	-0.4	15°	.20
D	-0.2 to -0.3	10°	.26
E	-0.1 to 0.3	5°	.39
F	0.4 to 1.1	2.5°	.48
(G)	(>1.2)	(1.7°)	

---

*From Ref. 5.

Lumley et al. (Ref. 27) prepared a nomogram relating these p values to the Monin-Obukhov length and the roughness length. This nomogram is illustrated in Fig. 5-25 where z_o is the roughness length and L' is the Monin-Obukhov length.

Although the values of p given in Table 5-2 are related to atmospheric conditions which may be similar in stability characteristics for which the values were determined, the conditions are probably not at all similar in the roughness length parameter. This concern is because the given p values were determined from measurements at a site where the roughness length varied between the values of approximately 0.5 to 1 meter. These values are extremely high and can in no way be realistically applied to typical airport sites except in the case of internal boundary layer creation due to very non-homogeneous terrain characteristics or obstacle effects.

Since L' is a function of friction velocity, temperature, specific heat, and the turbulent vertical heat flux which are parameters which cannot be easily determined for each experimental case, the most prominent problem is a method of determining the stability characteristics of the atmosphere in the experimental range below approximately 200 feet. This may be done by comparing the measured p values to various simple indices of stability conditions (e.g., the Pasquill classes determined from the surface conditions given in Table 5-1). Caution must be exercised in determining the most nearly correct p value to be assigned to a stability class.

Using the NAFEC tower data, the correlation coefficients, γ, of wind speed and the natural logarithm of height for a number of randomly selected wind profiles were determined by:

$$\gamma = \frac{\sum_{i=1}^{5} U_{z_i} (\ln z_i) - \dfrac{\left(\sum_{i=1}^{5} U_{z_i}\right)\left(\sum_{i=1}^{5} \ln z_i\right)}{5}}{\left\{\left[\sum_{i=1}^{5} U_{z_i}^2 - \dfrac{\left(\sum_{i=1}^{5} U_{z_i}\right)^2}{5}\right]\left[\sum_{i=1}^{5} (\ln z)_i^2 - \dfrac{\left(\sum_{i=1}^{5} \ln z_i\right)^2}{5}\right]\right\}^{1/2}}$$

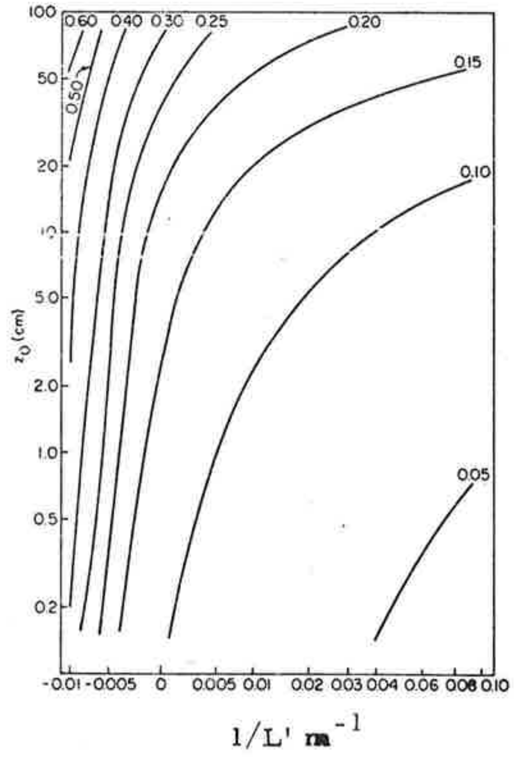

Fig. 5-25 - Variation of the Exponent p with Roughness z_0 and the Inverse of the Monin-Obukhov Length L' for the 11- to 46-meter Layer; a Zero Value of 1/L' Corresponds to Adiabatic Conditions (Ref. 27)

For those profiles whose values of γ exceed 0.95, a linear correlation may be assumed to be effective over the given range on a semilogarithmic scale. In such a case, the logarithmic wind profile relationship is valid and the values of z_o should be computed for each case where $\gamma > 0.95$. The mean of these values may be a very good estimation of the true value of z_o provided the conditions are appropriate. The relationship used for determining z_o is

$$z_o = \left[\frac{\sum_{i=1}^{5} \ln z_i}{5} - b_1 \frac{\sum_{i=1}^{5} U_{z_i}}{5}\right]$$

where

$$b_1 = \frac{\sum_{i=1}^{5} U_{z_i} \ln z_i - \frac{\left(\sum_{i=1}^{5} U_{z_i}\right)\left(\sum_{i=1}^{5} \ln z_i\right)}{5}}{\sum_{i=1}^{5} U_{z_i} - \frac{\left(\sum_{i=1}^{5} U_{z_i}\right)^2}{5}}$$

In practice this procedure may result in an inaccurate estimation of z_o depending on the true linearity of the wind as a function of height on a semi-logarithmic scale. For practical determinations of the roughness length, wind profiles should be taken over a small range of height (e.g., less than 10 meters) at five or six levels in order for the above procedure to be accurate.

Once a satisfactory value of z_o is determined, one may establish the range of values of $1/L'$ for each Pasquill class by use of Fig. 5-25 given by Lissaman. Finally, this range of values may be applied to the graph given in Fig. 5-25 in conjunction with the roughness length in order to determine the range of power values, p, to be used at the site for a particular Pasquill class.

The corresponding ground wind comparisons for the B747 flybys on 17 October 1972 generated by this application of the Pasquill class are shown in Fig. 5-26 (see Fig. 5-24 for tower hit comparison). The data correspond to a relatively high crosswind, and excellent agreement is seen to exist between prediction and measurement. No tower wind data are available for these particular runs due to a program malfunction at NAFEC.

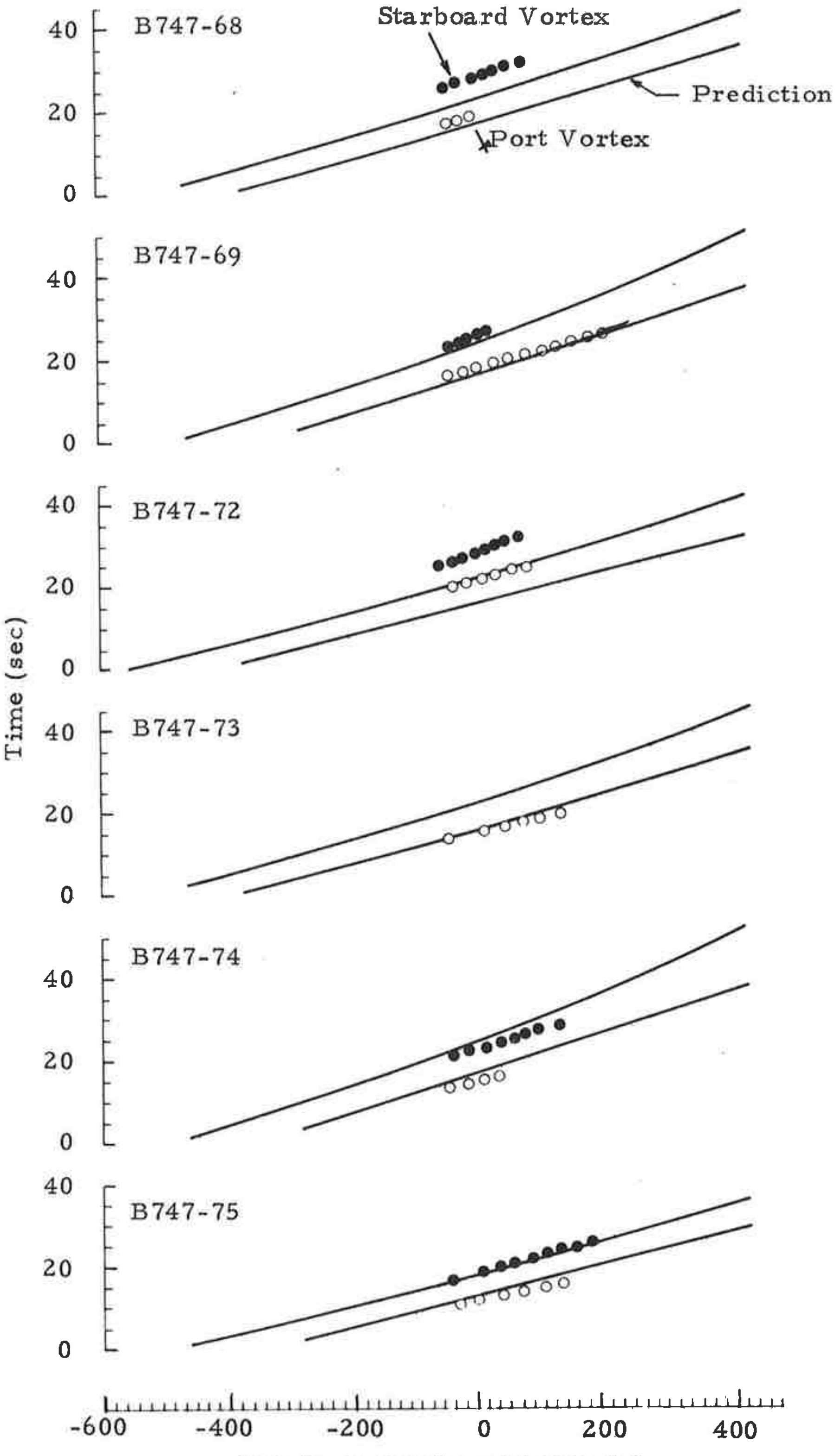

Fig. 5-26 - Ground Wind Vortex Tracks for Runs 68 through 75 on 17 October 1972 for B747 Aircraft

The data shown in Figs. 5-27 and 5-28 define the differences in the tower hit times for prediction based on the measured wind profile and that obtained by application of the power law technique to surface data routinely recorded at airports. These surface data were obtained from NOAA MF1-10A and 10B charts and were used in conjunction with the Pasquill class criteria outlined in Table 5-2. It is seen that the results compare very well with the tower hit times measured photographically. Figure 5-29 shows the results of using one wind point to determine the wind altitude relationship without utilizing the power law technique. It is seen that significant errors result thus emphasizing the importance of prevailing stability condition on the wind profile. The comparisons for predicted altitude versus that determined photographically for all of the previous cases are shown in Figs. 5-30 through 5-32, again showing a predicted sink rate somewhat less than actual.

5.4 REPRESENTATIVE VORTEX TRACKS FOR VARIOUS AIRCRAFT TYPES

DC-6 Aircraft

Vortex tracks corresponding to a DC-6 flyby on September 1972 are shown in Figs. 5-33 and 5-34 for a cross-section plot of altitude versus lateral displacement and time versus altitude, respectively. These results are typical of all of the DC-6 data analyzed. The actual sink rate is greater than that predicted as seen in both tracks, most notably in the time-altitude. The altitude is approximately 20-30 feet in error with the lateral position showing a 100 foot discrepancy caused by uncertainty in the wind profile.

B-727 Aircraft

Two consecutive flybys are shown in Figs. 5-35 through 5-38 for a B-727 aircraft on 13 September 1972. Excellent agreement is obtained for lateral position with some differences noted in the altitude for the downwind vortex. Analysis of several runs produced the observation that the B-727 aircraft generates vortices with sink rates very close to elliptical calculations shown in Fig. 5-36 (here the downwind vortex is rising). This may be caused by the outboard ends of the flaps coinciding very nearly to the calculated rolled-up position of the vortex pair based on elliptically loaded wing assumptions.

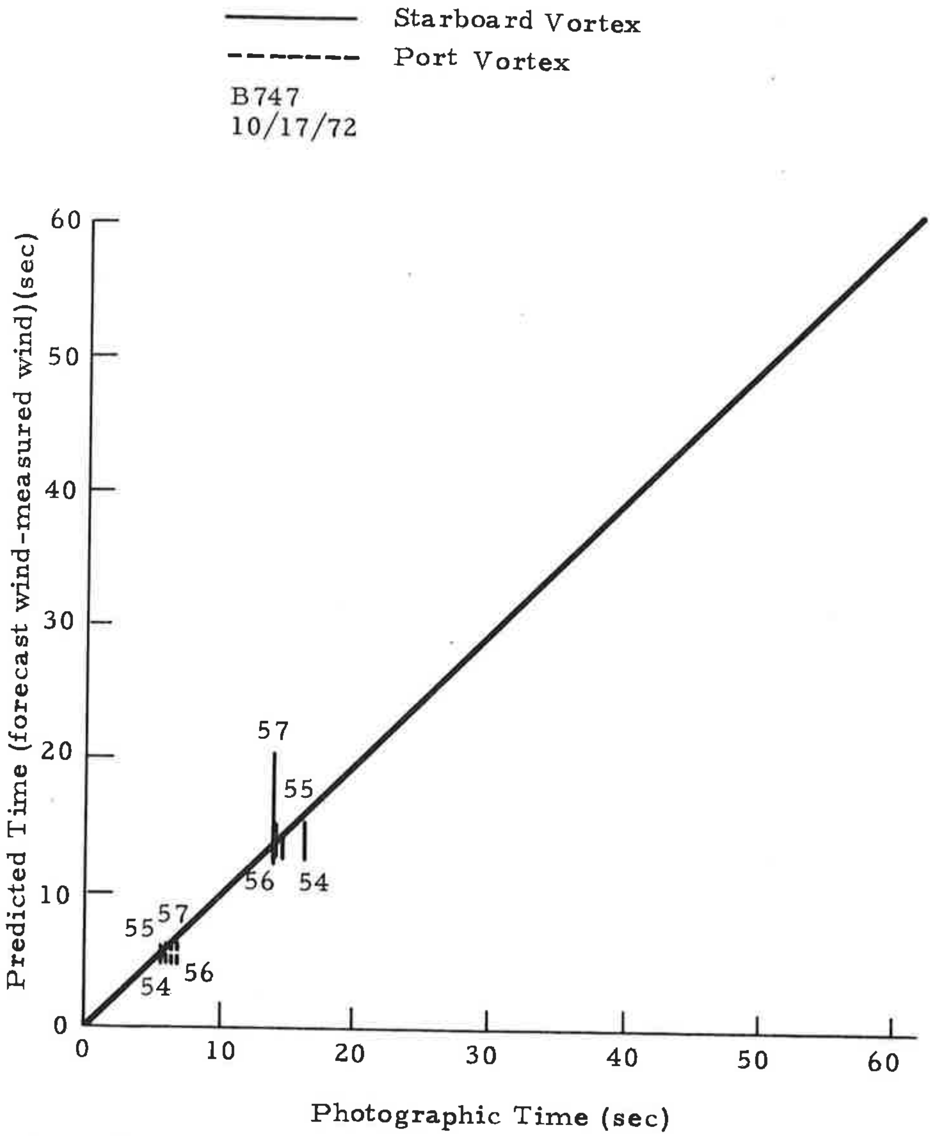

Fig. 5-27 - Comparison Between Differences in Predicted Tower Hit Times for Power Law Wind Profile and Actual Wind Profile Versus Photographically Determined Hit Time (17 October 1972)

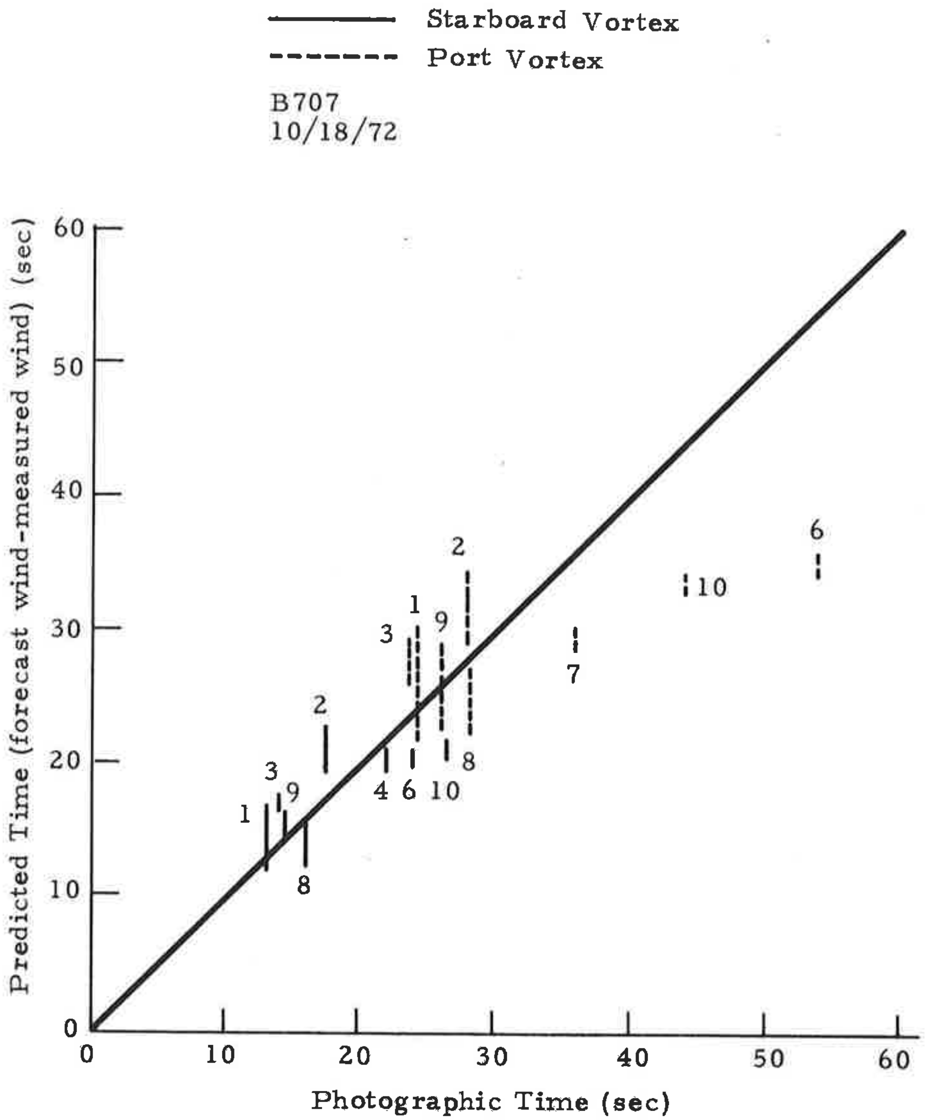

Fig. 5-28 - Comparison Between Differences in Predicted Tower Hit Times for Power Law Wind Profile and Actual Wind Profile Versus Photographically Determined Hit Time (18 October 1972)

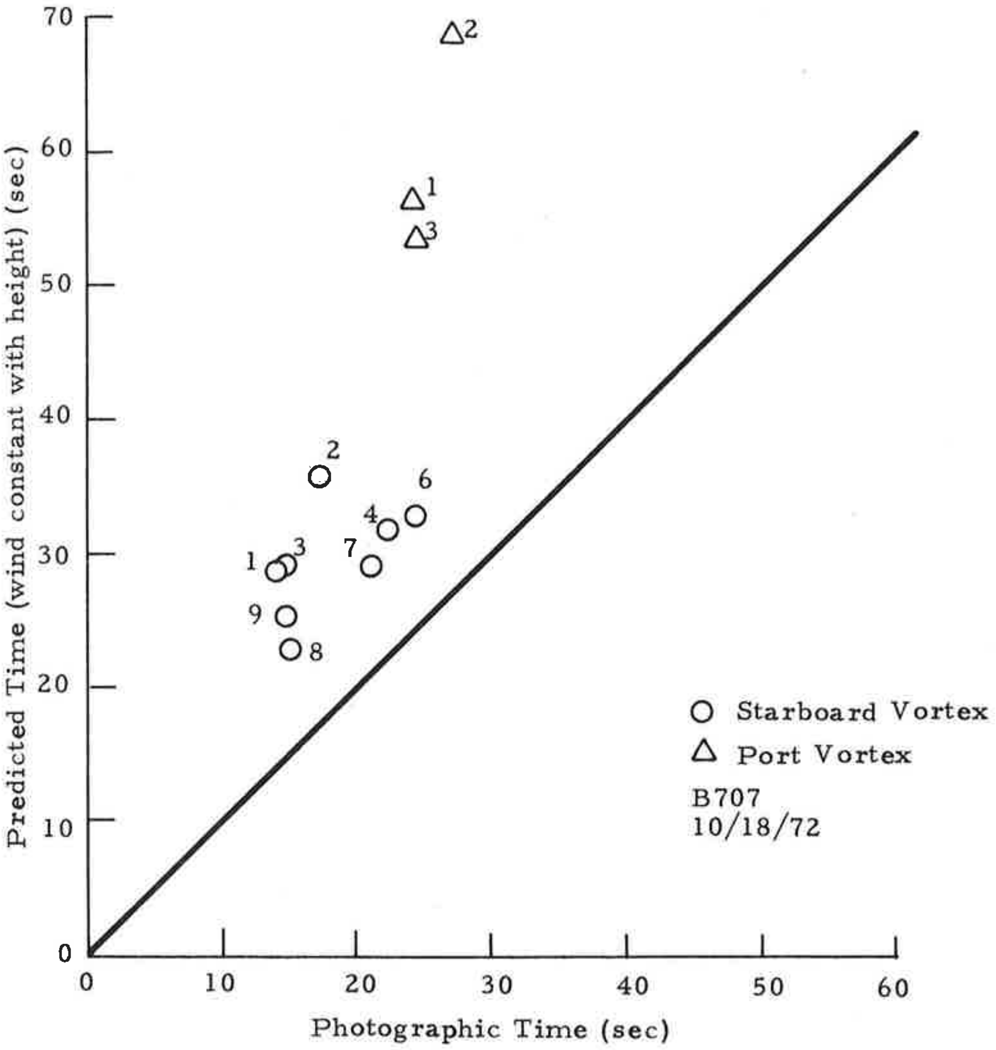

Fig. 5-29 - Comparison of Predicted Tower Hit Time Based on Surface Measurement Without Application of Power Law Technique Versus Photographic Time

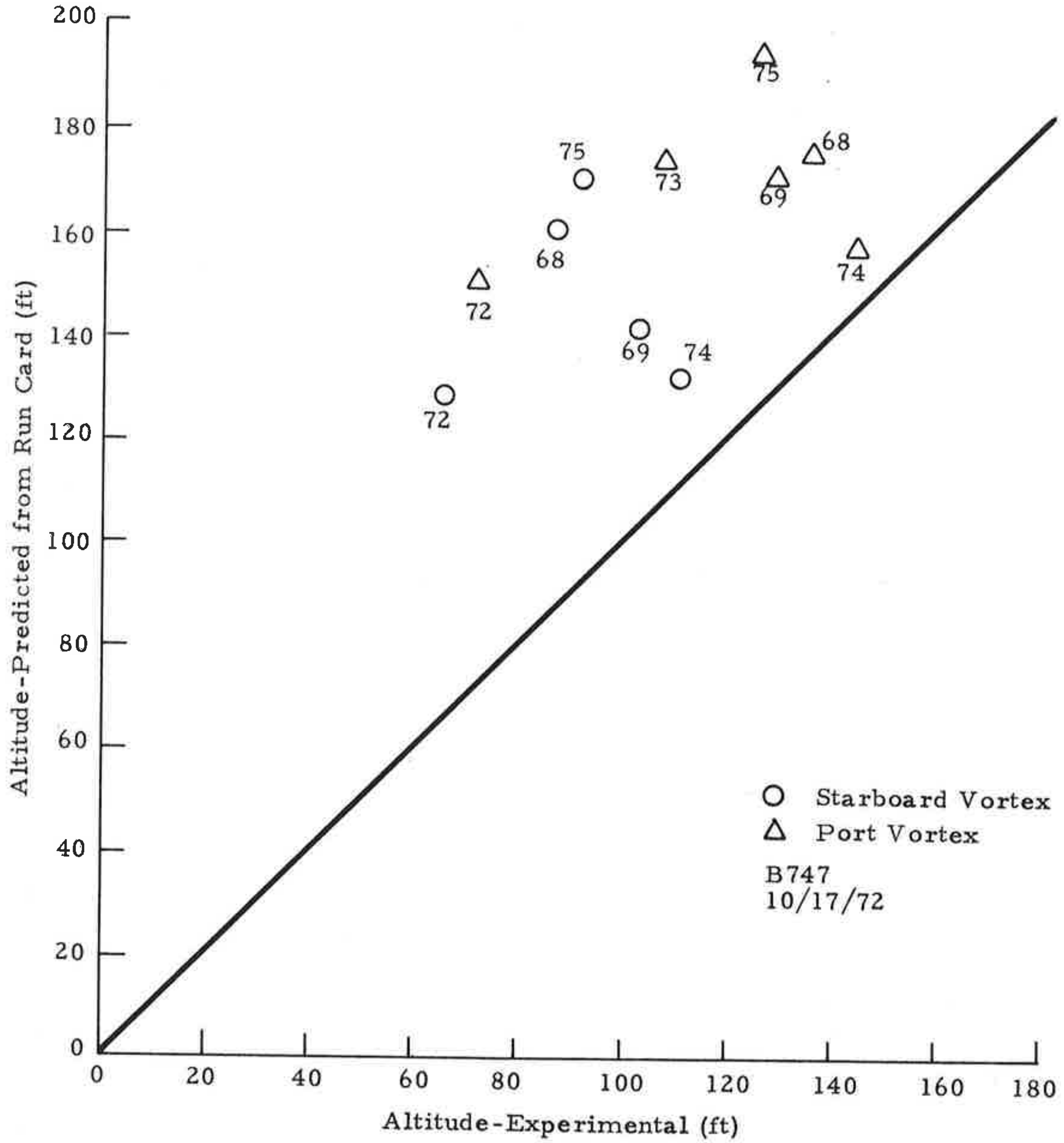

Fig. 5-30 - Comparison of Predicted Vortex Altitudes Based on Power Law Technique Versus Altitudes Measured Photographically

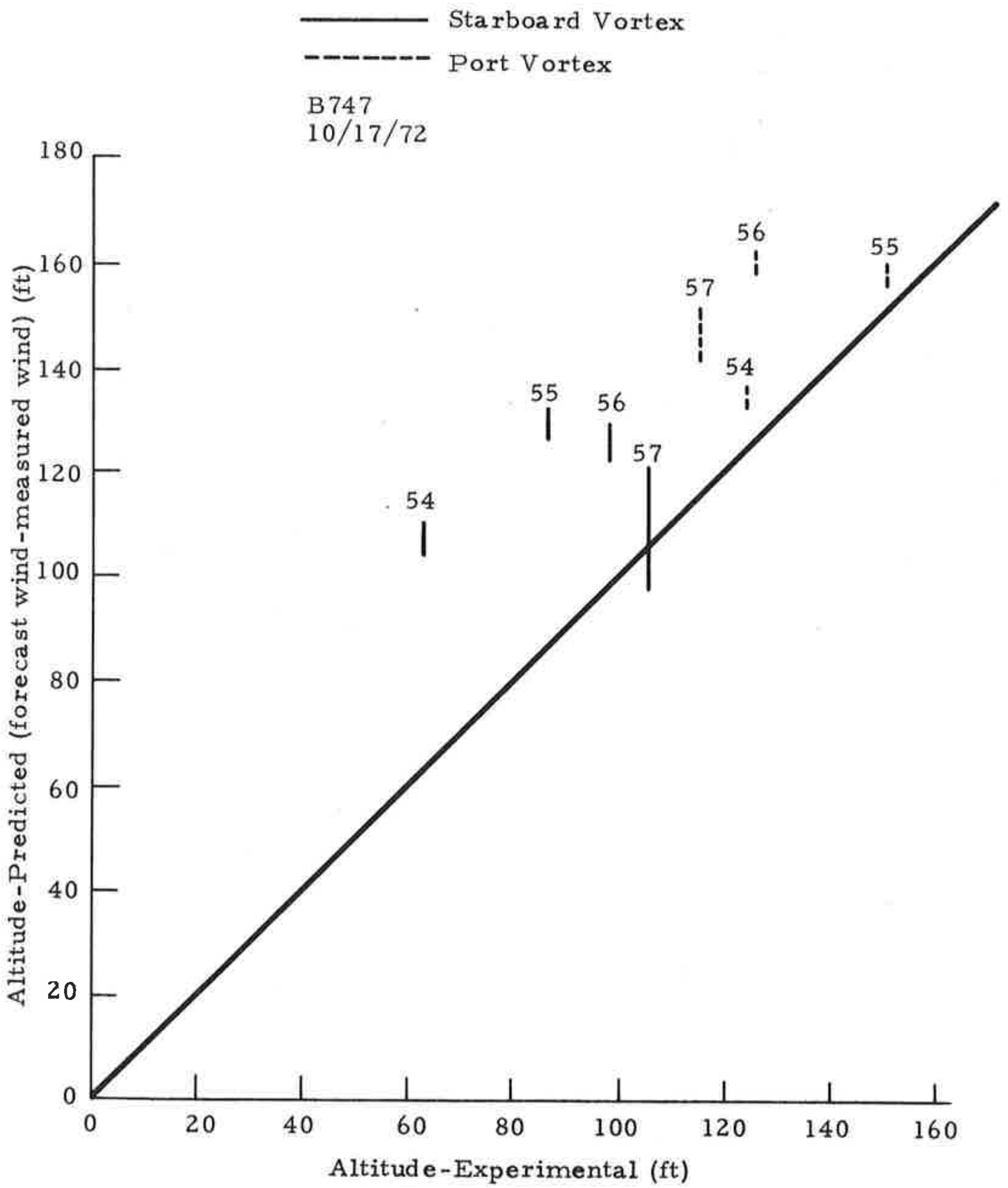

Fig. 5-31 - Comparison of Differences in Predicted Vortex Altitudes Based on Forecast and Measured Wind Profiles Versus Altitude Measured Photographically

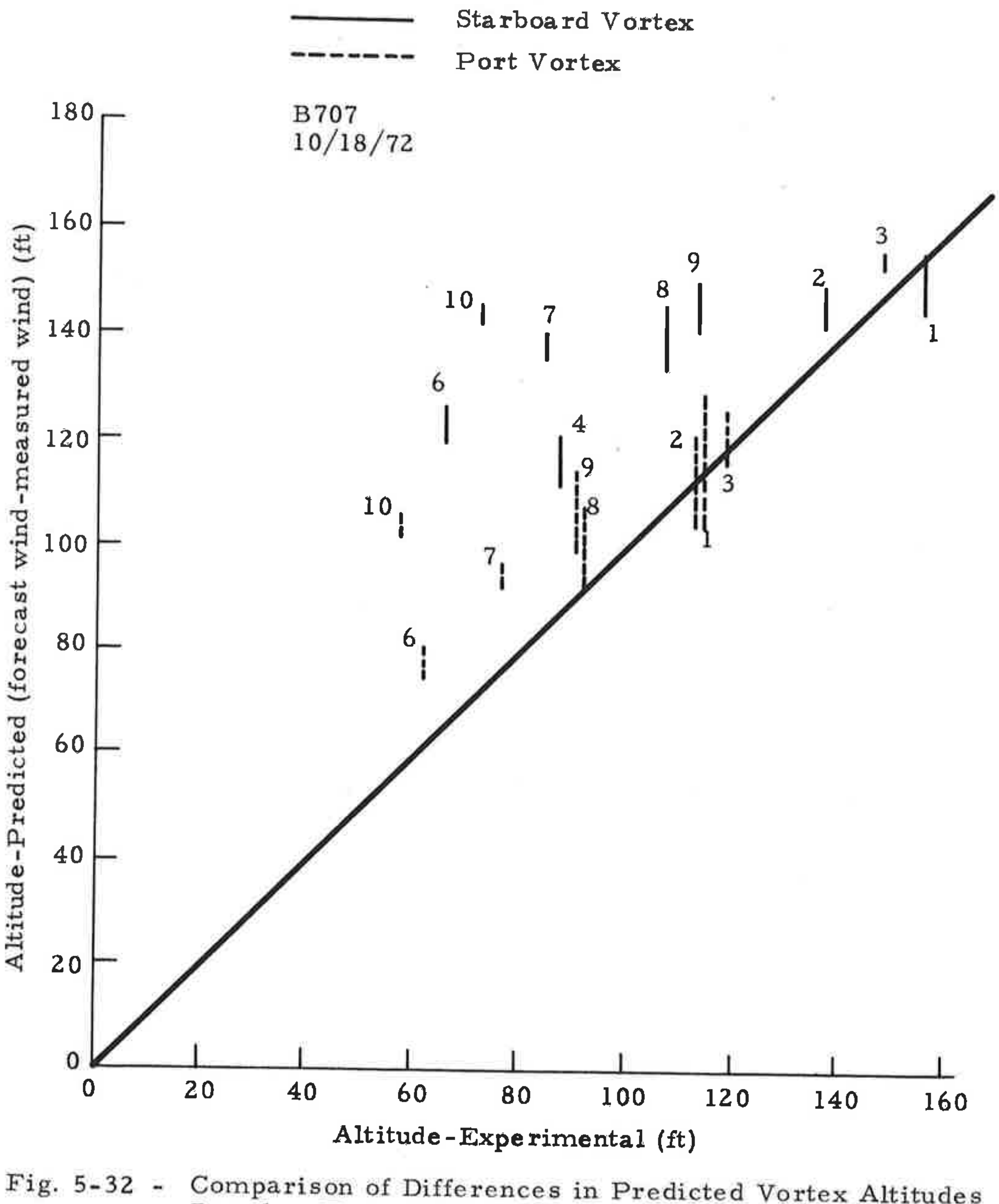

Fig. 5-32 - Comparison of Differences in Predicted Vortex Altitudes Based on Forecast and Measured Wind Profiles Versus Altitude Measured Photographically

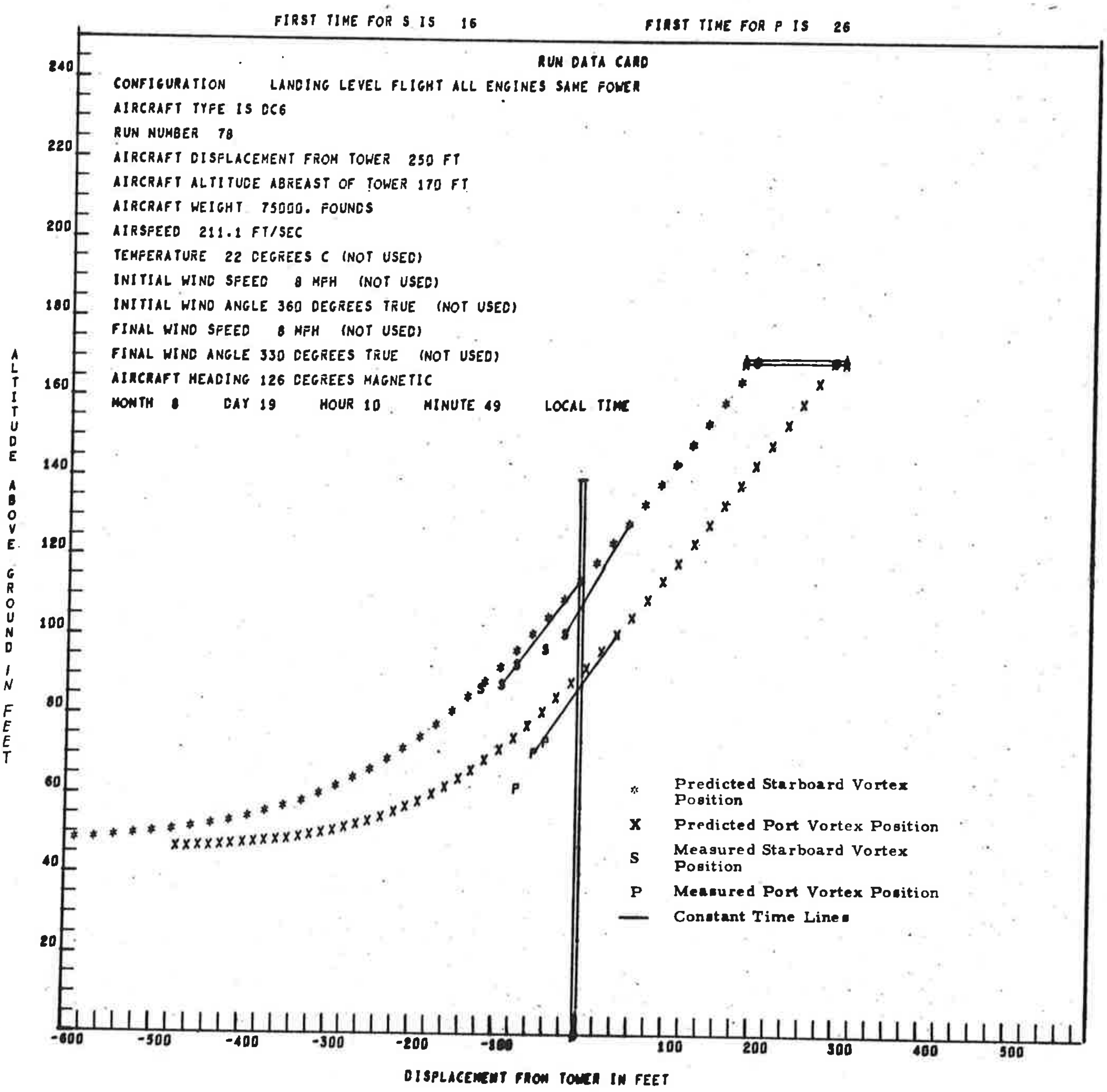

FIRST TIME FOR S IS 16 FIRST TIME FOR P IS 26

RUN DATA CARD

CONFIGURATION LANDING LEVEL FLIGHT ALL ENGINES SAME POWER

AIRCRAFT TYPE IS DC6

RUN NUMBER 78

AIRCRAFT DISPLACEMENT FROM TOWER 250 FT

AIRCRAFT ALTITUDE ABREAST OF TOWER 170 FT

AIRCRAFT WEIGHT 75000. POUNDS

AIRSPEED 211.1 FT/SEC

TEMPERATURE 22 DEGREES C (NOT USED)

INITIAL WIND SPEED 8 MPH (NOT USED)

INITIAL WIND ANGLE 360 DEGREES TRUE (NOT USED)

FINAL WIND SPEED 8 MPH (NOT USED)

FINAL WIND ANGLE 330 DEGREES TRUE (NOT USED)

AIRCRAFT HEADING 126 DEGREES MAGNETIC

MONTH 8 DAY 19 HOUR 10 MINUTE 49 LOCAL TIME

Fig. 5-33 - Comparison of Predicted Vortex Track with Photographic Data for DC6 Aircraft

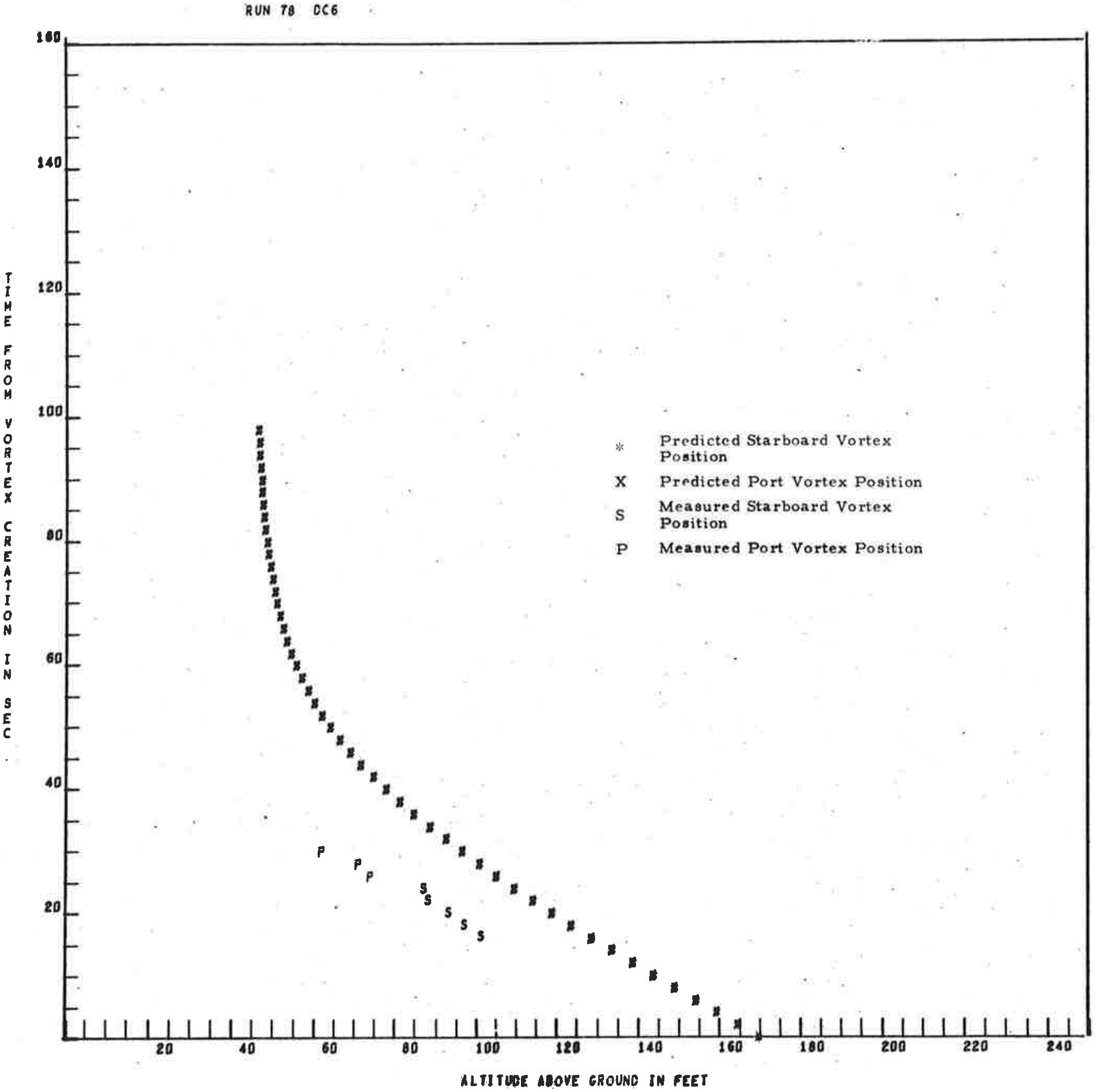

Fig. 5-34 - Comparison of Predicted and Measured Vortex Altitude for DC6 Aircraft

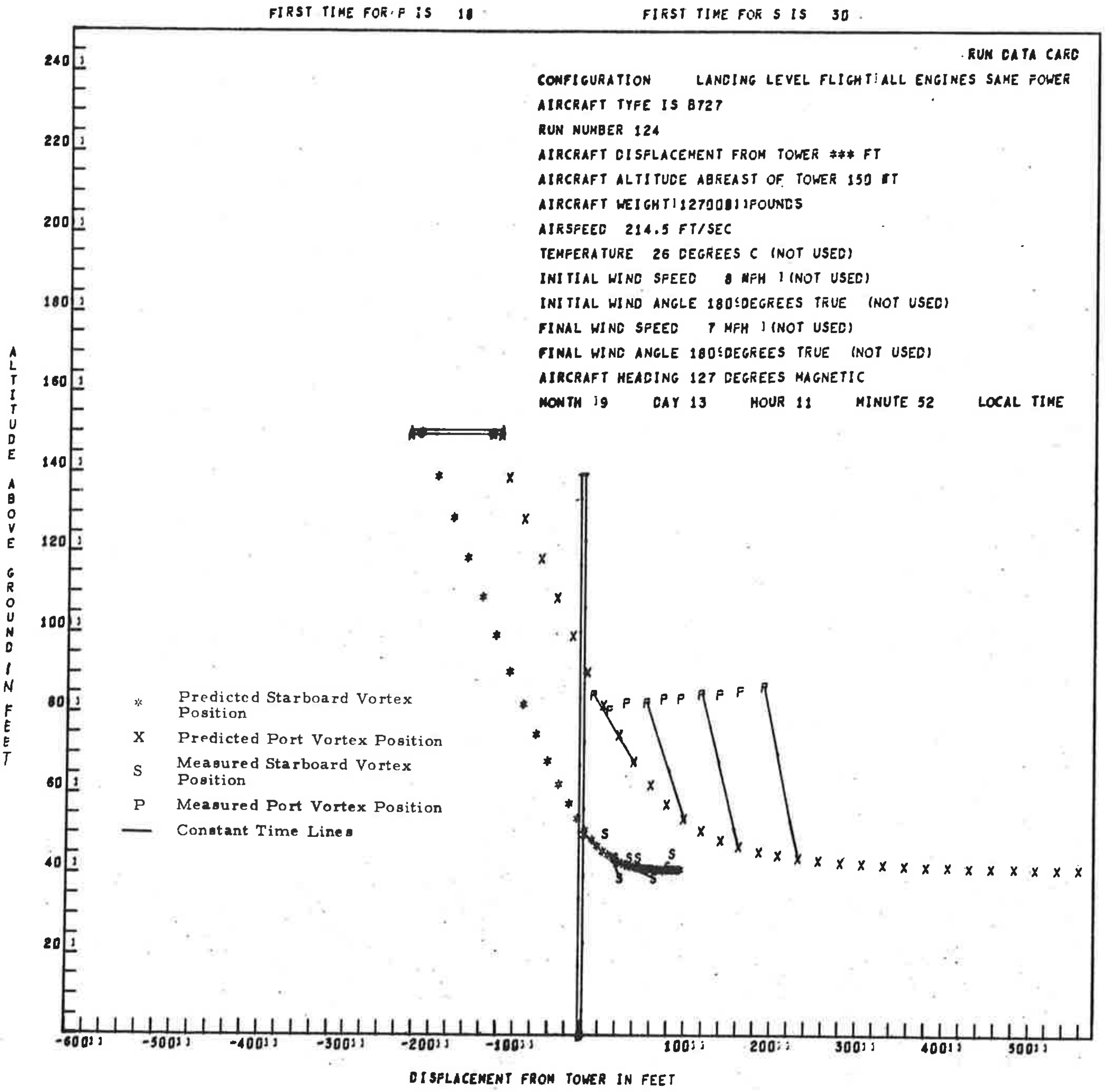

Fig. 5-35 - Comparison of Predicted Vortex Track with Photographic Data for B727 Aircraft Flyby 124 on 13 September 1972

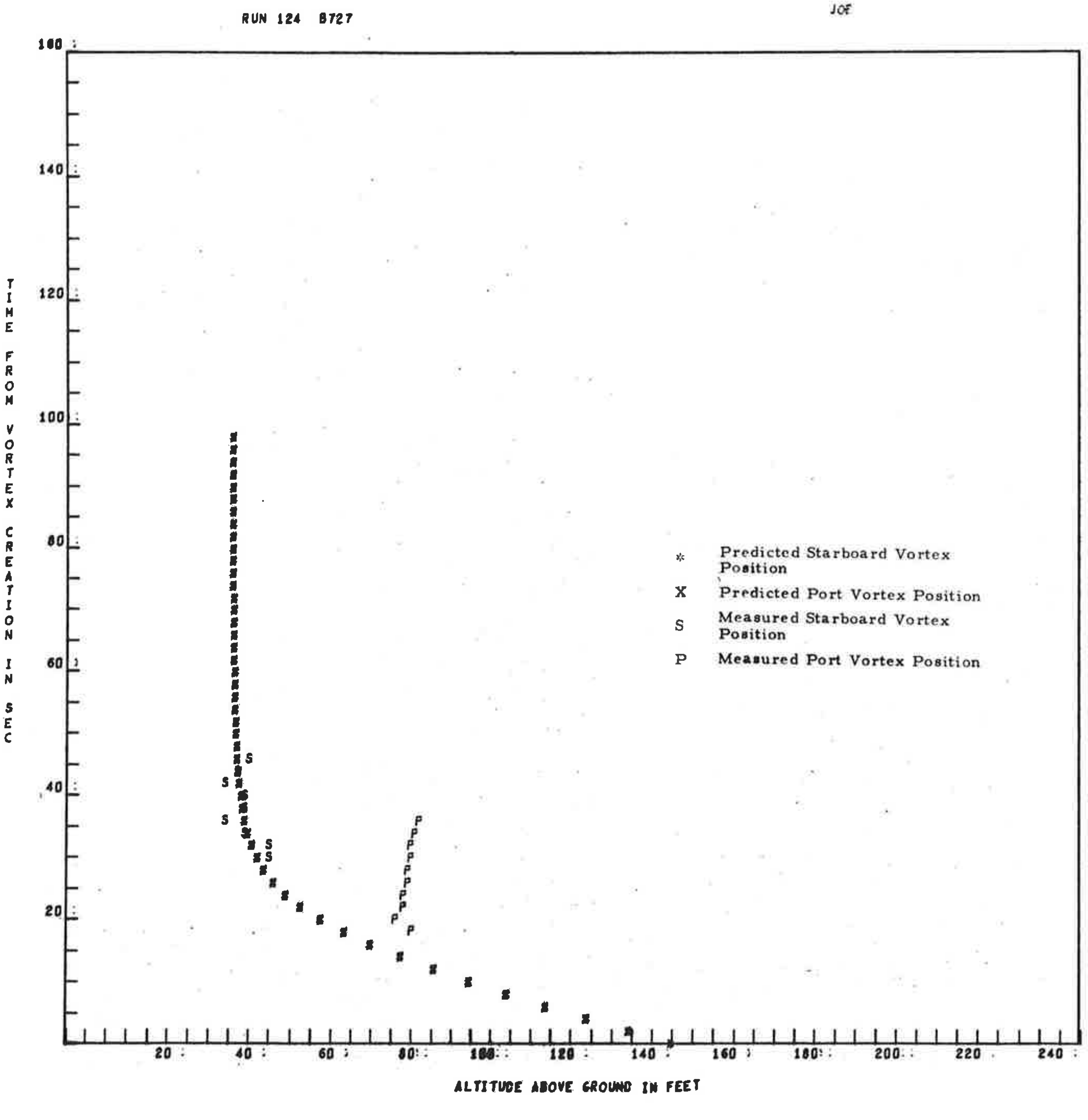

Fig. 5-36 - Comparison of Predicted and Measured Vortex Altitude for a B-727 Aircraft Flyby on 13 September 1972

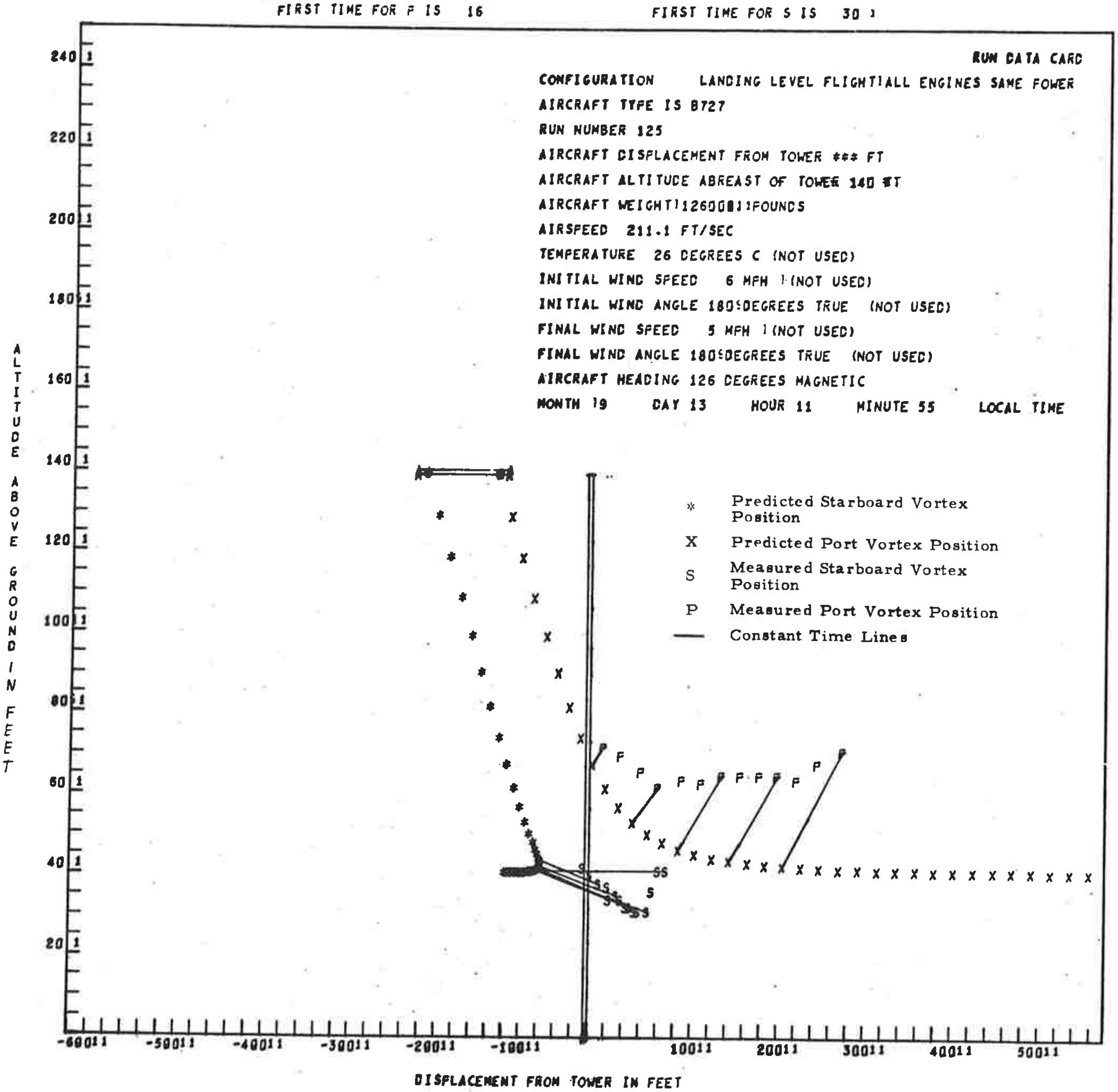

```
RUN DATA CARD
CONFIGURATION      LANDING LEVEL FLIGHT!ALL ENGINES SAME FOWER
AIRCRAFT TYFE IS B727
RUN NUMBER 125
AIRCRAFT DISPLACEMENT FROM TOWER *** FT
AIRCRAFT ALTITUDE ABREAST OF TOWER 140 FT
AIRCRAFT WEIGHT!126000!!FOUNDS
AIRSPEED  211.1 FT/SEC
TEMPERATURE  26 DEGREES C (NOT USED)
INITIAL WIND SPEED    6 MPH !(NOT USED)
INITIAL WIND ANGLE 180!DEGREES TRUE  (NOT USED)
FINAL WIND SPEED    5 MPH !(NOT USED)
FINAL WIND ANGLE 180!DEGREES TRUE  (NOT USED)
AIRCRAFT HEADING 126 DEGREES MAGNETIC
MONTH 19      DAY 13      HOUR 11      MINUTE 55      LOCAL TIME
```

Fig. 5-37 - Comparison of Predicted Vortex Track with Photographic Data for B727 Aircraft Flyby 125 on 13 September 1972

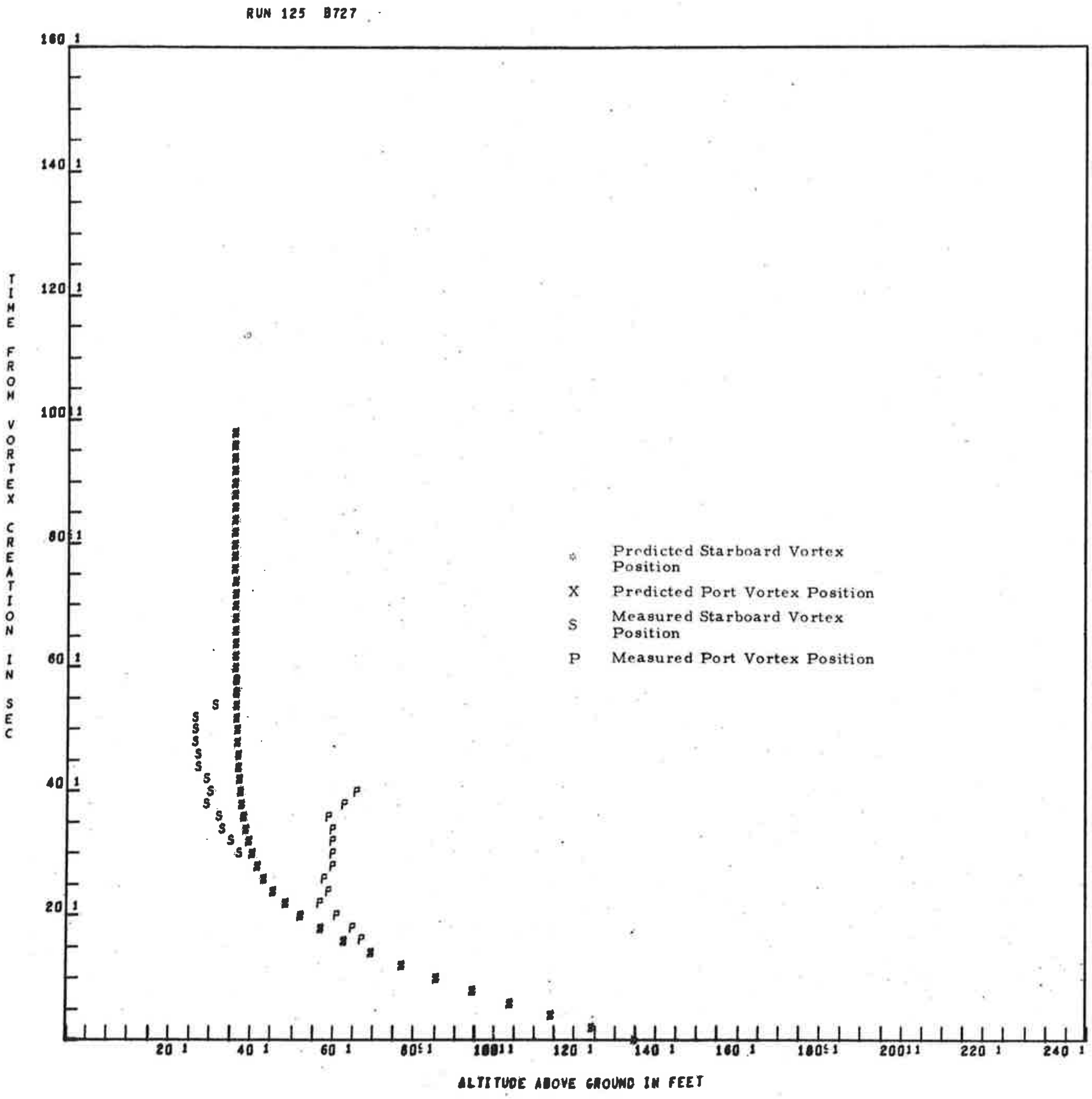

Fig. 5-38 - Comparison of Predicted and Measured Vortex Altitude for a B-727 Aircraft Flyby 125 on 13 September 1972

Run 125 shows essentially the same experimental data as the flight conditions and position are very nearly identical. This run does show lower equilibrium altitude (10 to 20 feet) due to a lower flight path (10 feet) as would be expected. However, the measured wind decreased between flybys as evidenced by the predicted stalling of the upwind vortex. When the wind after Run 125 was used, results similar to Run 124 were obtained. The predicted altitude passes between the measured port and starboard vortex altitudes as shown in Fig. 5-38. This is a very typical result when vortex tilting occurs.

Another pair of B-727 flybys are shown in Figs. 5-39 to 5-42 for 22 September 1972 for cases where no appreciable vortex tilting occurred. Note the altitude-time predictions are quite accurate which again emphasizes that the calculated sink.rates are very near the actual for B-727 aircraft.

B-747 Aircraft

Four typical comparisons of prediction versus measurement for B747 aircraft flybys are shown in Figs. 5-43 through 5-50 for 17 September and 17 October 1972. A very general observation is that the predicted sink rates are smaller than the observed thus producing a higher predicted altitude. All of these examples show that this is the case when vortex tilting is both present and absent.

As seen previously for B727 aircraft data when vortex tilting occurred, the predicted altitude was approximately the average of the port and starboard vortices. For the B747 case with vortex tilting the average is somewhat less than that predicted (Run 28). When no tilting occurs (Run 32) again there is the consistent trend of the predicted sink rate being less than that observed. Note that the average lateral uncertainty is considerably less than 100 feet for all of the runs with about a 30 foot difference in altitude at the equilibrium height.

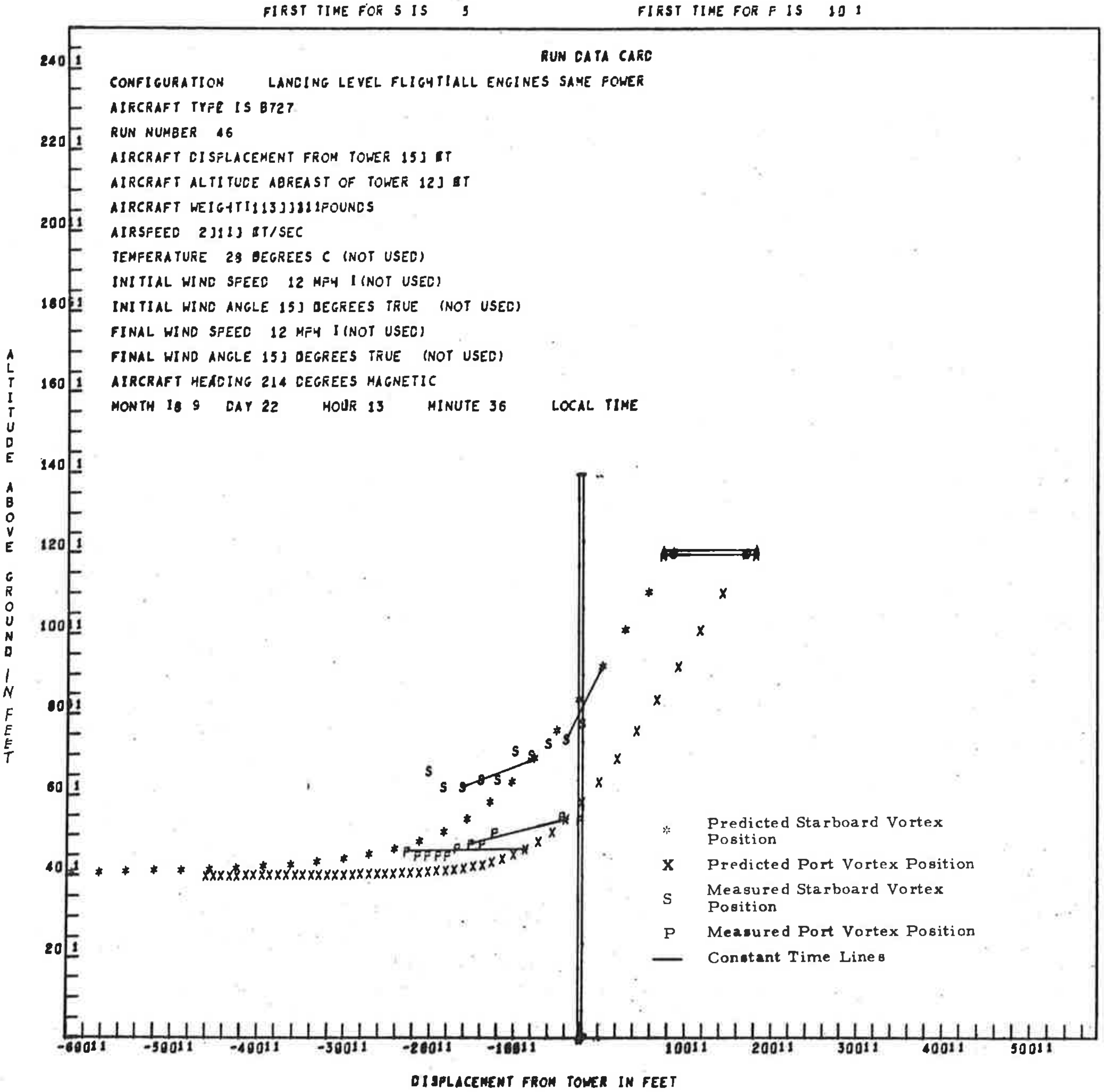

```
FIRST TIME FOR S IS    5                    FIRST TIME FOR P IS   10 1

                                        RUN DATA CARD
CONFIGURATION     LANDING LEVEL FLIGHTIALL ENGINES SAME POWER
AIRCRAFT TYPE IS B727
RUN NUMBER  46
AIRCRAFT DISPLACEMENT FROM TOWER 15] FT
AIRCRAFT ALTITUDE ABREAST OF TOWER 12] FT
AIRCRAFT WEIGHTI113]]]11POUNDS
AIRSPEED  2]11] FT/SEC
TEMPERATURE  28 DEGREES C (NOT USED)
INITIAL WIND SPEED  12 MPH I(NOT USED)
INITIAL WIND ANGLE 15] DEGREES TRUE  (NOT USED)
FINAL WIND SPEED  12 MPH I(NOT USED)
FINAL WIND ANGLE 15] DEGREES TRUE  (NOT USED)
AIRCRAFT HEADING 214 DEGREES MAGNETIC
MONTH I8 9   DAY 22     HOUR 13     MINUTE 36     LOCAL TIME
```

Fig. 5-39 - Comparison of Predicted Vortex Track with Photographic Data for B727 Aircraft Flyby 46 on 22 September 1972

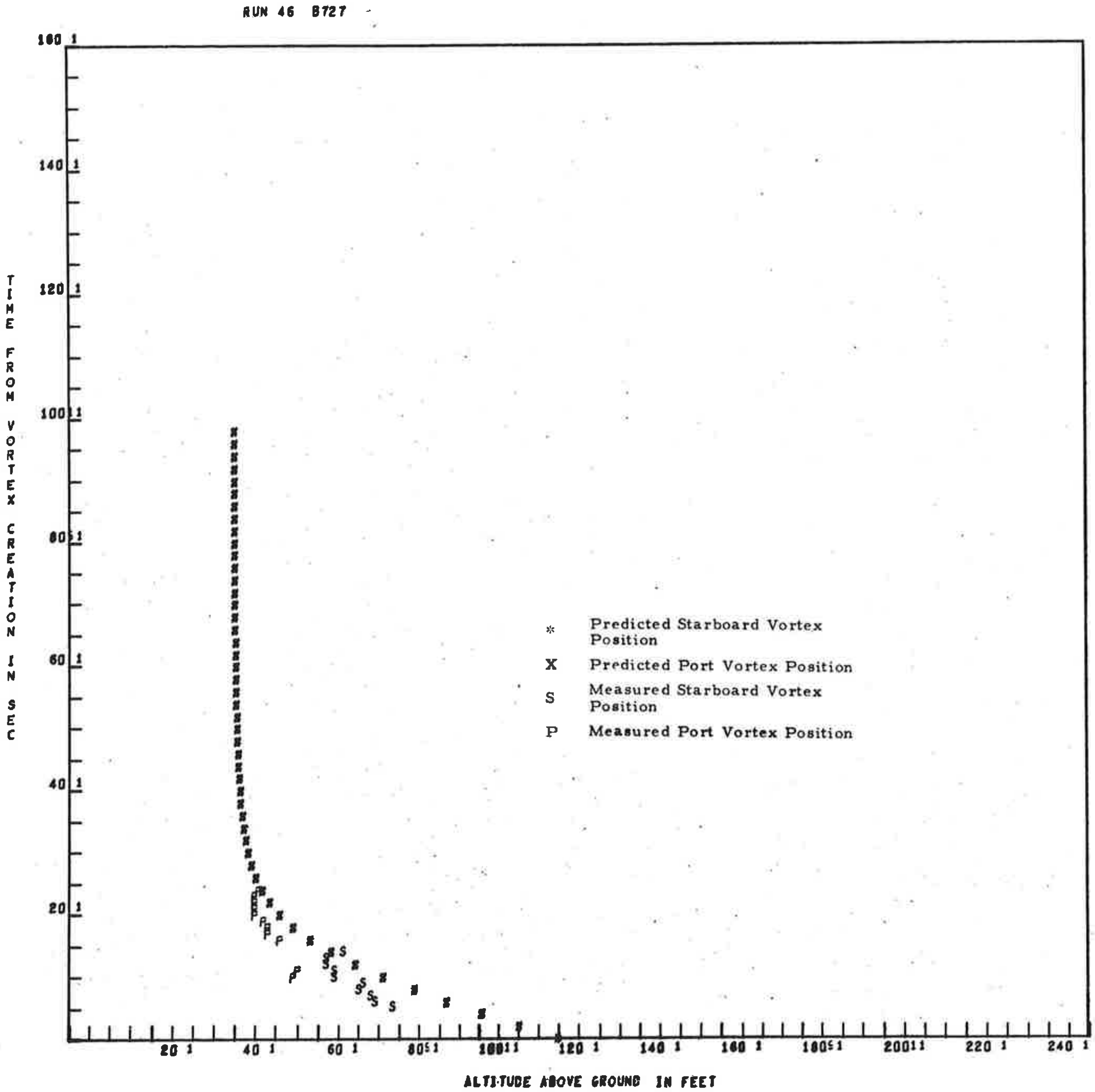

Fig. 5-40 - Comparison of Predicted and Measured Vortex Altitude for a B-727 Aircraft Flyby 46 on 22 September 1972

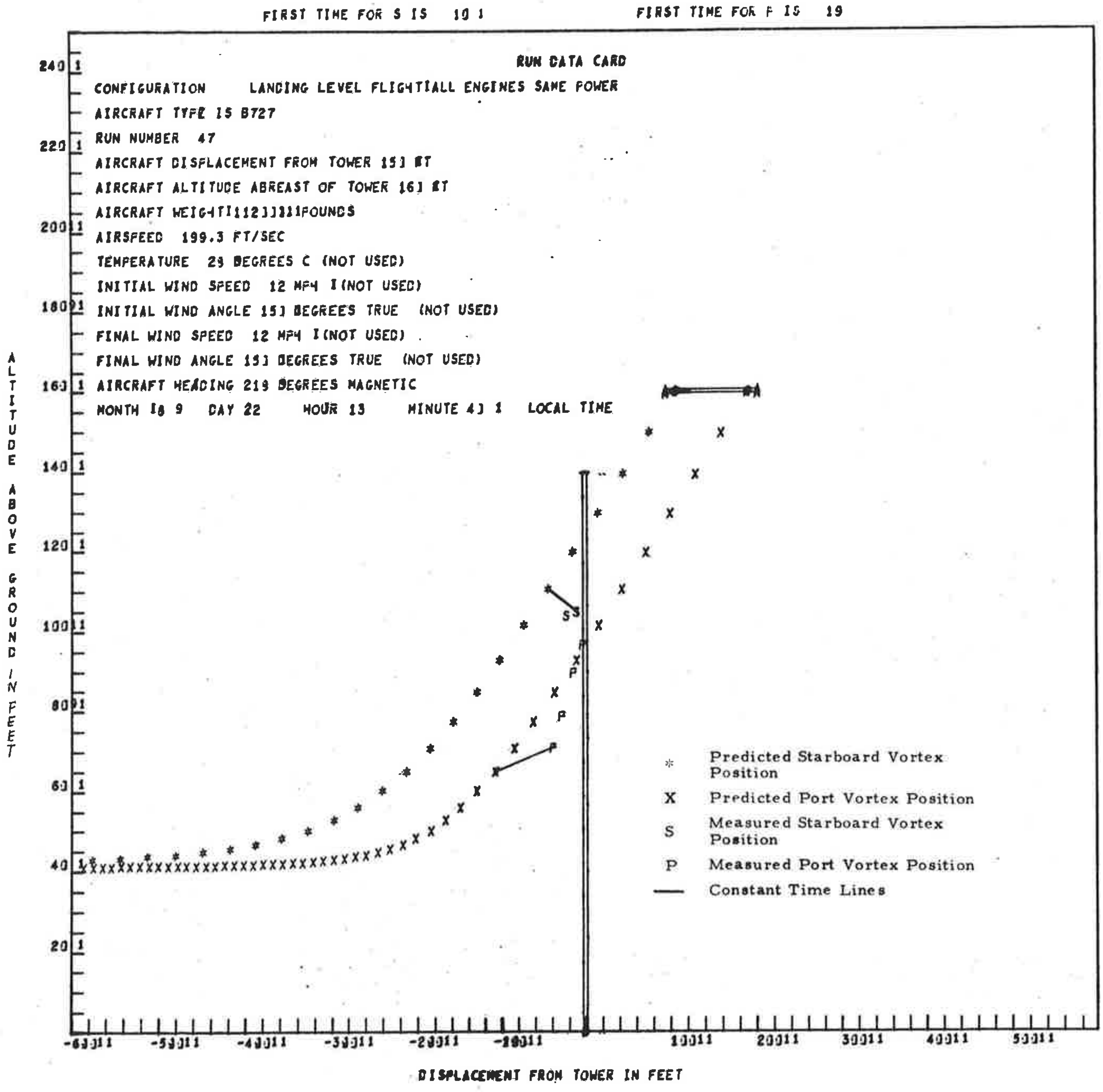

RUN DATA CARD

CONFIGURATION LANDING LEVEL FLIGHTIALL ENGINES SAME POWER
AIRCRAFT TYPE IS B727
RUN NUMBER 47
AIRCRAFT DISPLACEMENT FROM TOWER 15] FT
AIRCRAFT ALTITUDE ABREAST OF TOWER 16] FT
AIRCRAFT WEIGHTI1123]]11POUNDS
AIRSPEED 199.3 FT/SEC
TEMPERATURE 23 DEGREES C (NOT USED)
INITIAL WIND SPEED 12 MPH I(NOT USED)
INITIAL WIND ANGLE 15] DEGREES TRUE (NOT USED)
FINAL WIND SPEED 12 MPH I(NOT USED)
FINAL WIND ANGLE 15] DEGREES TRUE (NOT USED)
AIRCRAFT HEADING 219 DEGREES MAGNETIC
MONTH IS 9 DAY 22 HOUR 13 MINUTE 4] 1 LOCAL TIME

Fig. 5-41 - Comparison of Predicted Vortex Track with Photographic Data for B727 Aircraft Flyby 47 on 22 September 1972

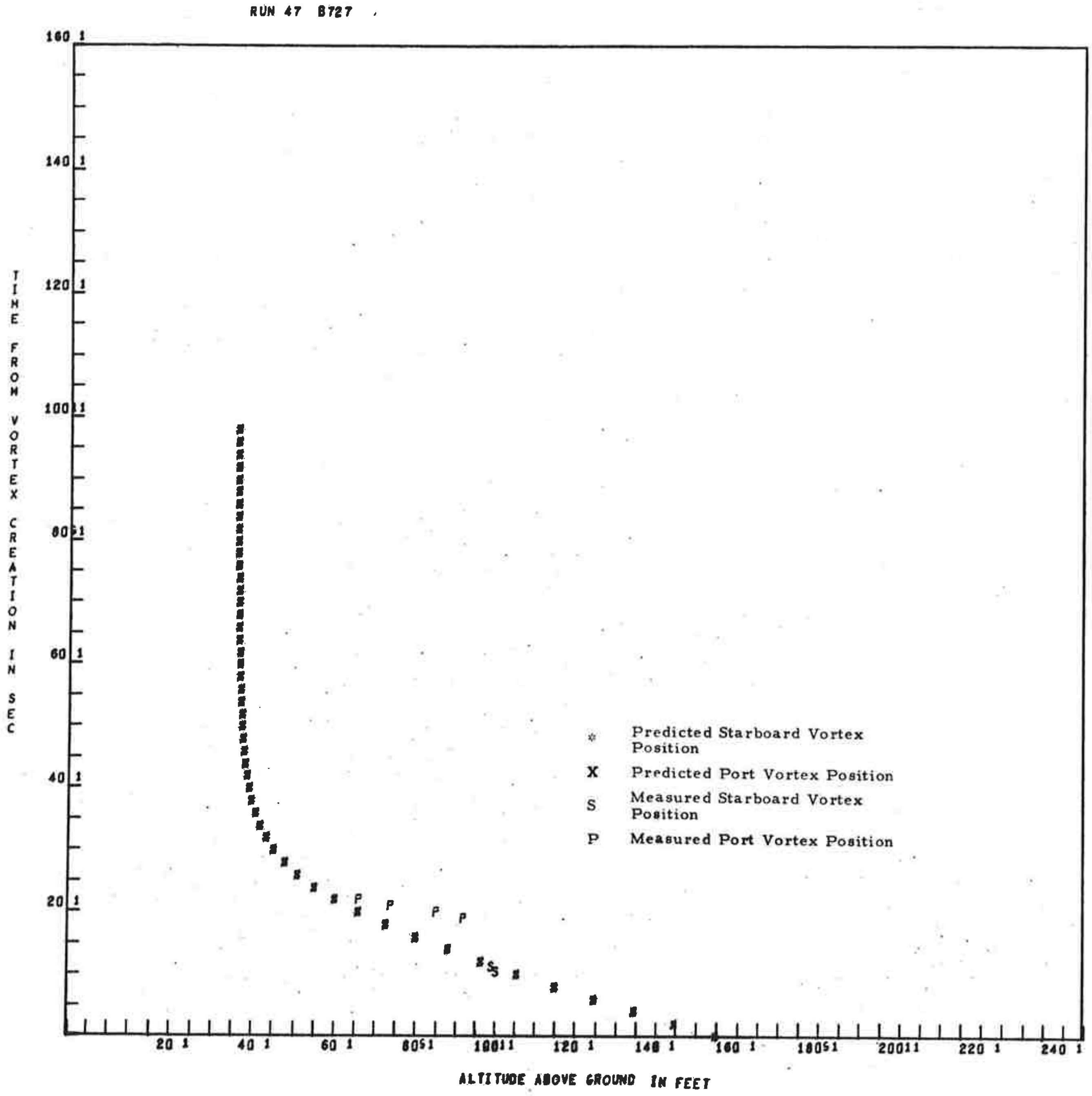

Fig. 5-42 - Comparison of Predicted and Measured Vortex Altitude for a B-727 Aircraft Flyby 47 on 22 September 1972

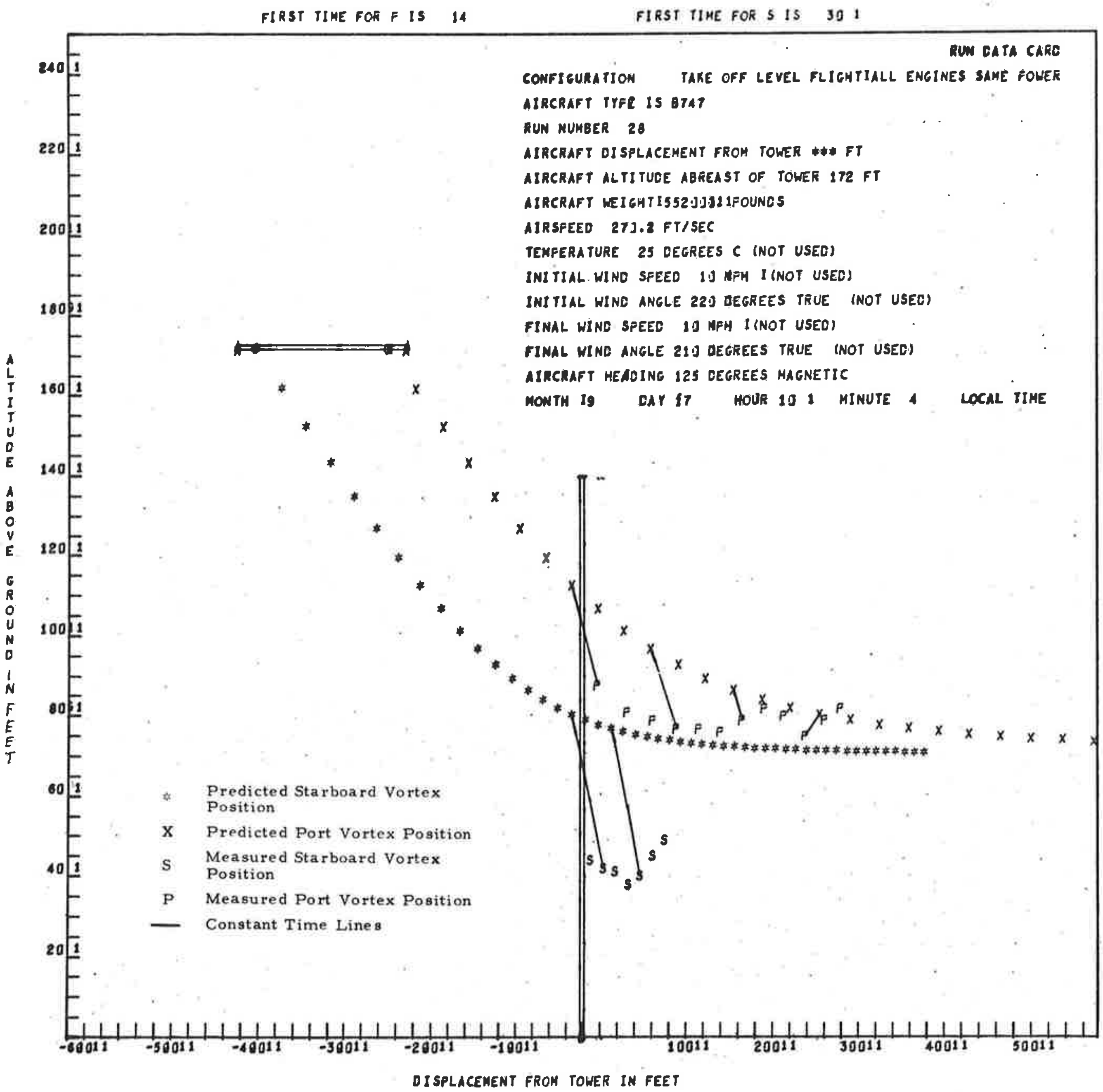

```
                                                        RUN DATA CARD
CONFIGURATION     TAKE OFF LEVEL FLIGHTIALL ENGINES SAME POWER
AIRCRAFT TYPE IS B747
RUN NUMBER  28
AIRCRAFT DISPLACEMENT FROM TOWER *** FT
AIRCRAFT ALTITUDE ABREAST OF  TOWER 172 FT
AIRCRAFT WEIGHTI55200011POUNDS
AIRSPEED  270.2 FT/SEC
TEMPERATURE  25 DEGREES C (NOT USED)
INITIAL WIND SPEED  10 MPH I(NOT USED)
INITIAL WIND ANGLE 220 DEGREES TRUE  (NOT USED)
FINAL WIND SPEED  10 MPH I(NOT USED)
FINAL WIND ANGLE 210 DEGREES TRUE  (NOT USED)
AIRCRAFT HEADING 125 DEGREES MAGNETIC
MONTH I9     DAY 17     HOUR 10 1   MINUTE  4     LOCAL TIME
```

Fig. 5-43 - Comparison of Predicted Vortex Track with Photographic Data for B747 Aircraft Flyby 28 on 17 September 1972

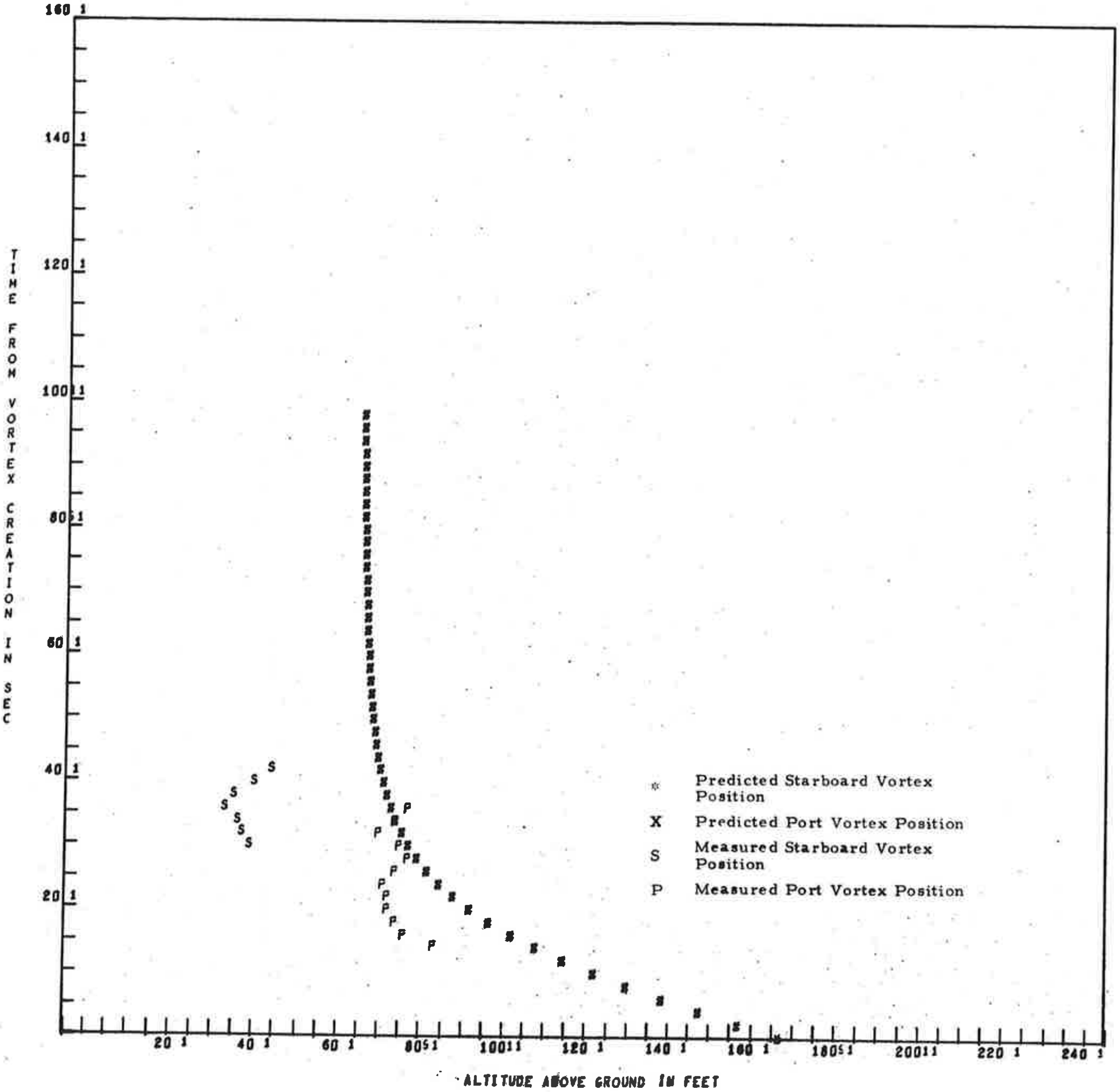

Fig. 5-44 - Comparison of Predicted and Measured Vortex Altitude for a B-747 Aircraft Flyby 28 on 17 September 1972

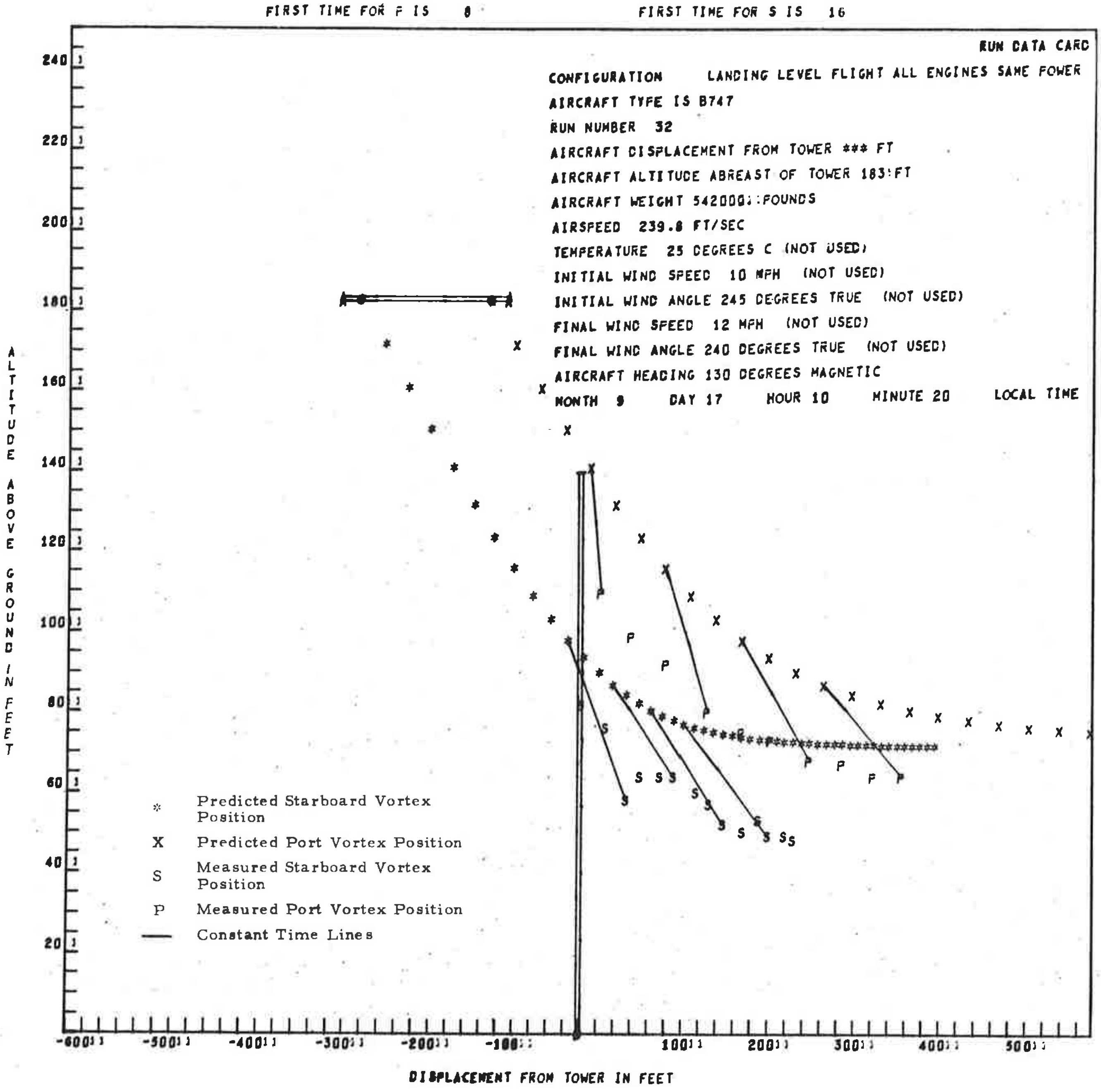

Fig. 5-45 - Comparison of Predicted Vortex Track with Photographic Data for B747 Aircraft Flyby on 17 September 1972

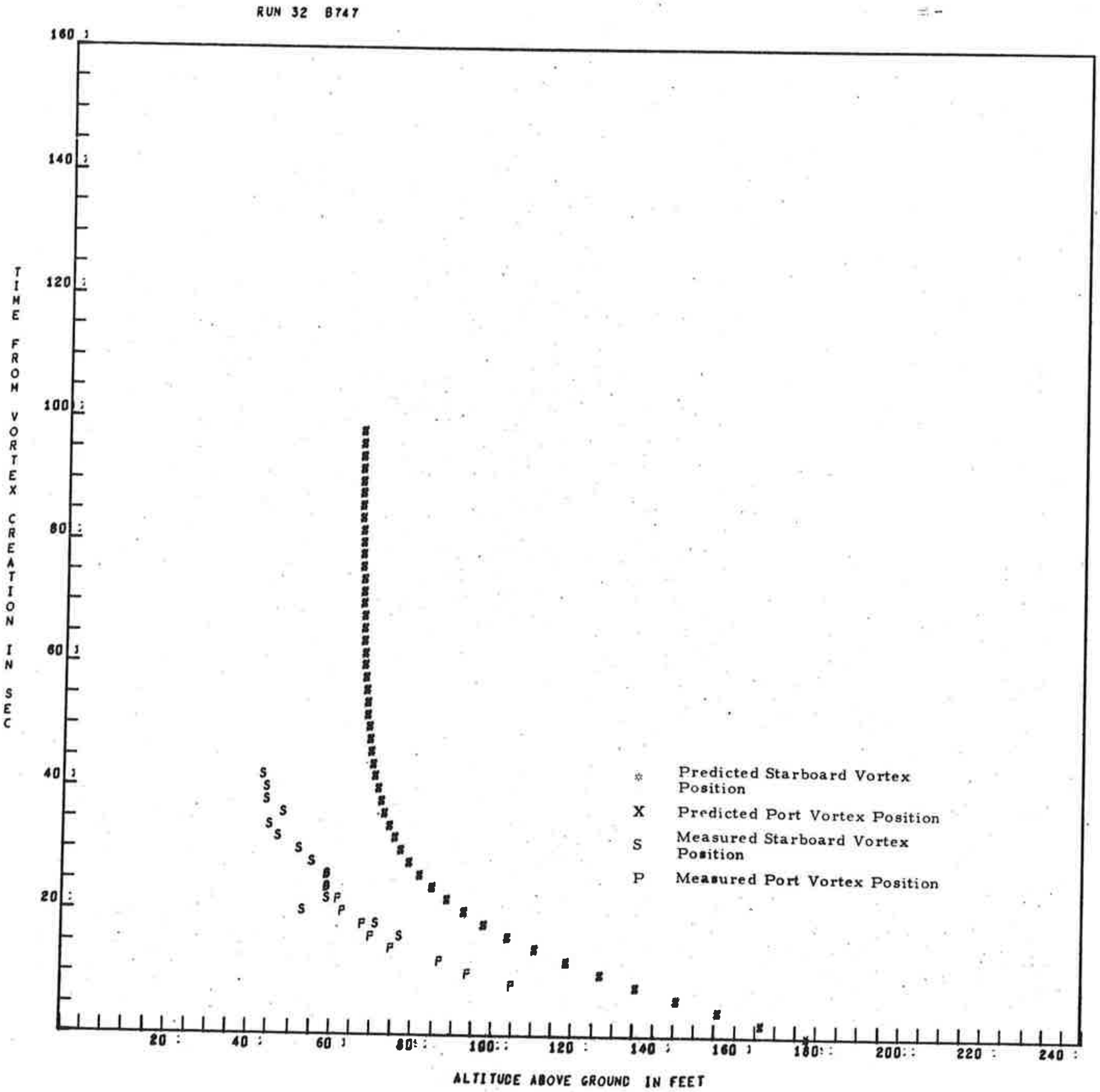

Fig. 5-46 - Comparison of Predicted and Measured Vortex Altitude for a B-747 Aircraft Flyby on 17 September 1972

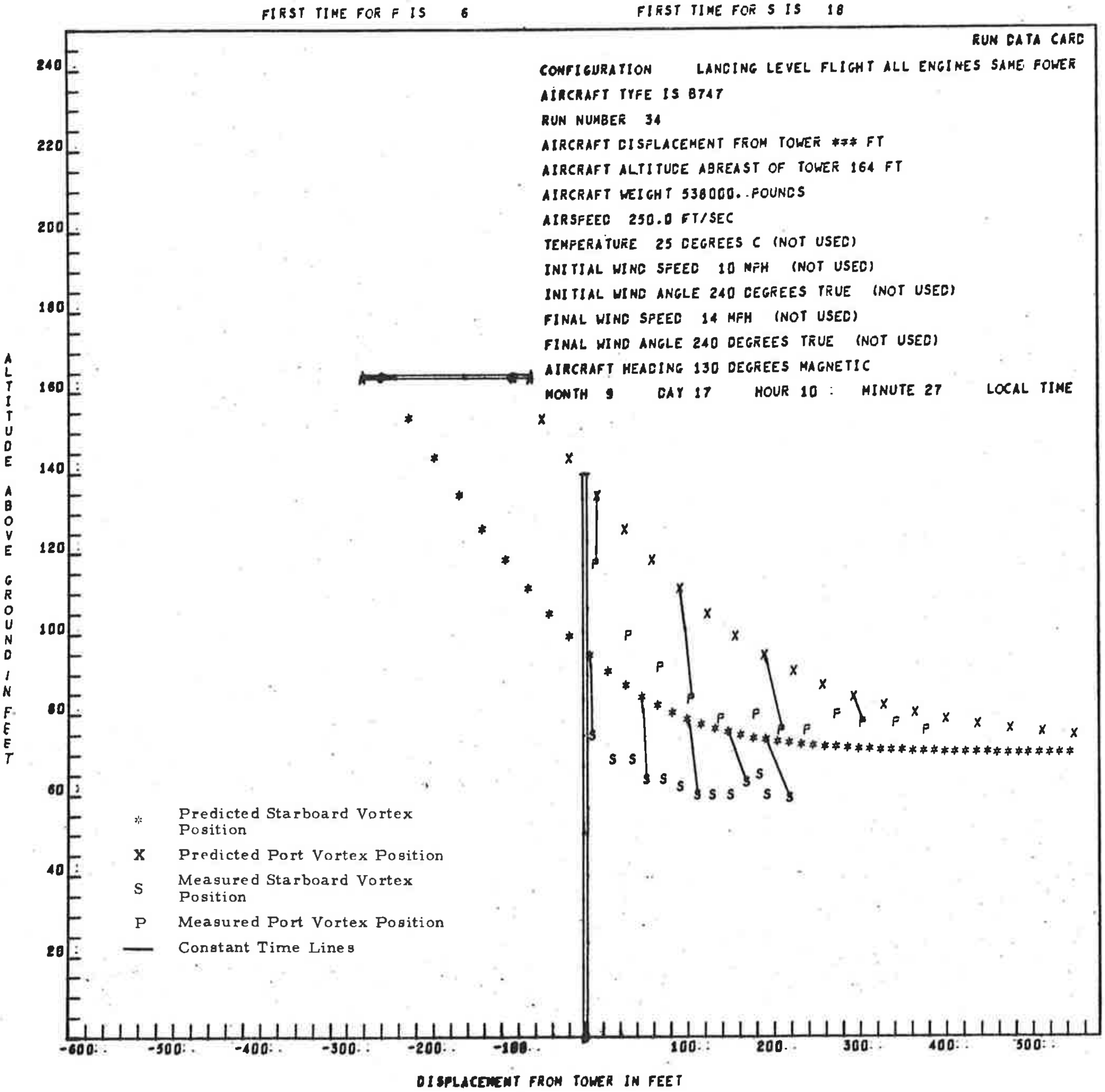

Fig. 5-47 - Comparison of Predicted Vortex Track with Photographic Data for B747 Aircraft Flyby 34 on 17 September 1972

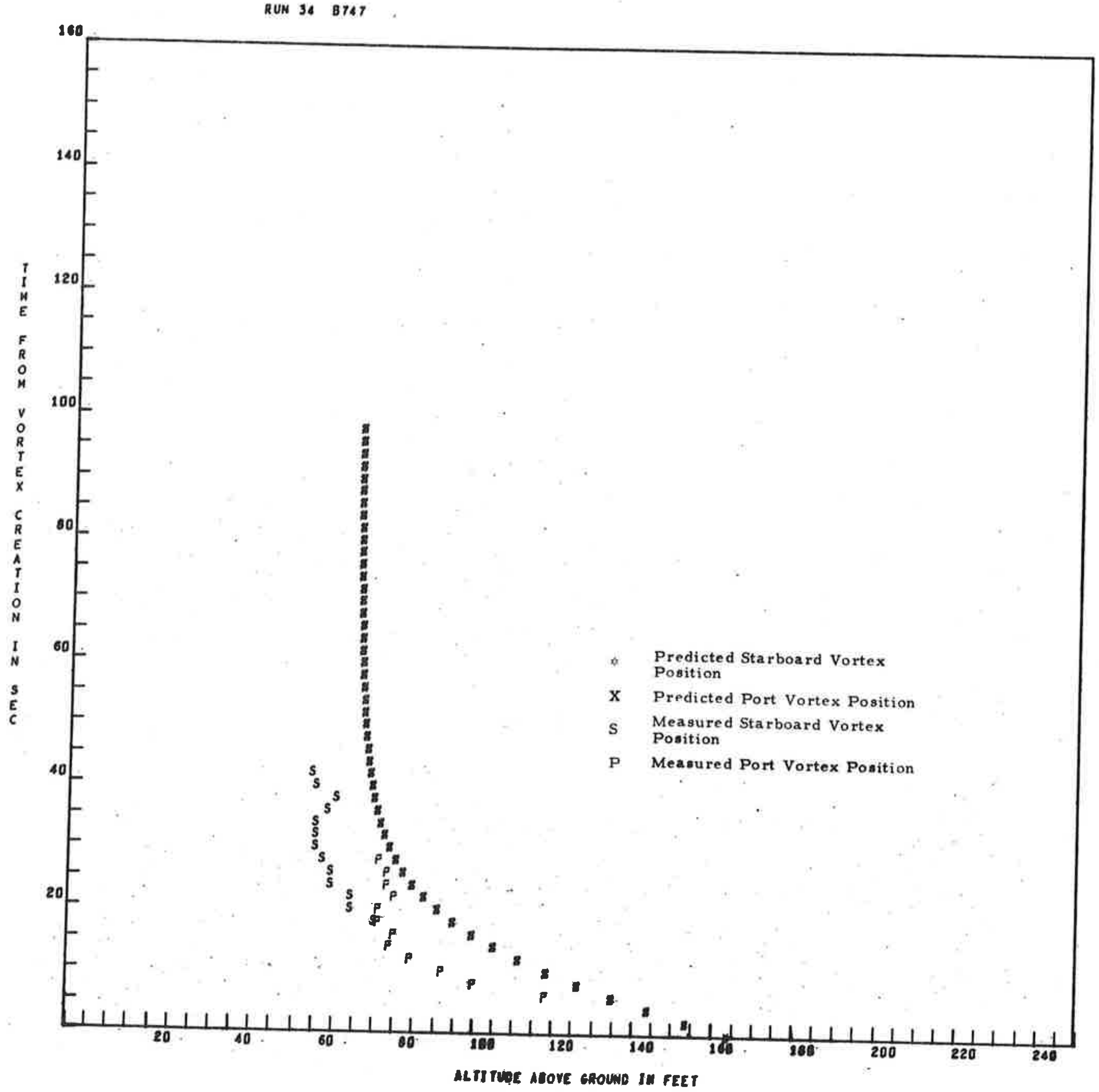

Fig. 5-48 - Comparison of Predicted and Measured Vortex Altitude for a B747 Aircraft Flyby 34 on 17 September 1972

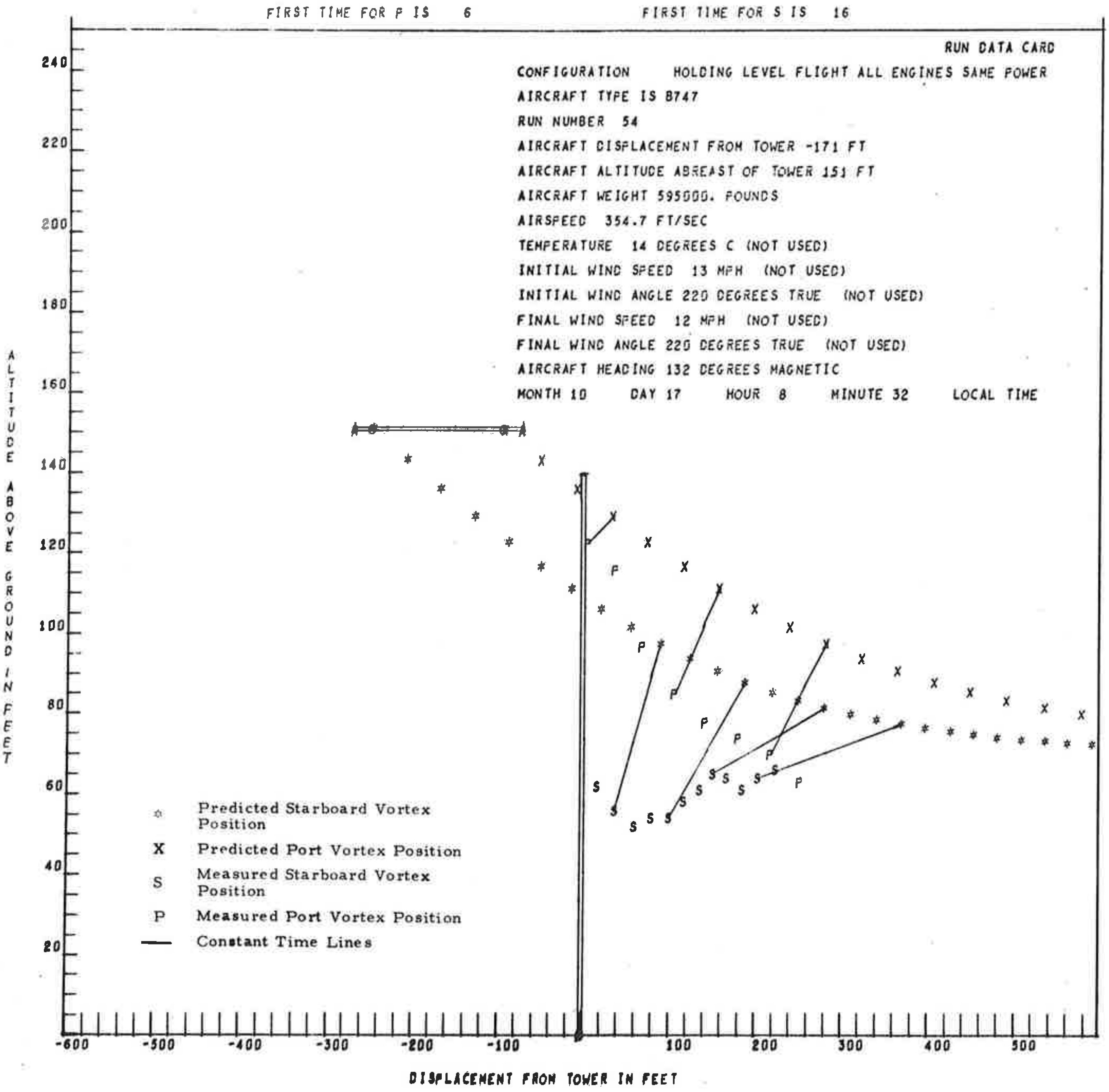

Fig. 5-49 - Comparison of Predicted Vortex Track with Photographic Data for B747 Aircraft Flyby on 17 October 1972

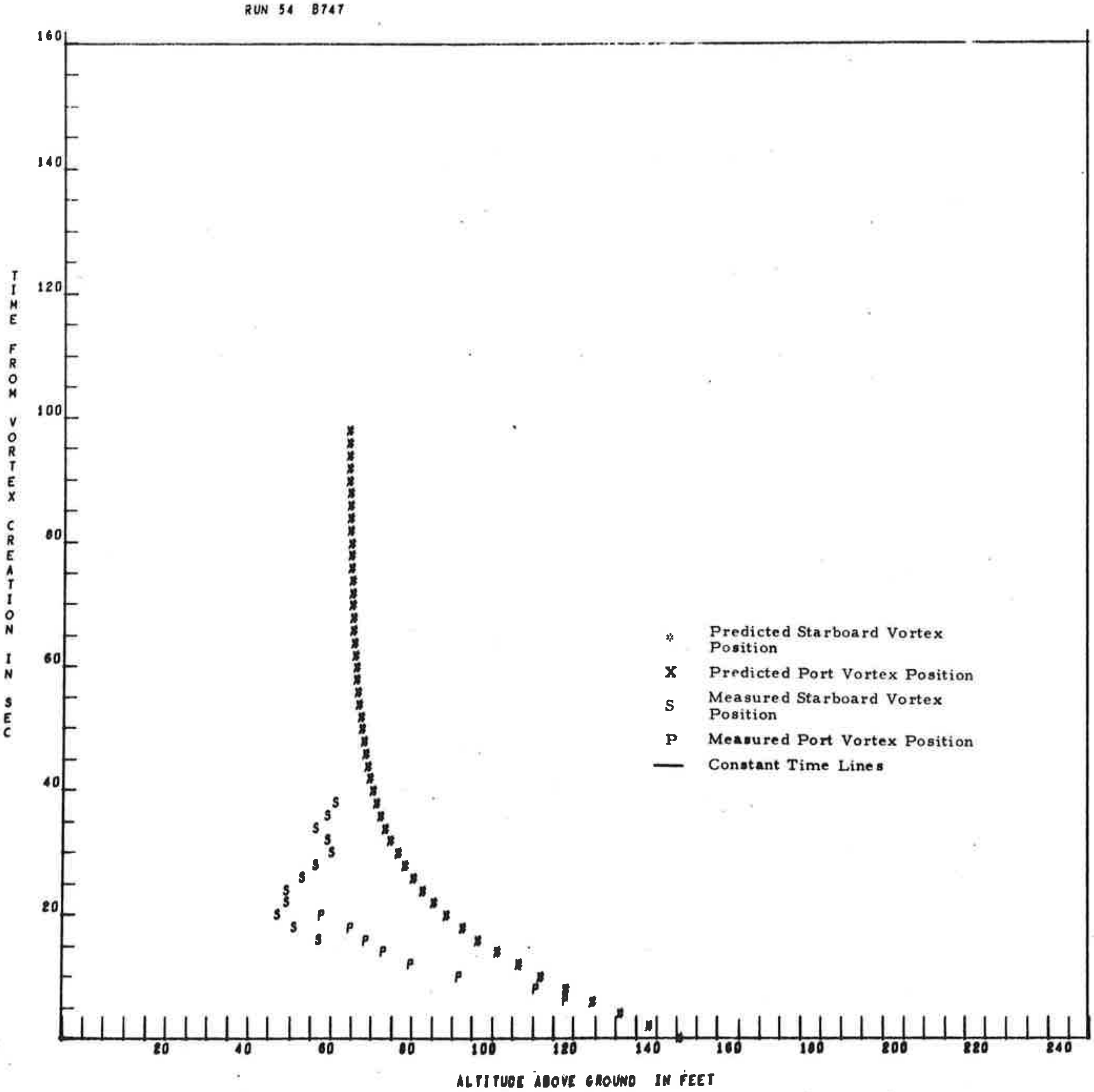

Fig. 5-50 - Comparison of Predicted and Measured Vortex Altitude for a B747 Aircraft Flyby on 17 October 1972

5.5 DETERMINATION OF WIND SHEAR

Wind speed and direction were measured at five different heights above the surface (23, 45, 70, 100 and 140 feet) by NAFEC during each aircraft flyby of the sensor tower. The vertical gradient of wind speed (z being positive from surface to space) is defined as the wind shear.

To uncover possible correlations that might exist between wind shear and vortex transport movement, $\Delta u/\Delta z$ was determined for each of the ten combinations of differences between two heights. These computations were made for each aircraft flyby where data were available and were based on only speed (not direction) in this first case. Histograms of the magnitudes of each of the ten computed wind shears were prepared for all runs. It was found that a significant difference existed between the standard deviation of the wind shear taken between any two consecutive heights. Therefore, if a correlation could be made between wind shear and uncertainty in predictive vortex tracks over this range, one should not assume that this correlation could be based on a computed wind shear between only two given heights. Bar graphs illustrating the wind shear magnitude versus the chronological order of data runs were also plotted for each positive height difference combination. Next, the component of each horizontal wind speed perpendicular to the aircraft flight path was computed by using the measured wind direction in conjunction with the aircraft heading for each run. The wind directions at each level indicated the presence of the Ekman spiral effect although the discontinuity of the measured directions in the majority of the cases suggests that there may be somewhat of a significant experimental uncertainty. Subsequent development of the theoretical spiral based on other available input parameters may assist in resolving this question. Histograms and bar graphs analogous to those plotted for total wind shear were prepared for component shear. The standard deviations of the component wind speed magnitudes are larger than in the non-component case.

5.6 EFFECT OF EKMAN SPIRAL ON CROSS-RUNWAY WIND PROFILE

The Ekman spiral effect causes the wind direction to rotate in the clockwise or counterclockwise direction as a function of increasing height in the northern and southern hemispheres, respectively. Therefore, not only knowledge of the absolute wind profile is important to the vortex problem, but the knowledge of the wind direction at every height is likewise important. This is especially true when a wind profile must be determined for a given constant direction of interest. For example, if the cross runway or perpendicular to flight path wind profile is essential in determining vortex behavior, then the product of the wind speed and the sine (or cosine) function of the wind direction and flight path difference must be approximately computed for every height between the ground and the height of generation of the vortices.

The magnitude of the wind with respect to height in the cross runway direction is important in establishing the cross runway wind shear between particular heights. Moreover, when at some height within the range of interest the wind direction is along or nearly along the flight path, the cross runway wind direction will change with respect to height. That is, the cross runway component will exhibit a 180-degree change in direction at one or more heights above the surface. Therefore, if wind direction is measured at one height, it is not necessarily true that the vortex displacement will be to that side of the runway which the measured direction indicates. This effect is illustrated in Figs. 5-51 through 5-53 for Run 41 (B707) on 1 November 1972. Figure 5-51 illustrates the measured absolute wind profile. Figure 5-52 illustrates the measured variation in direction with height. Note that the wind happens to be along the runway at a height somewhere between 45 and 100 feet. (This could just as easily have been the case at the standard airport anemometer height.) Figure 5-53 illustrates the cross runway wind velocity. Note that the direction changes between 45 and 70 feet and the magnitude range is from 10 feet per second in one direction to 20 feet per second in the other. Thus the difference between the absolute wind profile and the Ekman spiral produced cross-runway wind profile indicates that neglecting the effect of varying wind direction with height can produce serious errors.

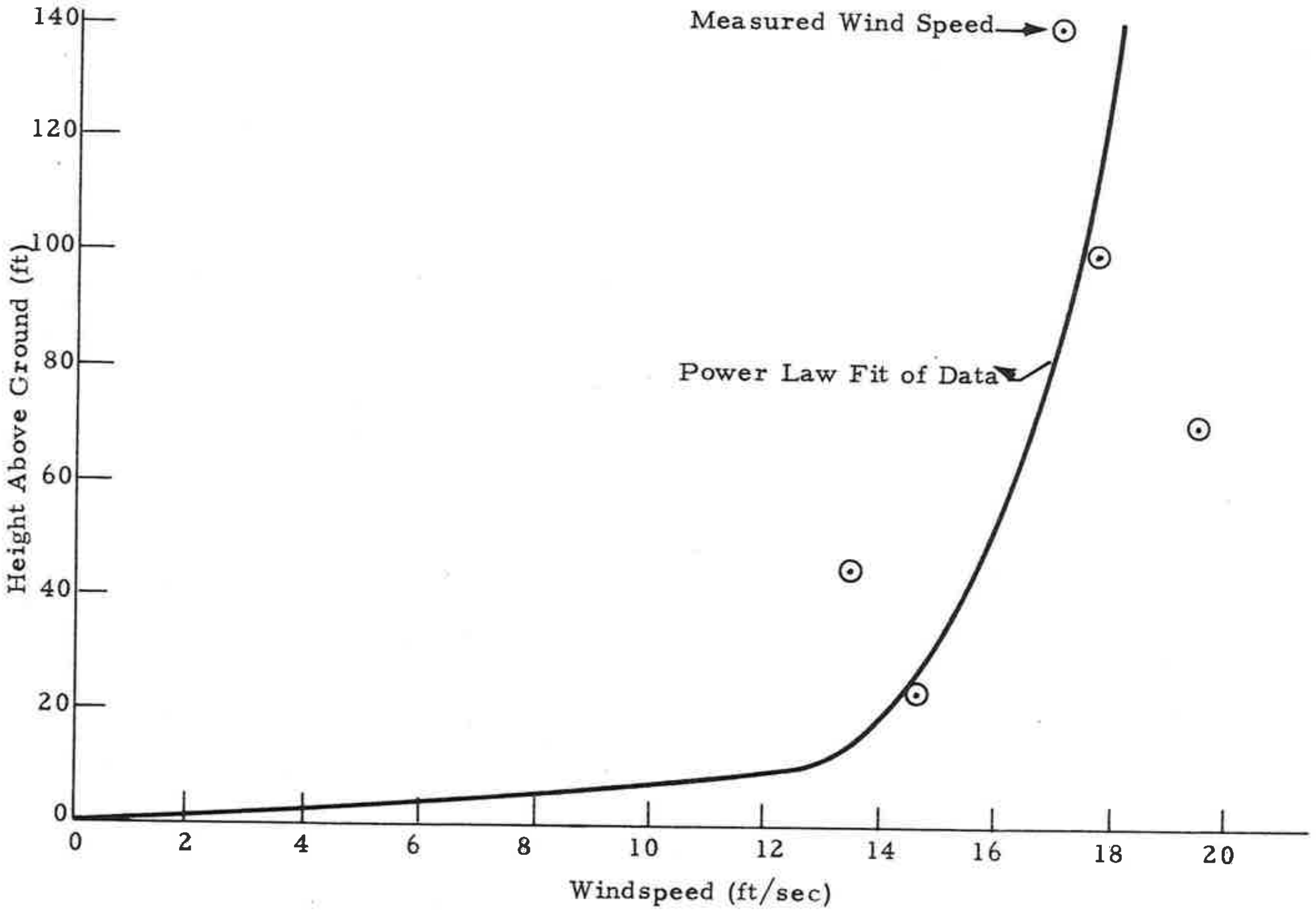

Fig. 5-51 - Total Wind Profile for Run 41 (B707) on 1 November 1972

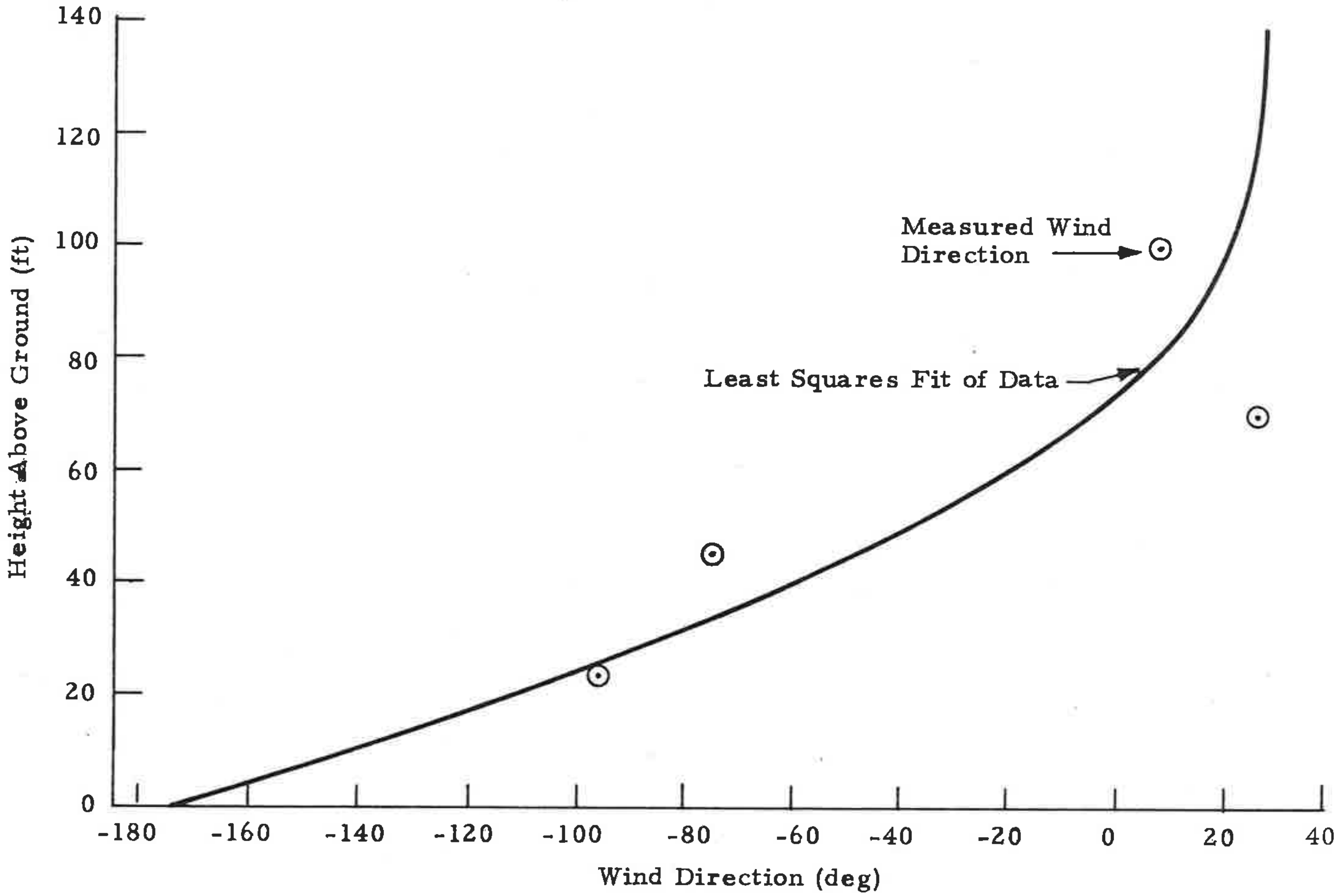

Fig. 5-52 - Wind Direction vs Altitude Depicting Ekman Spiral Effect for Run 41 (B707) on 1 November 1972

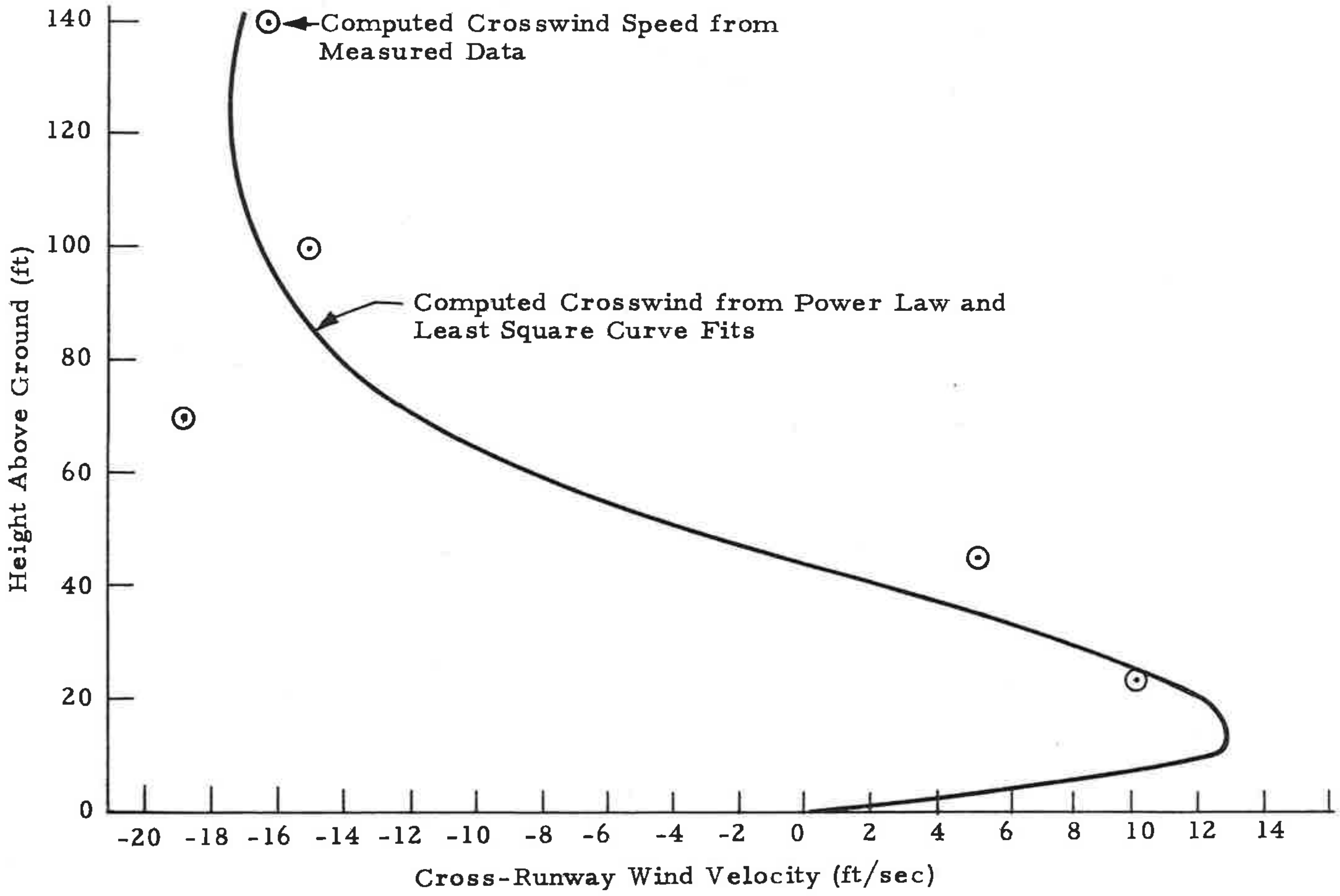

Fig. 5-53 - Cross Runway Component Profile Showing Flow Reversal Due to the Ekman Spiral Effect (Run 41 (B707) on 1 November 1972)

5.7 ANALYSIS OF VORTEX TILTING COMPUTED BY PHOTOGRAPHIC DATA REDUCTION

It was hypothesized that some correlation of vortex tilting (rotation rate of line connecting the two vortices) might exist with the wind shear as previously discussed. This line, at any given time, forms an angle, θ, with the horizontal ground plane. The following quantities were computed from the photographic data:

- Rotation rate where two or more common time points exist for the port and starboard vortices ($d\theta/dt$, positive in counterclockwise direction).
- Maximum rotation rate for each run with three or more common time points.
- Mean values of the above quantities.

Correlations were attempted with each of these calculated quantities with total wind shear, component wind shear (both with and without considering variations between height combinations) and temporal wind shear gradients as computed from the before and after winds. Some of these results are shown in Figs. 5-54 through 5-56.

The maximum rotation angle (θ_{max}) for each of the runs is plotted in Fig. 5-54 versus the approximate cross runway wind shear ($\partial v/\partial z$) that exists at the beginning of the run in the range of height which bounds the heights of the pair of vortices. The sign of the angle is chosen to be a negative value for the case of the downwind vortex rising and positive when the upwind vortex rises. There is somewhat of a trend for the upwind vortex to rise in heavy shear and the downwind vortex to rise in light shear as seen from the data in Fig. 5-54. The two runs deviating from this trend (Runs 13 and 18) the greatest are shown in Appendix G. Run 18 photographic data show a violent up and down motion (almost a V shape) at 45 seconds. Thus rotation in both directions occurred and a vertical velocity effect should be considered to explain this unusual motion as the upwind vortex would have been higher if this reversal would not have occurred. Run 13 photographic data indicate a vortex spacing of only 60 feet after 30 seconds. This also is an unusual

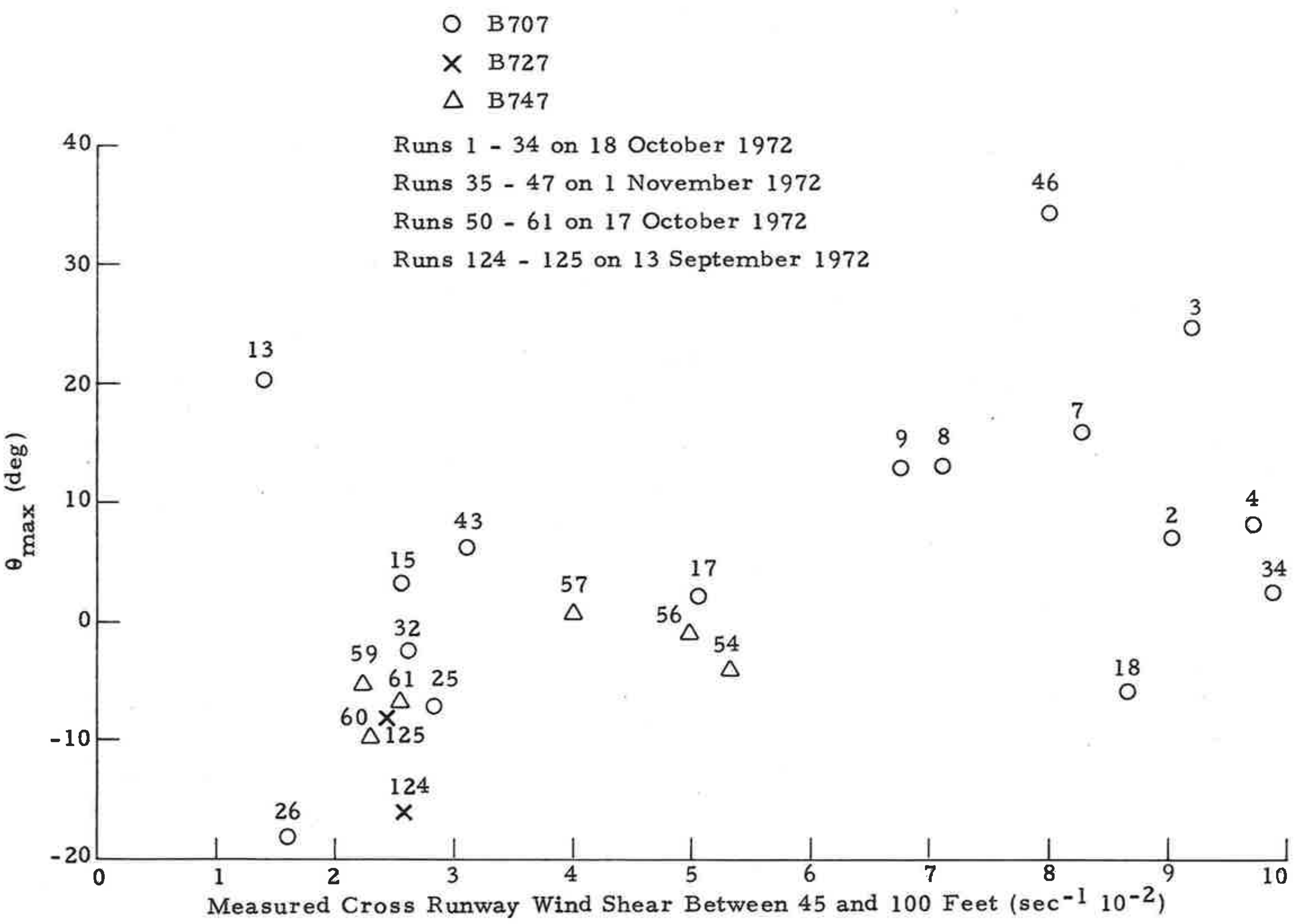

Fig. 5-54 - Vortex Tilting vs Wind Shear

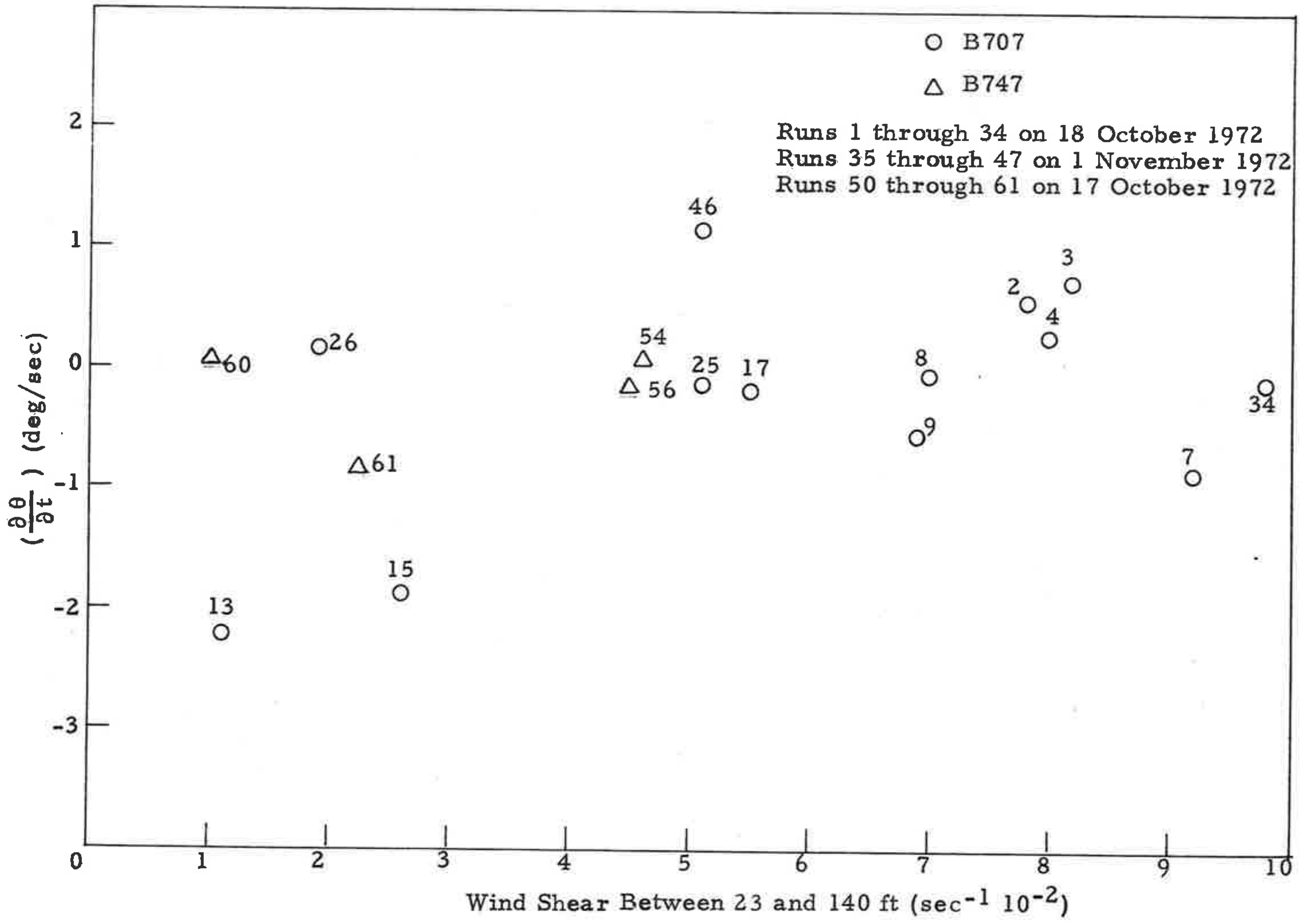

Fig. 5-55 - Mean Rotation Rate vs Cross Runway Wind Shear Between 140 and 23 Feet

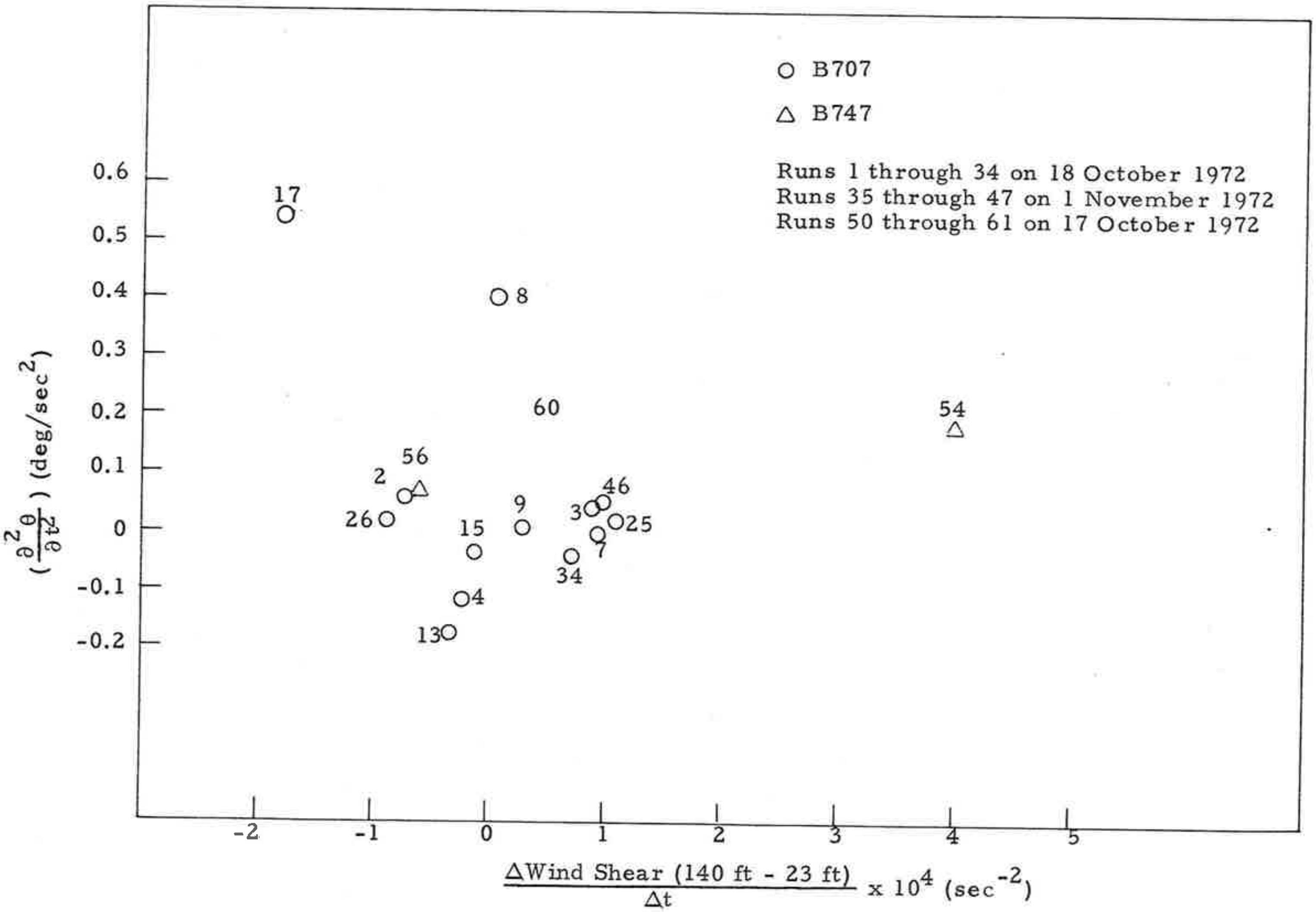

Fig. 5-56 - Rotation Acceleration vs Rate of Change of Cross Runway Wind Shear trend; this might be explained by significant horizontal shear. In any event the two runs failing to adhere to the conclusion that the upwind vortex rises in heavy shear while the downwind vortex rises in light shear appears to be affected by secondary factors which produce "unusual motions." Figure 5-55 is a plot of the mean rotation rate ($\partial \theta / \partial t$) for each of these runs versus the cross runway wind shear existing between 23 and 140 feet at the beginning of the runs. Figure 5-56 illustrates the rate of change of rotation ($\partial^2 \theta / \partial t^2$) for each of the runs versus the approximate change in cross-runway wind shear over a period which varies from 3 to 8 minutes.

There appears to be less conclusive information contained in these last two plots compared to Fig. 5-54 even though the data in Fig. 5-55 appear to be consistent with the previous conclusion of the effect of wind shear on vortex tilting.

Figure 5-57 shows the effect of considering the Richardson number as the independent parameter. Here again there appears to be a distinct trend in the data in that an increasing Richardson number appears to cause the upwind vortex to rise.

It should be understood that for a valid conclusion to be drawn as to the relation of these two isolated variables:

1. A statistically acceptable number of observations should be made, and
2. The temporal aspect of the problem must be brought into its proper perspective. That is, the wind shear which exists at the time that the rotation rate is computed is clearly not detectable via the presently available data.

Thus at this point only a tentative conclusion can be drawn. This concept is pursued in Section 6.

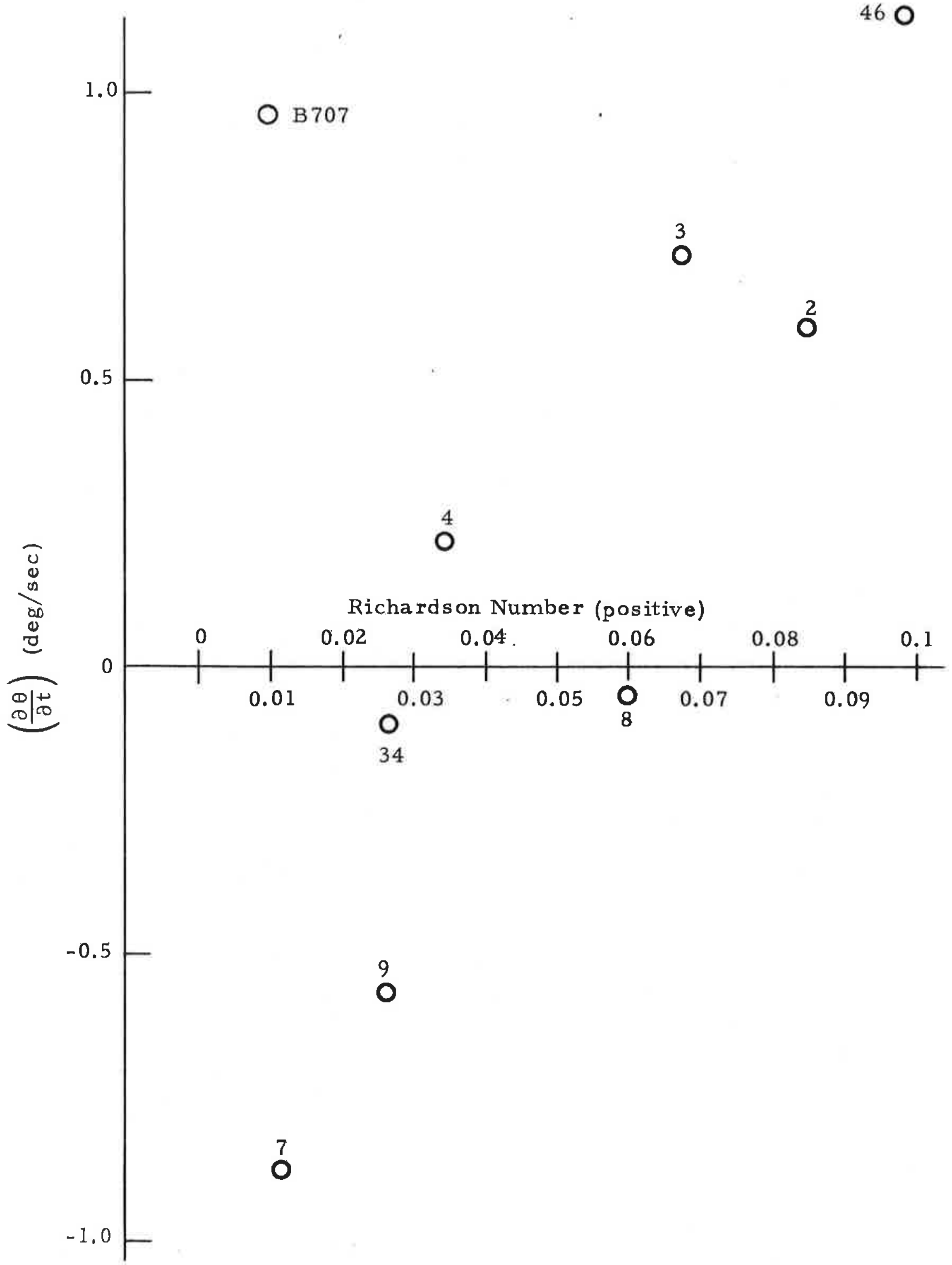

Fig. 5-57 - Mean Rotation Rate vs Richardson Number Between 23 and 140 Feet

5.8 COMPARISON OF PREDICTED VORTEX SEPARATION WITH MEASURED SEPARATION

The actual vortex pair sink rate has been shown to be somewhat greater than the predicted rate based on elliptical loading assumptions. This can be shown to be a result of a decreased separation between the vortices, which is probably due to the effects of a "dirty" wing. The obvious comparison to ascertain the actual decrease in separation is to plot the separation of the vortices for both prediction and measurement versus time.

This type of comparison is shown in Fig. 5-58 for Run 56 (B747) on 17 October 1973. This plot indicates a predicted separation greater than observed for all times; however, a plot removing the varying effect of the ground plane would be more quantitative. This is because at the same instant of time, two different effects due to ground plane are inherent in the data as the predicted and measured vortex altitudes are unequal. Thus it is postulated that this situation can be somewhat improved by considering a comparison of predicted and measured separation versus altitude. This result is shown in Fig. 5-59.

Even though this type of comparison removes the ground plane as a parameter, some difficulty is still associated with determining the decrease in separation accurately. This is due to the area of interest being the region of largest gradient, i.e., small changes in vortex altitude produce large changes in vortex separation. All of the photographic data are obtained in this region due to the height of the tower and size of the aircraft used in the tests. For example, a 5-foot uncertainty in the measured vortex altitude produces a 30-foot difference in the predicted altitude. This makes any empirical relation difficult. However, if one uses both comparisons as discussed here to determine the decrease in separation due to nonelliptical loading, these difficulties might be minimized. Using this criteria for the run of interest, one would obtain approximately a 10% decrease in separation based on separation versus time data, a 30% decrease based on separation versus altitude and maybe 20% considering both data types.

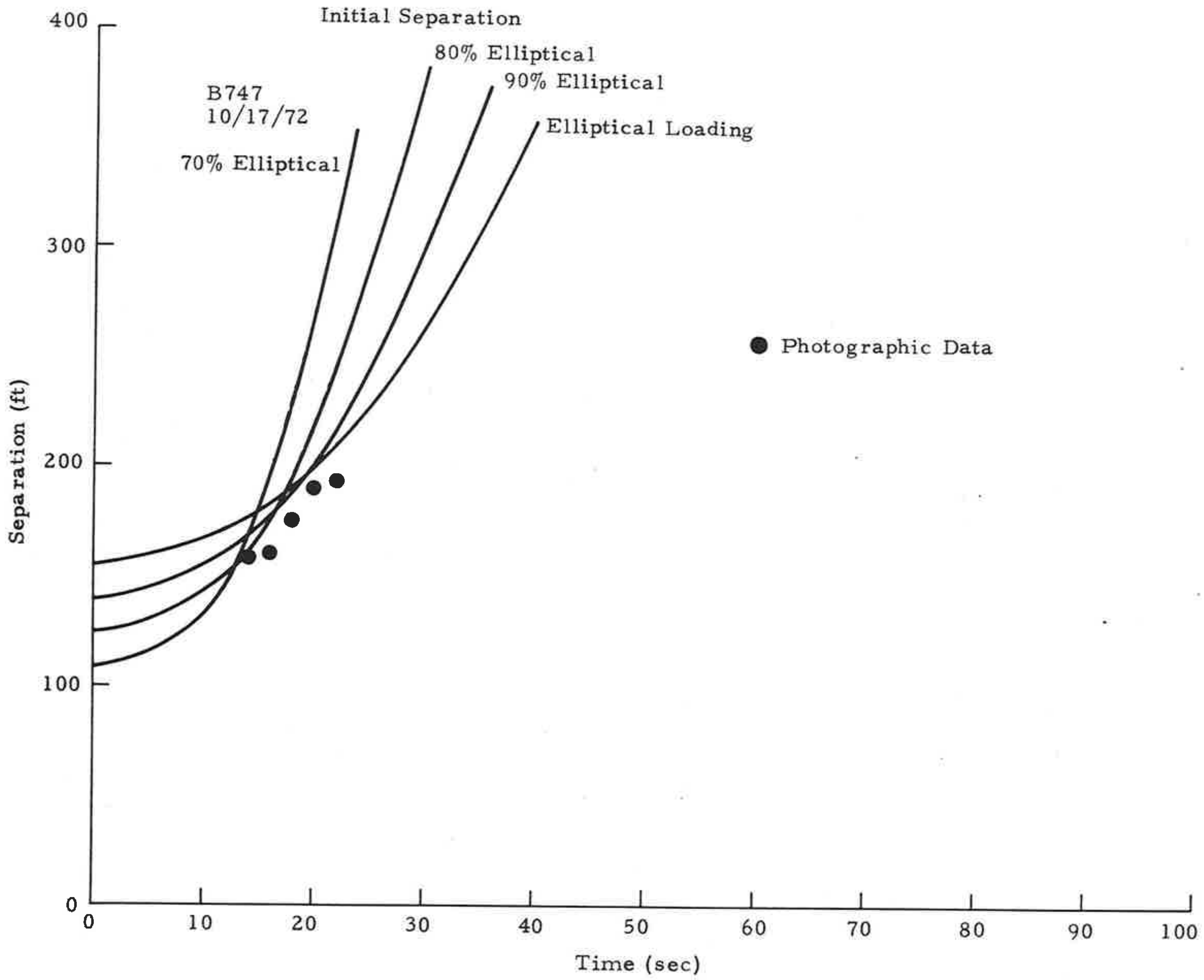

Fig. 5-58 - Comparison of Predicted and Measured Vortex Separation vs Time for Run 56 on 17 October 1972 (B747)

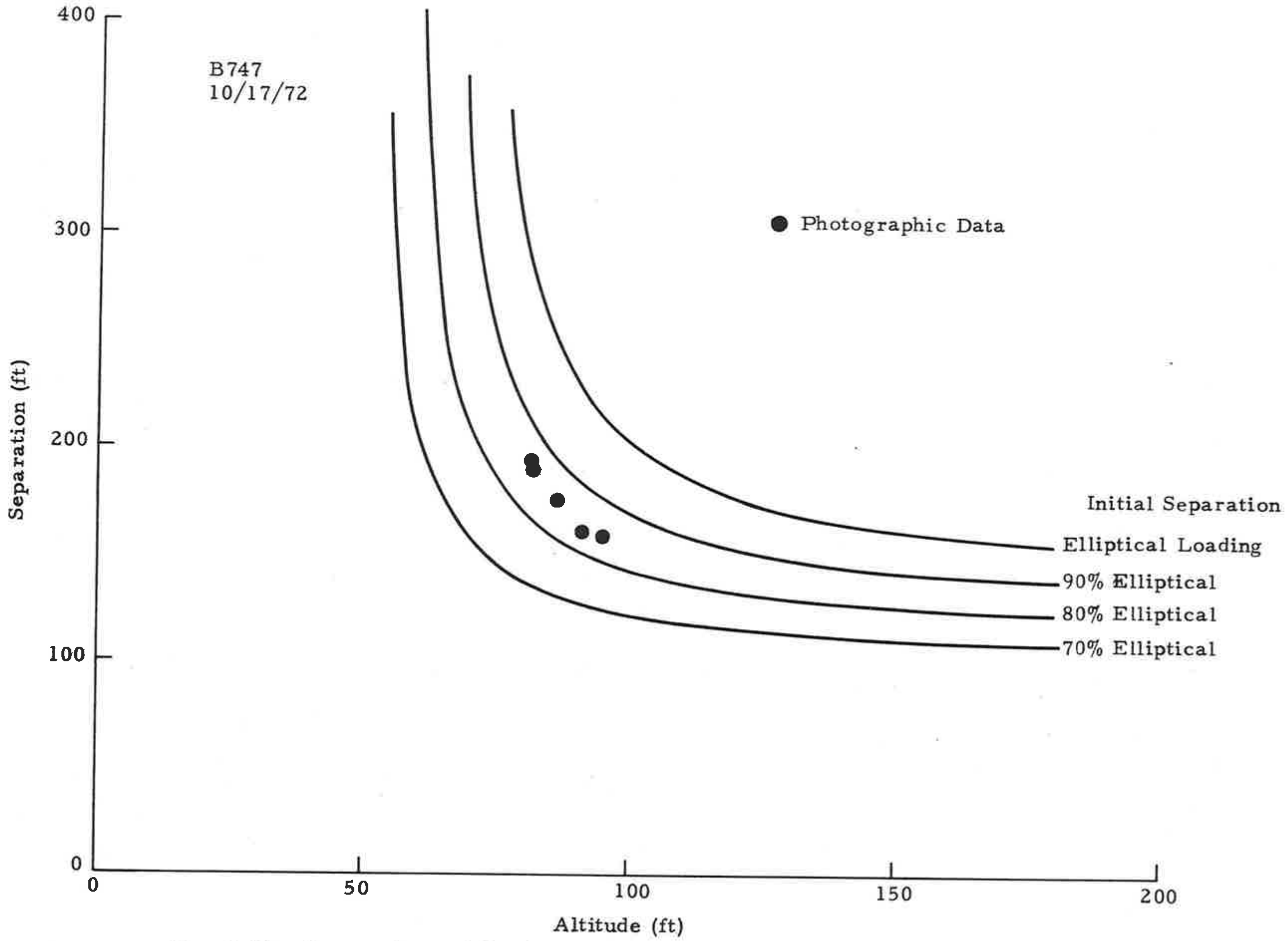

Fig. 5-59 - Comparison of Predicted and Measured Vortex Separation vs Altitude for Run 56 on 17 October 1972 (B747)

Figures 5-60 and 5-61 show the predicted vortex tracks for elliptical assumptions for Run 56. The underestimated sink rate is obvious in the cross sectional plot and altitude time plot. Figures 5-62 and 5-63 represent calculations based on a 10% reduction of vortex spacing (with appropriate increase in circulation strength to hold flight conditions constant). The results indicate that still an underprediction occurs which corresponds with the problems that pertain to using separation-time data for the empirical correlation as previously discussed. The difference, however, may be negligible.

The results corresponding to utilizing only separation-altitude information (30% reduction) are shown in Figs. 5-64 and 5-65 for the same run. These overpredictions demonstrate the difficulty in attempting to use the high gradient region for the empirical correlation. An average of 20% reduction was then assumed with the results shown in Figs. 5-66 and 5-67. Even though 20% appeared to be an "average" of the two data types, it is seen that an overprediction results when altitude-time data are considered. This implies that a value between 10% and 20% reduction in separation would be the optimum (probably less than 15%) and could realistically be determined by considering some sort of weighted (least squares) average of the range of the experimental data.

The corresponding comparisons of measured and predicted sink rates are shown in Figs. 5-68 and 5-69 for time and altitude as the independent variable, respectively. Again note the 10% reduction in separation appears to yield the best results. It should again be noted that this separation reduction is followed by an appropriate increase in circulation to hold the flight condition constant and also to preserve the proper moments of vorticity in the wake.

5.9 DISCUSSION OF CORE SIZE, MAXIMUM VELOCITY AND CIRCULATION DECAY

A discussion of calculated core size, maximum velocity and circulation decay is presented here to describe the predictive model fully. It is known that the size of the core greatly effects the usefulness of the vortex as a potential target. However, no significant effect of core size on the vortex transport has been noticed upon examination of the runs when engine power and flap setting were varied.

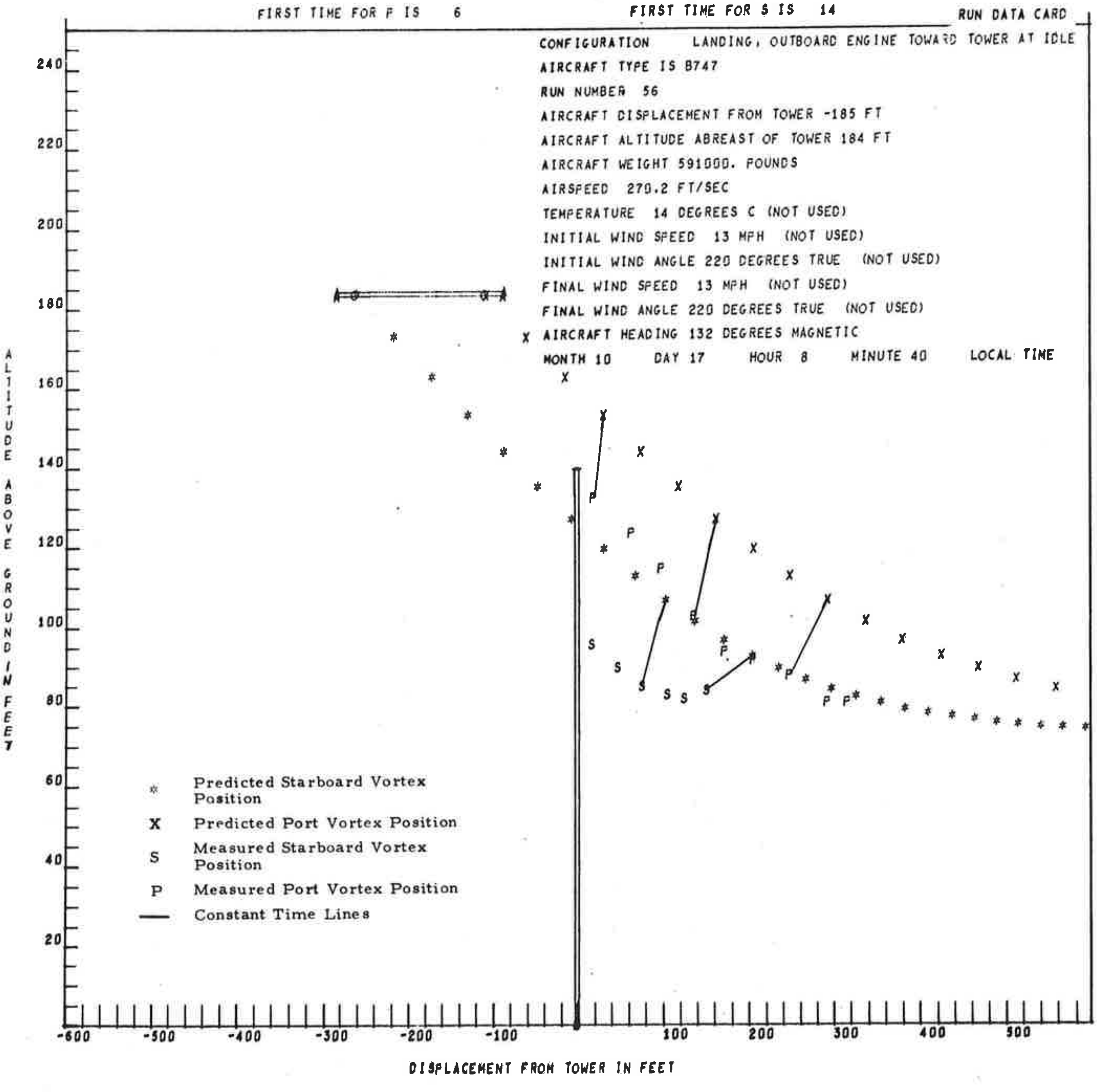
FIRST TIME FOR P IS 6

FIRST TIME FOR S IS 14

RUN DATA CARD

CONFIGURATION LANDING, OUTBOARD ENGINE TOWARD TOWER AT IDLE
AIRCRAFT TYPE IS B747
RUN NUMBER 56
AIRCRAFT DISPLACEMENT FROM TOWER -185 FT
AIRCRAFT ALTITUDE ABREAST OF TOWER 184 FT
AIRCRAFT WEIGHT 591000. POUNDS
AIRSPEED 270.2 FT/SEC
TEMPERATURE 14 DEGREES C (NOT USED)
INITIAL WIND SPEED 13 MPH (NOT USED)
INITIAL WIND ANGLE 220 DEGREES TRUE (NOT USED)
FINAL WIND SPEED 13 MPH (NOT USED)
FINAL WIND ANGLE 220 DEGREES TRUE (NOT USED)
AIRCRAFT HEADING 132 DEGREES MAGNETIC
MONTH 10 DAY 17 HOUR 8 MINUTE 40 LOCAL TIME

Fig. 5-60 - Comparison of Predicted Vortex Track with Photographic Data for B747 Aircraft Flyby 56 on 17 October 1972 (Elliptical Spacing)

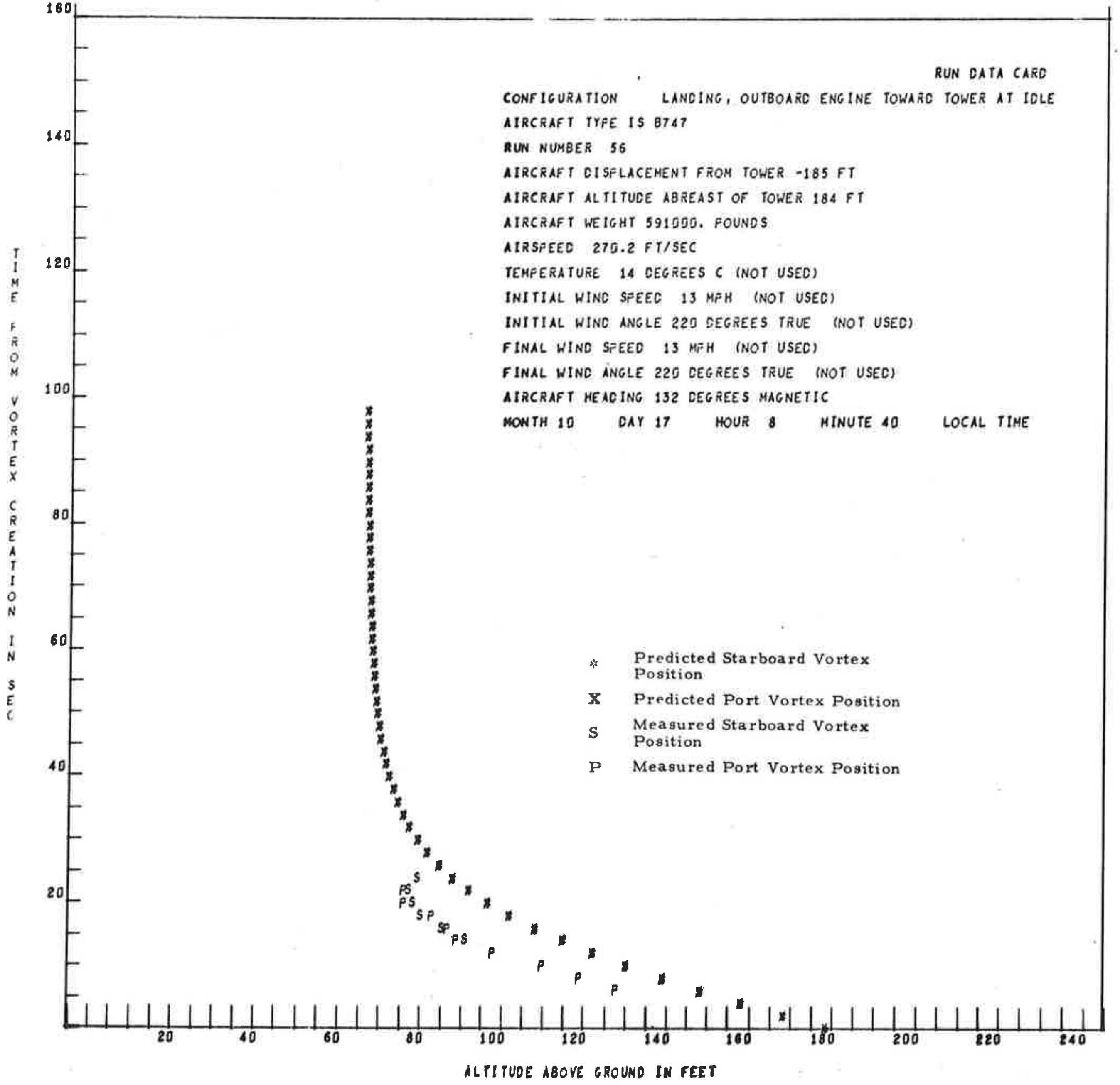

RUN DATA CARD

CONFIGURATION LANDING, OUTBOARD ENGINE TOWARD TOWER AT IDLE

AIRCRAFT TYPE IS B747

RUN NUMBER 56

AIRCRAFT DISPLACEMENT FROM TOWER -185 FT

AIRCRAFT ALTITUDE ABREAST OF TOWER 184 FT

AIRCRAFT WEIGHT 591000. POUNDS

AIRSPEED 270.2 FT/SEC

TEMPERATURE 14 DEGREES C (NOT USED)

INITIAL WIND SPEED 13 MPH (NOT USED)

INITIAL WIND ANGLE 220 DEGREES TRUE (NOT USED)

FINAL WIND SPEED 13 MPH (NOT USED)

FINAL WIND ANGLE 220 DEGREES TRUE (NOT USED)

AIRCRAFT HEADING 132 DEGREES MAGNETIC

MONTH 10 DAY 17 HOUR 8 MINUTE 40 LOCAL TIME

Fig. 5-61 - Comparison of Predicted and Measured Vortex Altitude for a B747 Aircraft Flyby on 17 October 1972 (Elliptical Spacing)

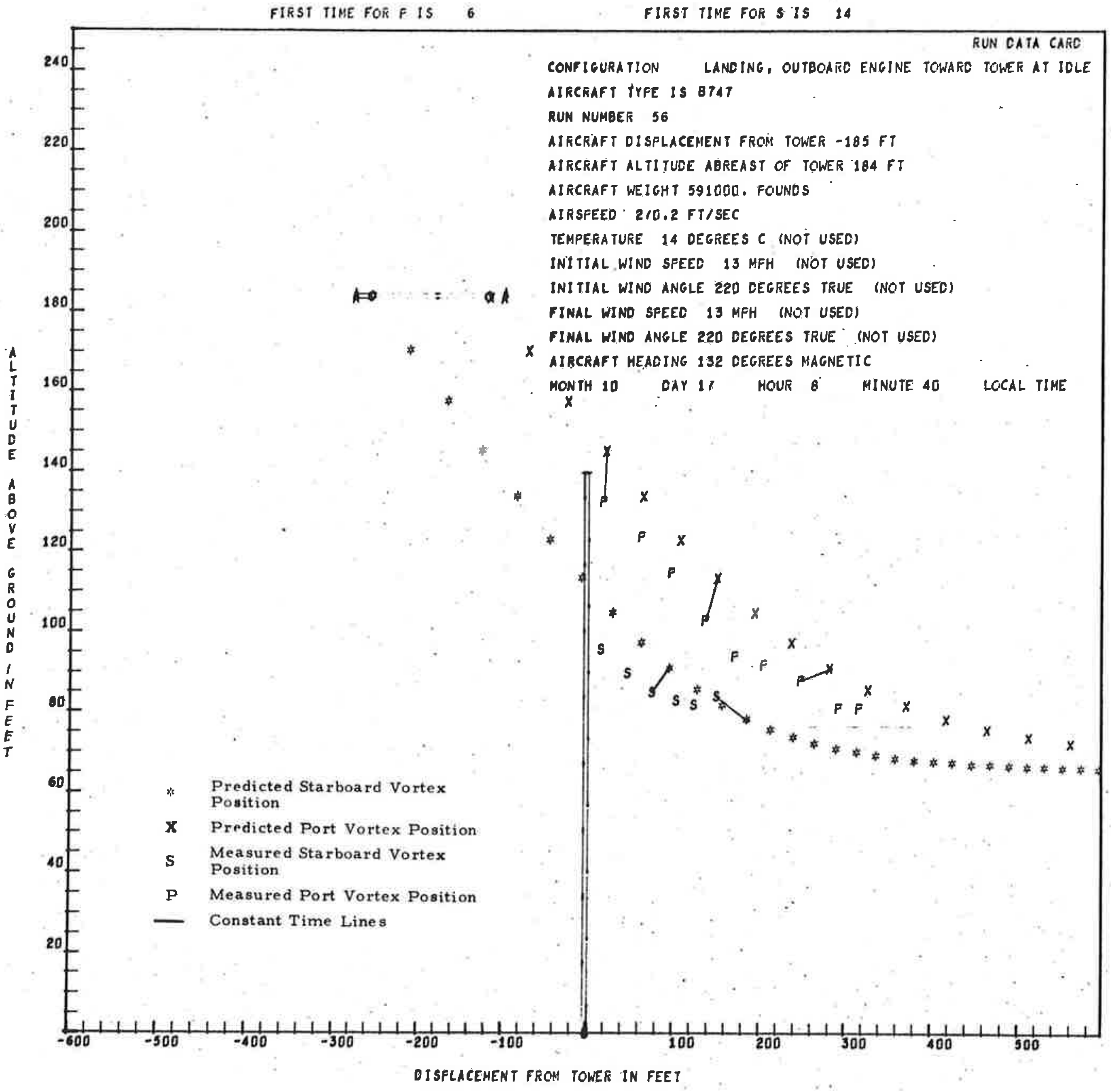

```
FIRST TIME FOR P IS     6                 FIRST TIME FOR S IS    14

                                                          RUN DATA CARD
CONFIGURATION      LANDING, OUTBOARD ENGINE TOWARD TOWER AT IDLE
AIRCRAFT TYPE IS B747
RUN NUMBER  56
AIRCRAFT DISPLACEMENT FROM TOWER -185 FT
AIRCRAFT ALTITUDE ABREAST OF TOWER 184 FT
AIRCRAFT WEIGHT 591000. FOUNDS
AIRSPEED  270.2 FT/SEC
TEMPERATURE  14 DEGREES C (NOT USED)
INITIAL WIND SPEED  13 MFH  (NOT USED)
INITIAL WIND ANGLE 220 DEGREES TRUE  (NOT USED)
FINAL WIND SPEED  13 MFH  (NOT USED)
FINAL WIND ANGLE 220 DEGREES TRUE  (NOT USED)
AIRCRAFT HEADING 132 DEGREES MAGNETIC
MONTH 10     DAY 17     HOUR  8     MINUTE 40     LOCAL TIME
```

Fig. 5-62 - Comparison of Predicted Vortex Track with Photographic Data for B747 Aircraft Flyby 56 on 17 October 1972 (90% Elliptical)

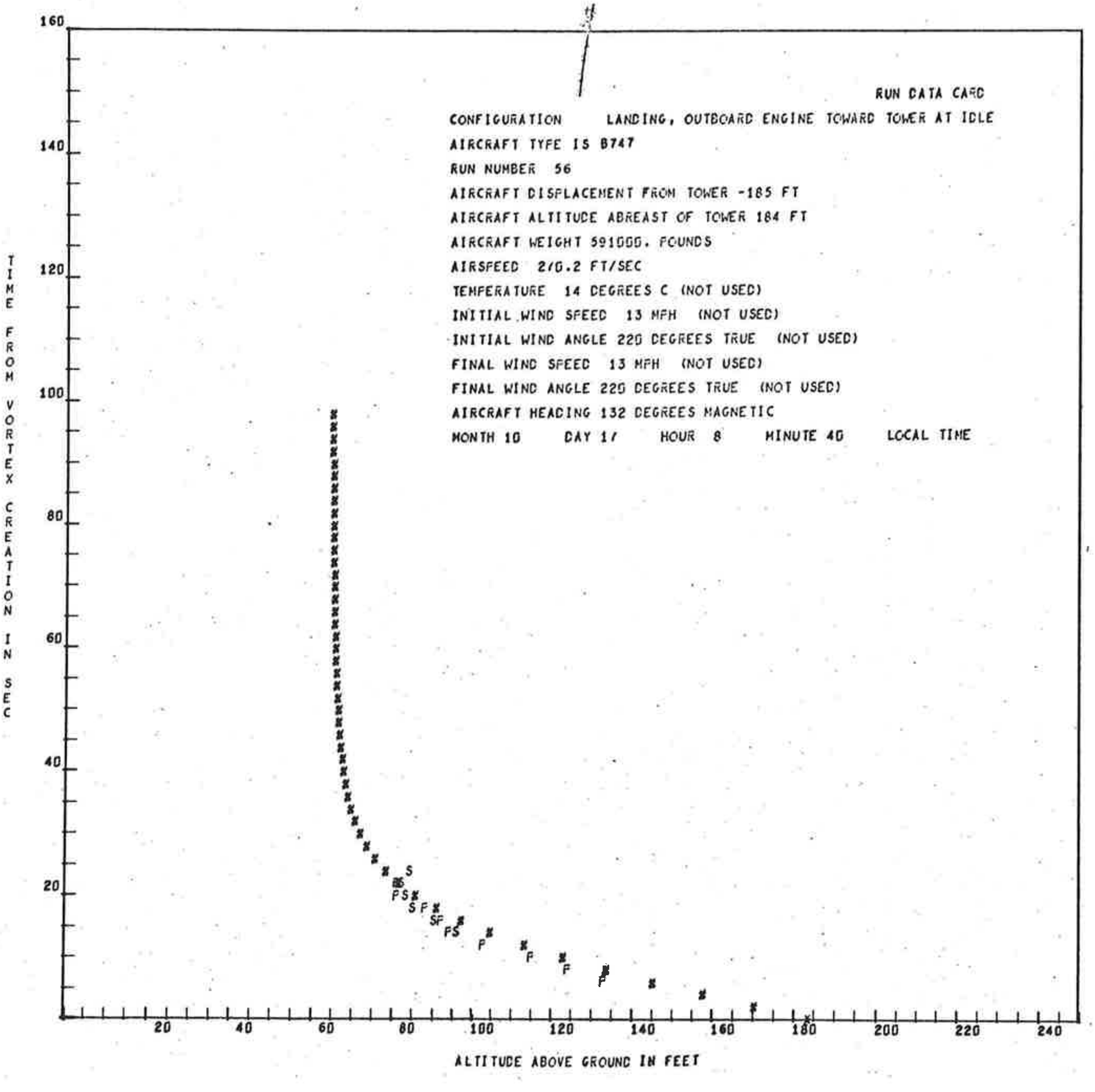

```
                                                   RUN DATA CARD
CONFIGURATION     LANDING, OUTBOARD ENGINE TOWARD TOWER AT IDLE
AIRCRAFT TYPE IS B747
RUN NUMBER  56
AIRCRAFT DISPLACEMENT FROM TOWER -185 FT
AIRCRAFT ALTITUDE ABREAST OF TOWER 184 FT
AIRCRAFT WEIGHT 591000. POUNDS
AIRSPEED  270.2 FT/SEC
TEMPERATURE  14 DEGREES C (NOT USED)
INITIAL WIND SPEED  13 MPH  (NOT USED)
INITIAL WIND ANGLE 220 DEGREES TRUE  (NOT USED)
FINAL WIND SPEED  13 MPH  (NOT USED)
FINAL WIND ANGLE 220 DEGREES TRUE  (NOT USED)
AIRCRAFT HEADING 132 DEGREES MAGNETIC
MONTH 10     DAY 17     HOUR  8     MINUTE 40     LOCAL TIME
```

Fig. 5-63 - Comparison of Predicted and Measured Vortex Altitude for a B747 Aircraft Flyby on 17 October 1972 (90% Elliptical)

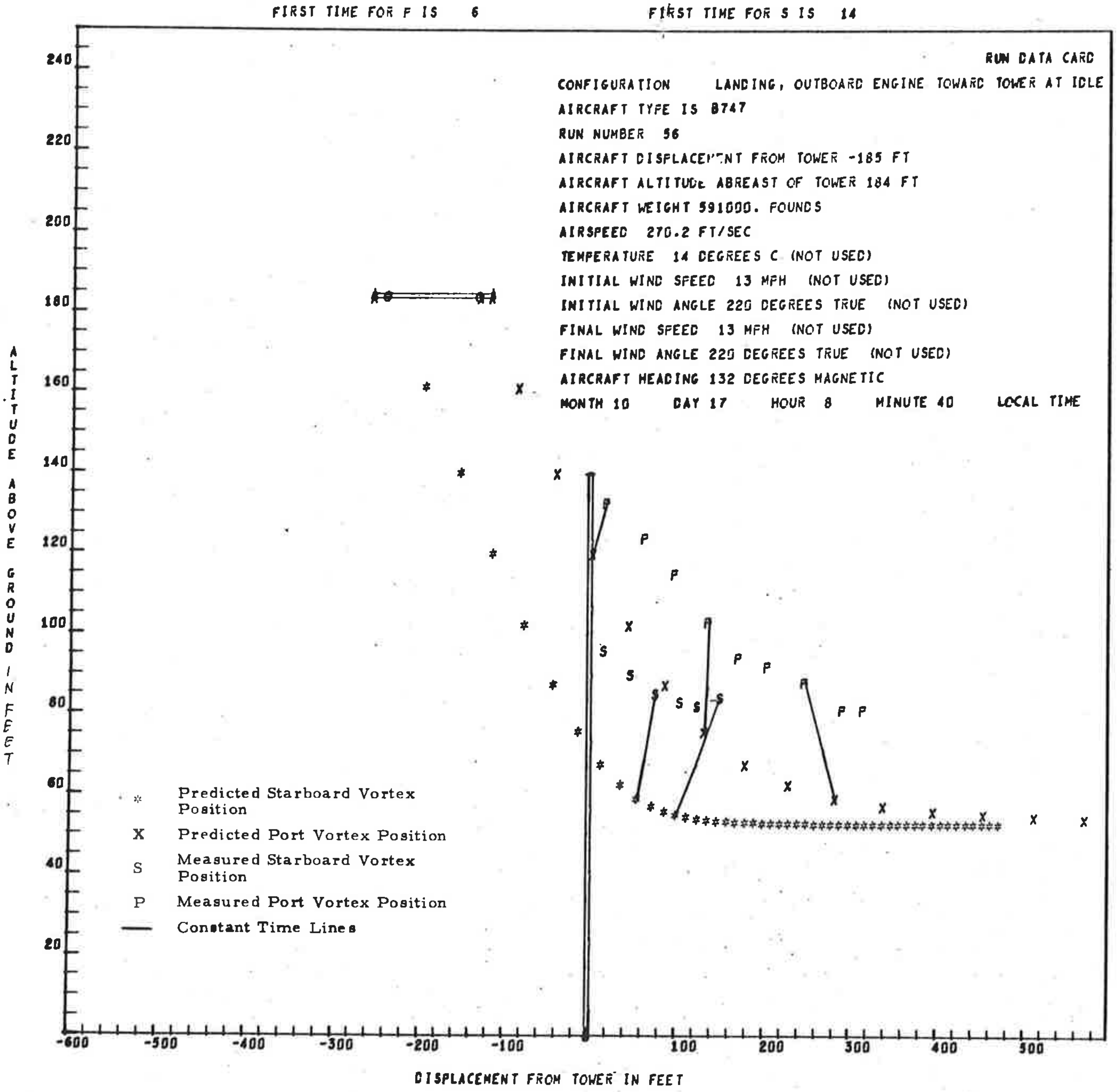
FIRST TIME FOR P IS 6

FIRST TIME FOR S IS 14

RUN DATA CARD

CONFIGURATION LANDING, OUTBOARD ENGINE TOWARD TOWER AT IDLE

AIRCRAFT TYPE IS B747

RUN NUMBER 56

AIRCRAFT DISPLACEMENT FROM TOWER -185 FT

AIRCRAFT ALTITUDE ABREAST OF TOWER 184 FT

AIRCRAFT WEIGHT 591000. POUNDS

AIRSPEED 270.2 FT/SEC

TEMPERATURE 14 DEGREES C (NOT USED)

INITIAL WIND SPEED 13 MPH (NOT USED)

INITIAL WIND ANGLE 220 DEGREES TRUE (NOT USED)

FINAL WIND SPEED 13 MPH (NOT USED)

FINAL WIND ANGLE 220 DEGREES TRUE (NOT USED)

AIRCRAFT HEADING 132 DEGREES MAGNETIC

MONTH 10 DAY 17 HOUR 8 MINUTE 40 LOCAL TIME

Fig. 5-64 - Comparison of Predicted Vortex Track with Photographic Data for B747 Aircraft Flyby 56 on 17 October 1972 (70% Elliptical)

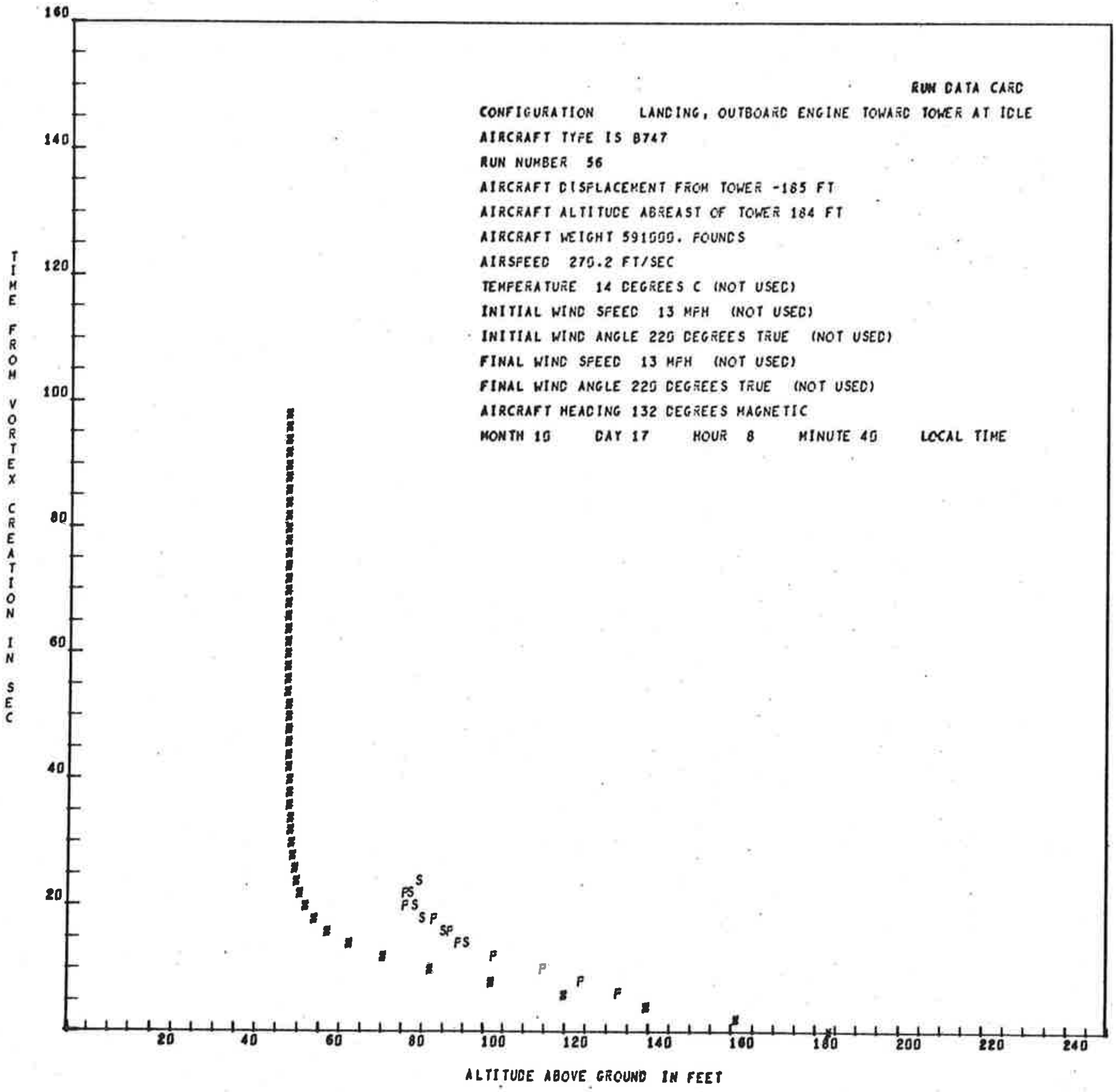

Fig. 5-65 - Comparison of Predicted and Measured Vortex Altitude for a B747 Aircraft Flyby on 17 October 1972 (70% Elliptical)

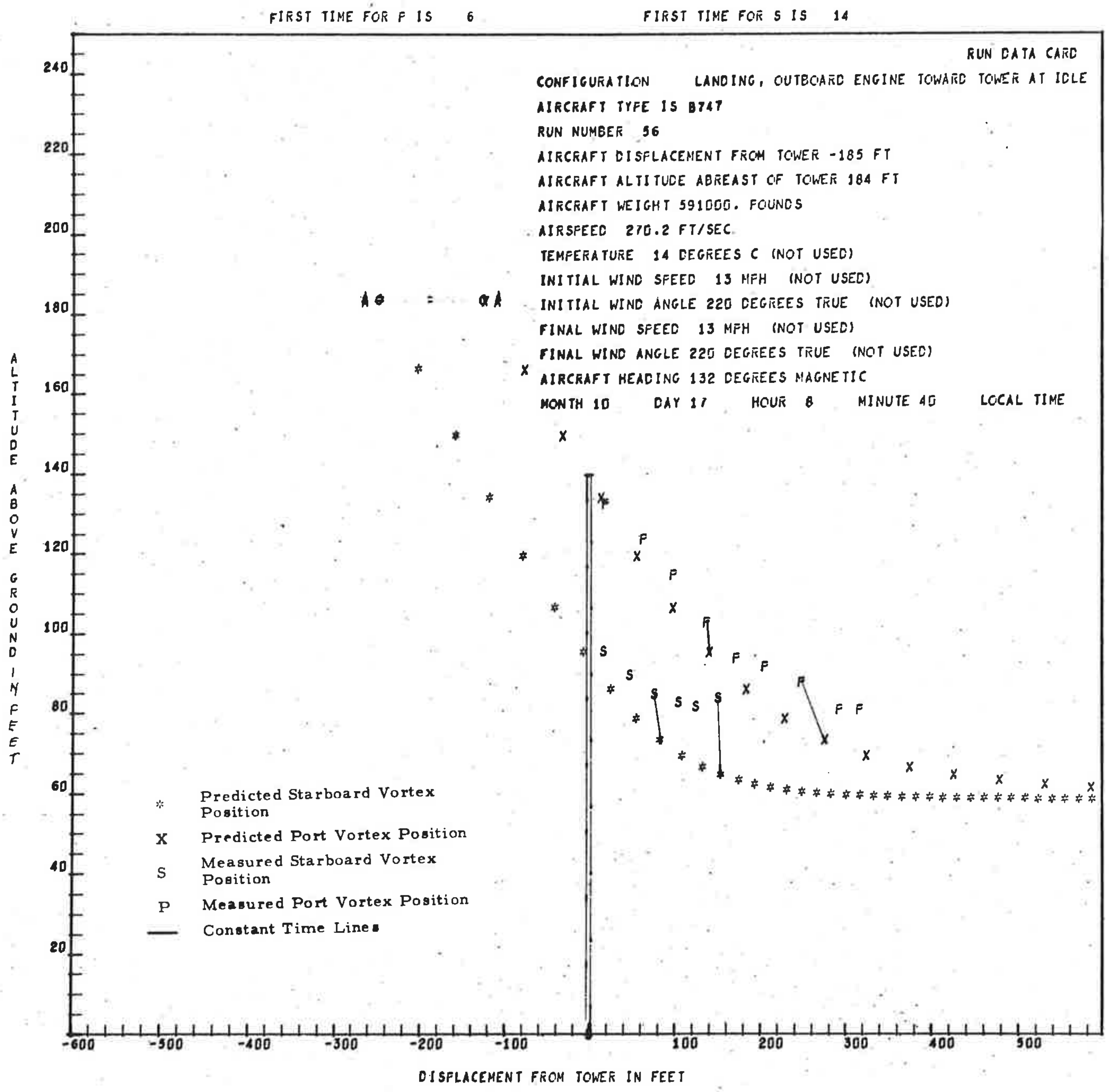

Fig. 5-66 - Comparison of Predicted Vortex Track with Photographic Data for B747 Aircraft Flyby 56 on 17 October 1972 (80% Elliptical)

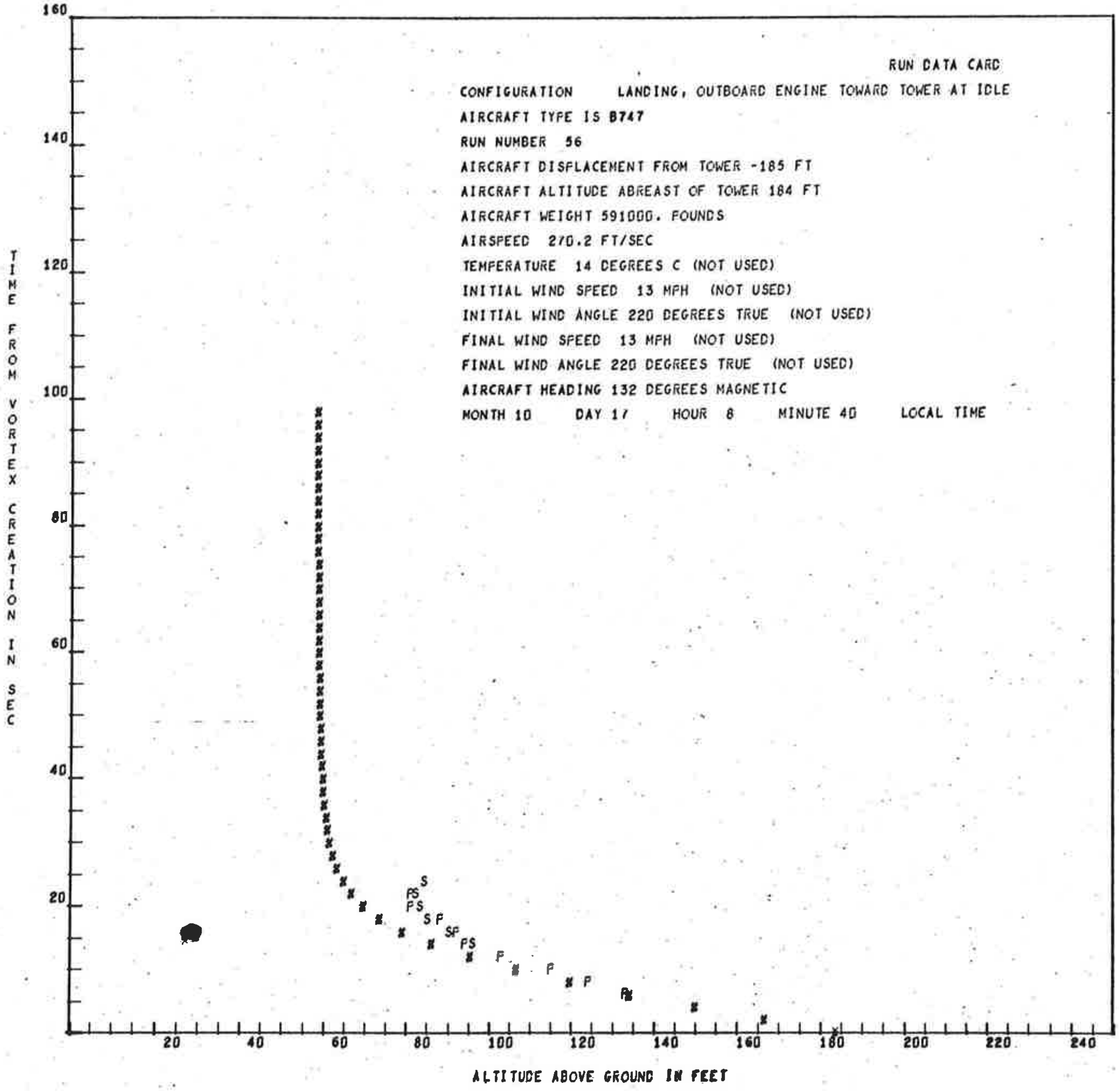

RUN DATA CARD

CONFIGURATION LANDING, OUTBOARD ENGINE TOWARD TOWER AT IDLE

AIRCRAFT TYPE IS B747

RUN NUMBER 56

AIRCRAFT DISPLACEMENT FROM TOWER -185 FT

AIRCRAFT ALTITUDE ABREAST OF TOWER 184 FT

AIRCRAFT WEIGHT 591000. POUNDS

AIRSPEED 270.2 FT/SEC

TEMPERATURE 14 DEGREES C (NOT USED)

INITIAL WIND SPEED 13 MPH (NOT USED)

INITIAL WIND ANGLE 220 DEGREES TRUE (NOT USED)

FINAL WIND SPEED 13 MPH (NOT USED)

FINAL WIND ANGLE 220 DEGREES TRUE (NOT USED)

AIRCRAFT HEADING 132 DEGREES MAGNETIC

MONTH 10 DAY 17 HOUR 8 MINUTE 40 LOCAL TIME

Fig. 5-67 - Comparison of Predicted and Measured Vortex Altitude for a B747 Aircraft Flyby on 17 October 1972 (80% Elliptical)

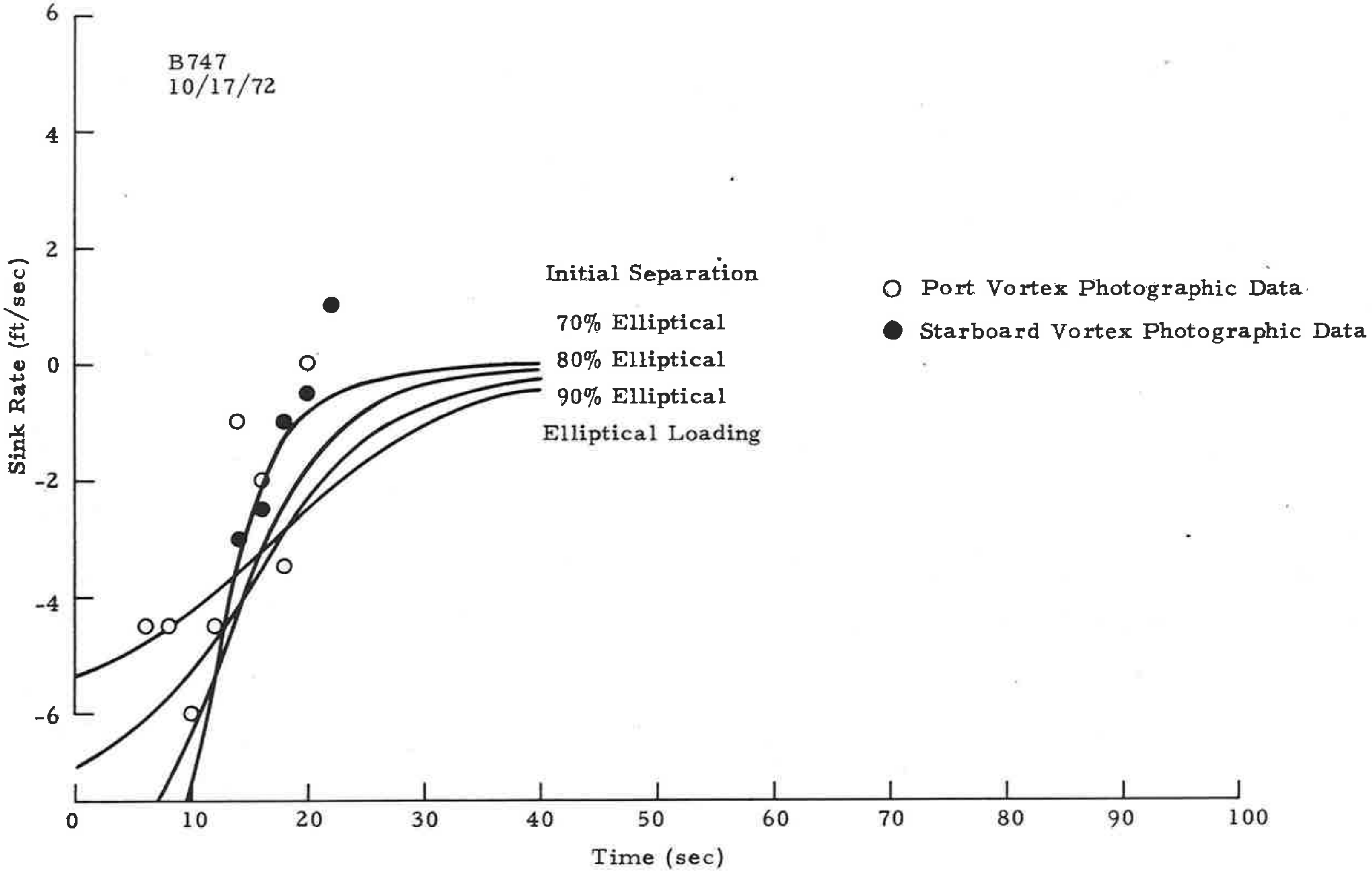

Fig. 5-68 - Comparison of Measured and Predicted Vortex Sink Rates vs Time for Run 56 on 17 October 1972 (B747)

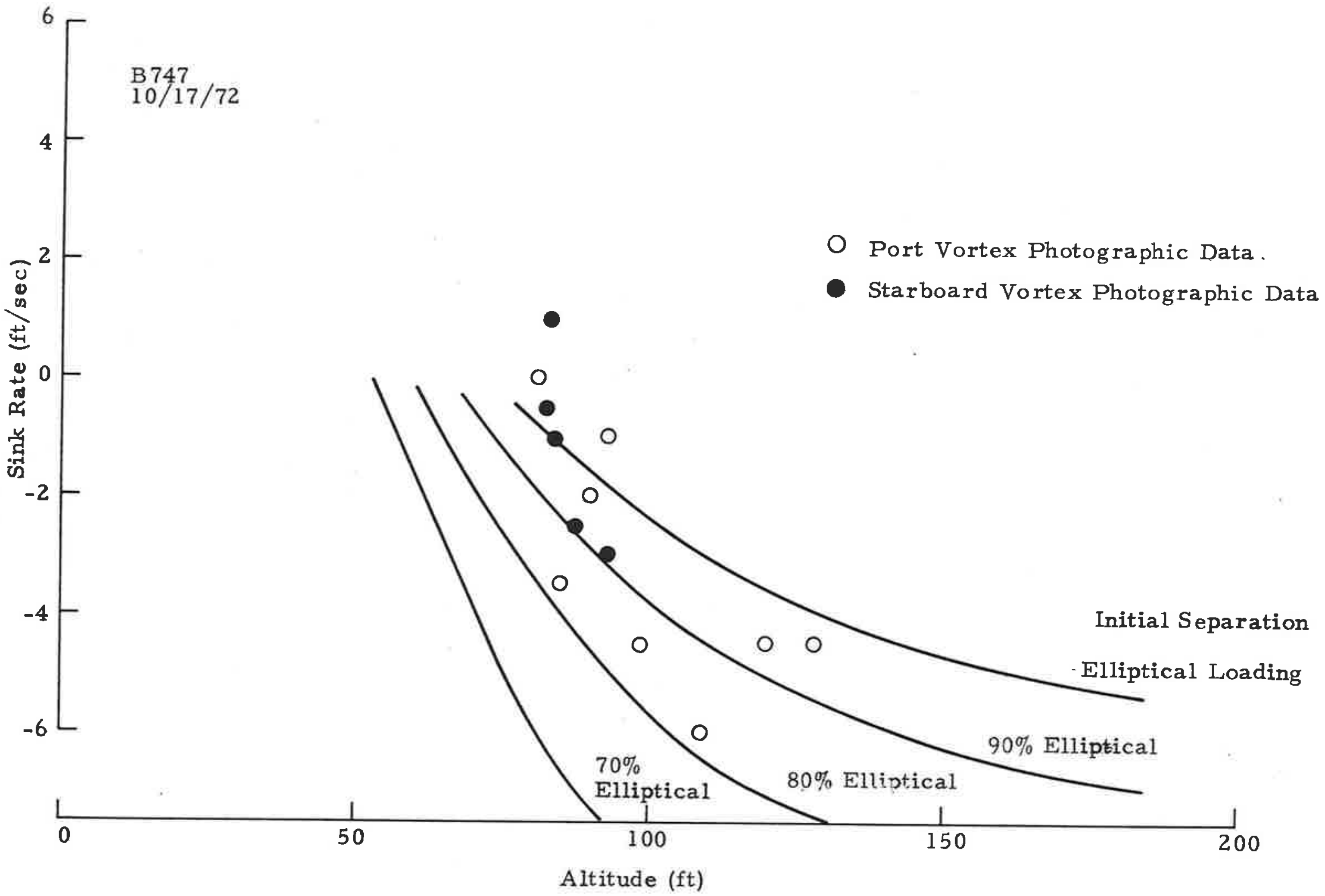

Fig. 5-69 - Comparison of Measured and Predicted Vortex Sink Rates vs Altitude for Run 56 on 17 October 1972 (B747)

The data corresponding to Run 16 on 18 October 1972 for a B707 aircraft flyby are used for the calculations. Predictive tracks for Run 16 are shown in Figs. 5-70 through 5-72. These results show the decreased descent due to the lower predicted sink rate. The ground wind track shows a starboard uncertainty of less than 40 feet for times up to 60 seconds. The port location uncertainty is approximately the same and excellent results were obtained for times up to two minutes.

Figures 5-73 through 5-75 depict the maximum velocity versus time, maximum velocity versus core radius and core radius versus time, respectively. These curves were computed from data corresponding to Run 16 on 18 October 1972. The only parameters entering into the prediction in this form are the initial circulation and the creation altitude in that the pressure and temperature are required for the eddy viscosity correlation.

A spatial location of -100 feet was chosen for display of the calculated quantities. This locates the starboard vortex at an altitude of approximately 73.5 feet at a time of 28 seconds and 47 feet altitude at 52 seconds for the port vortex. These data, used with the prediction in Figs. 5-70 through 5-72, give the results shown in Table 5-3. The results for the same calculations based on an 85% vortex spacing criteria are shown in the last two lines of Table 5-3. The corresponding velocity signatures for starboard and port vortex passage are shown in Fig. 5-74.

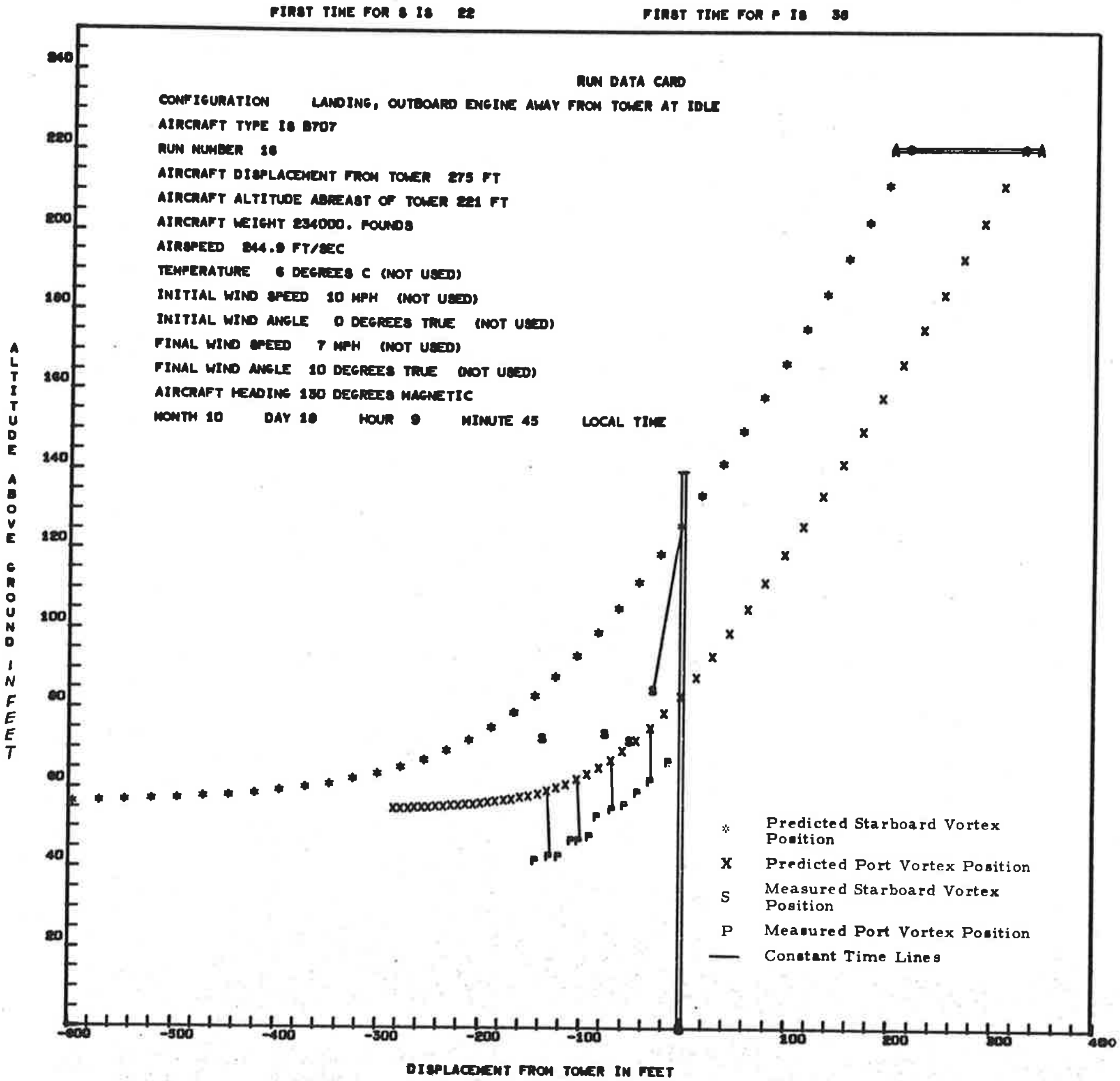

Fig. 5-70 - Comparison of Predicted Vortex Track with Measured Photographic Data for B707 Aircraft Flyby 16 on 18 October 1972

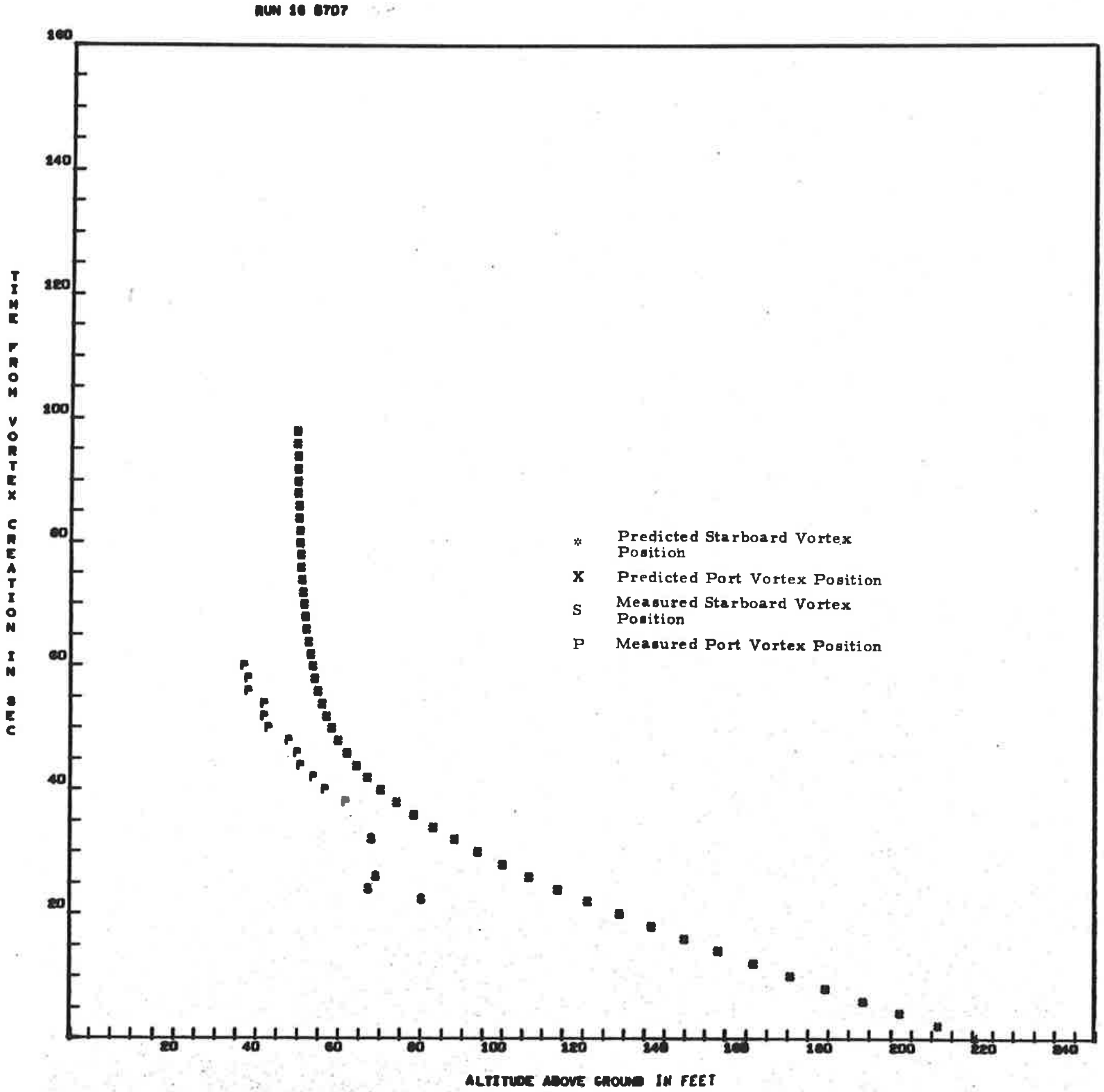

Fig. 5-71 - Comparison of Predicted and Measured Vortex Altitude for B707 Aircraft Flyby 16 on 18 October 1972

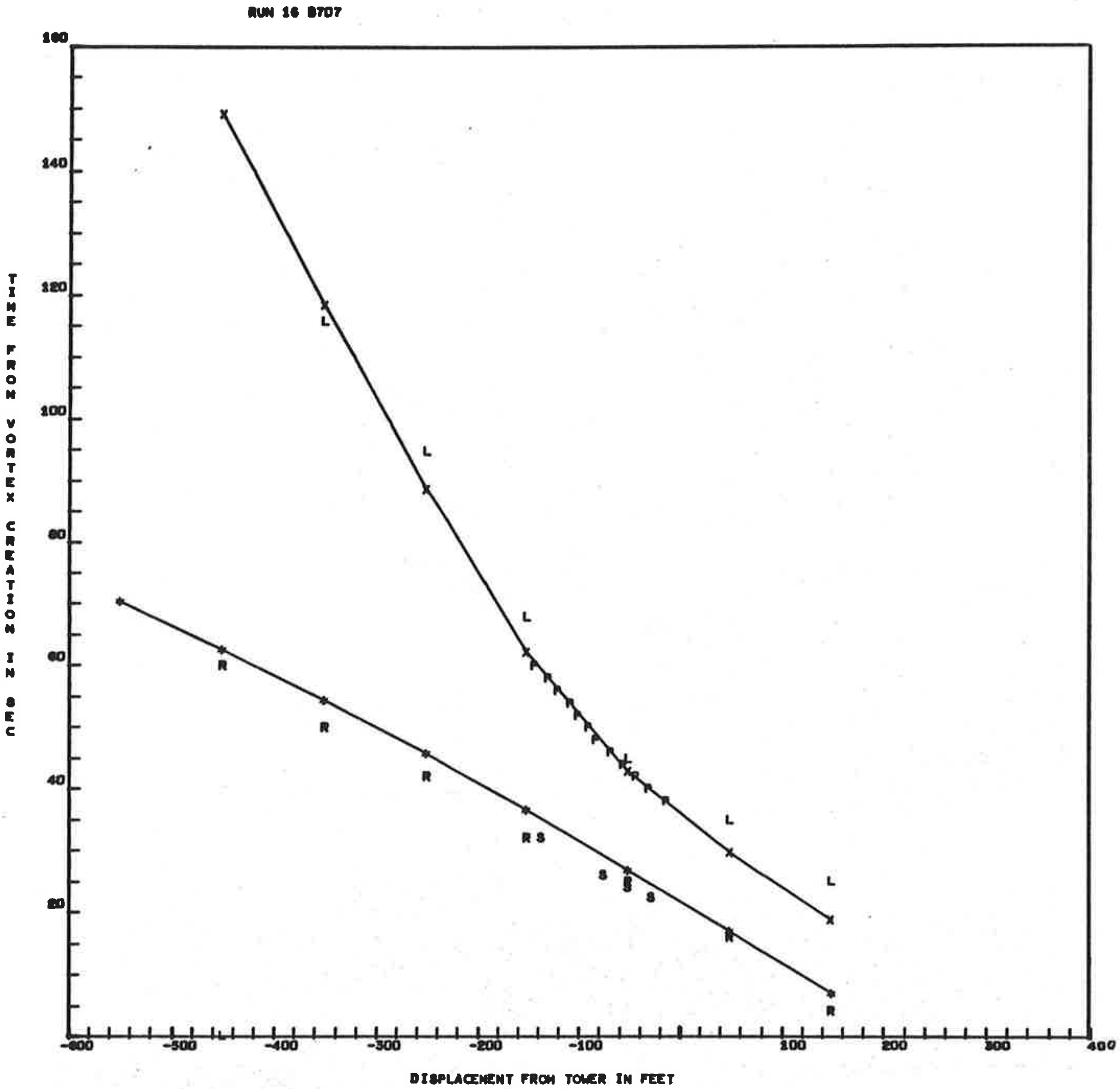

Fig. 5-72 - Comparison of Predicted and Measured Ground Wind Track for B707 Aircraft Flyby 16 on 18 October 1972

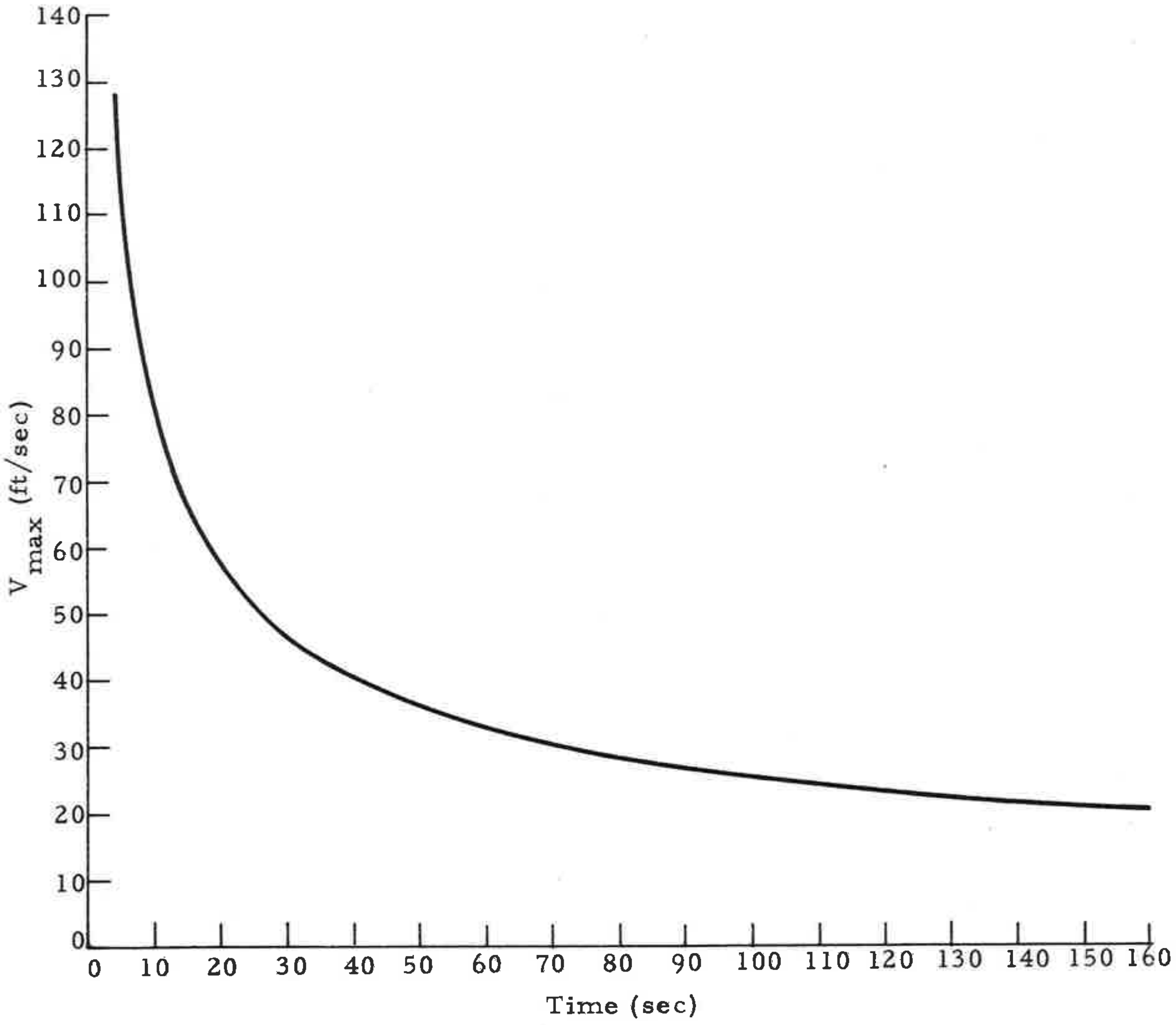

Fig. 5-73 - Maximum Tangential Velocity vs Time for Run 16 B707) on 18 October 1972

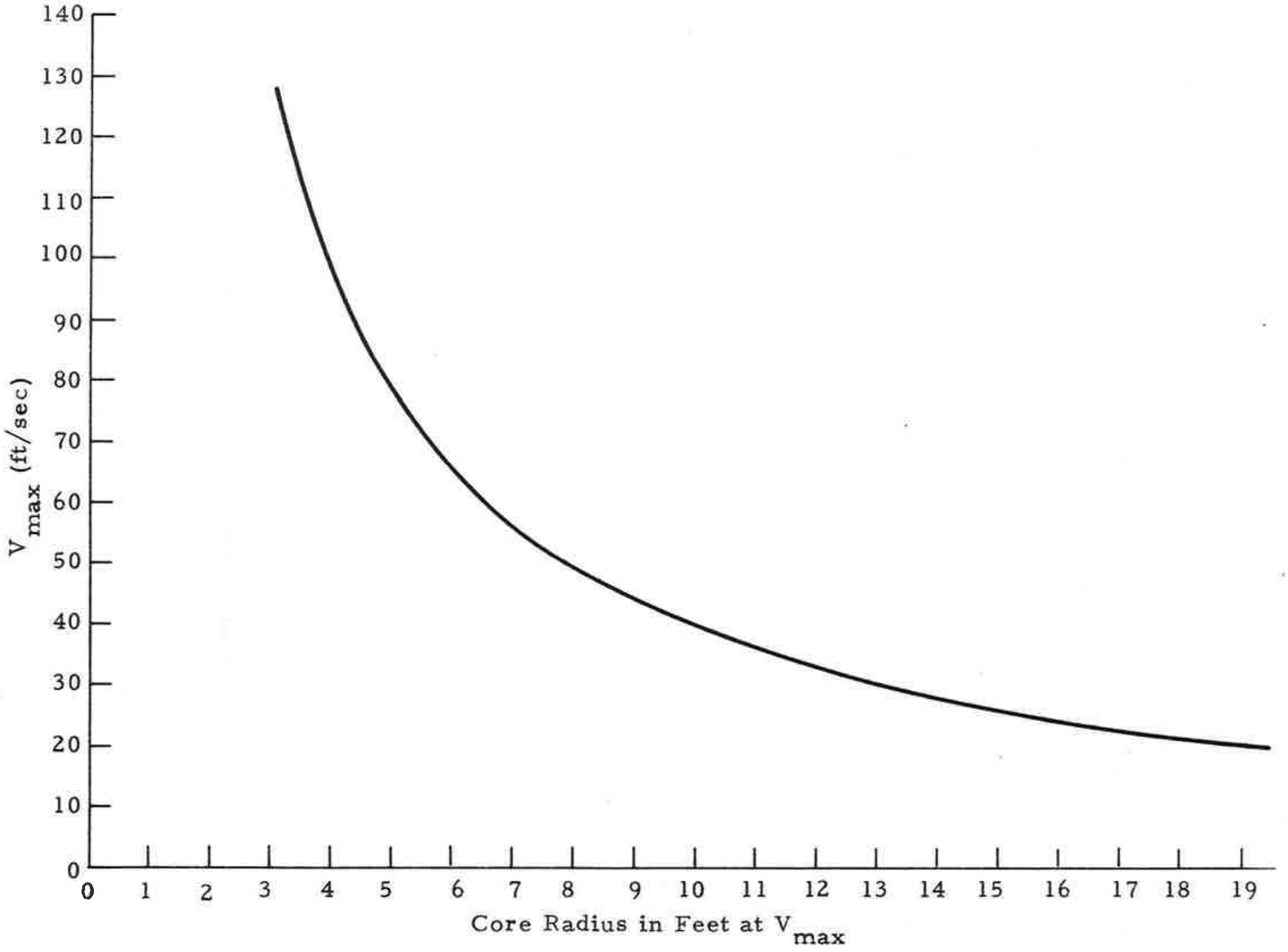

Fig. 5-74 - Maximum Tangential Velocity vs Core Radius for Run 16 (B707) on 18 October 1972

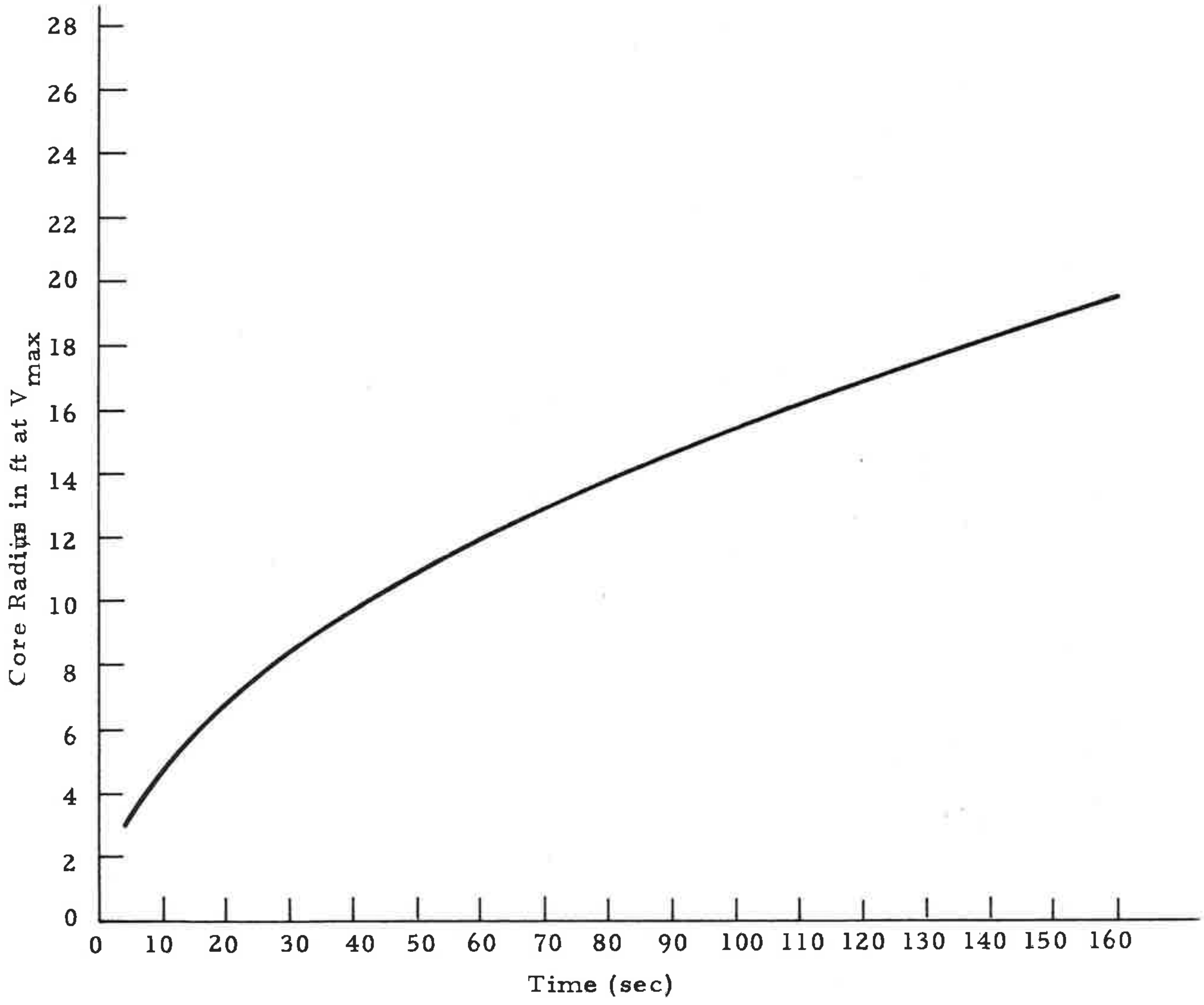

Fig. 5-75 - Core Radius vs Time for Run 16 on 18 October 1972 (B707)

Table 5-3

PREDICTIONS FOR RUN 16 ON 18 OCTOBER 1972 (B707)*

Data at Vortex Passage of Sensor	Starboard Vortex	Port Vortex
Maximum Tangential Velocity	48 ft/sec	35.5 ft/sec
Core Radius	8.2 ft	11.2 ft
Initial Circulation	-3463 ft^2/sec	3463 ft^2/sec
Circulation in Core	-2277 ft^2/sec	2477 ft^2/sec
Initial Circulation (85% Initial Vortex Spacing)	-4074 ft^2/sec	4074 ft^2/sec
Circulation in Core (85% Initial Vortex Spacing)	-2914 ft^2/sec	2914 ft^2/sec

*Calculations are for a point -100 feet from tower

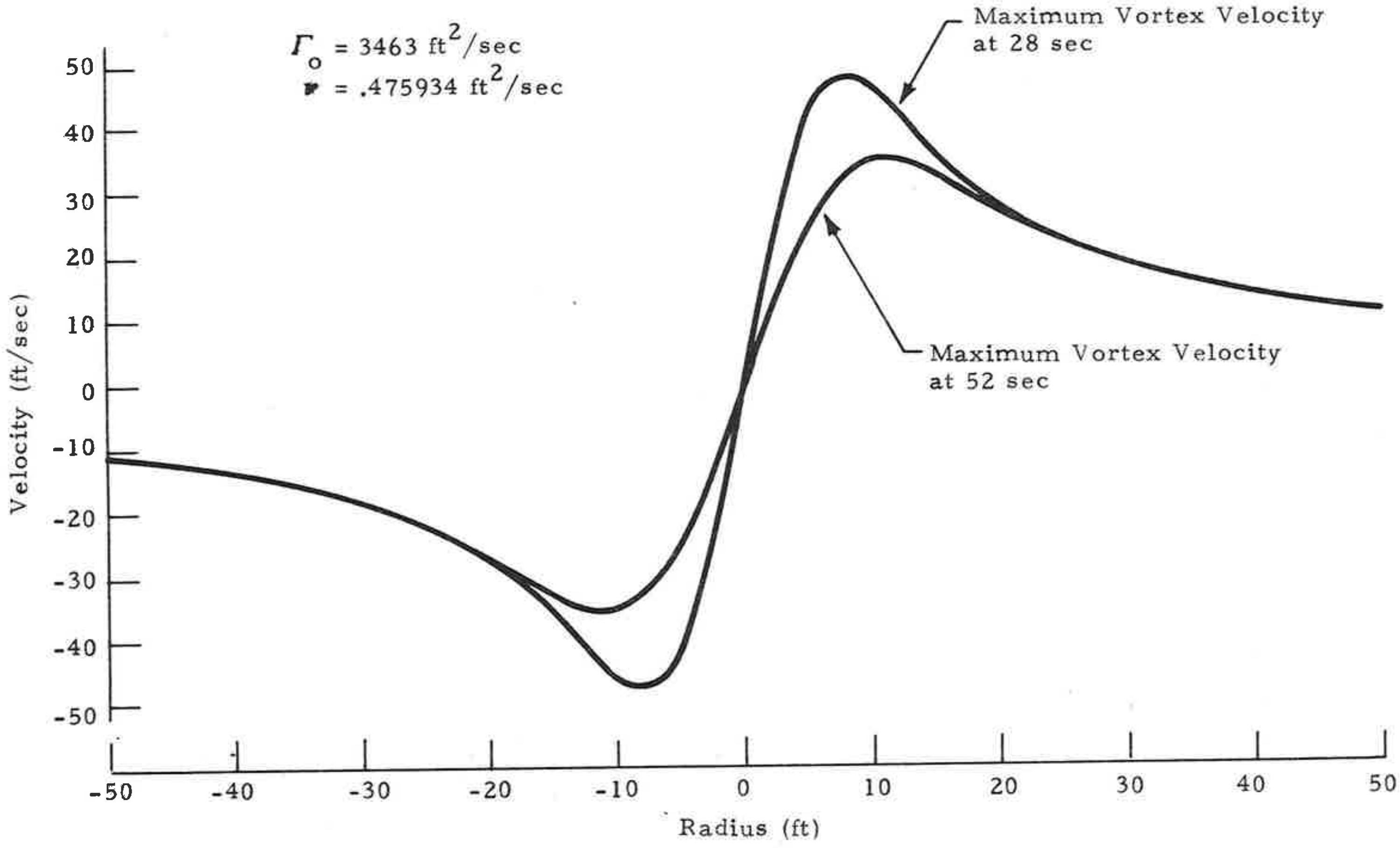

Fig. 5-76 - Velocity Signature vs Radius for Run 16 on 18 October 1972
(B707)

Section 6

ANALYSIS OF WIND SHEAR AND GROUND PLANE EFFECTS AS POSSIBLE MECHANISMS CAUSING VORTEX TILTING

6.1 STREAMLINES FOR A CLASS OF VORTEX FIELDS

To more fully understand the mechanisms involved in vortex tilting, an analysis was performed to determine the streamlines associated with the presence of a vortex pair above a ground plane; the vortex pair is also assumed to be acted upon by a wind shear (i.e., the velocity in the horizontal direction is a function of the altitude above the ground plane). The case of a vortex pair in which the individual vortices possess arbitrary circulation (i.e., the circulation is not assumed to be equal and opposite) and located at unequal heights was considered and formulated. However, due to the large number of parameters involved, it was deemed advisable to keep the initial study confined to the simpler case of a pair of vortices possessing equal and opposite circulation, Γ, and located at equal heights above the ground plane. The special case of the vortex pair at "infinite" distance above the ground plane has been previously considered by investigators at Aerovironment, Inc. (Ref. 5). The parameter σ defined below is the same as used in the Aerovironment studies; an additional parameter is introduced to describe the proximity of the ground plane. In the present study, however, a closed form solution was obtained for the special case of the absence of ground effects.

The defining mathematical equations are relatively simple. For this case, streamlines are to be calculated with respect to a coordinate system which has its x-axis passing through the centers of the vortex pair; the coordinate system will move with the vortex pair (e.g., as it descends and moves horizontally). Let the vortices be separated by a distance 2a and let the vortices be at a height b above the ground plane. The mutual attraction of the vortex pair and the image vortex pair will result in a settling motion (neglecting any buoyancy effects) given by the equation on the following page.

$$V_s = \frac{\Gamma}{4\pi a} \frac{b^2}{a^2 + b^2} .$$

It is assumed that the horizontal wind is described by U(h), where h denotes the height above the ground plane. In order to simplify the construction of the curves which represent the streamlines about the vortex pair, the coordinate system will be assumed to move horizontally with the velocity, U(b), and to descend vertically with the velocity, V_s.

The geometry is depicted in Fig. 6-1. The wind is assumed to be defined by a function U(h) which depends upon the height, $h = b + y$, above the ground plane.

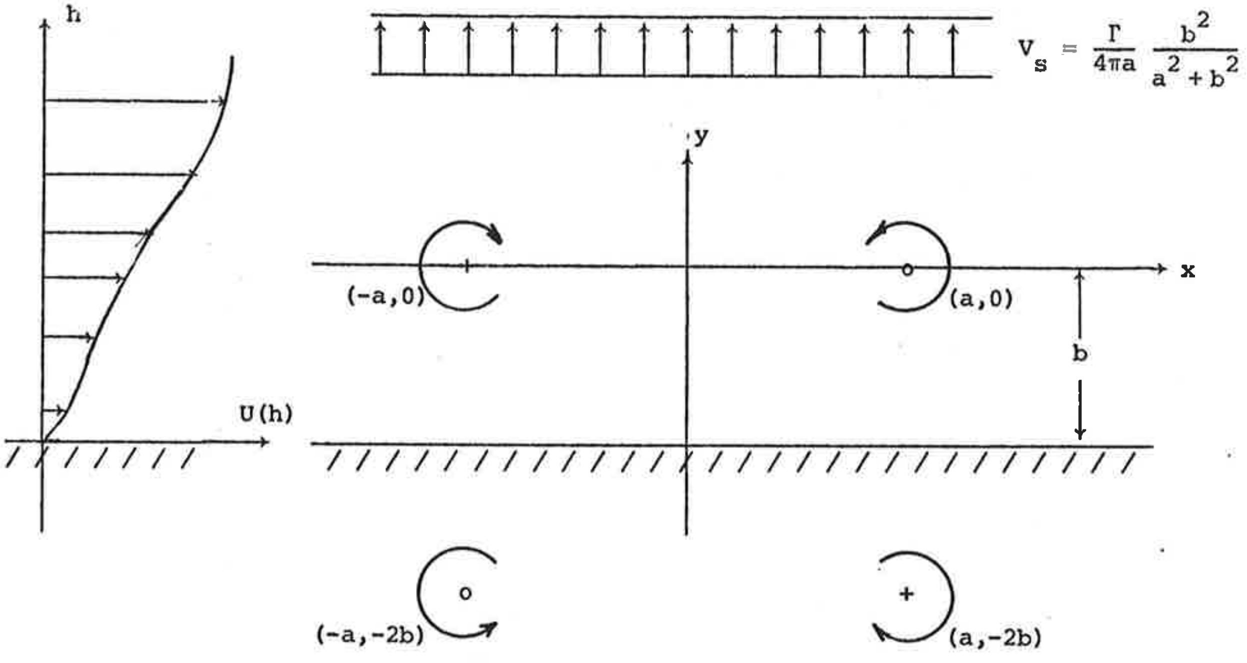

Fig. 6-1 - Coordinate System and Flow Geometry for Vortex Pair in Wind Shear Above a Ground Plane

The stream function for the flow field in the moving coordinate system is described by

$$\psi(x, y) = \int_0^y [U(y' + b)]dy' - \frac{\Gamma}{4\pi a} \frac{b^2}{a^2 + b^2} x$$

$$- \frac{\Gamma}{4\pi} \log_e \left\{ \frac{[(x - a)^2 + y^2][(x + a)^2 + (y + 2b)^2]}{[(x + a)^2 + y^2][(x - a)^2 + (y + 2b)^2]} \right\}$$

The velocities are determined by the equations

$$u(x, y) = \frac{\partial \psi(x, y)}{\partial y}, \quad v(x, y) = - \frac{\partial \psi(x, y)}{\partial x}.$$

For the purpose of presenting graphical presentations of the streamlines, it will be convenient to introduce the dimensionless coordinates

$$x' = \frac{x}{a}, \quad y' = \frac{y}{a}, \quad \epsilon = \frac{b}{a}, \quad \psi'(x, y) = \frac{4\pi}{\Gamma} \psi(x, y) .$$

It will be advantageous to consider the special case for which U(h) can be represented in the form

$$U(h) = K_0 + K_1(h - b) + K_2(h - b)^2 + \ldots$$

and terms involving $K_2, K_3, \ldots$ can be neglected. This then permits the use of the simplification

$$\int_0^y [U(y^* + b) - U(b)]dy^* \simeq \int_0^y K_1 y^* dy^* = \frac{1}{2} K_1 y^2 = \frac{1}{2} K_1 a^2 y'^2 = \frac{\Gamma}{4\pi} \sigma y'^2 ,$$

where

$$\sigma = 2\pi K_1 a^2 / \Gamma.$$

If we now agree to suppress the appearance of the "′" on x′, y′, and ψ′, we can express the defining equations in the form

$$\psi(x, y) = y^2 \frac{\epsilon^2}{1 + \epsilon^2} x - \log_e \left\{ \frac{[(x-1)^2 + y^2]\,[(x+1)^2 + (y+2\epsilon)^2]}{[(x+1)^2 + y^2]\,[(x-1)^2 + (y+2\epsilon)^2]} \right\}$$

$$= f_1(x, y; \sigma, \epsilon)$$

$$u(x, y) = f_2(x, y; \sigma, \epsilon) = 2\sigma y - \left\{ \frac{8xy}{[(x-1)^2 + y^2]\,[(x+1)^2 + y^2]} \right.$$

$$\left. - \frac{8x(y + 2\ )}{[(x-1)^2 + (y+2\epsilon)^2]\,[(x+1)^2 + (y+2\epsilon)^2]} \right\}$$

$$v(x, y) = f_3(x, y; \sigma, \epsilon) = \frac{2}{1 + \epsilon^2} + \left\{ \frac{4[(x^2 - 1) - y^2]}{[(x-1)^2 + y^2]\,[(x+1)^2 + y^2]} \right.$$

$$\left. - \frac{4[(x^2 - 1) - (y+2\epsilon)^2]}{[(x-1)^2 + (y + 2\ )^2\ [(x+1)^2 + (y+2\epsilon)^2]} \right\}$$

The equations for the streamlines can be generated by integration of the differential equation

$$\frac{dy(x)}{dx} = \frac{v(x, y)}{u(x, y)} = f_3(x, y; \sigma, \epsilon)/f_2(x, y; \sigma, \epsilon)$$

between x and x + dx when $|dy/dx| < 1$, and by integration of

$$\frac{dx(y)}{dy} = \frac{u(x, y)}{v(x, y)} = f_2(x, y; \sigma, \epsilon)/f_3(x, y; \sigma, \epsilon)$$

between y and y + dy when $|dx/dy| < 1$.

The numerical integration proposed above will break down when u(x, y) and v(x, y) vanish simultaneously at a stagnation point (x^*, y^*). Therefore, it is important to determine in advance the location of the streamline $f_1(x^*, y^*; \sigma, \epsilon) = f^*$ which passes through the stagnation point (x^*, y^*). This requires the determination of (x^*, y^*) by solving the set of simultaneous equations

$$u(x^*, y^*) = 0, \quad v(x^*, y^*) = 0 .$$

It is proposed that this pair of values (x^*, y^*) be determined by an iterative solution based upon the equations

$$\begin{aligned} x_{n+1} &= x_n - [A_{22}u(x_n, y_n) - A_{12}v(x_n, y_n)]/\Delta, \\ y_{n+1} &= y_n - [A_{11}v(x_n, y_n) - A_{21}u(x_n, y_n)]/\Delta, \end{aligned} \tag{6.1}$$

where

$$\Delta = A_{22}A_{11} - A_{12}A_{21} = A_{11}A_{22} - A_{21}A_{12}$$

and

$$\begin{aligned} A_{11} &= [u(x_n + \tfrac{1}{2}\delta, y_n) - u(x_n - \tfrac{1}{2}\delta, y_n)]/\delta , \\ A_{12} &= [u(x_n, y_n + \tfrac{1}{2}\delta) - u(x_n, y_n - \tfrac{1}{2}\delta)]/\delta , \\ A_{21} &= [v(x_n + \tfrac{1}{2}\delta, y_n) - v(x_n - \tfrac{1}{2}\delta, y_n)]/\delta , \\ A_{22} &= [v(x_n, y_n + \tfrac{1}{2}\delta) - v(x_n, y_n - \tfrac{1}{2}\delta)]/\delta . \end{aligned}$$

The starting values for the iteration will be selected by determining the values of (x^*, y^*) for the simpler case in which $\epsilon \rightarrow \infty$, i.e., the case in which the effect of the image vortex in the ground plane can be neglected. This problem involves the somewhat simpler problem defined by solving for (x, y):

$$0 = 2\sigma y - \left\{ \frac{8xy}{[(x - 1)^2 + y^2 \quad (x + 1)^2 + y^2]} \right\},$$

$$0 = 1 + \left\{ \frac{4[(x^2 - 1) - y^2]}{[(x - 1)^2 + y^2 \quad (x + 1)^2 + y^2]} \right\}.$$

These equations can be used to show that

$$y^2 = x^2 - 1 + \frac{x}{\sigma} .$$

The value of x can be determined from the equation

$$(x + \frac{1}{2\sigma})^2 = 1 + \frac{1}{\sigma x} ,$$

which is a cubic equation of the form

$$x^3 + px^2 + qx + r = 0$$

with

$$p = \frac{1}{\sigma}, \quad q = \frac{1}{4\sigma^2}, \quad r = - \frac{1}{\sigma} .$$

The solution can be expressed in the form

$$x = z - \frac{1}{3} p = z - \frac{1}{3\sigma} ,$$

where z is a solution of the cubic equation

$$z^3 + az + b = 0 ,$$

where

$$b = - \frac{72\sigma^2 + 1}{108\sigma^2}, \quad a = - \frac{12\sigma^2 + 1}{12\sigma^2} .$$

The nature of the roots are determined by the factor

$$Q = \frac{b^2}{4} + \frac{a^3}{27} = \frac{1 + 44\sigma^2 - 16\sigma^4}{432\sigma^4} .$$

This expression vanishes at $\sigma_c = \underline{+}1.665095388$ $[\sigma_c^2 = (11 + \sqrt{125})/8 = 2.772542486]$. From the theory of cubic equations it follows that x has one real root for $0 < \sigma < \sigma_c$; three real roots (two equal) for $\sigma = \sigma_c$; and three real roots (all different) for $\sigma > \sigma_c$. For $0 < \sigma < \sigma_c$ the real root is given by

$$x = \sqrt[3]{P + R} + \sqrt[3]{P - R} - \frac{1}{3\sigma} ,$$

where

$$P = \frac{72\sigma^2 + 1}{216\sigma^3}, \quad R = \sqrt{Q}$$

For $\sigma = \sigma_c$ the real roots are given by

$$x_1 = 2\sqrt[3]{P} - \frac{1}{3\sigma} = 0.9717365426 ,$$

$$x_2 = x_3 = -\frac{1}{2} x_1 = -0.485868271 .$$

For $\sigma > \sigma_c$ the three distinct real roots are given by

$$x_1 = A \cos(\theta) - \frac{1}{3\sigma}, \quad x_2 = A \cos(\theta + \frac{2\pi}{3}) - \frac{1}{3\sigma}, \quad x_3 = A \cos(\theta - \frac{2\pi}{3}) - \frac{1}{3\sigma} ,$$

where

$$A = \frac{1}{3\sigma} \sqrt{12\sigma^2 + 1}, \quad \cos(3\theta) = \frac{1}{\sqrt{12\sigma^2 + 1}} \, \frac{72\sigma^2 + 1}{12\sigma^2 + 1} .$$

The angle θ is 0 for $\sigma = \sigma_c$. For $\sigma \rightarrow \infty$,

$$\theta \simeq \frac{\pi}{6} - \frac{1}{3} \frac{72\sigma^2 + 1}{[12\sigma^2 + 1]^{3/2}} .$$

The only positive root is x_1. We observe that at $\sigma = \sigma_c$, the value calculated from $x = A \cos\theta - 1/3\sigma$ yields $x = 0.9717365426$ for $\sigma = \sigma_c$; this agrees with the value obtained from the expression $x = 2\sqrt[3]{P} - 1/3\sigma$ which is the limiting case of $x = \sqrt[3]{P + R} + \sqrt[3]{P - R} - 1/3\sigma$ as $\sigma \rightarrow \sigma_c$ from below. We observe that $x \rightarrow 0$ as $\sigma \rightarrow 0$ since $\sqrt[3]{P \pm R} \rightarrow 1/6\sigma$. The above equations completely define the value of x in terms of the parameter σ. The corresponding values of y are determined from $y^2 = x^2 - 1 + x/\sigma$. We observe that for $\sigma \rightarrow 0$ that $x \rightarrow 4\sigma$; therefore, $y \rightarrow \pm\sqrt{3}$ as $\sigma \rightarrow 0$.

These values provide a set of starting values for the more general case in which $\epsilon = b/a$ is finite. Note that if the wind shear cannot be expressed analytically in the form $U(h) = U(b) + K_1 (h - b)$ that one can obtain an approximate value of K_1 by means of $K_1 = [U(b + \delta) - U(b)]/\delta$ and therefore take σ to be defined by

$$\sigma = 2\pi[U(b + \delta) - U(b)] \frac{a^2}{\delta\Gamma} .$$

Observe that when $\sigma \rightarrow 0$ that the above initial values for the stagnation points are undefined. In this limiting case, $x = 0$ and $y = \pm\sqrt{3}$.

Experience with the above iterative formula for the roots for the case $\epsilon \neq \infty$ revealed that the starting values obtained for the case $\epsilon = \infty$ leads to numerical problems as $\epsilon \rightarrow 0$. This was "fixed" in the analysis by observing that the stagnation point nearest the ground plane has the approximate values $x = x^*$ and $y = -\epsilon$, where x^* is a solution of the equation $8x = \sigma(x^2 - 1)^2$. In practice it was found that a very satisfactory numerical problem was defined by merely setting $x = 1/2$ and $y = -\epsilon$ where ϵ was less than 0.7. It was also found useful to employ the results

$$x \simeq (4\sigma) - (4\sigma)^3 + 0.75\,(4\sigma)^5, \quad y \simeq 3 - 3(4\sigma)^2 + (4\sigma)^4,$$

for the starting values (i.e., the results for $\epsilon \to \infty$) when σ tends toward 0.

Figure 6-2 provides a chart from which the coordinates (x, y) (calculated from Eq. (6.1)) of the upper and lower stagnation points can be determined for any set of values of wind shear and ground plane proximity. Note that the values of y for the lower stagnation point are the absolute values of the actual coordinates. This graphic presentation of the roots (which yield the upper and lower stagnation points) indicates that under certain circumstances the upper stagnation point will rise rather drastically. This occurs for small values of σ as ϵ tends toward zero. Therefore, this effect occurs under the condition of a small wind shear (or large circulation) as the vortex pair descends toward the ground. This is seen to occur for all σ values other than 0.5 (actually some value between 0.4 and 0.5, but only these two discrete values are shown on the graph) as ϵ decreases in value from infinity. If the aircraft altitude is finite, which is certainly the case, the intersection of the initial altitude relative to the semi-span and the wind shear curves locates the initial point on the plot. For commercial jet aircraft outside the threshold, ϵ is approximately unity initially; thus the downwind upper stagnation point will rise for σ less than 0.3 (corresponding figures for the middle marker are $\epsilon \sim 4.0$ and $\sigma < 0.4$).

Figures 6-3 through 6-5 show the detailed streamlines for various values of ϵ corresponding to a heavy shear ($\sigma = 3.0$). Note the downwind vortex cell is strikingly smaller than the upwind cell (this was previously reported in Ref. 5 for the special case of $\epsilon \to \infty$). Note also that the upper and lower stagnation points are on different streamlines. This gives rise to a streamtube between the stagnation streamlines and the steady state case allows a "sweeping" motion of fluid in the external stream from the lower right around the upwind cell, back around the downwind cell and exiting via the upper right. In the actual case, this idealistic steady state situation does not exist. However, as the oval sinks, the tendency would be for a

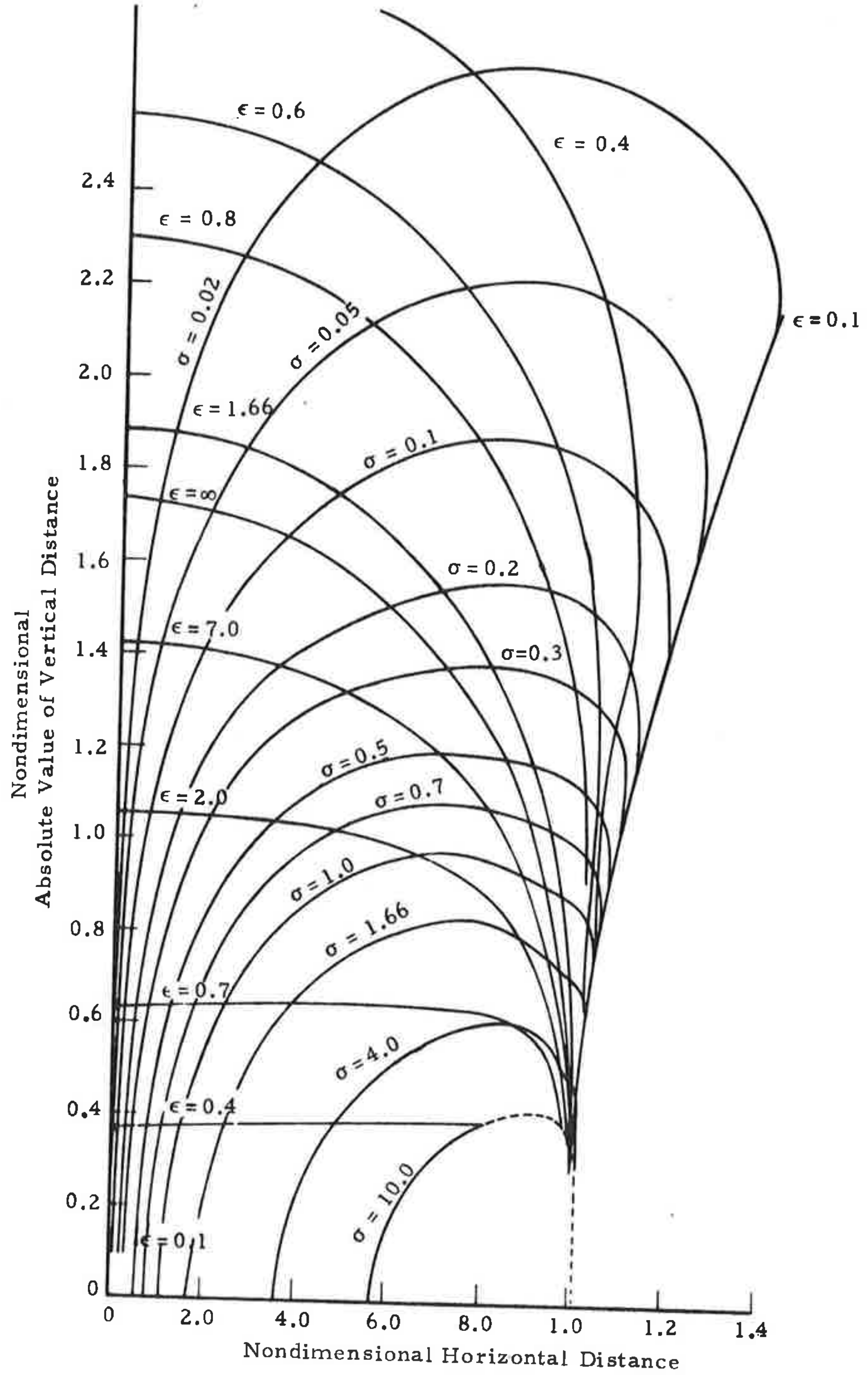

Fig. 6-2 - Location of Stagnation Points on Vortex Oval as a Function of Wind Shear and Proximity of Ground Plane

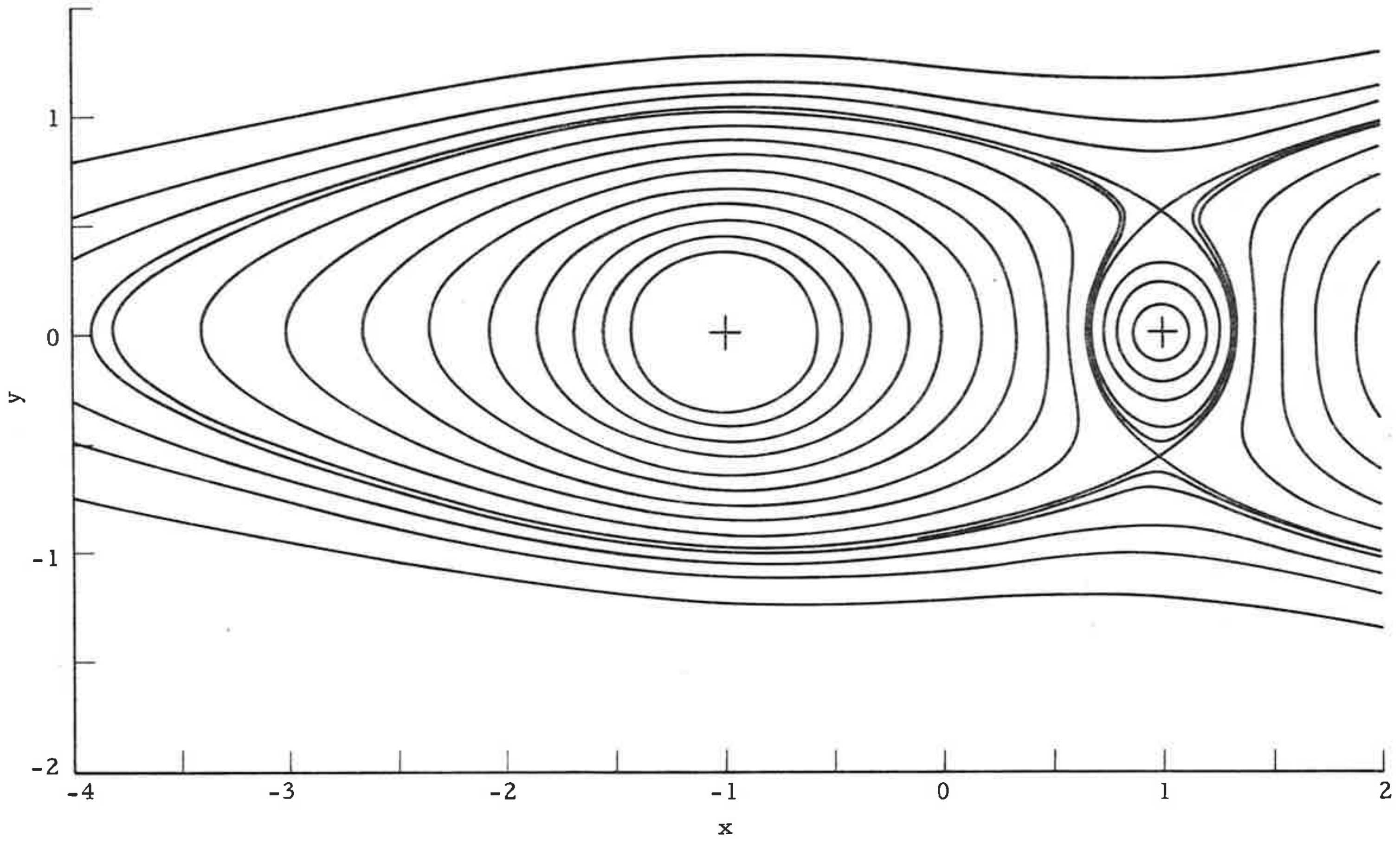

Fig. 6-3 - Streamlines for $\sigma = 3.0$, $\epsilon = 2.0$

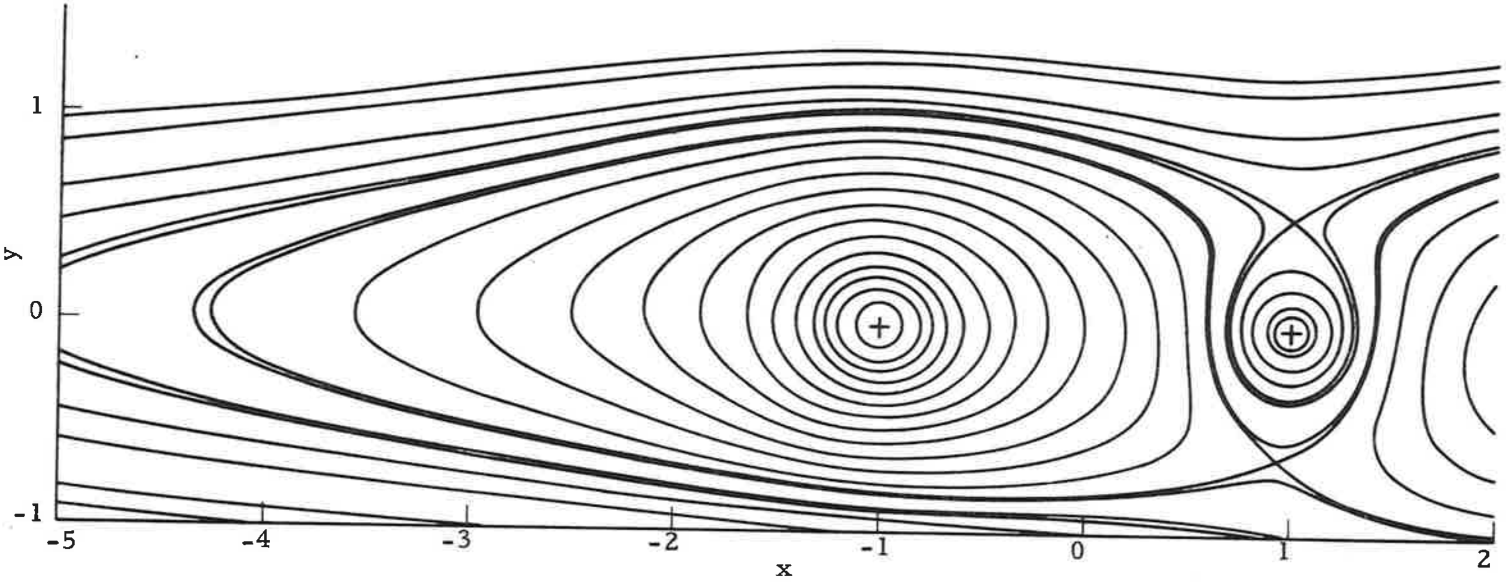

Fig. 6-4 - Streamlines for $\sigma = 3.0$, $\epsilon = 1.0$

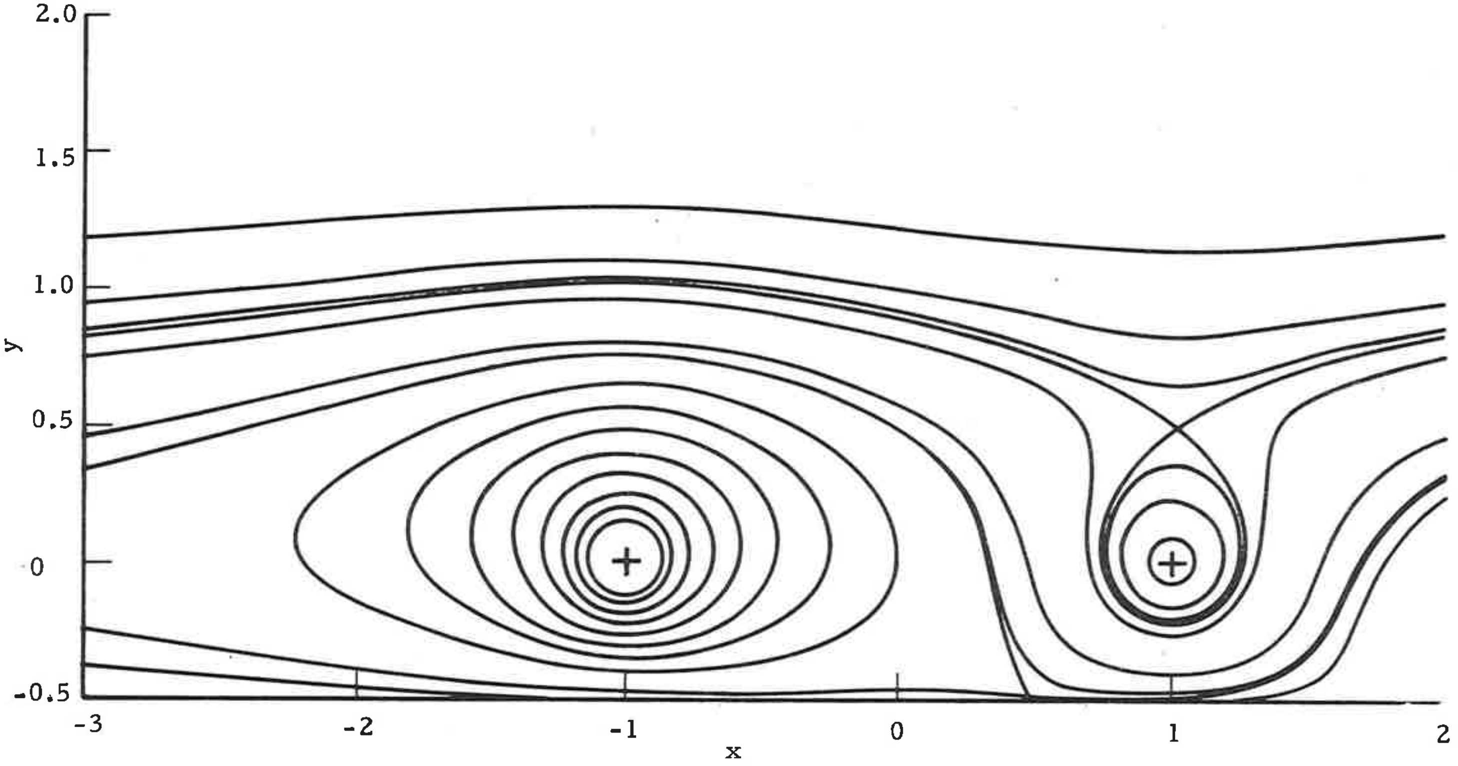

Fig. 6-5 - Streamlines for $\sigma = 3.0$, $\epsilon = 0.5$

detrainment of the upwind fluid to occur with the size of the streamtube increasing with decreasing ϵ as shown in Figs. 6-3 through 6-5.

The decrease in downwind cell area is shown in Figs. 6-6 through 6-8 for σ of 1.0, 2.0 and 3.0, respectively, for various values of ϵ. The scales of each figure are the same to show that increasing shear and decreasing ϵ reduce the size of the downwind vortex cell. An important observation is that the center of vorticity remains unchanged in this analysis ($y = 0$) but is not the center of the downwind cell. Corresponding streamlines passing through the lower stagnation point are shown in Figs. 6-9 and 6-10 for $\sigma = 1.0$, 2.0, respectively, for various values of ϵ.

6.2 ADDITIONAL THOUGHTS ON MECHANISM OF VORTEX TILTING

In Section 5.7 it was hypothesized that wind shear might correlate with vortex tilting. In Fig. 5-54 a slight trend was observed for the upwind vortex to rise in a heavy shear while the downwind vortex appeared to rise in a slight shear. Because of the limited amount of data available, however, no definite conclusion could be reached. Also no attempt was made to explain the mechanism.

Consider the data plotted in Fig. 6-11. This represents the maximum difference in altitude between the downwind and upwind vortices ($\Delta h\,max/\overline{h}$ positive means the downwind vortex is higher than the upwind) as a function of σ as previously defined. There appears to be a definite trend for the upwind vortex to be at a higher altitude for large shears and the downwind vortex to be higher in light shear. Also note the crossover point occurs at a σ of 0.3 to 0.4. The flybys were made with the aircraft at a 175-foot altitude ± 30 feet which defines the initial ϵ as roughly 3.0 for the B747, 4.0 for the B707 and 5.0 for the B727. Figure 6-2 shows the crossover point for these values of ϵ as between $\sigma = 0.3$ and $\sigma = 0.4$. This agrees surprisingly well with the experimental data if it is assumed that the upper stagnation point trend defines which vortex rises.

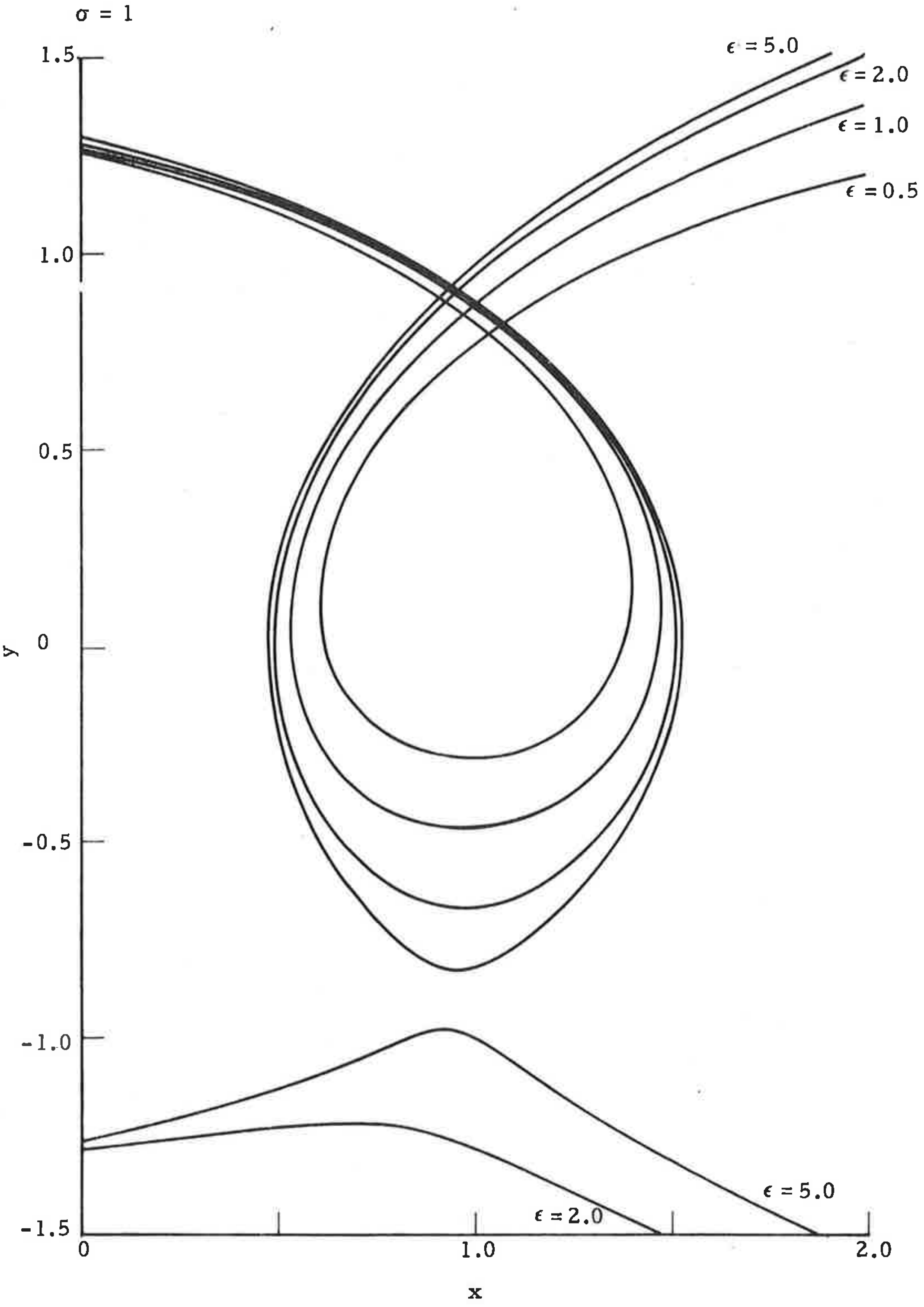

Fig. 6-6 - Streamlines Passing Through the Upper Stagnation Point for $\sigma = 1$ and Various Values of ϵ

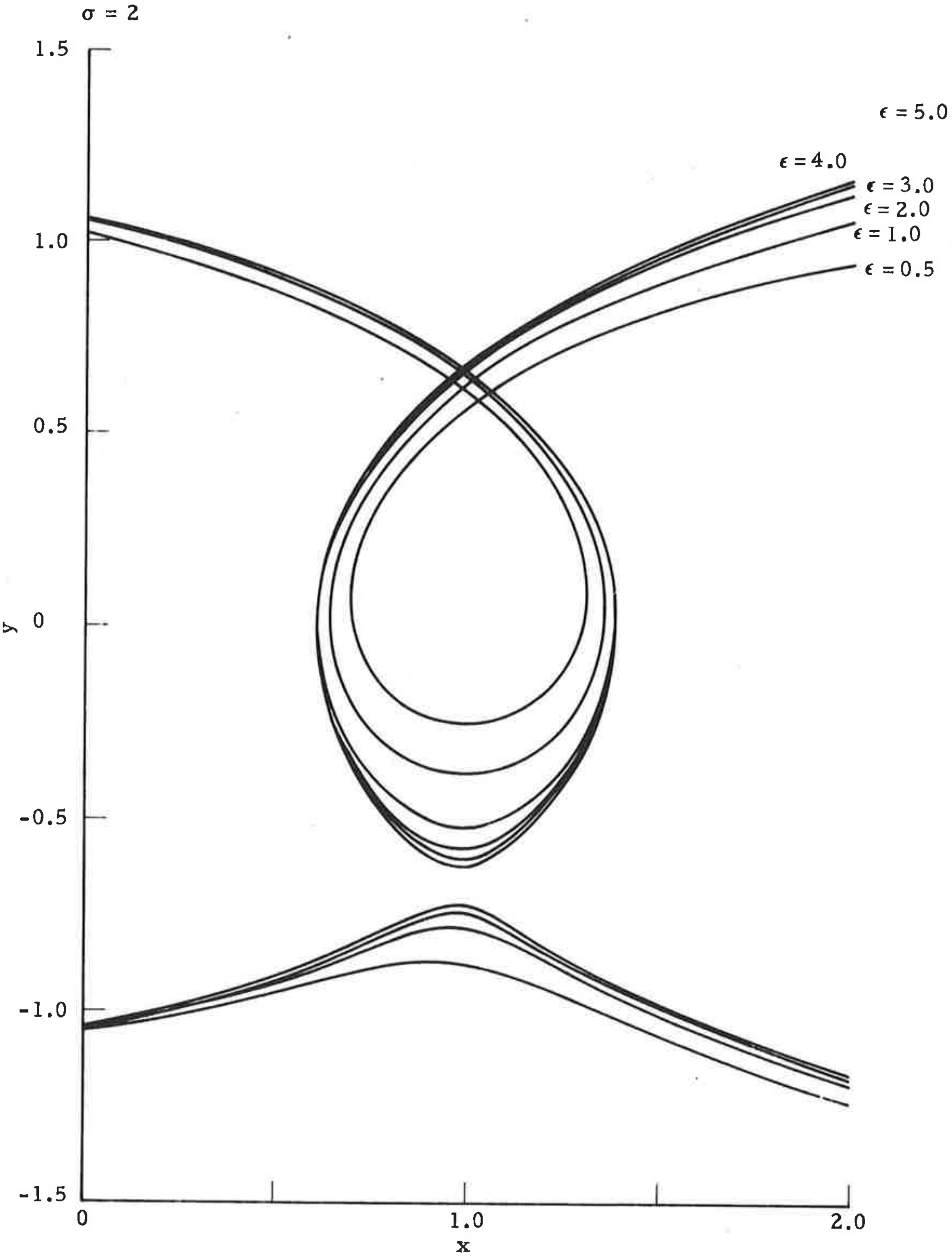

Fig. 6-7 - Streamlines Passing Through the Upper Stagnation Point for $\sigma = 2$ and Various Values of ϵ

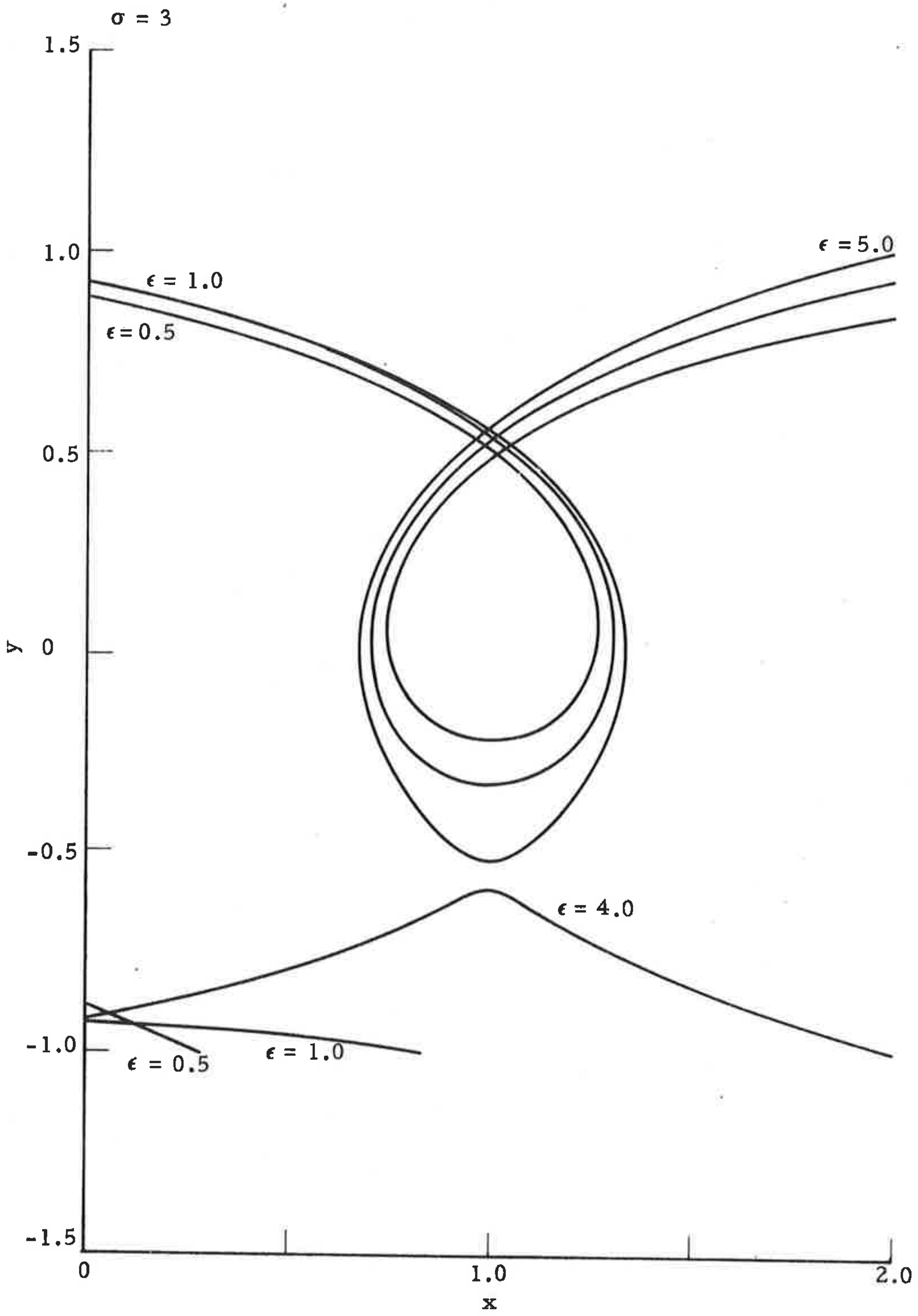

Fig. 6-8 - Streamlines Passing Through the Upper Stagnation Point for $\sigma = 3$ and Various Values of ϵ

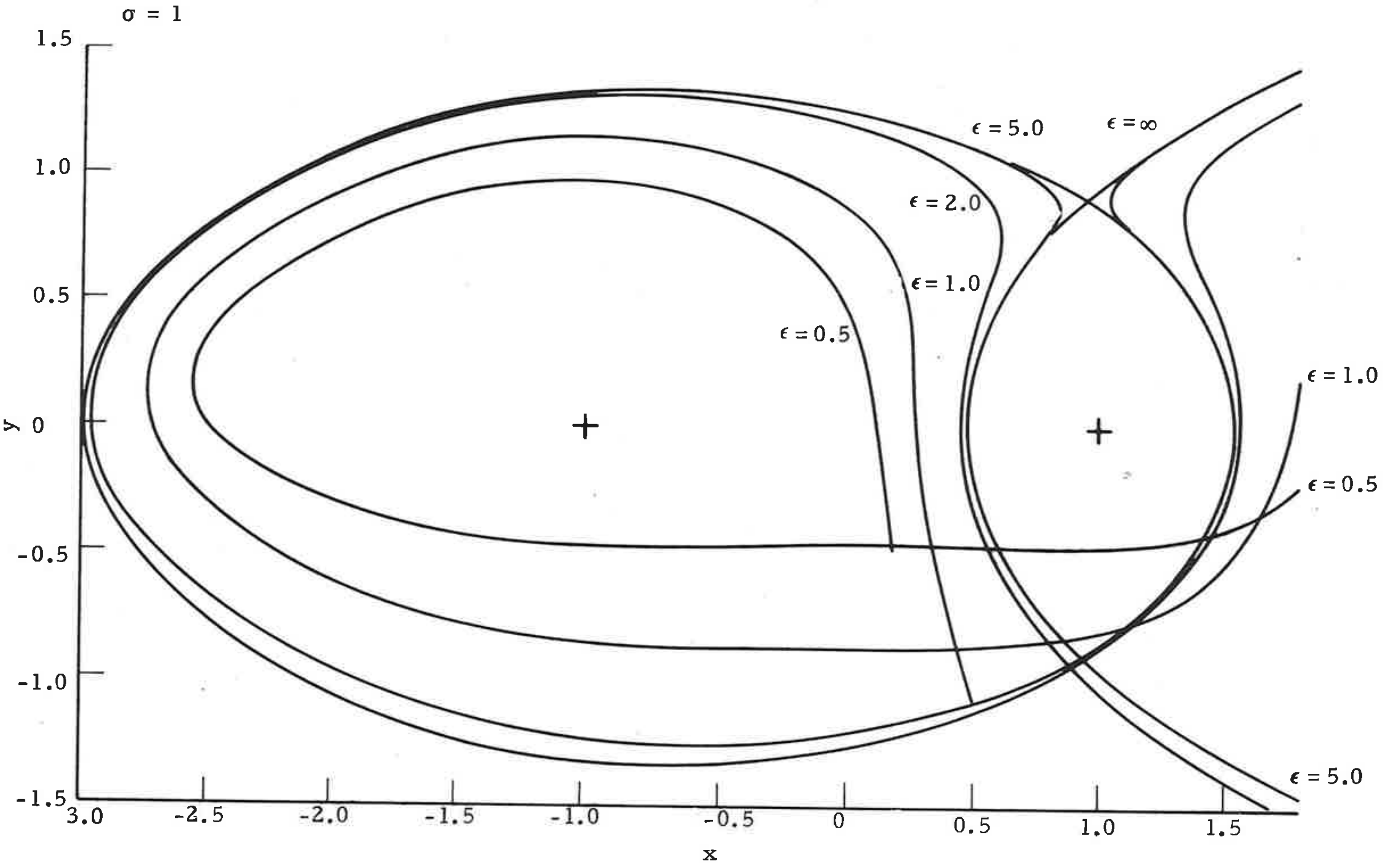

Fig. 6-9 - Streamlines Passing Through the Lower Stagnation Point for σ = 1 and Various Values of ϵ

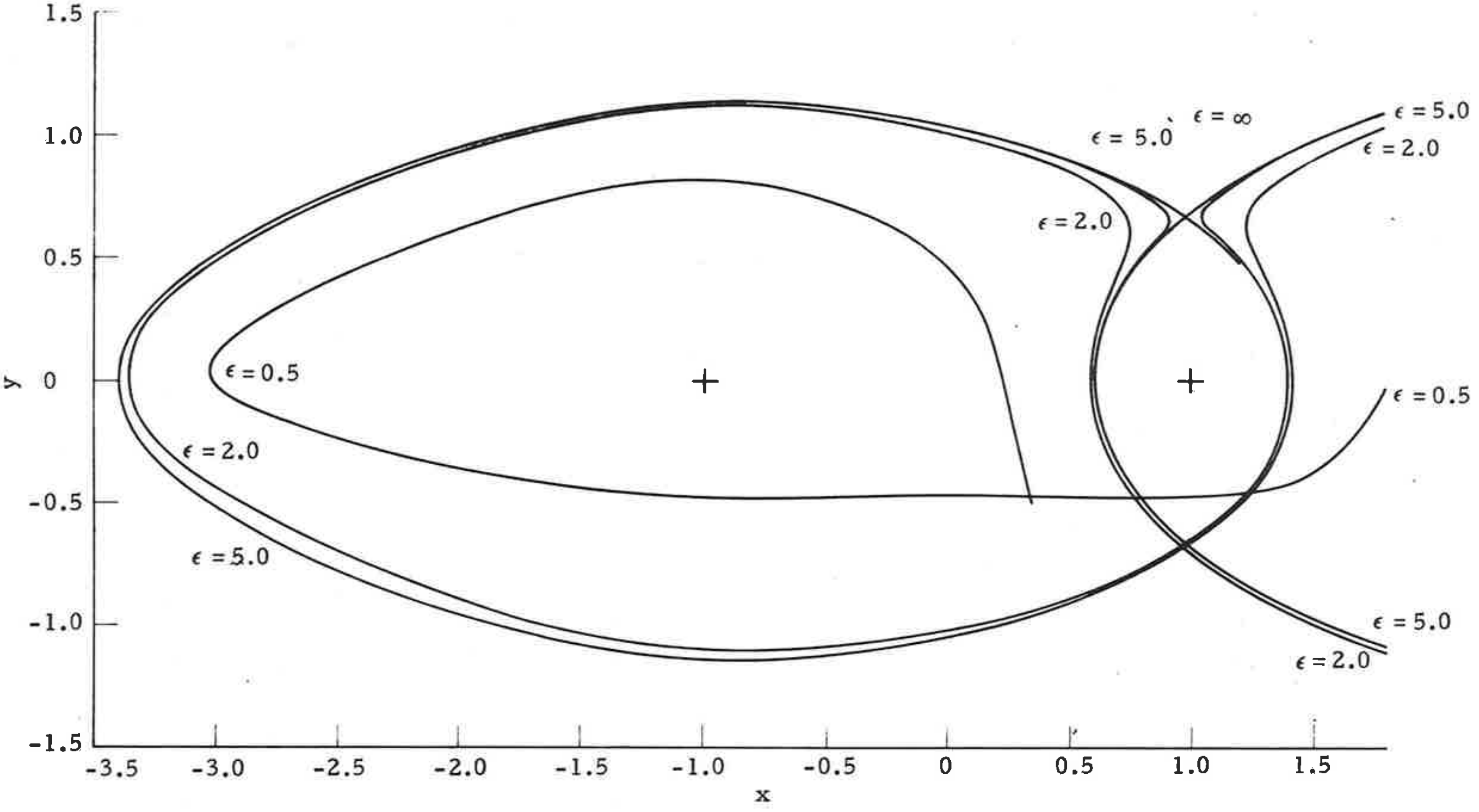

Fig. 6-10 - Streamlines Passing Through the Lower Stagnation Point for $\sigma = 2$ and Various Values of ϵ

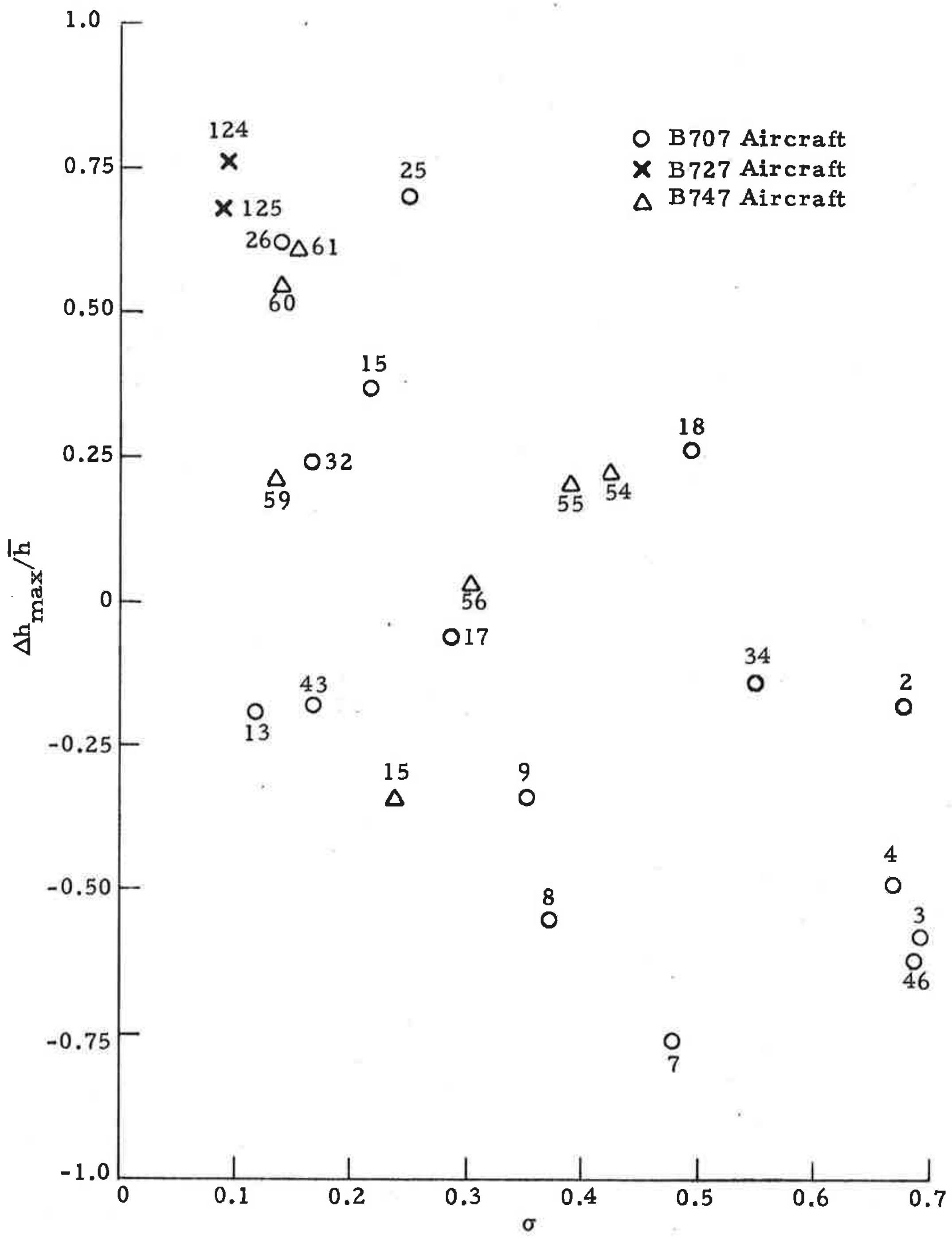

Fig. 6-11 - Vortex Altitude Mismatch vs Sigma

Figure 6-12 shows the same altitude differentials plotted versus a parameter containing lapse rate information (potential temperature, θ), wind shear and circulation. This is essentially an extension of the thought presented in Fig. 5-57 to include the parameter σ.

6.3 SUMMARY OF PRELIMINARY OBSERVATIONS ON VORTEX TILTING

6.3.1 Observations from the Simplified Theory

- In a light shear the upper stagnation rises as the oval descends toward the ground.
- In a strong shear the upper stagnation moves closer to the ground.
- Wind shear tends to move the stagnation points downwind.
- Ground proximity tends to draw both the stagnation points toward the ground in a strong shear.
- Ground plane tends to "open up" a region between the two cells and cause a sweeping motion of the external stream around the cells.
- The downwind cell gets smaller as wind shear and ground proximity increase.
- The upwind cell increases in area as wind shear increases and altitude increases.

6.3.2 Possible Implications of These Preliminary Results

- The downwind vortex cell shrinkage with increasing wind shear may give rise to an increased detrainment of vorticity as the increasing core size will encounter the inviscid cell boundary quicker than in the upwind case. This would cause the upwind vortex to rise due to the decreased induced velocity by the downwind vortex.
- The sweeping motion, as previously discussed, might cause upwind cell detrainment, thus causing the downwind vortex to rise.
- The asymmetry produced by the effects of wind shear and ground plane might cause illusions in the photographic data

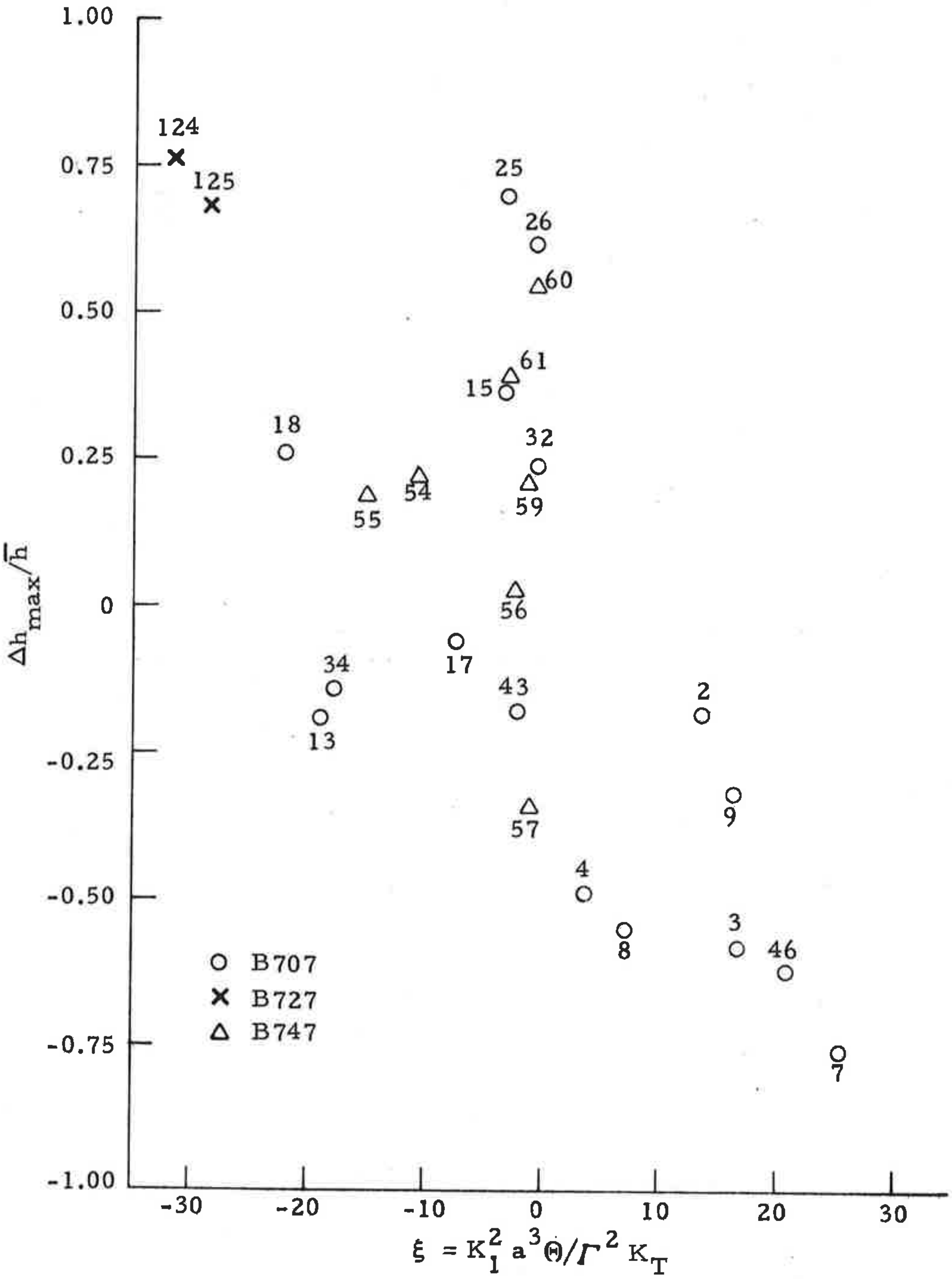

Fig. 6-12 - Vortex Altitude vs Mismatch Wind Shear-Buoyancy Parameter when vortex rising is seen. For example, it appears from the streamlines in Fig. 6-6 that the center of vorticity is at a higher altitude than it actually is, thus causing an illusion of downwind vortex rising if the center is chosen as the center of the core.

- This asymmetry might give rise to a reorientation of vorticity and actually cause one vortex to physically rise.
- Even though an extremely limited amount of data is available on vortex tilting, the fact that the crossover point between upwind and downwind vortex rising based both on the simplified theory and available data cannot be overlooked and should be investigated further.
- Buoyancy effects, may be important as some increased success was obtained by considering lapse rate in the attempted correlations.

Section 7

RECOMMENDATIONS FOR VORTEX DATA COLLECTION IN THE VICINITY OF AN AIRPORT

7.1 GENERAL

In the consideration of the design of a monitoring system, it is implicit that the configuration should be very sensitive to the meteorological input requirements. As will be discussed below, the following variables are of considerable importance in extending the WVAS proof of concept study into a predictive off-line model:

1. Horizontal components of mean wind field
2. Stability, and
3. Turbulence.

The following is a discussion of the recommended specific requirements for such a system.

7.2 TOWER ARRAY

To optimize data collection considerations, an L shaped array is recommended. This array would consist of one (1) 150 foot tower and four (4) 50 foot towers. The 150 foot tower would be spaced logarithmically in a line formed by two of the 50 foot towers which are equidistant from the middle marker and perpendicular to the flight path. The remaining two 50 foot towers would be logarithmically spaced in a line perpendicular to that line formed by the first three towers and in line with the outer 50 foot tower of the first three (see Fig. 7-1).

The horizontal momentum transfer would be larger in the direction of the wind and the wind direction is most frequently along the orientation of the runway. Also the spectra for high frequency turbulence in the direction of the wind are approximately 3/4 of those values perpendicular to the wind. This

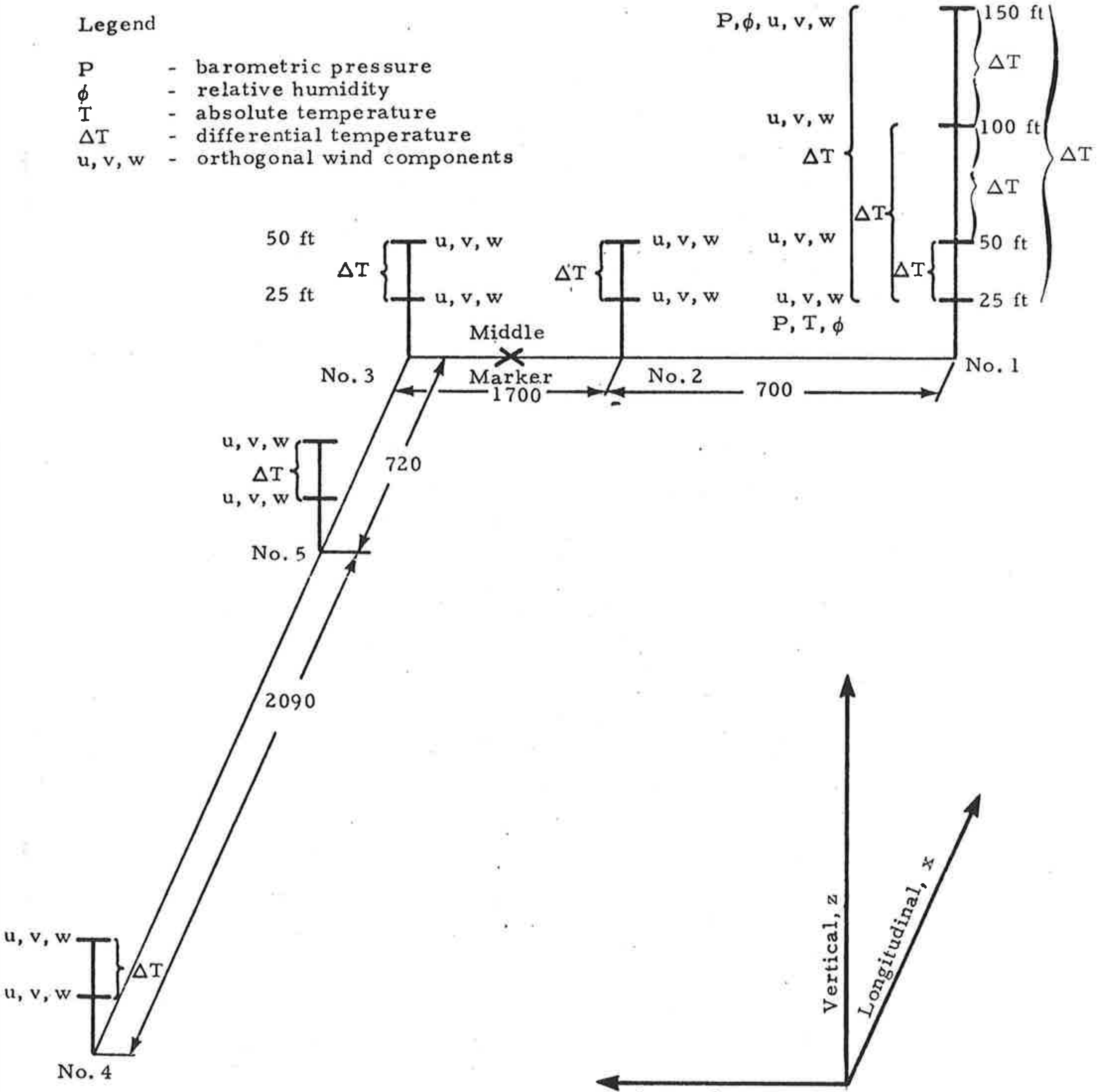

Fig. 7-1 - Schematic of Meteorological System implies a longer wavelength in the direction of the wind. Thus, the ultimate length of the longitudinal tower row (most frequent wind direction) should be greater than that of the lateral tower row. The order of magnitude of the tower row lengths is determined by a compromise between what is deemed necessary to correlate measurements among the towers and what is large enough to sense large scale horizontal momentum transfer. The value of adding a fifth 50 foot tower in order to create a rectangular region of measurement is questionable since it would not be expected that any significant lateral gradients that exist would vary over the longitudinal range of sensing provided that the topography (grass length, surface composition, surface flatness, etc.) is approximately homogeneous in nature. The homogeneous surface assumption would not be valid (laterally) in the vicinity of the runway itself due to the extreme differential between the radiative effects of it and the surrounding terrain. There is a substantial advantage in logarithmic spacing in the horizontal plane from a purely meteorological standpoint, and is recommended in order to optimize data considerations.

7.3 SENSOR LOCATIONS ON TOWERS

The stability conditions prevalent will be neutral or near-neutral most of the time. Under these conditions, the mean horizontal wind component will increase logarithmically with height. It is desirable, although not essential, to have the wind sensors spaced logarithmically in the vertical direction on the 150 foot tower in order to optimize the data reduction technique. The sensors will not be precisely spaced as such, however, due to the desirability to place the highest sensor on the top of the 150 foot tower. It would be desirable to place the sensors for various other parameters which need to be measured at equivalent heights (where necessary) to that of the wind sensors from a logistics standpoint.

In summary, it is recommended that the sensor locations be at the 25 and 50 foot levels on the 50 foot towers, and at the 25, 50, 100, and 150 foot levels on the 150 foot tower.

7.4 DATA SAMPLING RATES

The only parameter which would have a relatively high frequency input to the WVAS model would be the wind and thus would be the only measured quantity significantly constrained by the response of the sensors. In order to make full use of the instrumentation network, it is suggested that 12 samples per minute are sufficient for all quantities except wind. Statistically, 10 samples per second will satisfy the requirements for the wind energy spectra and is consistent with the proposed propeller anemometer distance constant.

7.5 WIND MEASUREMENT

The Gill UVW propeller anemometer is recommended for the proposed system. This decision was based on several reasons of which not the least important is the dependable, low cost, near trouble-free operational characteristics of the Gill. Before arriving at this decision, several other instruments were considered, including the wind component meter (WCM), vector-vane, sonic anemometer, hot wires, etc. The aforementioned instruments offer higher frequency response than the UVW; however, because of the physical dimensions of the proposed arrays (defined by the number of towers to be used) the high frequency information would be lost in the correlation. Furthermore, the small scale turbulence is not nearly as important as the low frequency components in defining the meteorological conditions in the sensing region. All of these reasons single out the Gill UVW as the basic instrument, especially considering the reliability of the final system.

In mounting this instrument, caution should be exercised such that minimum interference from the tower will be experienced. In its optimum configuration, the sensor unit would be mounted on a boom extending well away from the tower and at right angles to the prevalent wind direction.

7.6 TEMPERATURE MEASUREMENT

Only one absolute temperature sensor need be utilized. Its purposes would be to provide a parameter to correlate diurnal and seasonal trends in other phenomena related to the WVAS and to compute the potential temperature (by use with pressure). The sensor proper would be of the thermister probe type and be mounted in a radiation shield. The shield provides sensor protection from incoming shortwave solar radiation as well as outgoing longwave radiation. The shield should be power-aspirated to provide high heat transfer from the ambient air to the sensor. Under maximum solar radiation conditions the shield would maintain the sensor within approximately 0.50°C of the true ambient air temperature. Overall accuracy of measurement is expected to be ± 0.5°C. The Meteorology Research, Inc. (MRI) model number 8-40-5 is recommended.

Differential temperature (ΔT) measurements should be made on each of the towers. Sensor locations for these measurements will be at the 25-foot and 50-foot levels of the small towers. The large tower will have sensors located at the 25, 50, 100 and 150-foot levels. This sensor arrangement will provide one ΔT measurement from each of the four small towers, and six ΔT measurements from the large tower in addition to the absolute measurement. As will be explained later, ΔT measurements may be used to determine the atmospheric stability. In addition, if a quantitative measure of stability is determined to be of essence to the WVAS predictive model, ΔT may also be used to compute the Richardson number.

The adiabatic lapse rate for the atmosphere is approximately -0.01°C/meter; therefore, since the actual lapse rate will not differ substantially from this, an instrument which will provide a ΔT measurement of 0.09°C is sufficient over the range of 25 feet or greater. Thus, Meteorology Research Incorporated's best standard differential temperature measurement system (MRI Model 8-40-1-3) is suggested for this task. This system will provide differential temperature within 0.09°C including radiation errors as well as sensor element and electronics errors. The sensor is factory calibrated and seldom requires field calibration. A matched pair of thermisters is used as the sensing element in each end of the ΔT sensors.

7.7 BAROMETRIC PRESSURE MEASUREMENT

Pressure differentials in the vertical may be essential in establishing a correlative trend in the WVAS incorporating large periodic air mass modifications or frontal passages. Absolute barometric pressure measurements are also needed to compute the potential temperature near mid range of the ΔT measurements (by use with the absolute temperature measurement at 25 feet). Thus, it is suggested that two barometric pressure sensors be located on the 150 foot tower only, one at 25 feet and one at 150 feet. The sensor recommended is the MRI Model 1751 which incorporates several stacked diaphragms mechanically linked to a precision potentiometer and provides measurements in the range of 28 to 32 inches of mercury. The linearity of measurement is expected to be ±0.3% of range with a repeatability within 0.2%. The sensor is contained within a small weatherproof housing and is remote from the associated electronic package.

7.8 RELATIVE HUMIDITY MEASUREMENT

The measurement of relative humidity at the 25 foot level may be useful, although not absolutely essential, in establishing a necessary variable for computation of potential temperature. (The exponent usually used is that for dry air and does not as a rule create a significant error as an end result. This can be easily proven.) However, it would be most desirable to monitor this parameter in order to correlate its value with vortex behavior, particularly, decay rate. It is suggested that this parameter be monitored at the 25 and 150 foot levels on the large tower in order that a gradient, if one exists, may be detected. The recommended sensor is MRI model 8-40-5. The sensor proper is mounted in a power aspirated shield similar to that used for the absolute temperature probe. This shield provides protection from external influences while providing free access to the ambient air. The accuracy of measurement is expected to be ±3% of full scale (100% RH) with a repeatability within 0.5%. The sensor operates on the principle of a bimetallic strip sensitive to humidity rather than temperature. Changes in humidity influence the shape of the strip which is sensed by a strain gauge bridge circuit.

7.9 ACOUSTIC SOUNDER FOR DATA ABOVE TEST SITE

A standard monostatic acoustic sounder would be useful in the data collection. This device emits acoustic pulses which are reflected by thermal turbulence in the atmosphere (a bistatic version of the instrument would be sensitive to mechanical turbulence as well as thermal). Thermal layers and stratifications such as inversions are readily visible in the atmosphere with this type instrument. The instrument would be useful for providing data above the 150-foot tower. This region is not readily accessible with the instrumentation currently planned for the test site due to height limitations imposed by FAA rules. The acoustic sounder would provide data at these heights without imposing a safety hazard. The sounder suggested for this option is the AeroVironment Model 300-1. It has a minimum full scale range of 200 meters and provides a resolution of 10 meters. The unit uses a 6 ft. diameter parabolic antenna and has a 7° beam width between 1/2 power points. It transmits at a rate of 1 pulse/2.4 seconds (this may be altered to prevent cross talk with the acoustic vortex sensors). The unit comes with a chart recorder which runs at a rate of 1.25 inches/hr.

7.10 SUMMARY OF SENSOR LOCATIONS

Table 7-1 and Fig. 7-1 provide a summary of sensor locations discussed in previous paragraphs. Each sensor should be mounted in such a manner that tower influences have negligible effects.

Table 7-1

SUMMARY OF SENSOR LOCATIONS

Sensor	Location (in ft. above reference level)					
	Small Tower		Large Tower			
	25	50	25	50	100	150
Wind (u, v, w)	x	x	x	x	x	x
Temperature (absolute T)			x			
Temperature (ΔT)	x	x	x	x	x	x
Relative Humidity (ϕ)			x			x
Barometric Pressure (P)			x			x

Certain of the sensors are shielded to provide maximum accuracy and protection from external effects (such as solar radiation). Those sensors requiring shielding are the temperature probes and the relative humidity probes. In addition, the UVW anemometers have a small blower in the lower housing which maintains a small positive pressure inside the instrument. Filtered air moves continuously out through each sensor to the atmosphere. This prevents rain and dust from entering the precision ball bearings and other internal parts of the sensors.

Power required for the sensors is sensor excitation power (low level dc) and 110 Vac for the blower motors of the shields.

7.11 SENSOR CALIBRATION

The signal recording (and/or processing) of all the meteorological variables must be accomplished in such a manner to allow the "raw" temporal data to be recreated within the original tolerance of the measuring instruments. One very important consideration, however, remains to be discussed, namely, the calibration of the final operational system.

The pressure, temperature and humidity sensors should be calibrated in a twofold fashion. First, standard laboratory techniques will be used to establish the calibration of the entire data collection system. After tower mounting no special tests need be performed; however, due to the redundancy of the system, inconsistencies can be determined during normal operation. If during the test another pressure or temperature data point is needed, the local airport pressure and temperature can be obtained (say one sensor failed).

To calibrate successfully the wind measuring system a twofold approach is again suggested. First a laboratory (or field test off the tower) calibration should be performed by driving the tachometers with a synchronous motor at a prescribed rpm corresponding to either a head-on condition (21.3 mph) or a stall condition (3.55 mph). This will assure similar electrical characteristics of all of the instruments. The sensors should then be mounted on the tower at the chosen position and leveled along the u component chassis. (The orthogonality of the UVW's will be established by the vendor prior to tower mounting.) The relative position of the u and v components in the horizontal plane will next be established via survey techniques. This will be accomplished by previously equipping the UVW chassis with at least two cross hair targets (one on the central electrical housing and one near the end of the u-component axis) and aligning the system with one man on the tower at the instrument and one man on the ground with the transit. The system should be periodically recalibrated according to vendor specifications.

It is felt these suggested techniques are adequate to meet successfully the requirements of the system design and yet simple enough to be practical. The FAA provided Comanche aircraft with total temperature, turbulence, dew point and wind measurement instrumentation could be used for backup qualitative checks of system calibrations.

7.12 SENSOR RELIABILITY

The suggested sensors are all of proven designs that have demonstrated acceptable lifetimes under adverse conditions. Minimum replacements are anticipated with the possible exception of the propellers for the UVW anemometers. These propellers are constructed of polystyrene to achieve maximum sensitivity and fast response and are subject to damage from hail, bird, or insect activity, etc. Spare propellers would be available to replace any that are damaged. The dc tachometer generators in the anemometers have an expected lifetime of one billion revolutions (3 to 4 years of normal operation).

Replacement of sensors that fail in the field would be relatively simple for those mounted on the small towers. The small towers hinge at the 25-foot point and can be cranked down for calibration or replacement of sensors. Sensors mounted on the large tower would be accessible by climbing the tower and hauling up any replacements required. Booms extending out from the tower would be retractable types which facilitate instrument removal and/or service.

7.13 DISCUSSION OF COMPUTED METEOROLOGICAL VARIABLES

● Stability and Wind Profile Determinations

The determination of the proper wind profile is of profound importance in determining vortex movement behavior. The singular most important characteristic in determining the shape of the total horizontal mean wind profile is the stability condition present in the layer through which the vortex pair moves. By using a mean value determined from the various ΔT values or by using the ΔT value between 25 and 150 feet on the large tower and comparing these mean values with the general meteorological conditions (as given by standard airport measurements and observations) over a long period of time (on the order of several months), a cross correlation between wind profile curve fit, temperature gradients, and general meteorological conditions may be obtained. This, in essence, would provide a categorization of atmosphere stability. The results of this extension of the proof of concept would, in a predictive model, allow direct computation of the total horizontal mean wind profile by use of standard airport measurements providing that the aerodynamic roughness length is known. This will be discussed later.

It may also be desirable to determine the degree of correlation of vortex behavior and a quantitative measure of stability. The parameters measured directly are totally sufficient for a computation of the Richardson number which is such a quantitative measure.

● The Ekman Spiral Effect

The wind direction will rotate (change in azimuth) as a function of height. The rate of rotation may be determined theoretically by use of high altitude radiosonde data at any given site. The actual spatial rate of rotation would be more suitably determined by direct measurement and compared to the general meteorological conditions over a period of several months. There should not, at any given site, be an appreciable difference in the azimuth angle variation with height as a function of time. Therefore, the important consideration is to establish this profile once so that given a wind measurement at a given height, the remainder of the profile may be assumed in a predictive model.

- Wind Shears

Wind shears (velocity gradients in the vertical) may be computed and correlated to vortex behavior directly using the suggested instrumentation. Thus if a behavioral trend is defined to be a function of either total wind, cross runway (lateral), or down runway (longitudinal) shear magnitude and/or gradient sign in the proof of concept; the total wind profile in conjunction with the Ekman spiral effect as established previously may be used in a predictive model.

- Turbulence

Of all variables, turbulence in an uncontrolled environment is the most unpredictable. It may be expected that under increased velocity conditions, the effect of turbulence will change. Once the representative roughness length for the surface is determined, it is a simple matter to compute the turbulent energy for a particular frequency or scale of momentum transfer under neutral conditions. The computation of the exact turbulence level in conditions other than neutral is a problem which has not been suitably solved at this time. It is recommended that any application of this input to a model be observed closely for a period of several months. This may resolve the question of whether or not the assumption of neutrality is critical to vortex movement as a function of turbulence level.

- Convergence and Divergence

The vertical momentum exchange can be roughly estimated on a large scale basis by the input of the wind speed and direction along the boundaries of an imaginary horizontal plane. In this case, two such planes would be available such that there would exist an imaginary parallelopiped. Numerically, then, a downdraft/updraft can be estimated if a divergence/convergence to the parallelopiped is indicated. The occurrence of these phenomena can then be correlated to vortex behavior.

7.14 DETERMINATION OF A REPRESENTATIVE ROUGHNESS LENGTH

The roughness length or parameter, Z_o, cannot be suitably determined with the suggested long term instrumentation for two reasons:

- The large tower's top two sensors will extend out of the region of constant shear stress (the surface boundary layer) for most, if not all, of the time, and
- Two levels of measurement are insufficient for making even a rough estimation of Z_o due to the small order of magnitude of this number and the requirement that this determination be made under nearly neutral conditions.

It is recommended that a determination be made of Z_o separately over at least one representative segment of the site surface, but preferably three. Each surface studied would require at least one day of data collection. The instrument preferably would consist of five or six logarithmically spaced sensors on a low dynamic influence tower not exceeding 10 feet in height. The sensors recommended are fast response cup systems measuring horizontal wind only. Samples would, e.g., be taken as mean wind speeds over consecutive fifteen minute intervals. The samples exhibiting the most linear trend on a semi-logarithmic scale of height versus wind speed would be used to estimate the mean roughness length.

Section 8

CONCLUSIONS AND RECOMMENDATIONS

At the outset of this study a parametric study was performed to establish the relative magnitudes of the various mechanisms needed to define the total transport of aircraft wake vortices. In addition to defining these parameter magnitudes, a major objective was to define an uncertainty interval for the predictive vortex tracks to allow meaningful comparisons with the experimentally obtained vortex tracks. Initially these uncertainty increments were defined in terms of the standard deviations of the mean wind. It was found, however, that the resulting uncertainty in the predicted vortex tracks was too large to serve as a meaningful baseline uncertainty for both the parametric study and the experimental comparison. At this point the uncertainty due to the random velocity fluctuations occurring in the wind field was investigated as a candidate baseline uncertainty. This investigation resulted in choosing the baseline uncertainty as the difference in the lateral displacement for the upwind vortex at the middle marker and threshold points on the flight path. These lateral ranges were found to be typically ±140 feet after 60 seconds and ±200 feet after 120 seconds for the upwind vortex at the middle marker for a 20-foot per second wind perpendicular to the flight path. The uncertainties decrease in proportion to the square root of the mean wind and time. The corresponding values at the threshold are ±100 feet and ±150 feet for 60 and 120 seconds, respectively.

Comparison of parametric uncertainties with the baseline deviation established the following:

- Uncertainties of up to 25% in the initial vortex separation and 12% in circulation are contained in the uncertainty due to random fluctuations for winds above 6 feet per second for both the middle marker and threshold positions.

- General aircraft mix produces an uncertainty greater than the baseline value for both the middle marker and threshold positions.
- A light, medium and heavy aircraft mix classification produces uncertainties within the baseline errors and improves considerably from the middle marker inward.
- Three-sigma variations in approach altitude at the middle marker produce an uncertainty contained in the baseline value.
- Inside of the middle marker the aircraft altitude uncertainty becomes more important and the three-sigma range appears unacceptable.

After the baseline uncertainty range was established, the effect of this uncertainty was compared to differences noted between the predicted and measured vortex tracks. Twenty-five aircraft flybys were investigated to determine the magnitude of the predicted uncertainty versus actual difference between prediction and measurement. These comparisons were made for both the photographic data and the ground wind data. In all cases the downwind vortex predicted lateral range bounded the photographic and ground wind data. In most cases the upwind vortex track also bounded the data; however, when bounding did not occur the vortex tilting mechanism accounted for the discrepancy. This upwind vortex rising produces an increased downwind translation due to a higher wind or altitude. In any event, the predicted uncertainty increments bounded the experimental data. In fact, analysis of these 75 data sets (25 flybys with mean, plus and minus one standard deviation wind profiles) established that the aforementioned baseline uncertainty was in fact very conservative in nature as the difference between the mean prediction and measurement was consistently much less than that calculated from the baseline uncertainty. This gives rise to the general conclusion that reliable predicted vortex tracks can be generated with the resulting accuracy determined by how well one can specify the mean statistics of the wind field. The conclusion is subject to the restrictions in the forthcoming discussion on two sources of consistent error, namely the vortex tilting and non-elliptical wing loading.

The conclusions pertaining to determination of the wind profile are:

- Use of the NAFEC tower measurements for specifying the wind field was a reliable means except when vortex contamination of the data was involved and when the wind was blowing from zero to ±30 degrees. The former occurs when the one or two minutes of data used in the statistical analysis was affected by the induced velocity of the vortex pair (probably the upwind vortex). This occurred seldom as the raw data were scanned in an attempt to remove this problem. The latter occurs as a result of a 180-degree ambiguity in the wind direction around zero degrees in the data reduction program at NAFEC.
- The wind profile can accurately be determined without allowances for the Ekman spiral effect if an appreciable crosswind prevails. However, if the wind is predominantly along the flight path (headwind or tailwind) this effect must be included, or serious error may result.
- Application of the power law for wind profile calculations proved very successful. This conclusion is based on utilizing the standard NOAA surface charts routinely recorded at most airports for the reference velocity as well as any single-point measurement from the NAFEC tower. If a constant wind direction is assumed for all heights, precaution must be used for application of the power law class when the wind is along the flight path.

In general, excellent agreement was obtained between predicted and measured vortex tracks. However, two sources of consistent discrepancy were uncovered. First the predicted sink rate was consistently less than observed for most aircraft types (the B727 sink rate was very close to measurement which is probably due to the location of the outboard end of the flaps). It appears from preliminary data analysis that a 10 to 15% decrease in separation from elliptical calculations results for a B747 aircraft and DC-6 aircraft while a B707 yields a 5 to 10% decrease. No attempt has been made here to determine a detailed empirical relationship due to the limited amount of data giving the separation between the two vortices. This is because the smoke detrains (diffuses) so rapidly that there are not many common time points for any particular run. Also the ground wind sensor spacing is somewhat too coarse near the flight path to allow the initial vortex separation to be determined.

If a 20-foot spacing between ground wind sensors was employed near the flight path, the initial vortex separation could be obtained via a detailed aircraft type vortex separation correlation with the results then incorporated into the transport program for verification.

Secondly, the measured upwind vortex transport rate was found to be greater than predicted. This could be due to two separate reasons or a combination of both. A decrease in the upwind vortex vorticity due to the decreased cell size would give rise to an increased downwind translation rate as the tendency to move upwind is negated. The other consideration is that the vortex tilting causes the upwind vortex to be at a higher altitude, which means a larger wind, thus again decreasing the tendency to move upwind.

In summary it suffices to say that by inclusion of techniques to account for the nonelliptical wing loading and for vortex tilting, the vortex transport can reliably be computed with the concepts outlined in this study. The results obtained without the inclusion of these two mechanisms is surprisingly accurate with errors of 150 feet seldom occurring in the downwind vortex position. Also, the errors in the upwind vortex position are to the centerline side so the predicted track results in "safe" errors. However, this situation can give rise to unnecessary false alarms when applied to a wake vortex predictive system. Thus, additional work is warranted to include both nonelliptical loading considerations and a mechanism to reliably describe vortex tilting.

Other recommendations include producing predictive vortex tracks in an airport environment where the wind field is predominantly along the runway. To date, the analysis has centered around crosswind-type situations due to the testing requirements at NAFEC. In an airport environment more realistic data can be obtained. This will, however, prevent the uses of the smoke injection capability as used at NAFEC which has been a reliable source of experimental data.

REFERENCES

1. Gorstein, M., J. Hallock, and I. McWilliams, "Aircraft Wake Vortex Avoidance Systems," EASTCON-72 Proceedings, Washington, D.C., October 1972.

2. Wilson, D.J., M.R. Brashears, E.A. Carter, and K.R. Shrider, "Wake Vortex Predictive System," Lockheed Missiles & Space Company, Inc., Report FAA-RD-72-108 (also LMSC-HREC D306226), December 1972. (Summary presented at Accident Prevention Forum on Aircraft Approaches and Landings, National Transportation Safety Board, Washington, D.C., October 1972).

3. Brashears, M.R., and J.N. Hallock, "Aircraft Wake Vortex Transport Model," AIAA Paper 73-679, AIAA 6th Fluid and Plasma Dynamics Conference, Palm Springs, Calif., July 1973.

4. Tombach, I.H., "Observations of Atmospheric Effects on the Transport and Decay of Trailing Vortex Wakes," AIAA Paper 73-118, January 1973.

5. Lissaman, P.B.S., S.C. Crow, P.B. MacCready, Jr., I.H. Tombach, and E.R. Bate, Jr., "Aircraft Vortex Wake Descent and Decay Under Real Atmospheric Effects," Report FAA-RD-73-120, October 1973.

6. Crow, S.C., "Stability Theory for a Pair of Trailing Vortices," AIAA J., Vol. 8, 2172 (1970).

7. Lamb, H., Hydrodynamics, Dover Publications, 1945.

8. Spreiter, J.R., and A.H. Sacks, "The Rolling up of the Trailing Vortex Sheet and Its Effect on the Downwash Behind Wings," J. Aero. Sci., Vol. 18, No. 1, January 1951, pp. 21-32.

9. Betz, A., "Behavior of Vortex Systems," Zeit. für angewandte Math. und Mech., Vol. 12, No. 3, June 1932 (also NACA TM 713), June 1933.

10. Donaldson, C. duP., R.S. Snedeker, and R.D. Sullivan, "Calculation of the Wakes of Three Transport Aircraft in Holding, Takeoff, and Landing Configurations and Comparison with Experimental Measurements," Aero. Res. Assoc., Princeton, Report FAA-RD-73-42, March 1973.

11. Harvey, J.K., and F.J. Perry, "Flow Field Produced by Trailing Vortices in the Vicinity of the Ground," AIAA J., Vol. 9, August 1971, p. 659.

12. Burnham, D.C., "Effect of Ground Wind Shear on Aircraft Trailing Vortices," AIAA J., Vol. 10, August 1972, p. 1114.

13. Prandtl, L., and O.G. Tietjens, Fundamentals of Hydro- and Aeromechanics, Dover Publications, New York, 1957, p. 194.

14. Tombach, I.H., "Transport of a Vortex Wake in a Stably Stratified Atmosphere," in Aircraft Wake Turbulence and Its Detection, (ed. J.H. Olsen, et al.), Plenum Press, 1971, pp. 41-56.

15. Scorer, R.S., and L.J. Davenport, "Contrails and Aircraft Downwash," J. Fluid Mech. Vol. 43, 1970, pp. 451-464.

16. Tulin, M.P., and J. Shwartz, "The Motion of Turbulent Vortex-Pairs in Homogeneous and Density Stratified Media," TR 231-15, Hydronautics, Inc., 1971, AD 723 187.

17. Saffman, P.G., "The Motion of a Vortex Pair in a Stratified Atmosphere," Studies in Appl. Math., Vol. 51, 1972, pp. 107-119.

18. Kuhn, G.D., and J.N. Nielsen, "Analytical Studies of Aircraft Trailing Vortices," AIAA Paper 72-42, 1972.

19. Squire, H.D., "The Growth of a Vortex in Turbulent Flow," Aero. Quart., Vol. 16, August 1965.

20. Owen, P.R., "The Decay of a Turbulent Trailing Vortex," Aero. Quart., Vol. 21, February 1970.

21. Benjamin, T.B., "Theory of Vortex Breakdown Phenomena," J. Fluid Mech., Vol. 14, No. 4, 1962, pp. 543-629.

22. Harvey, J.K., "Some Observations of the Vortex Breakdown Phenomena," J. Fluid Mech., Vol. 14, No. 4, 1962, p. 629.

23. Ludwieg, H., "Zur Erklarung des Instabilitat des uber Angestellten Deltaflugeln Auftretenden Freien Werkelkerne," Z. Fluger., Vol. 10, 1962, p. 242.

24. Moore, D.W., and P.G. Saffman, "Structure of a Line Vortex in an Imposed Strain," in Aircraft Wake Turbulence and Its Detection, (ed. J.H. Olsen et al.) Plenum Press, 1971, p. 156.

25. Dee, F.W., and O.P. Nicholas, "Flight Measurements of Wing-Tip Vortex Motion Near the Ground," RAE Technical Report C.P.-1065, January 1968.

26. Hallock, J.N., D. Sheldon, and T. Foreman, to be published.

27. Lumley, J. L., and H. A. Panofsky, The Structure of Atmospheric Turbulence, Interscience Publishers, Wiley, New York, 1964.

28. Burnham, D. C., and T. E. Sullivan, "Preliminary Report, Calibration of Wake Vortex Sensors at NAFEC," to be published.

29. Thomson, J. A., "Study of Conceptual and Operational Feasibility of Laser Doppler Detection Systems," Progress Report for Contract NAS8-28410, November 1970.

30. Hallock, J. N., "Pressure Measurement of Wake Vortices near the Ground," J. Aircraft, April 1972, p. 311.

31. Burnham, D. C., J. N. Hallock, R. Kodis, and T. E. Sullivan, "Vortex Sensing Tests at NAFEC," DOT-TSC-FAA-72-2, January 1972.

32. Lau, Fisher and Fochs, "The Intrinsic Structure of Turbulent Jets," J. Sound Vib., Vol. 22, 1972, p. 379.

33. Pasquill, F., Atmospheric Diffusion, D. Van Nostrand Co., Ltd., London, 1962.